Probing organ structure, function and physiology using Quantitative Magnetic Resonance Imaging techniques

Christopher Richard Bradley MSci

Published works by staff candidate submitted to the

University of Nottingham

for the degree of Doctor of Philosophy

February 2023

Acknowledgments

It has taken a long time to complete the works within this thesis so there are a few people I would like to thank for their support whilst I collated this work.

Most importantly, I'd like to thank Prof Sue Francis who has supervised the work within this thesis. She is somehow available 24 hours of the day and always has a minute to talk about ongoing work, Sue is an inspiration, and I cannot thank her enough for the support and enthusiasm she has provided daily, which has led to multiple publications in this field.

I'd also like to thank Prof Neil Guha, Prof Guru Aithal, and Prof Dileep Lobo for their collaboration on this work and medical expertise to give insights into MRI measures' meaning with context to questions regarding physiology. Without them, their teams and research staff at the Nottingham Biomedical Research Centre, this work would not have been possible.

The Sir Peter Mansfield Imaging Centre has been a wonderful place to work, with an abundance of knowledge to tap into that has aided the research within this thesis. I'd like to thank the support staff, the technical staff, the research staff and in particular the hepatorenal group, Dr Eleanor Cox and Dr Charlotte Buchanan who have been great mentors and friends throughout.

I'd like to thank my parents and grandparents who pushed me toward academia after college and encouraged me to pursue a career in physics research that I have so far thoroughly enjoyed.

Finally, Lillie, who has stuck by me throughout this whole process, always there to pick me up through the difficult times, Lillie really has been an absolute rock for me on this journey and along the way gave me our three beautiful children Delilah, Dottie, and Koa. This is for us and for them, Delilah is 7 now and cannot believe how many words are in this thesis, I know she's proud, I know they all are and that is enough to keep me smiling every day.

Thank you.

"Chin chin" – Withnail

Table of Contents

Abstract

This thesis outlines four first author peer reviewed journal articles and three co-author peer reviewed journal articles submitted by the author for the award of the research degree Doctor of Philosophy by Published Works to the University of Nottingham. The focus of these works is to use novel Magnetic Resonance Imaging (MRI) techniques to probe the physiology of abdominal organ structure and function in healthy volunteers and patients with liver disease. The key aims of these published works were to: (**Publication I**) Cross sectionally delineate liver disease using MRI; (**Publication II**) Compute serial measures of the variation in quantitative MRI measures to understand the repeatability to aid the interpretation of data in future studies of clinical trials of drugs and interventions for disease progression; (**Publication III**) Use MRI to detect short terms changes to liver architecture in disease using a drug intervention; (**Publication IV**) Use MRI in healthy volunteers to dynamically observe changes to organ function during fluid infusions (colloid and crystalloid), to mimic the infusions typically used in gastrointestinal and liver surgery.

Publication I, titled '*Multi-organ assessment of compensated cirrhosis patients using quantitative magnetic resonance imaging'*, assessed multiple organs (heart, liver, kidneys, spleen and splanchnic systemic circulation) in a cohort of patients with liver disease in a single one hour scan session. This work showed that quantitative MRI measures have the power to predict negative liver related outcomes up to 2304 days before the event occurred. **Publication II**, titled '*Variability of Non-invasive MRI and Biological Markers in Compensated Cirrhosis: Insights for Assessing Disease Progression'* collected multiple organ (heart, liver, kidneys, spleen) serial quantitative MRI measures annually over a 3-year period in patients with severe but stable liver disease, and reports on the variability of these MRI measures. In this paper the annual variance in MRI measures is used to provide sample size calculations for prospective interventional studies investigating cirrhosis regression. **Publication III**, titled '*Short-term changes observed in multiparametric liver MRI following therapy*

with direct-acting antivirals in chronic hepatitis C virus patients', shows that quantitative MRI measures of the liver are sensitive enough to observe changes to liver structure in a 3-month window between pre- and post- treatment of a direct acting antiviral therapy in patients with chronic hepatitis C virus who achieved sustained virological response. **Publication IV**, titled '*A randomized, controlled, double-blind crossover study on the effects of isoeffective and isovolumetric intravenous crystalloid and gelatin on blood volume, and renal and cardiac hemodynamics'* showed that cardiac and renal quantitative MRI measures could detect haemodynamic changes over the time course of different crystalloid and colloid fluid infusion regimes typically used in gastrointestinal and liver surgery. There were no differences between infusion types despite the volume of a crystalloid infusion being three times that of one of the colloid infusions.

These research articles all applied MRI to evaluate abdominal organ physiology and present novel findings.

Three further co-authored publications are also briefly described. **Publication V**, titled '*Non-invasive assessment of portal hypertension using quantitative magnetic resonance imaging. Journal of hepatology*' demonstrated that quantitative structural and haemodynamic MRI measures can be used together to create a model that predicts portal pressure measurements, so MRI measures could be used as a surrogate for the hepatic venous pressure gradient (HVPG) procedure in patients with liver disease. This model was then applied to a validation cohort as proof of concept. **Publication VI,** *'Multiparametric renal magnetic resonance imaging: validation, interventions, and alterations in chronic kidney disease. Frontiers in physiology'* described a multiparametric quantitative MRI protocol for the assessment of the kidneys with recommendations for best practices and short term validation of measures. **Publication VII**, '*In silico evaluation and optimisation of magnetic resonance elastography of the liver*' used magnetic resonance elastography (MRE) simulations to evaluate current MRE techniques and offered optimisations to improve accuracy of MRE data acquisition and analysis.

Glossary

ADC – apparent diffusion coefficient

AIH – autoimmune hepatitis

ALD – alcohol related liver disease

ALT – alanine aminotransferase

APRI – AST to platelet ratio index

ASL – arterial spin labelling

AST – aspartate aminotransferase

bFFE – balanced fast field echo

BSA – body surface area

CC – compensated cirrhosis

CI – Cardiac Index

CO – Cardiac Output

CoV – coefficient of variation

DC – decompensated cirrhosis

DWI – diffusion weighted imaging

DTI – Diffusion Tensor Imaging

ELF – enhanced liver fibrosis

FEM – Finite Element Model

FIB4 – fibrosis-4 index

FID – free induction decay

GGT – Gamma-glutamyl Transferase

HA – Hepatic Artery

HBV – hepatitis B virus

HCV – hepatitis C virus

HV – healthy volunteer

HVPG – hepatic venous pressure gradient

INR – international normalised ratio

IR – Inversion Recovery

ISMRM – International Society for Magnetic Resonance in Medicine

IVIM – intravoxel incoherent motion

LA – Long Axis

LRO – Liver Related Outcome

LSM – liver stiffness measure

MELD – model for end stage liver disease

mFFE – multi fast field echo

MOLLI – modified Look Locker inversion recovery

MRI – magnetic resonance imaging

MRE – magnetic resonance elastography

NAFLD – non-alcoholic fatty liver disease

NICE – National Institute for Health and Care Excellence

NMR – nuclear magnetic resonance

NSBB – non-selective beta blockers

PIIINP – procollagen III amino-terminal peptide

PBC – primary biliary cirrhosis

PCA – phase contrast angiography

PPU – Peripheral Pulse

PSC – primary sclerosing cholangitis

PV – Portal Vein

QIBA – Quantitative Imaging Biomarker Alliance

RABF – renal artery blood flow

RCV – reference change value

RF – radio frequency

ROI – region of interest

SA – Short Axis

SE-EPI – spin echo - echo planar imaging

SMA – Superior Mesenteric Artery

SPA – Splenic Artery

SPIR – spectral presaturation with inversion recovery

TE – echo time

Td – trigger delay

Ti – inversion time

TIMP-1 – tissue inhibitor of matrix metalloproteinase 1

TR – repetition time

UKELD – United Kingdom model for end stage liver disease

VCG – Vector Cardiogram

VENC – Velocity Encoding

1. Introduction

1.1 Context of Thesis

The goal of this thesis is to provide an overview of the published works by Bradley *et al.* that investigate abdominal multi-organ (liver, kidneys, spleen, heart, and splanchnic systemic circulation) structure and function in patients with liver disease and healthy volunteers (HV) using quantitative magnetic resonance imaging (MRI).

The first publication (**Publication I**) evaluated significant differences in multiple organ structure and function using quantitative MRI between healthy volunteers, patients with compensated cirrhosis (CC) and patients with decompensated cirrhosis (DC) [1]. The second publication (**Publication II**) studied the year-on-year serial variability of clinical and quantitative MRI measures in a stable compensated cirrhosis cohort [2], giving insights into sample size calculations for longitudinal studies, for example for prospective studies of drugs such as antifibrotics. The third publication (**Publication III**) aimed to observe whether short term changes in quantitative MRI measures could be detected in response to antiviral treatment in a chronic hepatitis C virus (HCV) cohort [3], by collecting MRI scans pre- and <12 weeks post treatment. The final first author publication (**Publication IV**) compared peri-operative fluid balance [4] in healthy volunteers and showed that a smaller volume of a colloid infusion may be more beneficial than a larger volume of a crystalloid infusion [5] to some patient groups where water retention can be problematic and cause oedema within the extra cellular space.

In addition to these first author publications, co-authored publications are also outlined. The fifth publication (**Publication V**) used quantitative MRI to create a model that acts as a surrogate measure for hepatic venous pressure gradient (HVPG). The sixth publication (**Publication VI**) provided details of a multiparametric quantitative MRI protocol for assessment of kidney structure and function, offering best practices for such a protocol. The final publication

(**Publication VII**) used magnetic resonance elastography (MRE) simulations to evaluate current MRE techniques and offers optimisations to improve accuracy of MRE data acquisition and analysis.

Section 1 of this chapter provides a brief overview of the function of each of the organs studied within these works specifically the liver, kidneys, spleen, systemic circulation and cardiac system. The changes that occur as liver disease develops and the different aetiology of liver disease are shown. The current non-MRI reference standard methods used to assess the degree of liver injury are then outlined, including blood serum markers, biopsy, transient elastography liver stiffness measurement (LSM), and hepatic venous pressure gradient (HVPG). Section 2 then provides a classical explanation of the principles of nuclear magnetic resonance (NMR) and outlines quantitative magnetic resonance imaging (MRI) techniques used to study abdominal organ structure and function. Section 3 describes each of the four first author publications. Section 4 then provides a discussion of co-author publications and future works based on current literature and conference proceedings presented by the candidate. Section 5 concludes this thesis. Reprints of publications 1-VII and conference proceedings presented by the candidate are then provided in full.

1.2 Organ Physiology and Pathophysiology

Patients with liver disease are at an increased risk of the development of circulatory dysfunction that may potentially result in multiple organ failure [6]. Apart from the liver itself, this may affect the heart, kidneys, and other organ systems as outlined in **Figure 1**. As changes to various systems within the body occur as a result of liver disease, a therapeutic window has been proposed for therapies such as non-selective beta blockers (NSBB), outlining when such a treatment may have the most optimal positive outcome for a patient [7], see **Figure 2.**

1. Introduction

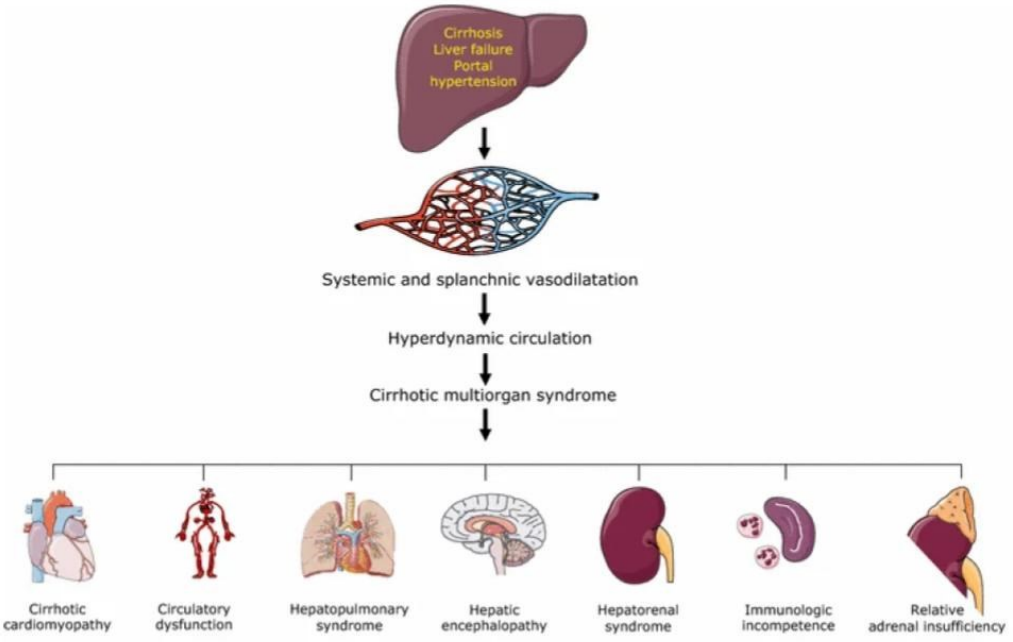

Figure 1: Infographic demonstrating changes to multiple organ systems within the body in response to liver disease, figure taken from [6], License agreement (**Appendix A**).

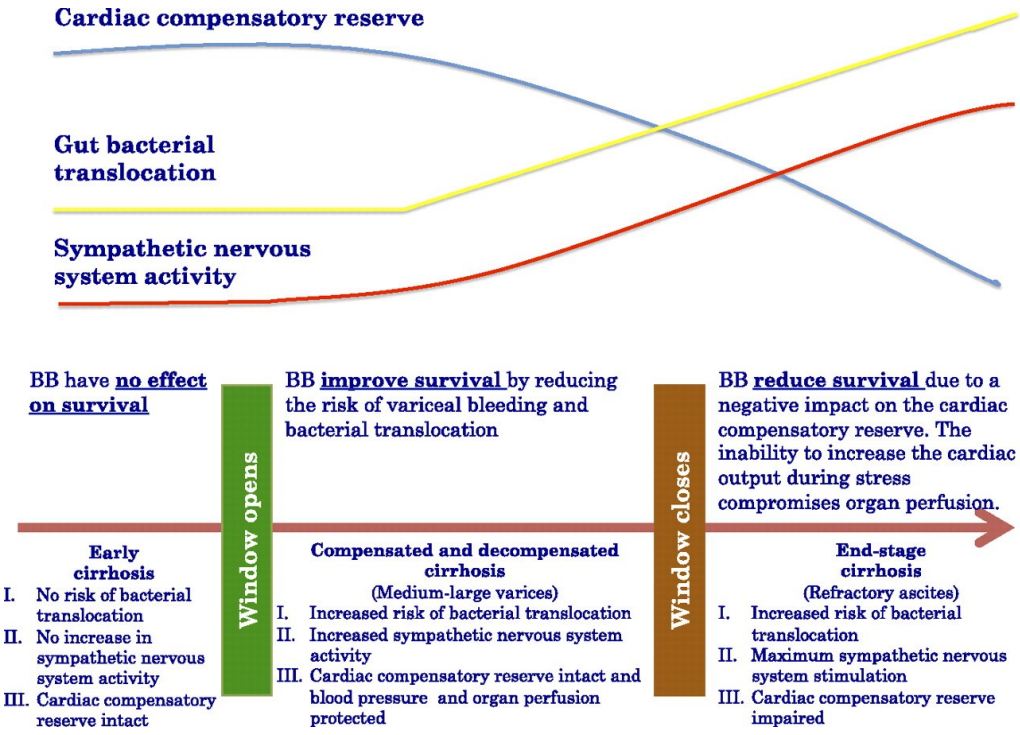

Figure 2: infographic detailing the therapeutic window and optimal time to treat patients with liver disease with non-selective beta blockers according to the stage of disease, figure taken from [7], License agreement (**Appendix B**).

Three of the published journal articles (**Publications I, II, III**) that form this thesis probe abdominal multi-organ structural and functional, in particular haemodynamic, changes in liver disease. **Publication IV** studies the changes that occur in cardiac and renal circulation in response to fluids given post gastrointestinal and liver surgery.

1.2.2 Abdominal organs and their function

Figure 3 shows the abdominal organs studied in this thesis, each of these are briefly described in the sections below.

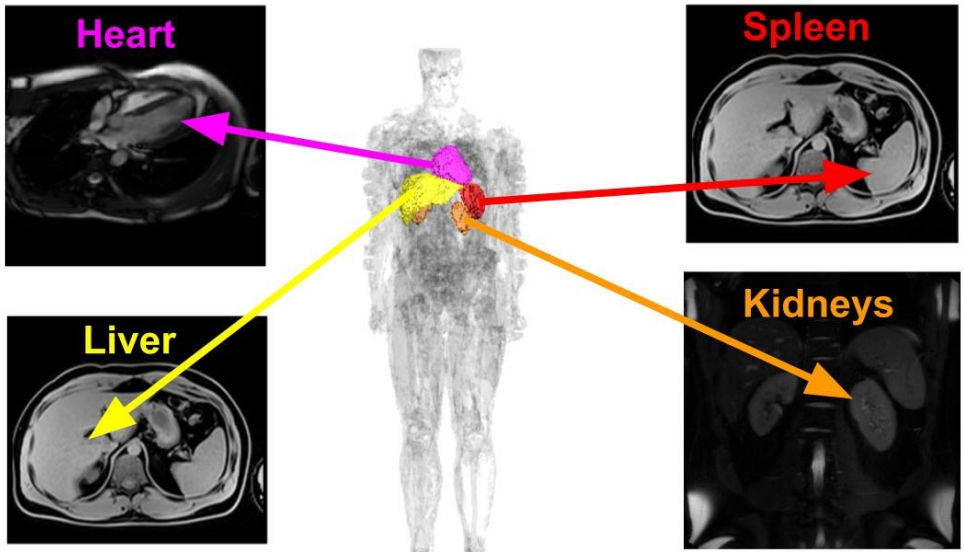

Figure 3: Whole body DIXON data 3D rendered with manual segmentation of the organs studied within the publications in this thesis and example data sets for each organ.

1.2.2.1 Liver

The liver activates enzymes for metabolising fats, proteins and carbohydrates within the blood that can then be used by other systems within the body. It is responsible for the production and excretion of bile that is then stored in the gall bladder. The liver excretes bilirubin, cholesterol and hormones as well as storing glycogen, vitamins, and minerals. The liver is unique in that it has both an arterial and venous blood supply, see **Figure 4**. Arterial oxygenated blood is delivered through the hepatic artery arriving from the abdominal aorta, whilst venous deoxygenated blood arrives through the portal vein from the stomach

and intestines. When the liver is diseased, several changes may occur from the presence of inflammation, this includes an increase in liver volume, and if the disease is chronic then scar tissue may also form within the liver parenchyma. In the later stages of disease, the vasculature of the liver may change, and shunting may occur where blood is rerouted directly back into the systemic circulation system away from the liver tissue capillary bed.

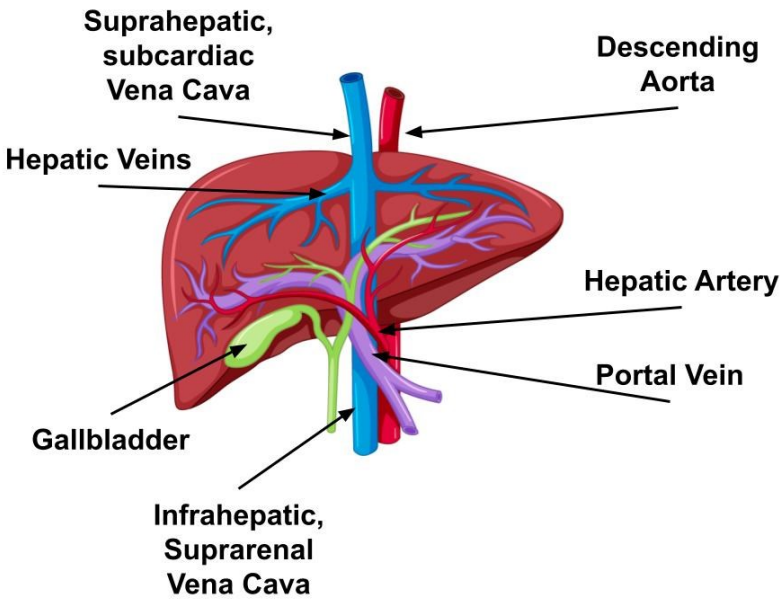

Figure 4: Diagram of the liver showing the dual blood supply to the liver through the Portal Vein and Hepatic Artery, and the Hepatic Veins that leave the liver. Image taken from © GraphicsRF / AdobeStock (**Appendix C**).

1.2.2.2 Kidneys

The kidneys filter blood as it arrives from the systemic circulation, with ~80% of the blood supply delivered to the renal cortex and the remaining ~20% delivered to the inner and outer medulla of the renal tissue [8]. The kidneys balance fluid within the body, removing waste water and maintaining the balance of salts and minerals. **Figure 5** outlines the anatomical regions of a kidney, cortex and medulla and its blood supply with delivery of oxygenated blood through the renal artery and deoxygenated blood leaving via the renal vein.

1.2.2.3 Spleen

The spleen regulates blood within the body, removing dead blood cells from circulation as well as maintaining white blood cell levels which are crucial for the fight against infection. Blood supply to and from the spleen is illustrated in **Figure 6**.

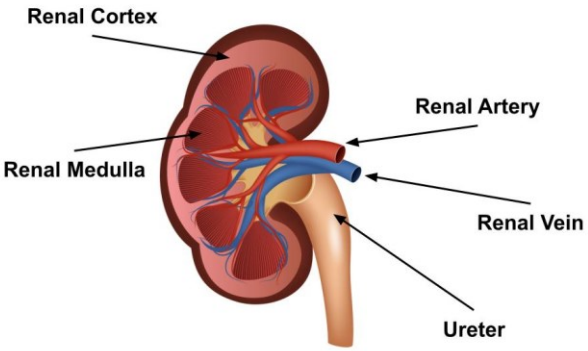

Figure 5: Diagram of a kidney, detailing inner and outer regions of the cortex and medulla, including renal blood supply through a renal artery. Image taken from © ajibon / AdobeStock (**Appendix C**).

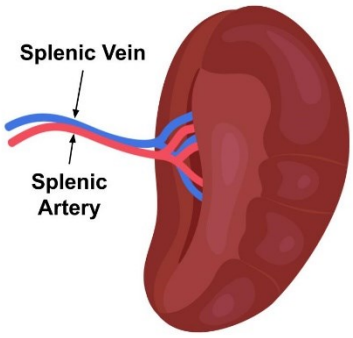

Figure 6: Diagram of blood supply to and from the Spleen. Image taken from © MihaiGr / AdobeStock (**Appendix C**).

1.2.2.4 Systemic and Portal Circulation

The systemic circulation comprises the blood supply flowing from the heart around the body to each organ apart from the pulmonary circulation. The systemic circulation carries blood to and from the liver, and the kidneys, as well as to the spleen. The portal circulation carries blood from the spleen, and gut

to the liver. In the published works within this thesis, blood flow (ml/s or ml/min) in the ascending aorta (AA), hepatic artery (HA) and portal vein (PV), splenic artery (SPA), superior mesenteric artery (SMA), renal arteries (RA) and renal veins (RV) are evaluated.

1.2.2.5 Cardiac system

The heart is comprised of four chambers divided into two pump like systems on the left and right, each with an atrium for arrival of blood, and a ventricle from where blood is pushed out of the heart toward other systems within the body. The right side of the heart pumps blood through the pulmonary system to the lungs, and the left side pumps blood through the systemic circulatory system, outlined in **Figure 7**.

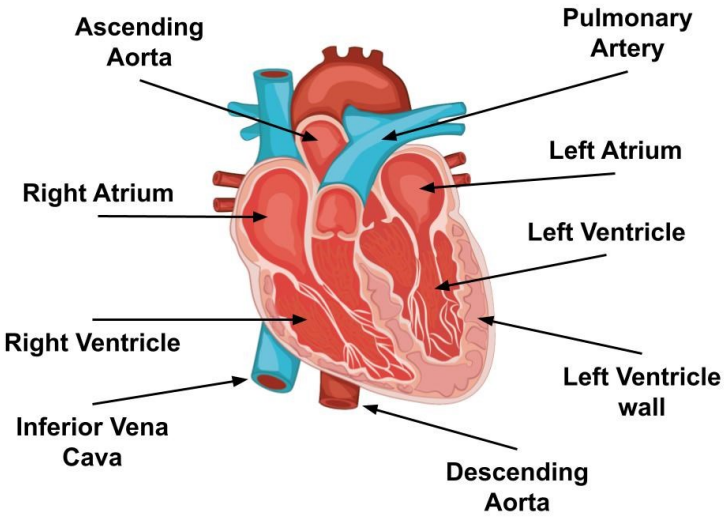

Figure 7: Anatomy of the heart, detailing the left and right side. Image taken from © okili77 / AdobeStock (**Appendix C**).

The heart controls the total global blood flow throughout both the pulmonary and systemic circulations. The volume of blood displaced by the cardiac system in a single heartbeat is termed the stroke volume. Multiplying the stroke volume by the number of heart beats in 1 minute (heart rate) gives the volume of blood pushed around the body within 1 minute and is defined as the cardiac output. Measures of cardiac output are typically normalized for body surface

area (BSA) to give cardiac index, which accounts for variations in human anatomy.

1.2.3 Pathophysiology of Liver Disease

There are many causes of liver disease, some hereditary, others the effect of lifestyle, and some a combination. In these published works, the most commonly evaluated liver disease types are non-alcoholic fatty liver disease (NAFLD), alcohol related liver disease (ALD), and Hepatitis C Virus (HCV), as well as haemochromatosis, primary sclerosing cholangitis (PSC), primary biliary cirrhosis (PBC), Autoimmune Hepatitis (AIH), and Hepatitis B Virus (HBV).

NAFLD is caused by a build up fat within the liver tissue. Though the presence of small amounts of fat within the liver tissue may not be harmful, larger amounts may lead to inflammation, fibrosis and eventually cirrhosis. ALD is caused by excessive intake of alcohol, either by consuming large amounts in a short period of time or moderate amounts over many years. Alcohol impairs liver function and excessive consumption eventually leads to inflammation and scarring of the liver tissue. HBV and HCV are both viruses spread through blood-to-blood contact such as sharing unsterilized needles. Once infected by a hepatitis virus, if left untreated, inflammation and eventually scarring will occur within the liver tissue. Haemochromatosis is a hereditary form of liver disease and causes people to absorb too much iron from their food, the accumulation of excessive iron over time will damage the liver and other organs in the body. PSC and PBC are less common and are caused by a reduction in the size of the bile ducts causing bile to remain in the liver which in turn damages the liver tissue. PSC is often associated with other inflammatory disease of the colon. AIH is an autoimmune disorder where the body's defensive system attacks its own cells, in the case of AIH the body has attack liver cells. Though there are many types of liver disease, the severity pathway is consistent across all types, with changes to steatosis, fibrosis, cirrhosis and finally cancer as shown in **Figure 8**.

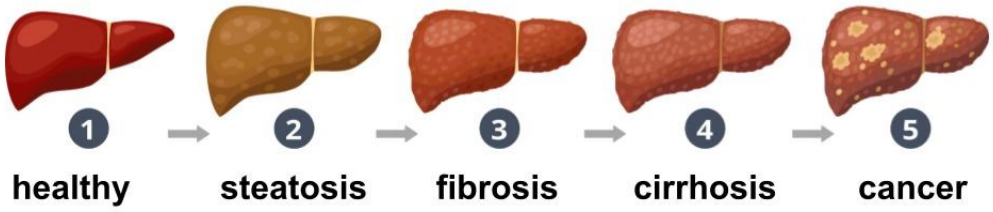

Figure 8: Stages of liver disease severity, from the healthy liver through to a cancerous liver. Image taken from © Bezvershenko / AdobeStock (**Appendix C**).

1.3 Clinical Measures of Liver Disease

1.3.1 Blood Test and Serum Markers

Blood serum markers are a minimally invasive biomarker of liver disease. These comprise measures of aspartate aminotransferase (AST), alanine aminotransferase (ALT), platelets, creatinine, bilirubin, sodium, hyaluronic acid, procollagen III amino-terminal peptide (PIIINP), and tissue inhibitor of matrix metalloproteinase 1 (TIMP-1). Multiple blood serum markers can be combined to compute scores including the AST to platelet ratio index (APRI) [9], Fibrosis-4 (FIB4) [10], enhanced liver fibrosis (ELF) [11], model for end stage liver disease (MELD) [12] and United Kingdom model for end stage liver disease (UKELD) [13]. MELD and UKELD use blood serum markers but also require an International normalized ratio (INR), a test to determine how quickly blood clots. Blood serum markers do not directly assess the liver and as such are non-specific, so there have been reports of lower accuracy in serum markers than for other tests [14].

1.3.2 Transient Elastography

Transient elastography (Fibroscan®) is an ultrasound-based technique that can be used to evaluate liver stiffness within ~ 6 cm diameter cylinder of the liver at 2.5 – 4 cm depth below the skin surface [15]. The technique is non-invasive and has no limitation on the number of measures that can be performed. For each measure a skilled operator typically takes 10 measurements of liver stiffness, the median of these measures is then computed as the resultant liver

stiffness if the IQR is <30% of the range [16]. Though this technique has been shown to delineate liver disease [17, 18], it has been shown to have high serial variability, so LSM should always accompany other markers rather than being the primary marker of liver disease itself [19, 20]. Higher failure rates are observed in patients who have large amounts of visceral fat as commonly seen in NAFLD. An alternative to transient elastography is Magnetic resonance elastography (MRE), which is a non-invasive technique that combines imaging with the delivery of low frequency vibrations to the liver to create a stiffness map. MRE has been shown to be able to evaluate liver stiffness across a range of liver disease states [21]. MRE is discussed in more depth in Section 4 and **Publication VII**.

1.3.3 Liver Biopsy

Liver biopsies are the leading measure of the degree of liver disease injury. A biopsy is acquired through the abdominal wall or intravenously as a secondary procedure to a hepatic venous pressure gradient (HVPG) measure. A biopsy is considered necessary for diagnosis of cirrhosis when transient elastography is not sufficient according to the National Institute for Health and Care Excellence (NICE) guidelines for diagnosis and management of cirrhosis in over 16s [16]. The major limitations of a liver biopsy are that this is an invasive procedure, so not routinely performed serially on patients with liver disease [22] due to the associated risks. Further limitations come from the sampling error, as only a small sample of the liver is obtained per biopsy, and interobserver variability [23–26].

1.3.4 Hepatic Venous Pressure Gradient (HVPG)

Hepatic venous pressure gradient (HVPG) is the reference standard for evaluating portal pressure, a catheter is inserted through the jugular vein, through the right atrium of the heart, to the hepatic vein where a balloon is inflated and mercury movement is scored. The median of three measures is taken as the resultant portal pressure in units of mmHg [27]. Limitations of the HVPG procedure are that the measurement is highly invasive and so there is reluctance to perform serial measures of HVPG. Further, the procedure itself

can only be undertaken at few specialist hepatology centers by skilled operators [28]. In Section 4, **Publication V** outlines a surrogate measure of portal pressure using quantitative MRI.

2. Magnetic Resonance Imaging (MRI) Overview

Nuclear magnetic resonance (NMR) imaging of the abdomen was first achieved in 1977 [29], cutting edge at the time, this provided a crude 4cm thick single slice in a 40-minute acquisition time. After decades of hardware and imaging sequence developments, it is now possible to achieve much higher spatial resolution and acquire multiple slices within a single short breath hold to assess quantitative measures of organ structure and function, see **Figure 9**.

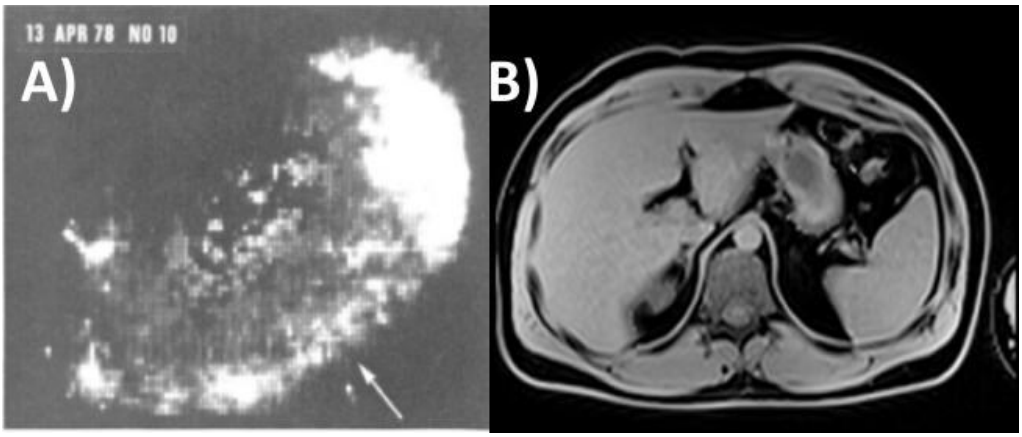

Figure 9: A) Transverse cross sectional NMR image of the abdomen taken from [29], License agreement (**Appendix D**). B) Transverse cross sectional NMR image of the abdomen acquired at the Sir Peter Mansfield Imaging Centre in 2022.

In this section the basic principles of NMR and MRI are briefly outlined. Specific examples are provided of how MRI can be applied to study the abdominal organs within the context of the publications in this thesis.

2.1 Principles of Nuclear Magnetic Resonance – Classical Explanation

Nuclear magnetic resonance is an observed phenomenon that is dependent on the composition of subatomic particles of atoms. Only select atomic nuclei with spin (*I*) can experience nuclear magnetic resonance. Nuclei possess half integer "spin" if the sum of constituent nucleons of a nuclei give an odd number, resulting in nuclei of resultant spin of 1/2, 3/2, or 5/2. Nuclei with such intrinsic properties include hydrogen (^{1}H), Carbon (^{13}C), fluorine (^{19}F), sodium (^{23}Na), and phosphorous (^{31}P), see **Table 1**. Nuclei may also possess even mass and be

composed of an odd number of protons and neutrons giving rise to integral spin. Examples of spin *I* = 1 nuclei are deuterium (^{2}H) and ^{14}N. Fortunately, hydrogen (^{1}H) has the highest NMR sensitivity of all nuclei due to its high gyromagnetic ratio, and is the most abundant nucleus, being found in water which makes up approximately 70% of the human body.

Nucleus	Spin (I)	Natural Abundance (%)	Gyromagnetic Ratio, γ (MHz/T)
Hydrogen (^{1}H)	1/2	99.95	42.58
Deuterium (^{2}H)	1	0.00015	6.54
Carbon (^{13}C)	1/2	1.11	10.71
Nitrogen (^{14}N)	1	99.64	3.077
Fluorine (^{19}F)	1/2	100	40.10
Sodium (^{23}Na)	3/2	100	11.26
Phosphorus (^{31}P)	1/2	100	17.24

Table 1: Common nuclei and their spin, natural abundance and gyromagnetic ratio, γ.

Spin causes the nuclei to behave like tiny rotating magnets. The magnetic moment ($\boldsymbol{\mu}$) of a spin is given by **Equation 1**, where γ is the gyromagnetic ratio and $\boldsymbol{J}$ is the spin angular momentum. The gyromagnetic ratio is a constant, unique for a given nucleus (see **Table 1**), and for ^{1}H this takes a value of 2.68 x 10^{8} rads^{-1}T^{-1} or 42.58 MHz/T.

Equation 1:

$$\boldsymbol{\mu} = \gamma \boldsymbol{J}$$

When nuclei with a magnetic moment, μ, are placed in a large external magnetic field $\boldsymbol{B}$ (often termed B_0), their magnetic moment aligns with the direction of the field. However, because the nucleus is spinning, the resultant movement is not simply an alignment with the external magnetic field, but results in precession of the magnetic moment about the external magnetic field (like a gyroscope), as shown in **Figure 10** and described mathematically in **Equation 2**.

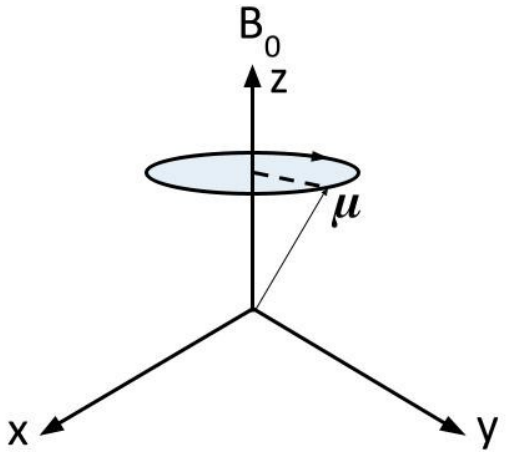

Figure 10: Precession of the magnetic moment, μ, about the externally applied magnetic field (B or B_0).

Equation 2:

$$\frac{d\boldsymbol{\mu}}{dt} = \gamma\boldsymbol{\mu} \times \boldsymbol{B}$$

The frequency of precession about B is termed the Larmor frequency, ω_0, and is given by **Equation 3**.

Equation 3:

$$\omega_0 = \gamma B_0.$$

For ^{1}H (water) in an external magnetic field B_0 of 1.5T and 3T (typical field strengths of clinical MR systems), the Larmor frequency is 63.86MHz and 127.72MHz respectively.

The magnetic moment possesses Spin angular momentum, ***J***. This is a vector quantity with magnitude given by $|J| = \hbar\sqrt{I(I+1)}$ where *I* is the spin quantum number, and $\hbar$ is Plank's constant divided by 2π. There are (2*I* +1) eigenstates (spin states) related to the magnetic spin quantum number, m_I. This reflects the fact that the orientation or direction of angular momentum is quantised. For a proton for which *I* = 1⁄2, m_I can take the values of ± 1⁄2. The potential energy of a magnetic moment inside an external magnetic field is given by $E = -\boldsymbol{\mu} \cdot \boldsymbol{B}$ which for protons means there are two possible energy levels, termed the Zeeman energy levels, dependent on whether the spins are

aligned along the field (m_I = +1/2 or spin ↑) or against the field (m_I = -1/2 or spin ↓).

In a human there are millions of spins which are distributed between the Zeeman energy levels according to the Boltzmann distribution given by **Equation 4**.

Equation 4:

$$\frac{n_{\downarrow}}{n_{\uparrow}} = e^{-\frac{\Delta E}{k_B T}} = e^{-\frac{\gamma \hbar B_0}{k_B T}}$$

where k_B is the Boltzmann constant. This gives rise to a net longitudinal magnetisation (M) along the z-axis given in **Equation 5**.

Equation 5:

$$M = \frac{1}{4}\frac{N\,(\hbar\gamma)^2 B_0}{k_B T}$$

where, N is the total number of spins. Note that the net magnetization is proportional to the external magnetic field, B_0, so a higher external magnetic field results in a larger net magnetisation, M. The net magnetisation is also inversely proportional to temperature (T).

Nuclei experience a resonant phenomenon that is dependent on the large external magnetic field, as described in Equation 3. But when ^{1}H nuclei are bound to more complex molecules where multiple hydrogen atoms are present, such as in hydrocarbon chains that make up substances such as fat, the interaction between chemically bound ^{1}H atoms within the molecule causes a very small change in the resonant frequency (**Figure 11**), known as the chemical shift, δ. The chemical shift is measured in parts per million and is given by **Equation 6** where υ_{sample} is the absolute resonant frequency of the sample and $\upsilon_{reference}$ is the absolute resonant frequency of a reference compound. The chemical shift of fat is 3.5ppm compared to water leading to a frequency shift of 150Hz/T or 220Hz at 1.5T and 440Hz at 3T.

Application of a time varying radiofrequency (RF) magnetic field (B_1) matched to a nuclei's specific resonant frequency will cause the spins to precess around the direction of the applied B_1 field as shown in **Figure 12.** Energy will be absorbed following the RF pulse giving rise to a small re-emitted radio frequency magnetic field, it is this that forms the NMR signal known as the free induction decay (FID).

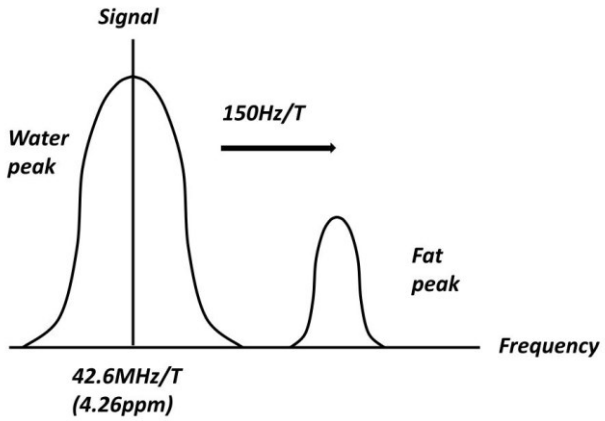

Figure 11: Diagram of ^1H spectra within liver tissue showing that the resonant frequency of fat is shifted by 150Hz/T from that of water.

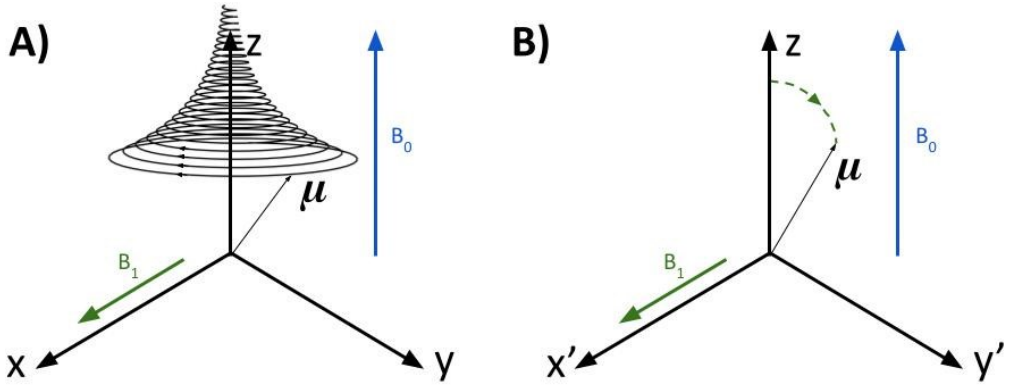

Figure 12: A) The laboratory frame of reference when observing μ precess about the B_0 field. B) When an external time varying radiofrequency is applied (B_1) at a frequency that exactly matches the Larmor frequency, a much slower precession occurs about the direction of the applied field (B_1). This is shown here in the rotating frame of reference (x', y', z) which allows the direct observation of the effect of B_1 on the magnetic moment, μ.

Equation 6:

$$\delta = \frac{\upsilon_{sample} - \upsilon_{reference}}{\upsilon_{reference}}$$

Following an RF pulse of 90^0, the spins are knocked into the transverse plane (M_{xy}) *and* then precess at the Larmor frequency. The signal emitted from the spins decays exponentially with the transverse relaxation time T_2* with the signal termed the Free Induction Decay (FID), back toward the equilibrium state in which no spins are aligned in the transverse plane, as shown in **Figure 13**.

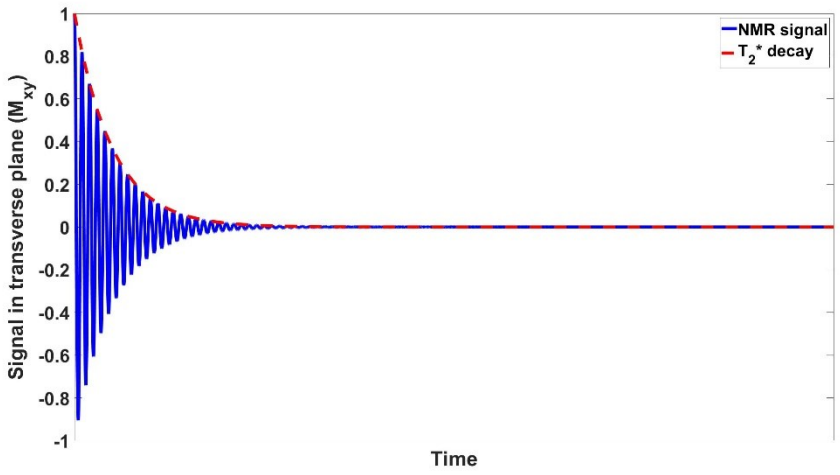

Figure 13: Schematic of the Free Induction Decay (FID) after a 90^0 RF pulse showing the signal oscillating at the Larmor frequency with an exponential decay given by the T_2*.

T_2 is the spin-spin time constant or the transverse relaxation time and is the "natural" or "true" T_2 of the tissue being imaged. It is affected by the degree of coupling with adjacent hydrogen atoms which alters the precession rate causing decay of signal as spins become more and more out of phase. T_2* can be considered an "observed" or "effective" T_2, T_2* results principally from inhomogeneities in the main magnetic field. These inhomogeneities may be the result of intrinsic defects in the magnet itself or from susceptibility-induced field distortions produced by the tissue or other materials placed within the field. T_2* is always less than or equal to T_2 as described in **Equation 7** where T_2' is the relaxation term corresponding to field inhomogeneities.

Equation 7:

$$\frac{1}{T_2^*} = \frac{1}{T_2} + \frac{1}{T_2'}$$

Following an RF pulse that completely inverts the magnetisation in the longitudinal plane (M_z), the recovery of the magnetization along the longitudinal plane back to the equilibrium magnetisation M_0 is governed by the longitudinal relaxation time constant T_1, see **Figure 14**. T_1 is also known as the spin-lattice or longitudinal time constant and is mostly affected by chemical bonds within the molecules surrounding the resonating hydrogen atom, as spins return to a low energy equilibrium state, RF energy is released back into the surrounding lattice.

Both T_1 and T_2 are phenomenological, unique to the substance that the ^1H atoms (or other nuclei with spin) are present in. In human tissues, both T_1 and T_2 are longer when more water (hydrogen) is present. T_1 is also dependent on the field strength, being longer at higher field strength, with the typical T_1 of healthy abdominal tissues given in **Table 2** [30]. While T_2/T_2* will reduce with field strength and typical abdominal tissues values are given in **Table 3.**

Organ	1.5T (ms)	3T (ms)
Liver	586 ± 39	809 ± 71
Spleen	1057 ± 42	1328 ± 31
Renal Cortex	966 ± 58	1142 ± 154
Renal Medulla	1412 ± 58	1545 ± 142
Pancreas	584 ± 14	725 ± 71

Table 2: T_1 relaxation time of abdominal organs at 1.5 and 3 T, taken from [30].

Organ	1.5T (ms)	3T (ms)
Liver	46 ± 6	34 ± 4
Spleen	79 ± 15	61 ± 9
Renal Cortex	87 ± 4	76 ± 7
Renal Medulla	85 ± 11	81 ± 8
Pancreas	46 ± 6	43 ± 7

Table 3: T_2 relaxation time of abdominal organs at 1.5 and 3 T, taken from [30].

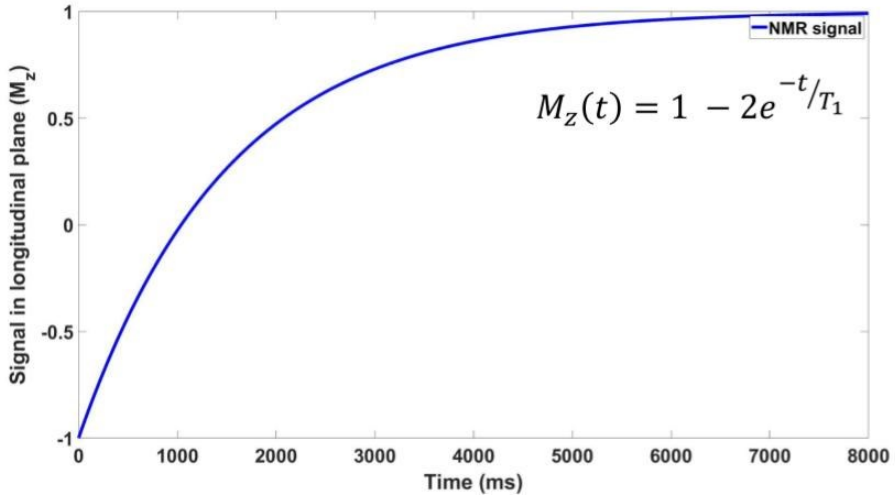

Figure 14: Inversion recovery curve for a sample with a longitudinal relaxation time of 1500 ms.

In liver disease, T_1 of the liver is observed to increase with disease severity [31]. Hepatic Iron content has been shown to increase as a side effect of liver disease, iron present within imaging voxels will cause more field inhomogeneity which in turn will cause a shortening of the transverse T_2* decay [32]. Longer T_2 and therefore T_2* decays are observed in tissue where inflammation is present [33], so when considering T_2* as a marker of liver disease it is important to consider the effect of both the presence of iron and inflammation.

2.2 Magnetic Resonance Imaging

NMR measures the signal from a large (whole volume) that has not been localised. Magnetic resonance imaging (MRI) works to spatially localise this signal using magnetic field gradients (G_x, G_y, G_z) to impart spatial sensitivity on the frequency and phase of the spins. This is illustrated in the pulse sequence diagram of a simple gradient echo imaging sequence shown in **Figure 5.** Here slice selection, frequency encoding and phase encoding are used to form an image.

First, slice selection is performed to excite a specific volume in a given plane (slice) of known thickness. This is achieved by applying a RF pulse together with

a slice-select gradient (G_z) along an axis perpendicular to the plane of the desired slice, resulting in a linear variation of resonance frequencies in the slice direction. A specially tailored RF-pulse is applied simultaneously with the slice-select gradient, whose frequency components match the narrow range of frequencies contained in the desired slice. Having selected a slice, the application of a magnetic field gradient in the frequency encoding direction (G_y) will spatially alter the B_0 field and in doing so will alter the resonant frequency of nuclei present in the field in a spatially dependent manner, this is known as frequency encoding. By applying a phase encoding gradient (G_x) perpendicular to the frequency encoding applied gradient field, the phase of the nuclei will rely on another spatially changing gradient field, as shown in **Figure 15**.

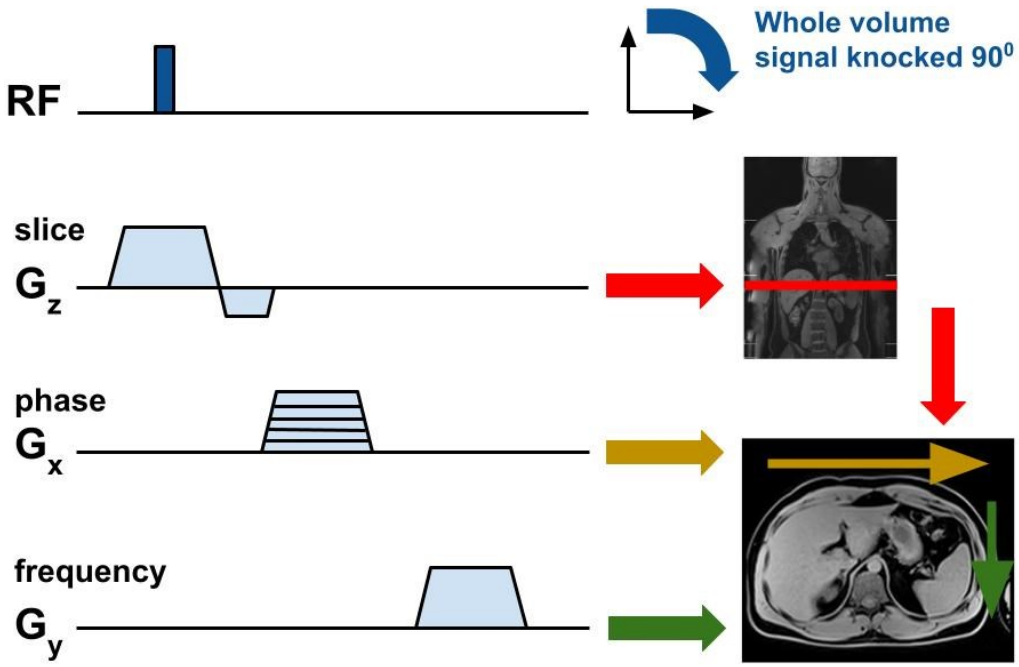

Figure 15: The application of gradient fields in the three orientations to spatially encode data. Slice selection (G_z) is applied from foot-head to generate an axial slice, which is encoded in-plane using the phase (G_x) and frequency (G_y) encoding gradients.

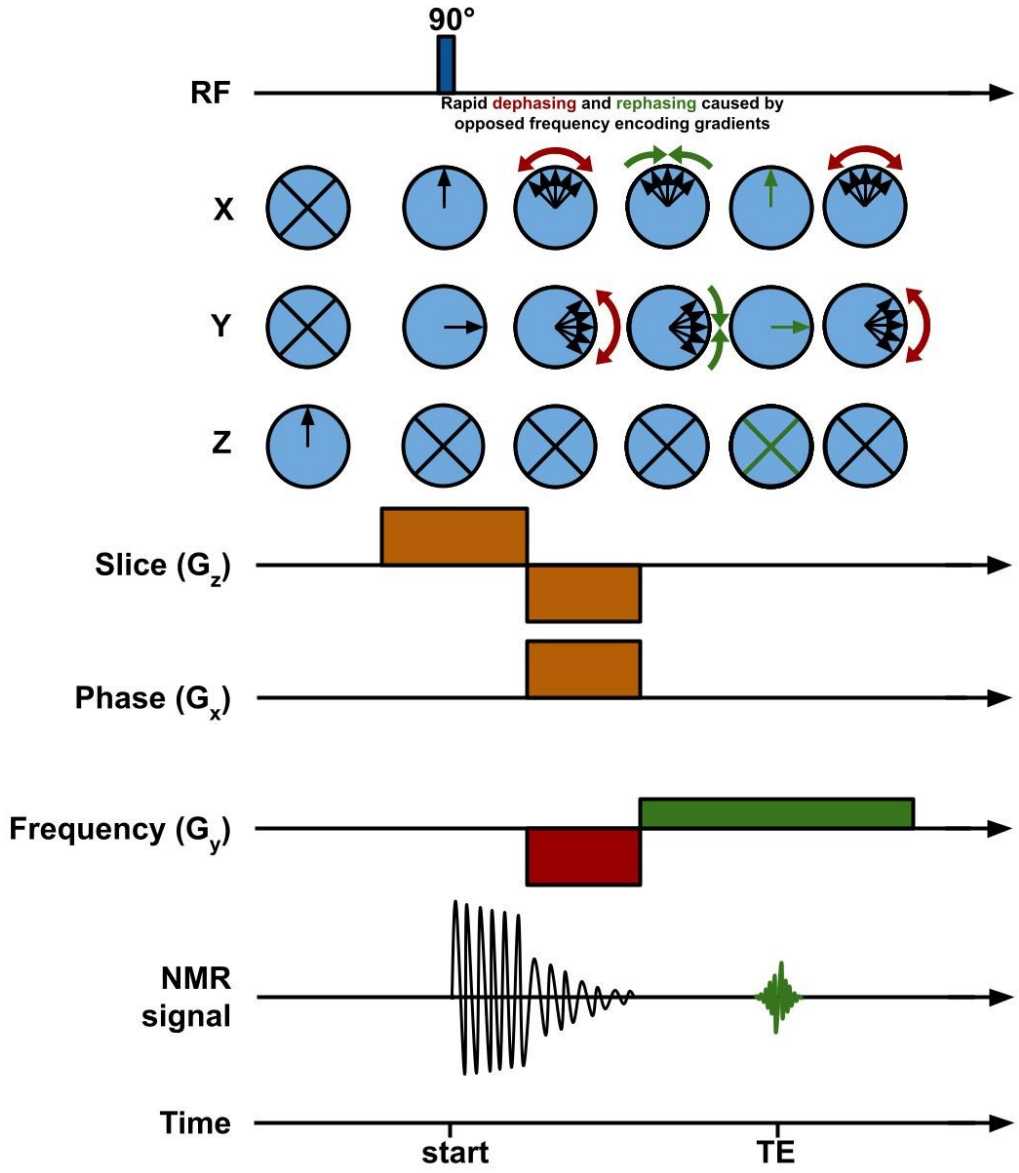

Figure 16: Schematic of spin vector alignment during a gradient-echo acquisition showing spin dephasing after a 90^0 RF pulse and further rapid dephasing after an applied gradient field (G_y) with rephasing after an opposed gradient field (G_y) is applied to acquire an echo in a short acquisition time, the echo time (TE) is the time between the 90^0 RF pulse and the returned echo.

By applying RF pulses and gradients at specific timings in a given pulse sequence, gradient or spin echo schemes are formed for spatial encoding, resulting in spatial signal intensity maps forming an image with various contrasts. A gradient echo is formed by applying a single RF pulse followed by

a dephasing and immediately after rephasing gradient field within the FID to obtain a gradient echo as shown in **Figure 16**.

Alternatively, a spin echo can be formed by applying a 90° RF pulse followed by a 180° RF pulse at a time τ later to rephase the spins to form a spin echo, as shown in **Figure 17**.

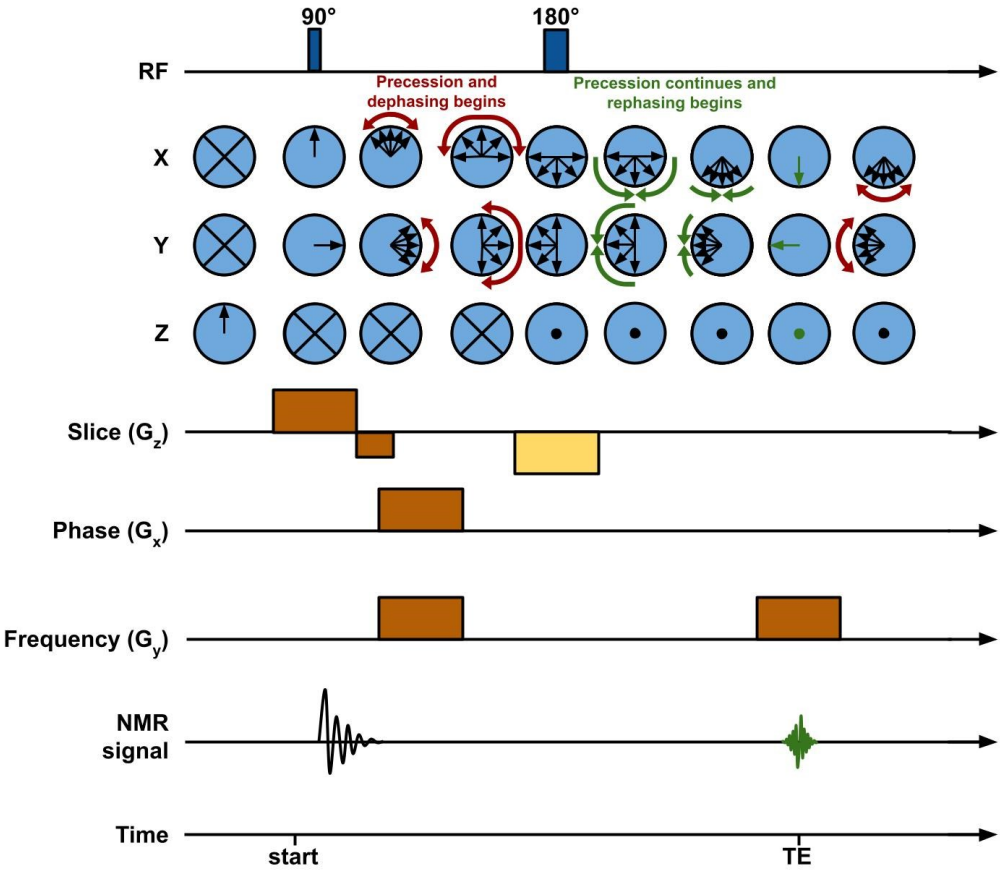

Figure 17: Schematic of spin vector alignment during a spin-echo acquisition showing spin dephasing after a 90^0 RF pulse and then rephasing after a 180^0 RF pulse at a time (TE/2) later. Note the slice select gradient (yellow) applied during the 180^0 pulse is reversed compared to the z-gradient applied during the 90^0 pulse to dephase the signal from the fat [34], this is important in abdominal imaging and has been used for all abdominal imaging in the published works in this thesis.

Within the publications that form this thesis, both gradient echo (fast field echo (FFE) as named on the Philips systems) and spin-echo echo planar imaging (SE-EPI) are used to collect measures within the abdomen. The choice of the

specific imaging readout is discussed in the sections below. Within the abdomen, an image will show different signal intensities across the different abdominal organs due to their unique tissue structure resulting in differing T_1 and T_2/T_2* relaxation times.

2.3 MRI of the abdomen

One of the main challenges of applying MRI in the abdomen is respiratory motion. As a result, each imaging sequence in this thesis is acquired either using a breath hold to fit the scan within a length of time that a patient can tolerate, so of ~20 seconds or less, or it is collected respiratory triggered by placing respiratory bellows around the participants chest to track inhalation and exhalation. To help to achieve the image acquisition in a reasonable time, image acceleration can be used to speed up the image acquisition, for example applying sensitivity encoding (SENSE) implemented on the Philips scanners [35]. Respiratory triggering uses the bellows to allow a small part of the data acquisition to be captured at a given matching phase of the respiratory cycle. Respiratory triggering is often easier for patient populations who may have difficulty complying with multiple breath holds. A third option is to perform free breathing with navigator triggering based on the signal fluctuation in a given ROI in the image (typically a 1-dimensional profile of the sharp signal transition between the lung and liver, which can be monitored prospectively using an edge-detection algorithm) and then the image is acquired within a predetermined window. After respiratory motion considerations have been made in the data acquisition, further steps are often required during analysis to realign or discard mismatched or mis-triggered images.

When imaging the abdomen, further challenges exist resulting from tissue interfaces and abdominal gas that can cause magnetic field inhomogeneity (ΔB_0) and magnetic susceptibility artefacts in images. In larger subjects, imaging of the abdominal organs also requires a larger field of view (FOV) which can increase both the breath hold time and pose difficulties of shimming to achieve a homogeneous B_0 field over such a large volume, as well as having sufficient

fat suppression. Further, a homogenous B_1 field is also required, which can be enhanced using adaptive RF shimming on the Philips scanner.

Cardiac imaging provides challenges as not only does the respiratory motion need to be considered but also the cardiac motion. To account for this, images are typically acquired using either a vector cardiogram (VCG) or the peripheral pulse (PPU) device to trigger from the cardiac motion, along with the data being acquired in a breath hold.

The data within these publications was all acquired on either a 1.5T or 3T Philips Achieva scanner located at the Sir Peter Mansfield Imaging Centre (SPMIC), University of Nottingham. The techniques used in these published works include T_1 mapping, T_2 and T_2* mapping, arterial spin labelling (ASL), phase contrast angiography (PCA), diffusion weighted imaging (DWI), and cardiac cine MRI. These techniques are described below.

2.3.1 Longitudinal Relaxation time (T_1) Mapping

Longitudinal relaxation time T_1 has been shown to be a promising parameter for the assessment of microstructure in abdominal tissues [36–41]. In general, T_1 is lengthened in tissue where there is the presence of inflammation and fibrosis.

In the publications within this thesis, T_1 is mapped within the abdominal organs using a respiratory triggered inversion recovery scheme. This is performed by applying a pulse sequence which uses a non-selective adiabatic inversion pulse followed by the sequential acquisition of multiple spin-echo echo-planar imaging or balanced fast field echo slices through the organ of interest at an inversion time (Ti) after the inversion pulse, with each slice being separated by a temporal slice delay (T_{SLICE}). After the images have been acquired, a repetition time (TR) allows the longitudinal signal to fully return to equilibrium, this recovery time needs to be in the order of 5 x T_1 and so in this work requires a TR of >8s meaning this is typically two respiratory cycles (see **Figure 13**). This process is repeated for multiple different inversion times in order to build up images with signal intensities that correspond to a number of points on the

inversion recovery curve. To ensure the abdominal images collected at the different Tis are aligned, the images are acquired using respiratory triggering. The trigger is taken at the peak of the inhalation respiratory trace and a trigger delay (Td) is applied before the inversion pulse. The value of Td is changed for each Ti so that all images are acquired at the same phase of the respiratory cycle (i.e. for long inversion times a short T_d is used, whilst for short inversion times a long T_d is used) as shown in **Figure 18**.

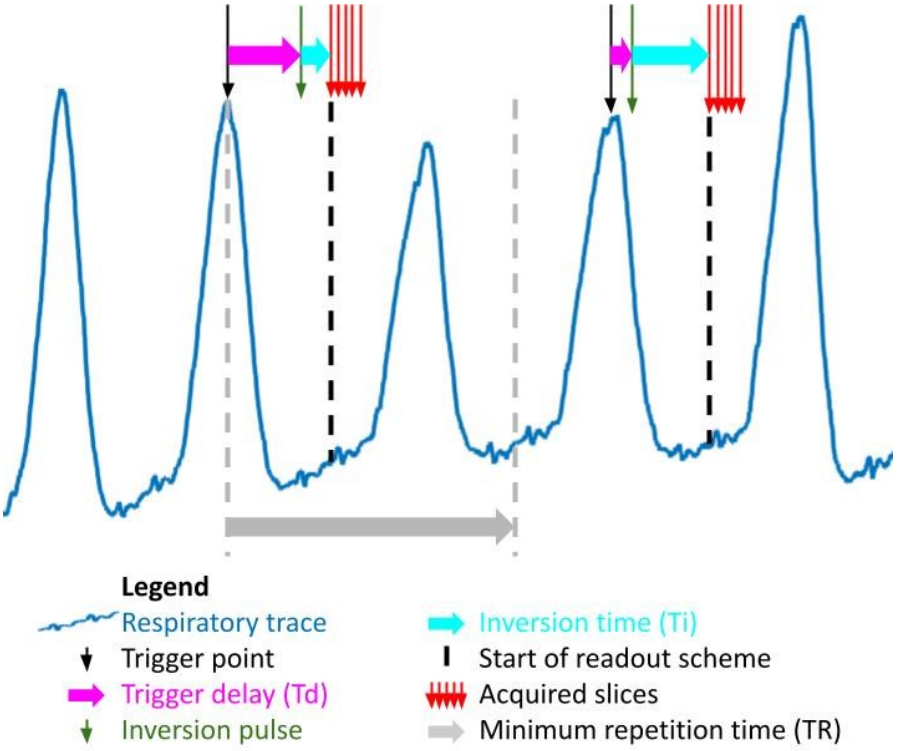

Figure 18: Schematic of the respiratory triggered inversion recovery scheme showing that the imaging readout always occurs at the same phase of the respiratory cycle by varying the trigger delay (Td) and inversion time (Ti). Gaps between red arrows demonstrate the temporal slice spacing (T_{SLICE}). A minimum repetition time (TR) allows for the inverted signal to fully recover before the next inversion pulse.

To assess liver microstructure this respiratory triggered inversion recovery scheme was used either with a SE-EPI readout (**Figure 19**) comprising 9 axial SE-EPI slices collected in a sequential order with fat suppression using spectral presaturation with inversion recovery (SPIR) prior to each excitation pulse, or a

balanced Fast Field Echo (bFFE) readout (**Figure 20**) comprising 3 sagittal slices (**Publications I, II, V**). For the SE-EPI acquisition, images are acquired in both foot-to-head and head-to-foot slice order to increase the dynamic range of inversion times (**Figure 21**, **Publication III, Conference Proceedings B, D, E**). In the SPIR scheme, a fat selective spectral RF pulse is applied which inverts only the longitudinal signal from the fat and after a short time at the null of the fat signal the SE-EPI imaging readout is applied to collect the signal from the water signal only, a spoiler gradient after the inversion dephases any fat signal that was not perfectly inverted. Fat suppression is needed for accurate estimation of liver T_1, as signal from the fat in the imaging readout will alter the measured T_1 within the liver [42, 43].

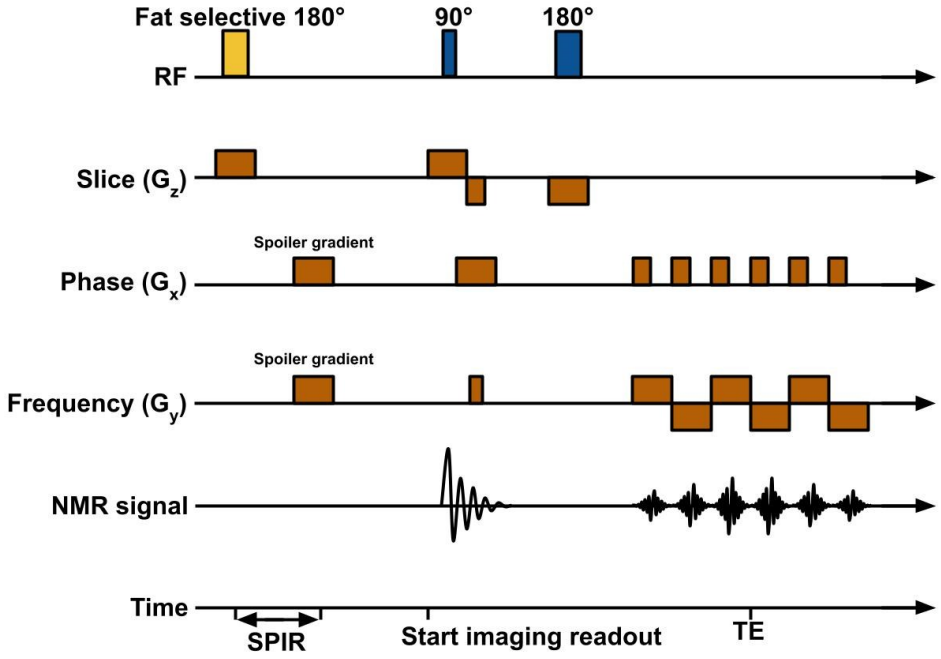

Figure 19: A pulse sequence diagram of a spin-echo echo planar imaging scheme (SE-EPI). This technique is advantageous for T_1 measurement as multiple slices can be acquired quickly after the inversion pulse with a short temporal slice spacing, and a SPIR scheme can be added prior to the readout to suppress signal from fat.

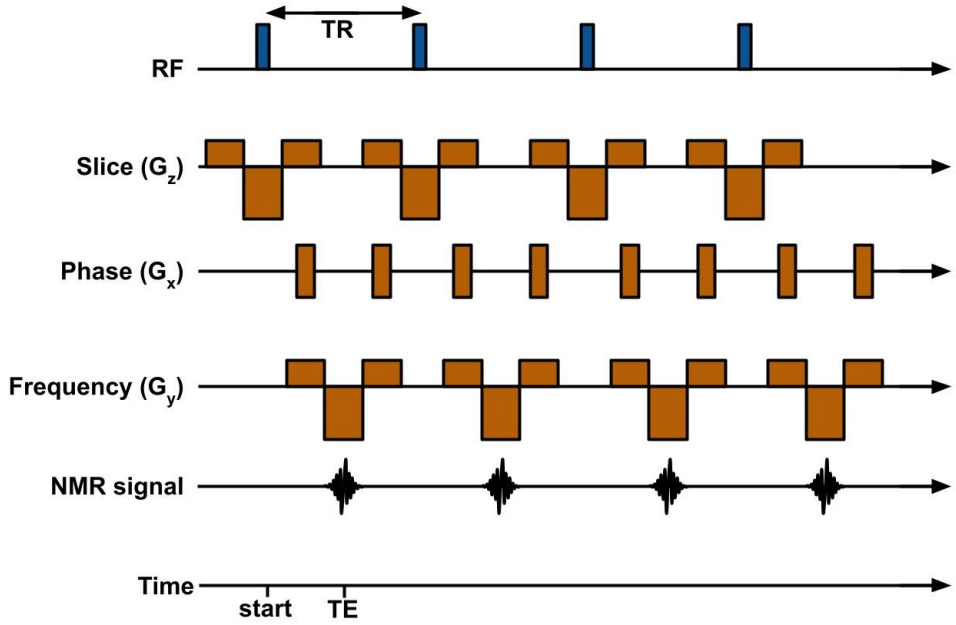

Figure 20: Pulse sequence diagram of a balanced fast field echo (bFFE) readout. The three gradient fields have equal and opposite gradients around the returned signal resulting in a net zero magnetisation, TE = TR/2 where TR << T_2.

For SE-EPI, if no fat suppression is applied then, because of the shorter T_1 of fat, the measured liver tissue T_1 would be shortened in fatty liver due to the partial voluming effect. For a bFFE readout, there is a more complex effect of fat [42], as a bFFE sequence causes water and fat signals to have opposite phase when the repetition time (TR) is ~2.3 ms at 3T due to the chemical shift of the fat signal being around 3.5 ppm from water (See **Figure 11**) which corresponds to ~440 Hz, a TR of 1/440 = 2.23 ms. Thus, in voxels that contain both fat and water, the T_1 measurement is influenced by the choice of TR and off-resonance effects. This can both increase and decrease the measured T_1 of the tissue depending on the off-resonance and TR, see **Figure 22**. For example, at 3T, using a bFFE sequence with TR of 2.3 ms results in a higher measured T_1 in subjects with high lipid content than low, which must be taken into account if aiming to study underlying inflammation/fibrosis.

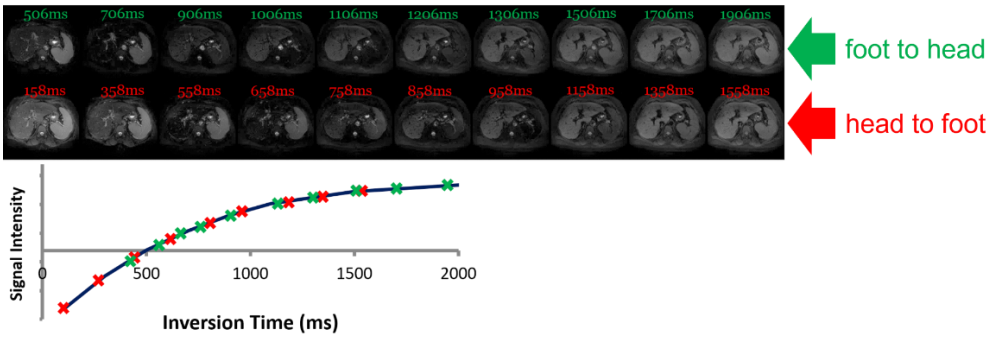

Figure 21: Spin echo EPI datasets acquired at different inversion times (X) for readouts with slice ordering in the foot-to-head and head-to-foot order. Images are shown taking into consideration the temporal slice spacing between the given slices.

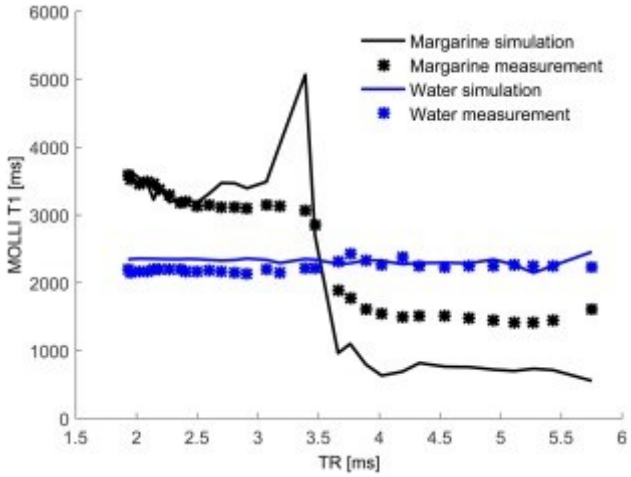

Figure 22: The effect of chosen TR of the bFFE readout on T_1 measured using MOLLI from water and margarine samples, taken from[42], License agreement (**Appendix E**).

Having collected inversion recovery data at a range of inversion delays (TI), the T_1 data is then fit on a voxel-by-voxel basis across all TIs to compute T_1 maps using **Equation 8**.

Equation 8:

$$S(TI) = S_0(1 - 2e^{-TI/T_1})$$

Equation 8 assumes a 100% efficient inversion pulse is achieved using an adiabatic inversion pulse. **Publication V** compares both bFFE and SE-EPI readouts for an inversion recovery scheme to estimate T_1 in the liver.

To assess renal and spleen microstructure the same respiratory triggered inversion recovery scheme was used in this thesis. For renal T_1, a bFFE readout was used but data was collected in a coronal oblique orientation through the long axis of the kidney (**Publications I, II, IV, V**). Spleen T_1 values were assessed in **Publications I, II** using a coronal oblique bFFE readout and in **Publication III,** and **Conference Proceedings B, D, E** using an axial SE-EPI readout.

2.3.2 Transverse Relaxation Time (T_2 and T_2*) mapping

T_2* mapping has been shown to accurately predict hepatic iron content [44]. T_2 mapping has been shown to correlate with hepatic inflammation [33]. In **Publication III**, T_2 and T_2* mapping was applied to assess degree of inflammation of the liver in response to drug intervention.

For T_2 mapping, a spin-echo echo planar imaging image readout was used with 9 axial slices that geometrically matched the axial T_1 slices. Six echo times of TE =27, 35, 42, 50, 60, 70 ms were acquired using respiratory triggered scans to assess the transverse signal decaying within the liver tissue (**Publication III**).

The T_2* mapping used multi-fast field echo (m-FFE) data with 12 echoes with 9 geometrically matched axial slices to the T_1 mapping scheme. The first echo time of the twelve was 2.5ms and subsequent echoes were collected at 2.5ms intervals. T_2 and T_2* data were fit to **Equation 9** on a voxel-by-voxel basis. An example T_2* decay is shown in **Figure 23**.

Equation 9:

$$S(TE) = S_0 e^{-TE/T_2^*}$$

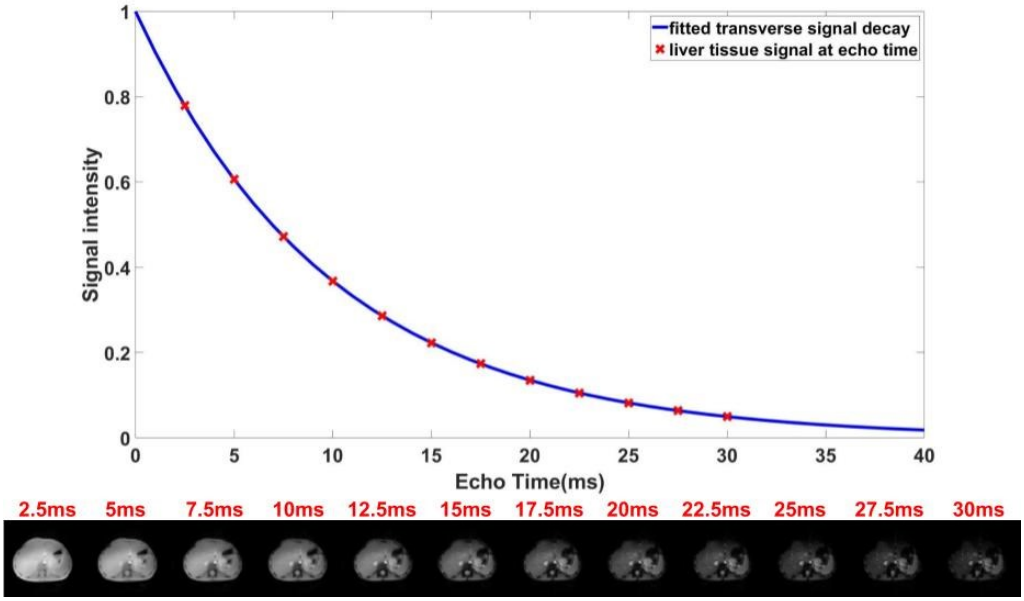

Figure 23: Example echo times of the liver T_2* data and the signal decay from the liver with a fitted T_2* value of **20**ms.

2.3.3 Phase-Contrast MRI

Phase contrast MRI (PC)-MRI is a method used to evaluate the velocity of moving blood within vessels and from this together with the vessel cross sectional area, blood flow can be calculated. In PC-MRI a velocity encoding bipolar gradient field is applied in the direction perpendicular to the imaging plane. Spins moving through the imaging plane will experience dephasing and rephasing as a result of these equal and opposite gradient fields being applied. Because the spins are moving within the blood this will result in a net velocity dependent phase shift (ϕ) as shown in **Figure 24**, whilst any static spins have zero phase shift.

Since the net phase shift of the moving spins is proportional to the velocity it can be used to quantify the velocity of the blood as shown in **Equation 10**, where υ represents velocity and M_1 represents the product of the gradient amplitude and time of application of the gradient field. It is beneficial to optimise the velocity encoding (V_{ENC}) gradient so that there is a sufficient dynamic range of the phase shift and thus flow measures. In these publications, the blood vessels and their specific chosen V_{ENC} are shown in **Table 3,** where

peak velocity was higher than the chosen V_{ENC} the sequence was reran with a higher selected V_{ENC} to avoid phase wrap within the blood vessel of interest.

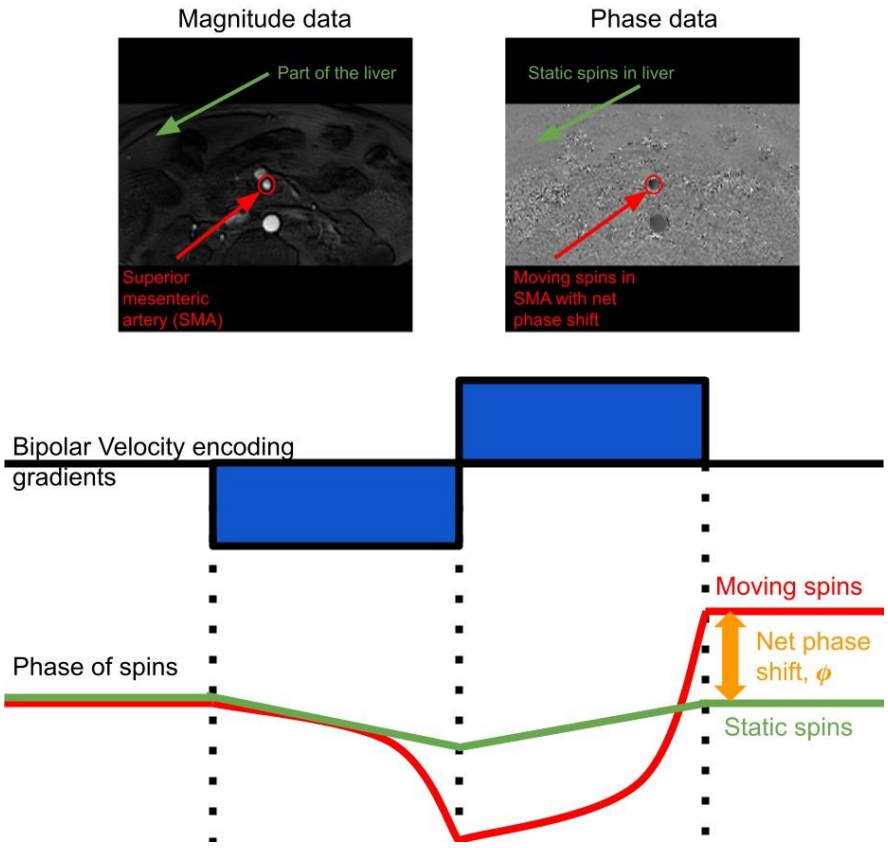

Figure 24: Effect of a bipolar velocity encoding gradient used in PC-MRI. This results in dephasing and rephasing of moving spins and a resultant phase shift which is velocity dependent, whilst stationary voxels have no net phase shift. Magnitude and phase PC-MR images are shown.

PC-MRI acquires a snapshot of velocity at a single timepoint during the cardiac cycle. To gain information about global flow through a blood vessel, multiple images (phases) must be acquired at different time points of the cardiac cycle. In all the publications that form this thesis, data is retrospectively cardiac gated and continuously acquired after each heartbeat during a 15-20 second breath hold for a predetermined number of phases (15-20). The scanner software bins the images and selects those acquired at evenly distributed time points over the cardiac cycle to return. This data can then be interpreted by drawing an ROI around the vessel of interest, for example using a ViewForum workstation

(Philips, Best, The Netherlands). The ROI is drawn on a phase where the cross section of the vessel appears most circular (subject to the operator's determination), this ROI is then propagated to all phases using Philips' vessel tracking software and copied onto the corresponding phase data. A velocity profile over the cardiac cycle can then be computed which is used in combination with the cross-sectional area of the vessel (area of the ROI) to compute blood flow through each vessel.

Equation 10:

$$\phi = -\gamma v M_1$$

Vessel	V_{ENC} (cm/s)	Publication
ascending aorta	200	I, II, IV
superior mesenteric artery	140	I, II, III
hepatic artery	100	I, II, III
splenic artery	100	I, II, III
renal artery	100	I, II, IV
renal vein	50	IV
portal vein	50	I, II, III

Table 3: Velocity encoding (V_{ENC}) values used for specific arteries and veins used in the published works in this thesis.

2.3.4 Arterial Spin Labelling

Arterial spin labelling (ASL) is used to assess organ perfusion in all of the published works of this thesis. The specific method used is the pulsed ASL Flow-sensitive Alternating Inversion Recovery (FAIR) technique. In this scheme, inflowing blood is magnetically labelled with an adiabatic inversion pulse and then imaged within the imaging plane of the tissue of interest at an inversion time (TI) later. This TI time needs to be sufficiently long enough for the inverted blood to travel to and perfuse the capillary bed of the tissue of interest in the imaging plane. ASL data is collected in pairs, with a 'label' image as described previously, and a 'control' image also acquired with a slice selective inversion pulse in which the inflowing blood is fully recovered (**Figure 25** for kidney ASL**, Figure 26** for liver ASL). The subtraction of the non-selective from selective

image generates a perfusion weighted difference image. The effect of post label delay can also be observed as in **Figure 27** [45].

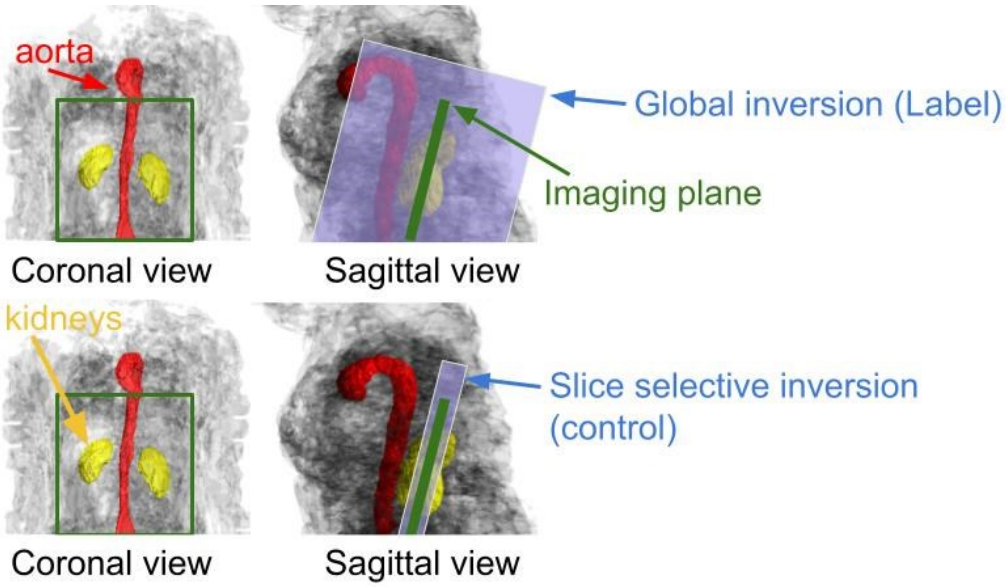

Figure 25: Orientation of ASL data acquired to obtain perfusion measurements of the kidneys, a coronal oblique slice is shown passing through the long axis of both kidneys, the 'label' is a non-selective inversion whilst the selective inversion pulse avoids inverting any blood in the aorta for the acquired 'control' image.

Because the signal-to-noise ratio (SNR) of ASL is low, due to a typical ASL perfusion weighted signal change of 1 – 3 % dependent on the organ of interest, many ASL label-control pairs are acquired, their subtractions are averaged together to create an average perfusion weighted (PW) difference image. Each voxel in this PW difference image is then quantified using a kinetic model [46] as described by **Equation 11** to compute tissue perfusion (f) maps in units of ml/100g/min.

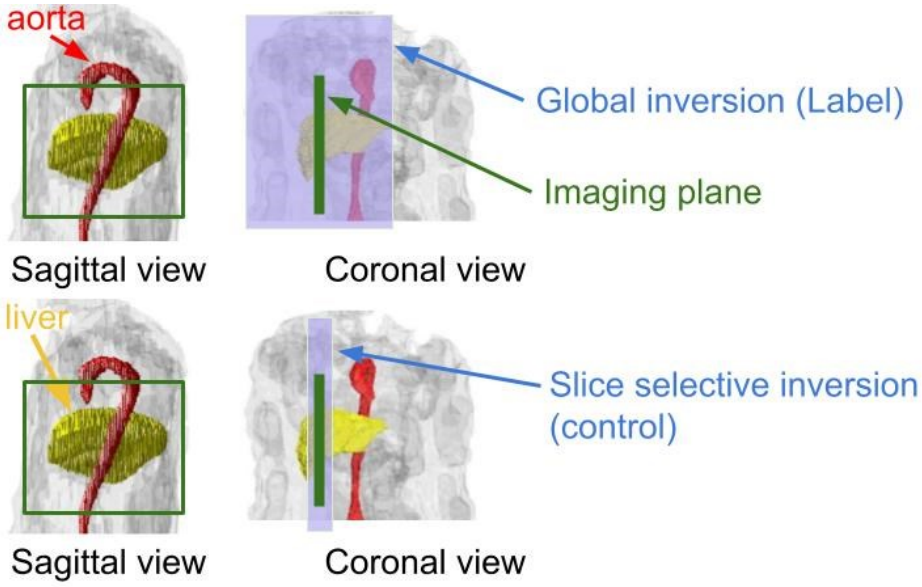

Figure 26: Orientation of ASL data acquired to obtain perfusion measurements of the liver, a sagittal slice is shown passing through the right lobe of the liver, the 'label' is a non-selective inversion whilst the selective inversion pulse avoids inverting any blood in the aorta and portal vein for the acquired 'control' image.

Equation 11:

$$\Delta S(PLD) = 2S_0 \frac{f}{\lambda} \frac{e^{PLD/T_{1,app}} - e^{PLD/T_{1,blood}}}{1/T_{1,blood} - 1/T_{1,app}}$$

where,

$$\frac{1}{T_{1,app}} = \frac{1}{T_1} + \frac{f}{\lambda}$$

$T_{1,blood}$ is assumed to be 1.36s at 1.5T and 1.55s at 3T [47], and the blood-tissue partition coefficient, λ, is assumed to be 0.8 ml/g. ASL is applied to abdominal organs in **Publications I,II,III,IV,VI**.

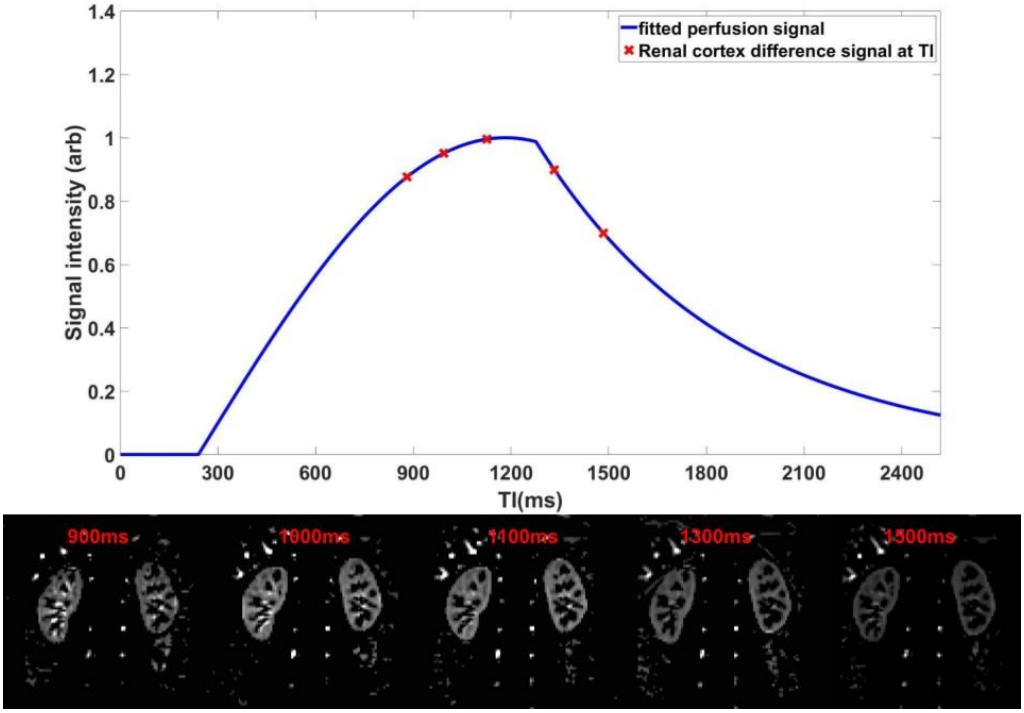

Figure 27: The effect of chosen TI on the perfusion weighted signal of the kidney, the plot shows an ROI within the renal cortex and the associated fit to Equation 10 with a resultant perfusion value of 200 ml/100g/min.

2.3.5 Diffusion Weighted Imaging

Diffusion weighted imaging (DWI) is a technique used to assess the random Brownian motion of water within a voxel that contains tissue cells or extracellular space. In the presence of fibrosis diffusion of water molecules is hindered, reducing the measured MR diffusion parameters. To measure diffusion, strong gradients are applied symmetrically on either side of a 180^0 pulse, typically in three perpendicular directions, as shown in **Figure 28**, although more directions are used for diffusion tensor imaging (DTI).

The degree of diffusion weighting is determined by the duration of the applied diffusion gradient (δ), the time interval between the diffusion gradients (*Δ*) and the amplitude (*G*)). The combination of these factors generates the b value, see **Equation 12**.

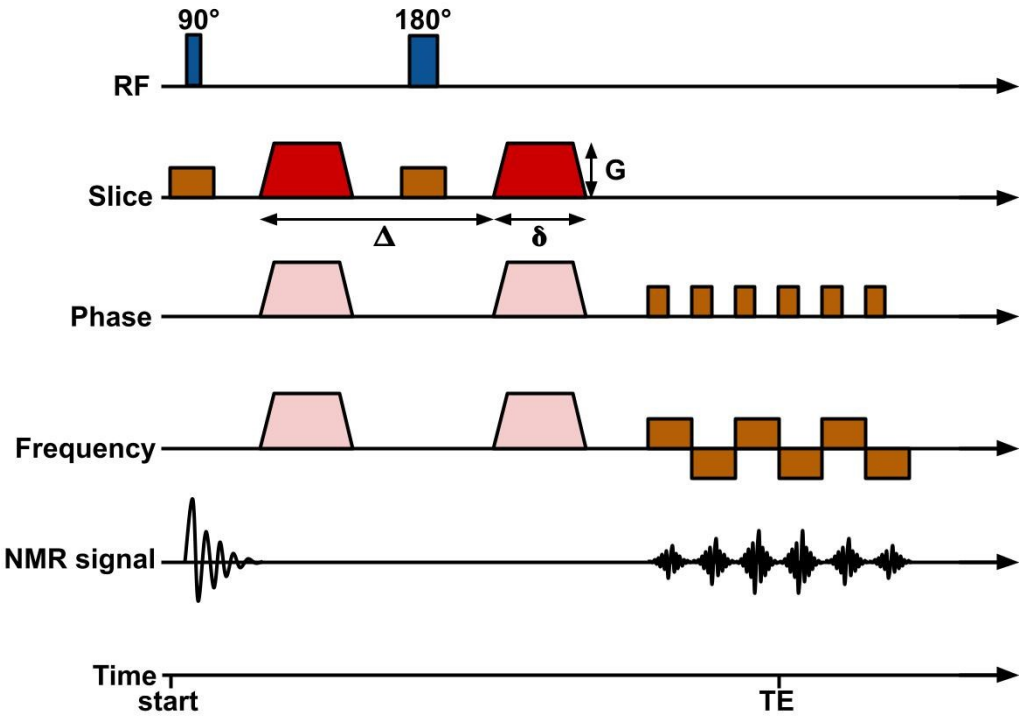

Figure 28: Pulse sequence diagram of a spin-echo echo planar imaging diffusion weighted imaging scheme where the dephasing and rephasing diffusion gradients are shown in red. Note that these gradients have the same polarity because of the 180^{o} pulse between them. In diffusion weighted imaging the scheme is then repeated with the diffusion gradient applied along each perpendicular direction. The three acquired images are averaged together to represent global diffusion weighting in all 3 planes.

Equation 12:

$$b = \gamma^2 G^2 \delta^2 (\Delta - {}^{\delta}/_{3})$$

The faster the diffusion, the more attenuated the signal will be, this is more clearly observed at larger b-values. To estimate diffusion properties of tissues, images are collected at multiple different b-values. In the published works in this thesis, diffusion weighted images are acquired using a respiratory triggered scheme. Modelling of the decay in diffusion signal removes inherent T_2 weighting within the image itself. Note that the higher the b-value the longer the echo time to allow the diffusion gradients to fit. Data is then fit on a voxel-by-voxel basis across the b-value images using **Equation 13** to yield apparent

diffusion coefficient (ADC) maps. ADC is very sensitive to subtle changes in microstructure and is used in **Publication IV,** though other parameters of diffusion (D), pseudo diffusion (D*) and perfusion fraction (PF) were analysed, data showed no significant differences and so was not shown. In **Publications IV**, the b-values used were 0, 5, 20, 60, 120, 190, 270, 370, 470, 580, 700 s/mm^2 to provide a good b-value range of diffusion weighted images for ADC computation, representative images are shown in **Figure 29.**

Equation 13:

$$S(b) = S_0 e^{-b.ADC}$$

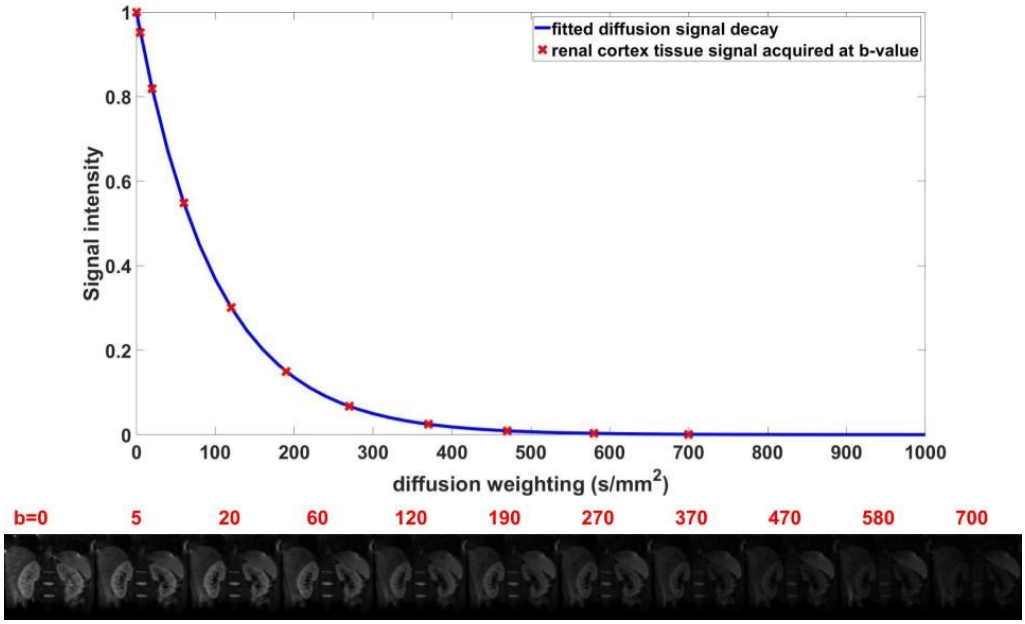

Figure 29: Example diffusion weighted b-value images of the kidney, and an example decay curve in the renal cortex with resultant measured ADC of 2 x 10^{-3}mm^2/s.

2.3.6 Cardiac cine MRI

Cine MRI is used to assess cardiac function. Typically, a 2 chamber and 4 chamber cine are first collected, as shown in **Figure 30**. This is then followed by cine imaging of multiple slices of the short axis of the left ventricle over time, as shown in **Figure 30**. The images are retrospectively cardiac gated in the same way as PC-MRI. Multiple images are then reconstructed at different phases of

the cardiac cycle. In **Publications I, II, IV,** 12 slices were acquired through the short axis of the heart with 30 phases across the cardiac cycle, for this acquisition 3 slices were collected in each 15-20 s breath hold. In **Publications I, II** left ventricle (LV) wall mass index is used as a marker of cardiac function. A ViewForum workstation (Philips, Best, The Netherlands) was used to analyse the cardiac data for LV wall mass by manually segmenting the cardiac muscle on the end diastole slice with the software propagating contours to other cardiac phases. Then, LV wall mass index (g/m^2) was computed by correcting for body surface area (BSA). Using the ViewForum workstation, cardiac output (CO) was computed from the same data based on the change in the blood pool within the left ventricle on the short axis data over the course of the acquired cardiac cycle phases. Cardiac output can then be corrected for BSA to yield cardiac index (CI).

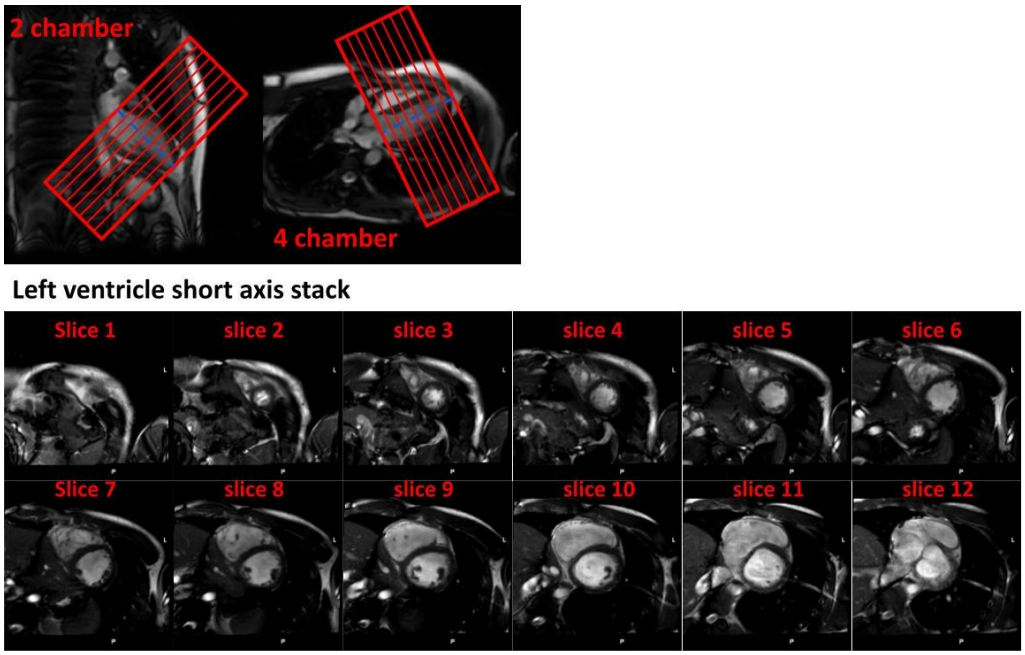

Figure 30: 2 and 4 chamber cine datasets used to plan a 12-slice short axis stack cine dataset for which 30 phases are collected across the cardiac cycle.

3. Overview of published works

Quantitative MRI has the capability of evaluating both structure and function of multiple organs within a single scan session, providing a comprehensive assessment of potential comorbidities within a patient group. The following sub-sections provide an overview of each of the first author published works that form this thesis.

3.1 Using MRI to delineate liver disease and predict outcome

In ***Publication I: Bradley et al., 2018***, the structure and haemodynamic function of multiple organs are evaluated in three participant groups; healthy volunteers, patients with compensated cirrhosis and patients with decompensated cirrhosis.

Advancing liver disease results in deleterious changes to critical organs, as shown in **Figure 1**. The aim was to establish the feasibility of performing a single MRI scan to assess the changes to multiple abdominal organs resulting from compensated cirrhosis, and to assess if baseline MRI can be used to predict disease severity, by studying future liver-related outcomes up to 6 years after the baseline MRI scan.

60 patients with compensated cirrhosis, 40 healthy volunteers and 7 patients with decompensated cirrhosis were recruited to the study. In a single 1-hour scan session, MRI measures were evaluated comprising blood flow in renal, liver, and splanchnic abdominal vessels; perfusion of the liver, spleen and renal tissue; liver, spleen, and kidney longitudinal relaxation time T_1; cardiac index; and volume assessment of the liver, spleen, and kidneys. The association between MRI parameters and disease severity was explored. 11 (18%) of the 60 patients with compensated cirrhosis cohort experienced a liver related outcome at some time after their baseline MRI scan, differences between this group and those remaining in the stable compensated cirrhosis group were evaluated.

In compensated cirrhosis, structural changes were observed in the liver, reflected by increased T_1 with progressive disease ($p < 0.001$) as well as an increase in liver volume when compared to healthy volunteers ($p = 0.006$). This was also associated with a progressive reduction in liver ($p < 0.001$) and splenic ($p < 0.001$) perfusion. A significant reduction in renal cortex T_1 and increase in both cardiac index and superior mesenteric arterial blood flow was seen with increasing disease severity as shown in **Figure 31**.

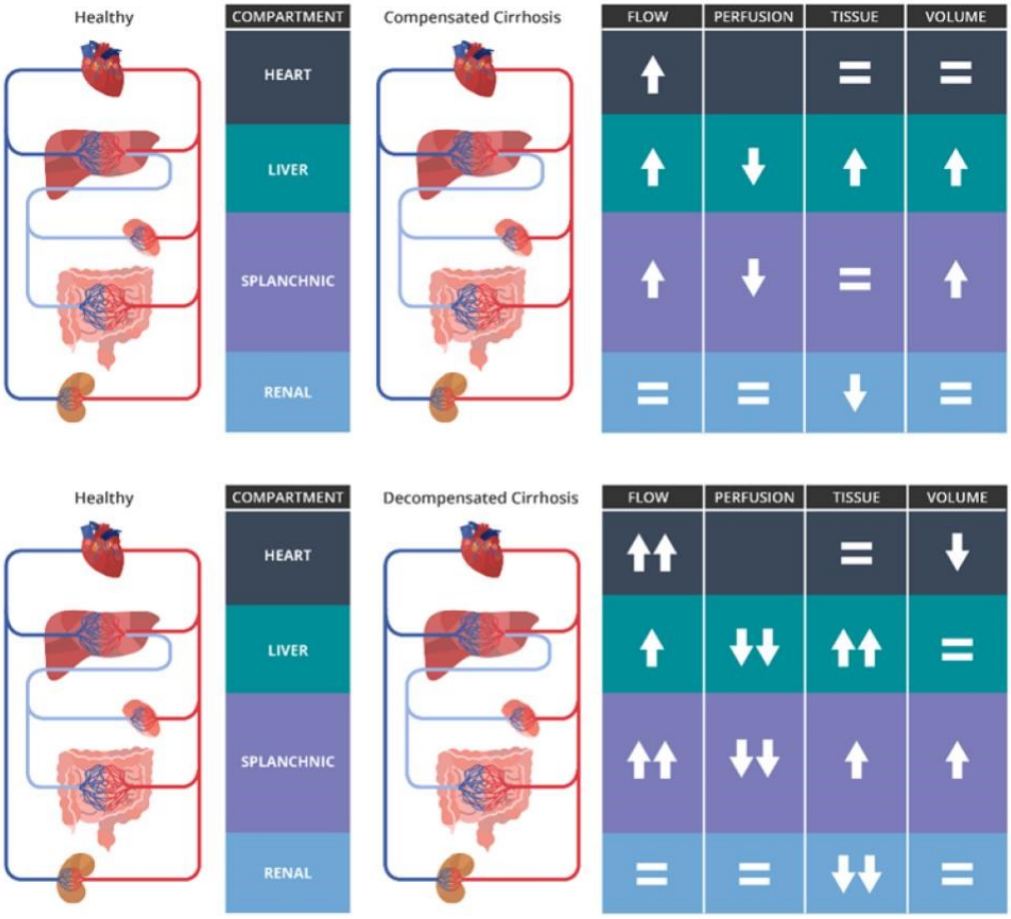

Figure 31: Infographic to pictorially illustrate the changes in critical organs (heart, liver, splanchnic and kidney) demonstrated in this study of contemporaneous MR measures in compensated and decompensated cirrhosis [1], License agreement (**Appendix E**).

Baseline liver T_1 ($p < 0.01$), liver perfusion ($p < 0.01$), and renal cortex longitudinal relaxation time T_1 ($p < 0.01$) were shown to be significantly different in patients with compensated cirrhosis who subsequently went on to

develop a negative liver related outcome (LRO) compared to those who did not have an outcome (**Figure 32**).

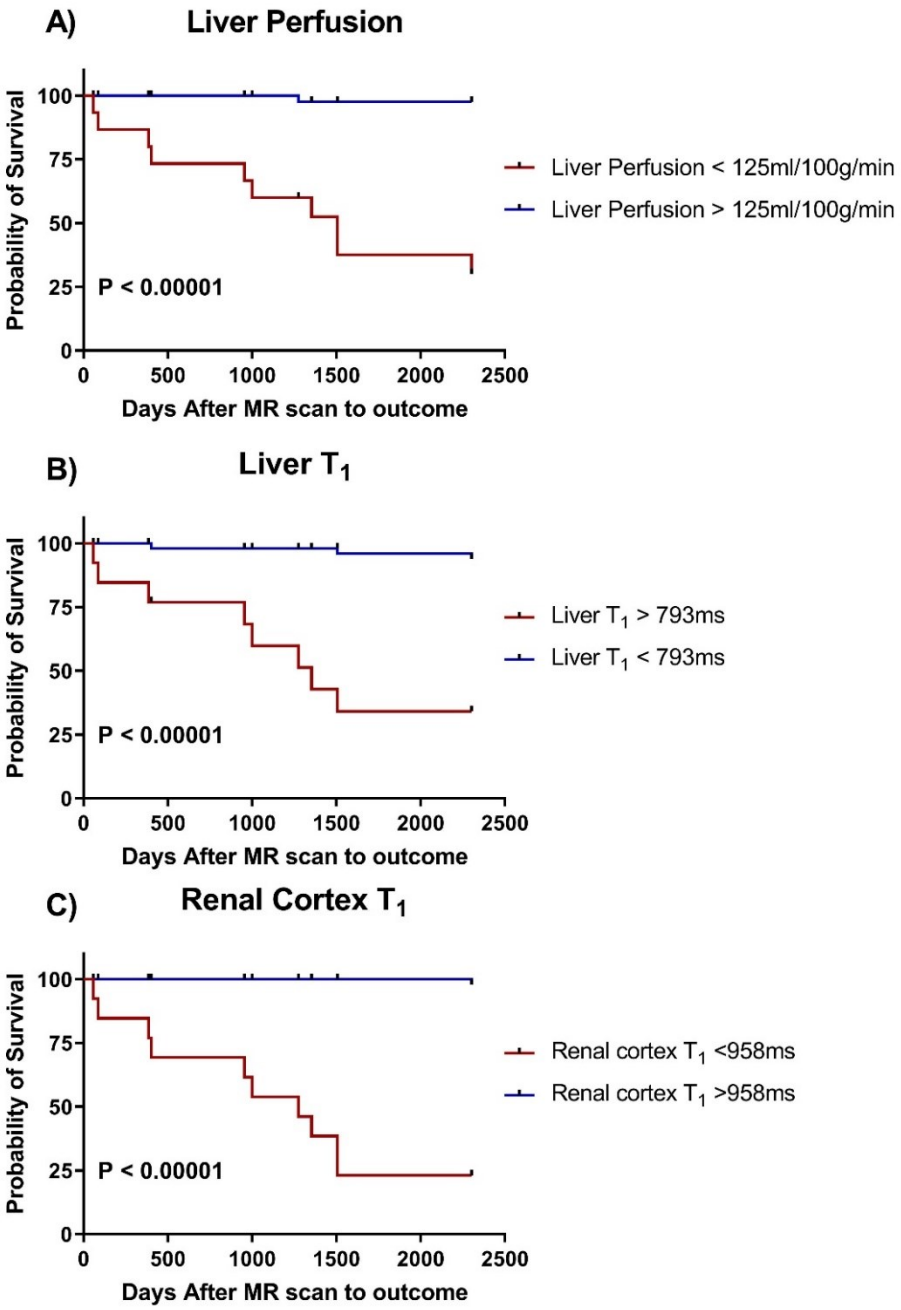

Figure 32: Kaplan-Meier survival analysis showing the tertile cut-off for liver perfusion (A), liver tissue T_1 (B) and renal cortex T_1 (C) for a negative liver related clinical outcome which occurred up to 2304 days after the baseline MRI scan in the compensated cirrhosis patient group [1], License agreement (**Appendix E**).

The main outcome of this work was to demonstrate that MRI enabled the contemporaneous assessment of both the structure and function of multiple organs in participants with liver cirrhosis in a single 1-hour scan session without the requirement for any contrast agent. This work also showed that baseline MRI measures of liver perfusion and T_1 as well as renal cortex T_1 can predict longer term negative liver related clinical outcomes.

3.2 Serial Variation in MRI measures in stable compensated cirrhosis

Knowing the expected variation in a quantitative MRI measure (repeatability) is key to the interpretation of measures taken at different points in time, for example in disease monitoring and studies of intervention assessment. Without this prior knowledge it is not possible to determine whether a change in a parameter reflects a significant change in progression or regression of disease state, or response to intervention. In Bradley *et al*. 2022, (**Publication II**), MRI measures collected in the liver, kidneys, spleen, and heart are evaluated over a 3-year period in patients with stable compensated cirrhosis. To assess this, a comprehensive evaluation of the metrics of variance were assessed, including the coefficient of variation across each group (CoV_G), the year-to-year percentage change, the coefficient of variation over time (CoV_T), and the reference change value (RCV). These values are then used to calculate a prospective sample size for a hypothetical study aiming to test a new potential drug to observe regression from the clinical Ishak score[48] F4 (advanced liver scarring) to F3 (severe liver scarring).

Patients with stable compensated cirrhosis were annually monitored to evaluate serial variation in blood serum, liver stiffness (Fibroscan®) and MRI measures, as described in **Publication I**, to determine which increases/decreases over time would be of statistical significance and correspond to a true pathological change in disease state.

In **Publication II**, patients were recruited from the prospectively followed CC cohort studied in **Publication I**, with annual assessments made in a stable group of 28 CC patients with no clinical outcomes reported on. In this group, over a

3-year period, measures were made of blood markers, transient elastography liver stiffness measure (LSM) and multiparametric MRI (organ volume, abdominal tissue T_1-mapping, blood flow, perfusion) of the liver, spleen, kidneys, and heart. Measures were also collected in a healthy volunteer group for comparison.

The total coefficient of variation was assessed between healthy volunteers and compensated cirrhosis and shown to be comparable for all measures including quantitative MRI measures and blood serum measures. Variability in Enhanced Liver Fibrosis (ELF) score was low (CoV_T < 5%) compared to Fibrosis-4 (FIB4) Index and AST to Platelet Ratio Index (APRI). A large CoV_T (20.7%) and RCV (48.3%) was observed for Fibroscan® liver stiffness measure though this must be considered against the absolute change in Fibroscan liver stiffness found within disease. Liver, spleen and renal cortex T_1 had a low CoV_T (<5%) and RCV (<8%), volume measures also had low variation (CoV_T < 10%, RCV < 16%), while haemodynamic measures were higher (CoV_T 12 - 25%, RCV 16 - 47%). For those patients with stable compensated cirrhosis who completed all 4 annual visits, data is shown year-on-year in **Figure 33**.

Hazard ratios were computed from the RCV divided by the corresponding total difference in a value between groups, for both healthy volunteer to compensated cirrhosis and compensated cirrhosis to decompensated cirrhosis. The sign of the hazard ratio indicated whether the measure increased or decreased with disease progression. Note, not all measures consistently increased/decreased with disease, for example liver volume was shown to increase from a healthy state to compensated cirrhosis state, and then decrease as decompensation occurred (**Figure 34**).

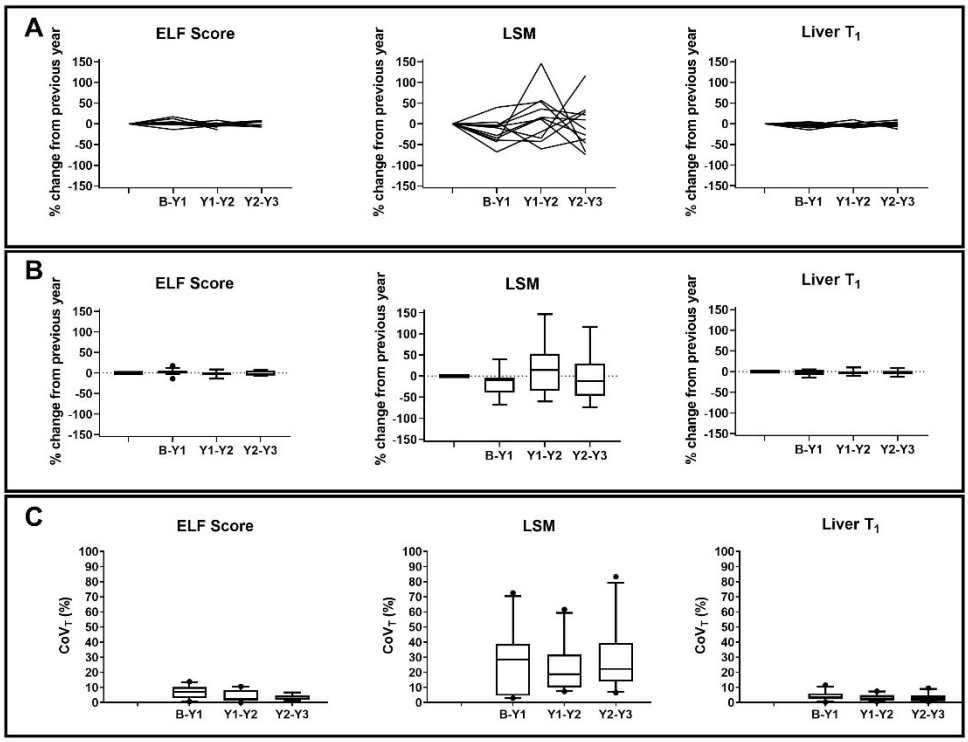

Figure 33: Assessing serial change in measures in those compensated cirrhosis (CC) who completed all study visits. A) Percentage change from previous year measurement for Enhanced Liver Fibrosis (ELF) scores, transient elastography Liver Stiffness Measure (LSM) and liver tissue T_1. B) Groupwise percentage change from previous measurements results for ELF scores, LSM and liver tissue T_1. C) Total coefficient of variation over time (CoV_T) between years for ELF score, LSM and liver tissue T_1 [1], License agreement (**Appendix E**).

A 55ms decrease in liver tissue T_1 measured at 1.5T corresponds to a disease state change from Ishak score F4 to F3 [31]. Using the RCVs computed in this work, sample size calculations were prepared for a prospective study aiming to observe cirrhosis regression from F4 to F3 (**Figure 35**).

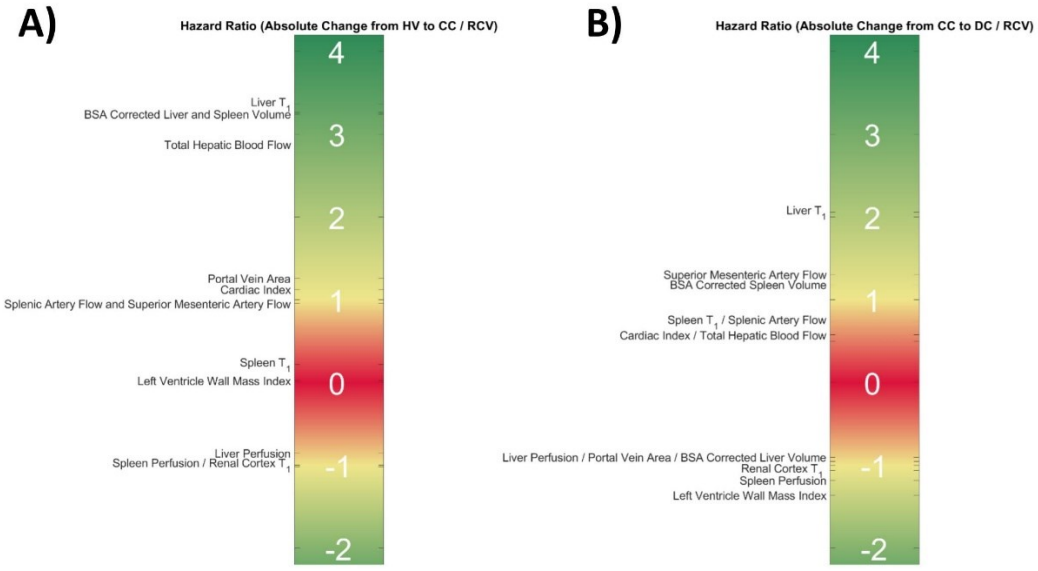

Figure 34: Hazard ratios for MRI measures using reference change values (RCV) with respect to absolute change in measures between A) healthy volunteers to patients with compensated cirrhosis (HV to CC) and B) patients with compensated cirrhosis to patients with decompensated cirrhosis (CC to DC) [2], License agreement (**Appendix E**).

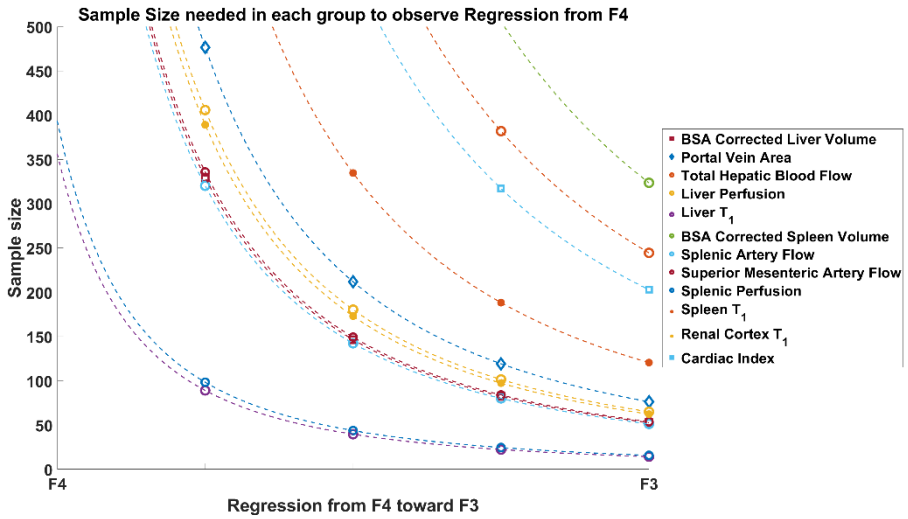

Figure 35: Sample size required to observe a change from F4 to F3 with a power of 80% and confidence of 0.95, points and lines indicate quartiles of change from F4 toward F3 [2], License agreement (**Appendix E**).

The data presented in **publication II** provides key measures for the interpretation of longitudinal monitoring of disease progression/regression

and intervention assessment when designing a study with MRI measures as endpoints in patients with compensated cirrhosis.

3.3 MRI for assessment of drug intervention

The work in Bradley et al. 2019 (**Publication III**), investigates the structure and haemodynamics of liver tissue before and up to 12 weeks after direct acting antiviral therapy to treat chronic hepatitis C virus. Multiparametric MRI was performed to assess changes in liver structure, and haemodynamics in 17 patients with chronic hepatitis C virus before direct-acting antiviral therapy and after treatment was completed within 12 weeks of the last direct acting antiviral tablet. Changes were observed in hepatic structure indicated by a significant reduction in liver T_1 by 35 ± 4 ms, liver T_2 by 2.5 ± 0.8 ms and liver T_2* by 3.0 ± 0.7 ms, as shown in **Figure 36**.

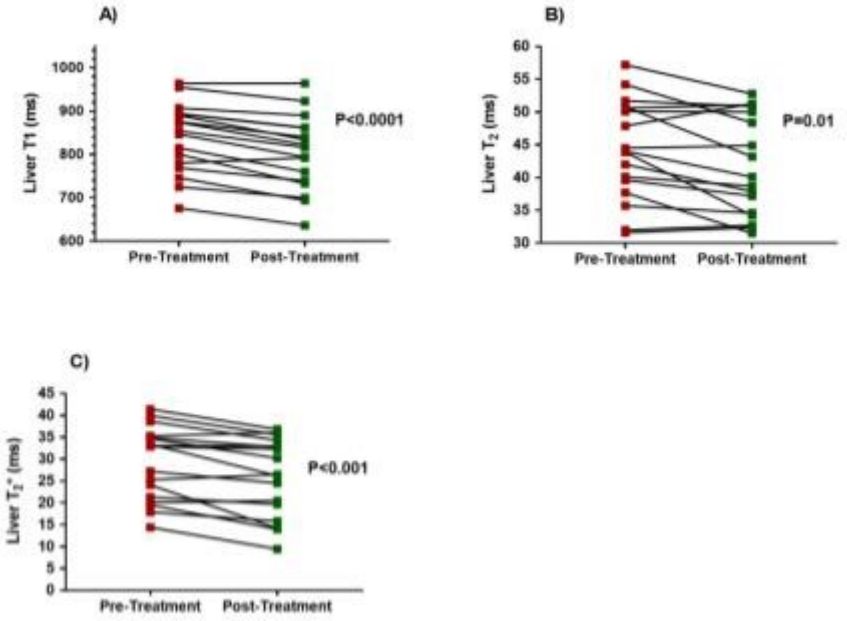

Figure 36: Pre and post treatment measures for A) liver T_1, B) liver T_2 and C) liver T_2*. All measures showed a significant reduction post treatment [3], License agreement (**Appendix E**).

An example of these structural changes in a patient pre- and post- treatment is shown in **Figure 37**. Changes were also observed in the liver haemodynamics, with liver perfusion evaluated using ASL showing an average increase of

perfusion of 28 ± 20 ml/100g/min (p = 0.03). This haemodynamic change is likely linked to reduced pro-inflammatory milieu, including interstitial oedema, within the liver.

No changes were observed in the liver or spleen blood flow, splenic perfusion, or superior mesenteric artery blood flow. This was likely due to a combination of the short period of time between measurements and the larger technical variation on the blood flow measurements (as outlined in **Publications I, II**) meaning that these measures were not sensitive enough to observe a significant change.

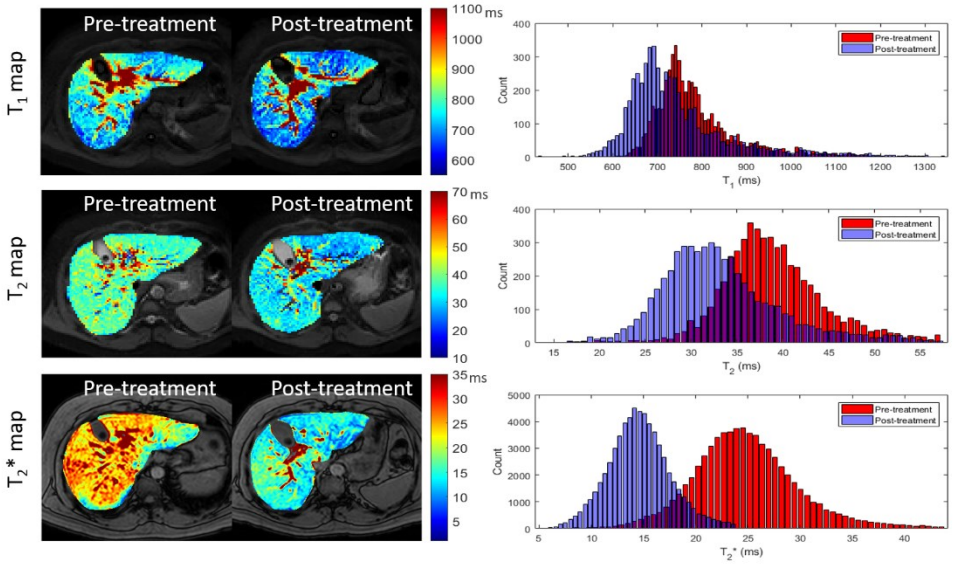

Figure 37: Example axial T_1 and transverse T_2 and T_2* liver maps in a patient pre- and post direct acting antiviral therapy, with accompanying histograms of regions of interest shown in the liver reflecting the change in the relaxometry colour maps of the liver parenchyma [3], License agreement (**Appendix E**).

This paper showed for the first time that treatment of hepatitis c virus with direct acting antiviral therapy in patients with cirrhosis leads to an acute reduction in liver T_1, T_2 and T_2* and an increase in liver perfusion. The ability of MRI to characterise changes in both structure and haemodynamics of the liver in patients with cirrhosis after a short term intervention will enhance our

understanding of the natural history of regression of liver disease and potentially influence clinical decision algorithms.

3.4 MRI for fluid balance assessment

As well as cross sectional assessment of abdominal organ structure and function with respect to disease state and evaluation pre- and post- drug intervention, MRI has the capability to dynamically assess organ function during an intervention. In Bradley et al. 2020, **Publication IV**, MRI is used to dynamically study the effects of the administration of intravenous fluids as given during GI and liver surgery on abdominal organs. In previous studies, MRI has been shown to be sensitive enough to observe differences in renal MRI measures between two infusions of 0.9% saline and plasma-lyte® 148 of the same 2l volume [49], with the blood volume expanding properties of colloids being superior to crystalloids [50]. In addition to oncotic/osmotic properties, the electrolyte composition of infusions may have important effects on visceral perfusion, with infusions containing supraphysiological chloride causing hyperchloremic acidosis and decreased renal blood flow.

Publication IV of this thesis performed a non-inferiority study to assess cardiorenal function responses to three different fluid balance regimens in healthy volunteers by using MRI measures collected throughout the fluid infusions. A validated healthy human subject model was used to compare effects of colloid (4% succinylated gelatin) and crystalloid fluid regimens on blood volume, renal function, and cardiac output. Healthy male participants were given infusions over 60 minutes with at least a 7 day wash out period in a randomized, crossover manner. The reference infusion was 1.5 litres of Sterofundin ISO, the isoeffective infusion was 0.5 litres of 4% Gelaspan®, and the isovolumetric infusion was 0.5 litres of 4% Gelaspan® with 1 litre of Sterofundin ISO (all supplied by B. Braun, Melsungen, Germany). Participants were studied over a period of 240 minutes (**Figure 38**). Baseline MRI measures of structure and function were collected, and these were repeated both during the infusion and on recovery after the infusion had finished. Changes in blood volume were calculated from changes in weight and hematocrit. Renal volume,

renal artery blood flow (RABF), renal cortex perfusion and diffusion, and cardiac index were measured using MRI.

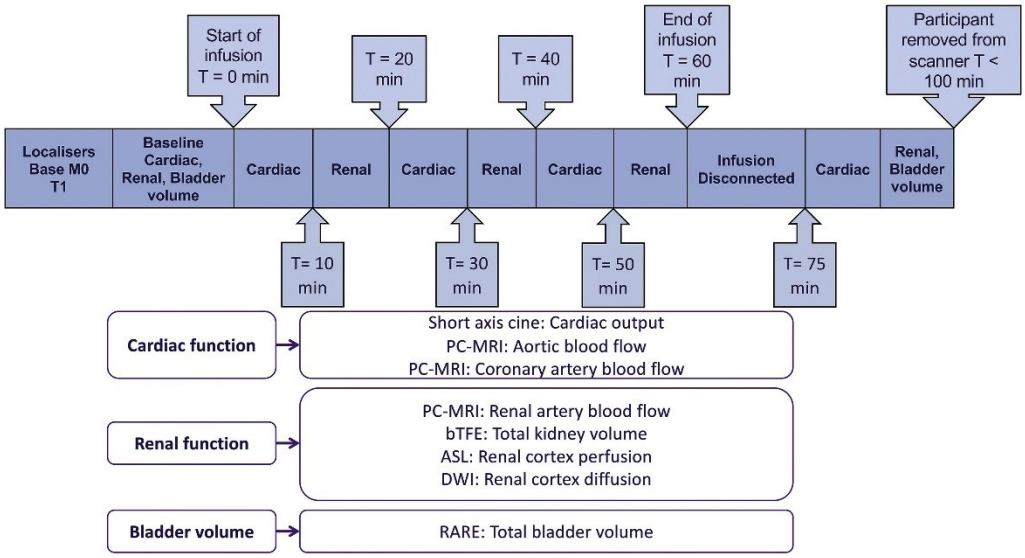

Figure 38: The study day protocol for MRI scan collection. During each of the infusion blocks, cardiac and renal MRI scans were collected. The protocol comprised scans collected at baseline, which were repeated at 20-minute intervals over the 60-minute infusion and repeated once post-infusion. This allowed assessment of the time-course of renal and cardiac responses to be monitored [5], License agreement (**Appendix E**).

Ten healthy male volunteers [mean (standard error) age 23.9 (0.8) years] completed the study. Increase in body weight and extracellular fluid volume were significantly less after the isoeffective infusion than the reference or isovolumetric infusion, but changes in blood volume did not significantly differ between infusions. All infusions increased renal volume, with no significant differences between infusions. There was no significant difference in renal artery blood flow across the infusion time course or between infusion types. Renal cortex perfusion decreased during the infusion (mean 18% decrease from baseline observed), with no significant difference between infusions. There was a trend for increased renal cortex diffusion (mean 4.2% increase from baseline) during the crystalloid infusion. All infusions led to a significant increase in cardiac index as shown in **Figure 39**.

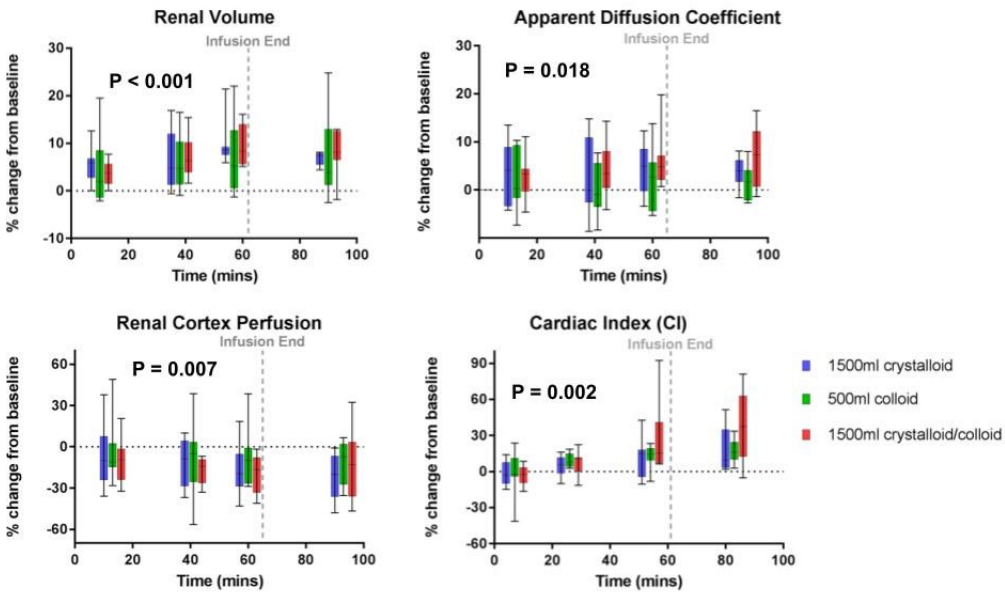

Figure 39: MRI measures over the time course of the infusions, p values correspond to significant changes over the time course of the infusion. No differences were seen between infusion type at any time point [5], License agreement (**Appendix E**).

This publication showed that a smaller volume of colloid (4% succinylated gelatin) was as effective as a larger volume of crystalloid at expanding blood volume, increasing cardiac output, and changing renal function, while significantly less interstitial space expansion occurred as a result of the colloid infusion.

4. Preliminary and Future work

The sections below outline the co-author publications and conference proceedings the candidate has presented at the '*International Society for Magnetic Resonance in Medicine (ISMRM)'*. This work will form the foundation for future projects on applying abdominal MRI to study liver disease through studies performed with the NIHR Nottingham Biomedical Research Centre (BRC).

4.1 Using MRI to derive a surrogate measure of Portal Pressure

In co-author work (**publication V**), non-contrast based MRI measures of liver tissue T_1 measured using SE-EPI and mean superior mesenteric artery velocity at 1.5 T have been shown to be a good surrogate predictor of portal pressure using HVPG [51]. This work also included an assessment of the value of spleen T_1. In follow-on work by the candidate, the relationship between MRI measures and portal pressure have also been studied at 3T (**Conference Proceedings B and D**). **Conference Proceedings D** demonstrated that the relationship between liver T_1 and portal pressure holds true at 3T, though when data from 1.5T and 3T were pooled, it was observed that a positive linear correlation between SMA blood flow velocity and HVPG holds true only up until a measured HVPG of 15 mmHg, as shown in **Figure 40**. This suggests that as splanchnic flow increases and splenic venous flow into the portal vein is impeded by elevated portal pressure, congestion of intrasplenic blood and therefore spleen enlargement occurs. In **Conference Proceedings B** the two methods of liver T_1 data acquisition (SE-EPI and MOLLI) are directly compared to HVPG, and the effect of liver tissue fat fraction on the difference in measured T_1 between SE-EPI and MOLLI is observed, as shown in **Figure 41**.

In future work, having shown that both 1.5T and 3T liver SE-EPI T_1 and SMA blood flow velocity non-invasive MRI can be used as a surrogate measure to determine portal pressure, it is planned to translate these methods to create a non-invasive tool to apply in the clinical setting for testing.

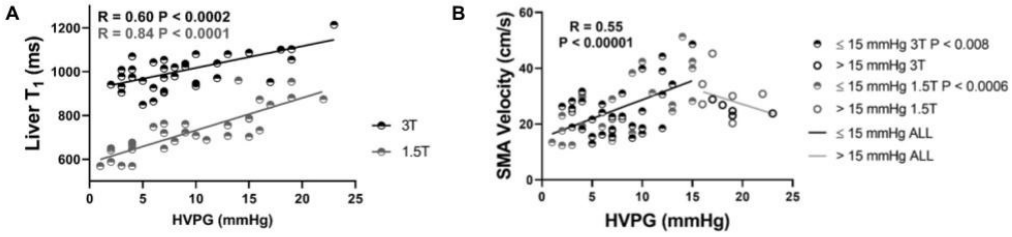

Figure 40: Relationship between MR parameters of (A) structure using SE-EPI liver T_1 over the full range of measured hepatic venous pressure gradient (HVPG) and (B) flow using PC-MRI SMA velocity up to a HVPG of 15 mmHg.

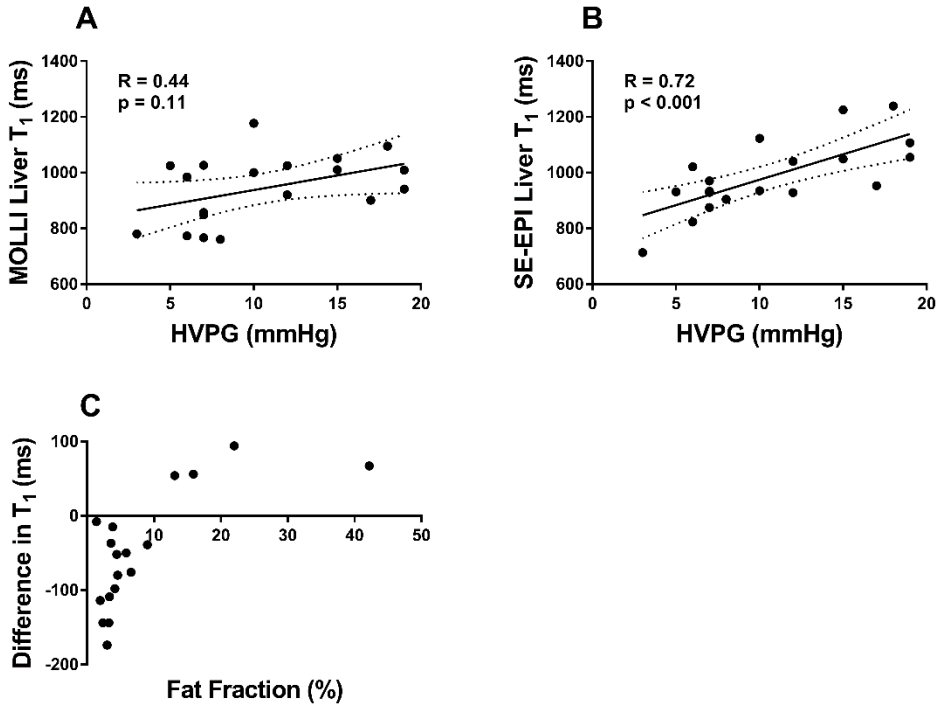

Figure 41: In a subset of patients with liver disease from **Conference Proceedings B**, who underwent both SE-EPI liver T_1 and MOLLI liver T_1, A) MOLLI liver T_1 did not significantly correlate with HVPG whereas, B) SE-EPI liver T_1 did correlate with HVPG. C) The relationship between the difference in measured T_1 from the 2 acquisition techniques and fat fraction is observed.

Recently, others have reported that dynamic contrast enhanced MRI can provide a surrogate measure of HVPG, though this method requires the injection of a gadolinium based bolus and so is more invasive [52, 53].

Estimated hepatic artery fraction using phase contrast MRI caval subtraction (a technique whereby blood flow is measured using PC-MRI in the suprahepatic, subcardiac vena cava and the infrahepatic, suprarenal vena cava) and portal vein flow phase contrast MRI have also been linked with portal pressure yielding promising results in nine participants ($R = 0.78$, $p = 0.014$) [54] (vessels labelled in **Figure 4**).

There are also considerations to be made for information that more recent techniques such as Magnetic Resonance Elastography (MRE), which measures liver stiffness, can play in the role of detecting portal pressure. MRE has also been shown to correlate with HVPG over a range of 5 – 29 mmHg [55]. In **Publication VII,** a finite element model (FEM) simulation was employed to evaluate liver MRE accuracy and offer best practices for optimisation of data acquisition methodology. This publication demonstrated that the resultant stiffness was dependent partly on acquisition voxel resolution and recommended that the optimal voxel size was a 4-6mm isotropic voxel [56], unlike current typically reported acquisitions that us the Quantitative Imaging Biomarkers Alliance (QIBA) recommendations for MRE [57]. The QIBA recommended protocol is known to have a technical CoV in the range of 20% [57], larger than that of relaxometry measures [58]. In **Conference Proceedings C** it is demonstrated that at 3T the number of voxels fitted within the liver tissue with a confidence >0.95 correlated with the T_2* value of the liver tissue for gradient echo MRE, likely as a result of the long gradient echo times needed to achieve sufficient motion encoding within the readout, which enhances spin dephasing and results in poorer image quality and phase coherence. MRE acquisitions utilizing a spin-echo readout have been demonstrated to be an option where gradient echo MRE fails [59] and should be investigated further with other quantitative MRI measures. This led to preliminary work assessing MRI relaxometry, haemodynamic measures and MRE stiffness measures against disease severity (**Conference Proceedings E**), **Figure 42**. In future work, it will be assessed as to whether the combination of MR measures with minimally invasive blood markers of liver disease can better predict portal

pressure as in a recent study for non-alcoholic steatohepatitis disease severity where it was determined that using a marker that is a score computed from a combination of MR relaxometry, AST and Gamma-glutamyl Transferase (GGT) gave best results [60].

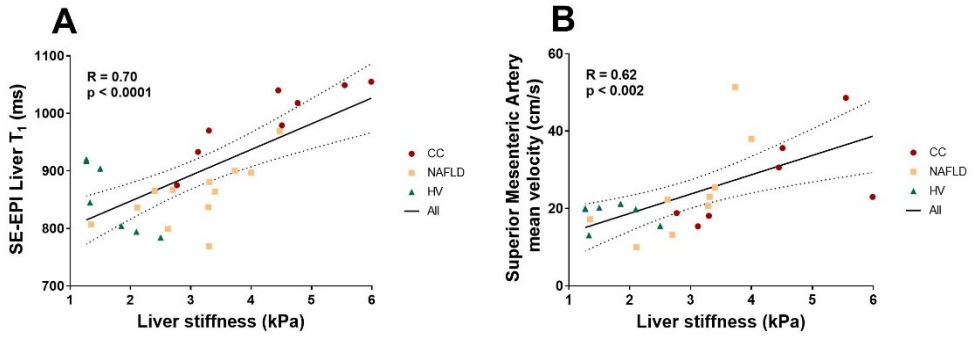

Figure 42: A strong correlation is seen between (A) liver tissue T_1 and liver stiffness as assessed with MRE ($R = 0.70$, $p < 0.0001$) and (B) superior mesenteric artery mean velocity and MRE liver stiffness ($R = 0.62$, $p < 0.002$).

The ultimate goal of this work is to in future combine quantitative MR surrogate HVPG methods into a standardised protocol for prediction of portal pressure, field strength and MR vendor agnostic where data can be quality assured with robust quality management to enable clinical use. However, importantly before such quantitative measures can be adopted they require standardization, consistent acquisition and analysis, and rigorous quality control as is outlined in [61]. Work is currently underway to establish this as is detailed in **Conference Proceedings F**. For example, to study HVPG pre-surgery where those patients with portal hypertension have worse outcomes, or help to aid and improve the determination of the therapeutic window [7] for patients who would benefit from non-selective beta blocker therapy.

4.2 Clinical applications in transplant and response to treatment.

Publications I and II describe a single session < 1-hour multi-organ MRI protocol. The goal is to now perform this protocol in patients awaiting liver transplant. Such a scan in this setting would help determine whether other organs within the recipient could tolerate the transplanted liver. This study

would need to be observational and offered secondary to the patient's routine pathway and care.

The methods described in this thesis are also now being used to study potential anti-fibrotic treatments, as was suggested in **Publication II**. A study is currently underway to determine the efficacy for the use of sirolimus as an anti-fibrotic treatment in patients with advanced, chronic liver disease. This is a Phase II, randomised, patient-blinded, placebo-controlled, proof of concept, parallel group single centre trial. 45 participants are being randomised to sirolimus or placebo in a 2:1 ratio for 6 months. In this study patients are undergoing trans-jugular liver biopsy and MRI including structural/architecture of the liver, spleen, and kidneys, haemodynamics of splanchnic and collateral circulation, and cardiac structure and output, with measures collected at baseline and after 6 months of sirolimus treatment.

5. Conclusion

The published works that form this thesis show a substantiative contribution to knowledge in the field of abdominal multi-organ evaluation in liver disease using quantitative MRI. They demonstrate that it is possible to study multiple organ structure and function in a single MRI scan session. It is shown that quantitative MRI has the sensitivity and power to delineate liver disease severity as well as track disease progression. This thesis has also shown that MRI is sensitive enough to observe changes in liver structure in as little as 12 weeks and so shows the potential for use as an endpoint in future clinical trials. Importantly, the work here demonstrates that completely non-invasive quantitative MRI aids in giving a better picture of both the structure and haemodynamic function of abdominal organs like no other imaging modality without contrast agents. Quantitative MRI is also shown to be able to study the acute effect of fluid regimes used perioperatively.

Early results show that quantitative MRI offers a promising alternative to invasive testing in clinical practice in liver disease, which can be used as endpoints in clinical trials. The large multi centre European wide study: “Liver Investigation: Testing Marker Utility in Steatohepatitis (LITMUS)”, a consortium of researchers currently aims to assess and validate imaging modality performance, including structural quantitative MRI measures, specifically addressing markers of non-alcoholic fatty liver disease and its severity.

In future, it is aimed to collect the main outcome measures of **Publication I and II** (SE-EPI liver T_1, SMA blood flow velocity, liver T_2*) in a short ~20 minute consolidated protocol across MR vendors (Philips, General Electric and Siemens) for clinical translation to evaluate if MRI can aid in the decision making for surgery by defining those patients with portal hypertension who are at increased risk of mortality with surgery. Ultimately, the long-term goal is to provide a short protocol of key measures that is automatically analysed with quality assured results for clinical studies of portal pressure.

6. References

1. Bradley CR, Cox EF, Scott RA, et al (2018) Multi-organ assessment of compensated cirrhosis patients using quantitative magnetic resonance imaging. J Hepatol 69:1015–1024. https://doi.org/10.1016/J.JHEP.2018.05.037

2. Bradley CR, Cox EF, Palaniyappan N, et al (2022) Variability of noninvasive MRI and biological markers in compensated cirrhosis: insights for assessing disease progression. European Radiology Experimental 2022 6:1 6:1–15. https://doi.org/10.1186/S41747-022-00303-Y

3. Bradley C, Scott RA, Cox E, et al (2019) Short-term changes observed in multiparametric liver MRI following therapy with direct-acting antivirals in chronic hepatitis C virus patients. Eur Radiol 29:3100–3107. https://doi.org/10.1007/S00330-018-5788-1/FIGURES/4

4. Lobo DN, Macafee DAL, Allison SP (2006) How perioperative fluid balance influences postoperative outcomes. Best Pract Res Clin Anaesthesiol 20:439–455. https://doi.org/10.1016/J.BPA.2006.03.004

5. Bradley CR, Bragg DD, Cox EF, et al (2020) A randomized, controlled, double-blind crossover study on the effects of isoeffective and isovolumetric intravenous crystalloid and gelatin on blood volume, and renal and cardiac hemodynamics. Clin Nutr 39:2070–2079. https://doi.org/10.1016/J.CLNU.2019.09.011

6. Møller S, Bendtsen F (2015) Cirrhotic Multiorgan Syndrome. Digestive Diseases and Sciences 2015 60:11 60:3209–3225. https://doi.org/10.1007/S10620-015-3752-3

7. Krag A, Wiest R, Albillos A, Gluud LL (2012) The window hypothesis: haemodynamic and non-haemodynamic effects of β-blockers improve survival of patients with cirrhosis during a window in the disease. Gut 61:967–969. https://doi.org/10.1136/GUTJNL-2011-301348

6. References

8. Moorthy AV, Blichfeldt TC (2009) Anatomy and Physiology of the Kidney. Pathophysiology of Kidney Disease and Hypertension 1–15. https://doi.org/10.1016/B978-1-4160-4391-1.50007-2

9. Wai CT, Greenson JK, Fontana RJ, et al (2003) A simple noninvasive index can predict both significant fibrosis and cirrhosis in patients with chronic hepatitis C. Hepatology 38:518–526. https://doi.org/10.1053/JHEP.2003.50346

10. Sterling RK, Lissen E, Clumeck N, et al (2006) Development of a simple noninvasive index to predict significant fibrosis in patients with HIV/HCV coinfection. Hepatology 43:1317–1325. https://doi.org/10.1002/HEP.21178

11. Rosenberg WMC, Voelker M, Thiel R, et al (2004) Serum markers detect the presence of liver fibrosis: A cohort study. Gastroenterology 127:1704–1713. https://doi.org/10.1053/J.GASTRO.2004.08.052

12. Kamath PS, Wiesner RH, Malinchoc M, et al (2001) A model to predict survival in patients with end-stage liver disease. Hepatology 33:464–470. https://doi.org/10.1053/JHEP.2001.22172

13. Barber K, Madden S, Allen J, et al (2011) Elective liver transplant list mortality: development of a United Kingdom end-stage liver disease score. Transplantation 92:469–476. https://doi.org/10.1097/TP.0B013E318225DB4D

14. Stevenson M, Lloyd-Jones M, Morgan MY, Wong R (2012) Non-invasive diagnostic assessment tools for the detection of liver fibrosis in patients with suspected alcohol-related liver disease: a systematic review and economic evaluation. Health Technol Assess 16:. https://doi.org/10.3310/HTA16040

15. Sandrin L, Fourquet B, Hasquenoph JM, et al (2003) Transient elastography: a new noninvasive method for assessment of hepatic

fibrosis. Ultrasound Med Biol 29:1705–1713. https://doi.org/10.1016/J.ULTRASMEDBIO.2003.07.001

16. Cirrhosis in over 16s Assessment and management NICE guideline NG50

17. Nahon P, Kettaneh A, Tengher-Barna I, et al (2008) Assessment of liver fibrosis using transient elastography in patients with alcoholic liver disease. J Hepatol 49:1062–1068. https://doi.org/10.1016/J.JHEP.2008.08.011

18. Siddiqui MS, Vuppalanchi R, van Natta ML, et al (2019) Vibration-Controlled Transient Elastography to Assess Fibrosis and Steatosis in Patients With Nonalcoholic Fatty Liver Disease. Clinical Gastroenterology and Hepatology 17:156-163.e2. https://doi.org/10.1016/J.CGH.2018.04.043

19. Castera L, Yuen Chan HL, Arrese M, et al (2015) EASL-ALEH Clinical Practice Guidelines: Non-invasive tests for evaluation of liver disease severity and prognosis. J Hepatol 63:237–264. https://doi.org/10.1016/J.JHEP.2015.04.006

20. Thiele M, Madsen BS, Hansen JF, et al (2018) Accuracy of the Enhanced Liver Fibrosis Test vs FibroTest, Elastography, and Indirect Markers in Detection of Advanced Fibrosis in Patients With Alcoholic Liver Disease. Gastroenterology 154:1369–1379. https://doi.org/10.1053/J.GASTRO.2018.01.005/ATTACHMENT/1E9B3B2D-4E2A-42D7-98D9-EEF47BB79289/MMC1.PDF

21. Yin M, Talwalkar JA, Glaser KJ, et al A Preliminary Assessment of Hepatic Fibrosis with Magnetic Resonance Elastography

22. Cadranel JF, Rufat P, Degos F (2000) Practices of liver biopsy in France: results of a prospective nationwide survey. For the Group of Epidemiology of the French Association for the Study of the Liver (AFEF). Hepatology 32:477–481. https://doi.org/10.1053/JHEP.2000.16602

23. Maharaj B, Leary WP, Naran AD, et al (1986) Sampling variability and its influence on the diagnostic yield of percutaneous needle biopsy of the liver. Lancet 1:523–525. https://doi.org/10.1016/S0140-6736(86)90883-4

24. Regev A, Berho M, Jeffers LJ, et al (2002) Sampling error and intraobserver variation in liver biopsy in patients with chronic HCV infection. Am J Gastroenterol 97:2614–2618. https://doi.org/10.1111/J.1572-0241.2002.06038.X

25. Bedossa P, Dargère D, Paradis V (2003) Sampling variability of liver fibrosis in chronic hepatitis C. Hepatology 38:1449–1457. https://doi.org/10.1016/J.HEP.2003.09.022

26. Colloredo G, Guido M, Sonzogni A, Leandro G (2003) Impact of liver biopsy size on histological evaluation of chronic viral hepatitis: the smaller the sample, the milder the disease. J Hepatol 39:239–244. https://doi.org/10.1016/S0168-8278(03)00191-0

27. Groszmann RJ, Wongcharatrawee S (2004) The hepatic venous pressure gradient: Anything worth doing should be done right. Hepatology 39:280–283. https://doi.org/10.1002/HEP.20062

28. Guha IN, Myers RP, Patel K, Talwalkar JA (2011) Biomarkers of liver fibrosis: What lies beneath the receiver operating characteristic curve? Hepatology 54:1454–1462. https://doi.org/10.1002/HEP.24515

29. Mansfield P, Pykett IL, Morris PG, Coupland RE (1978) Human whole body line-scan imaging by NMR. British Journal of Radiology 51:921–922. https://doi.org/10.1259/0007-1285-51-611-921

30. de Bazelaire CMJ, Duhamel GD, Rofsky NM, Alsop DC (2004) MR Imaging Relaxation Times of Abdominal and Pelvic Tissues Measured in Vivo at 3.0 T: Preliminary Results1. https://doi.org/101148/radiol2303021331 230:652–659. https://doi.org/10.1148/RADIOL.2303021331

31. Hoad CL, Palaniyappan N, Kaye P, et al (2015) A study of T1 relaxation time as a measure of liver fibrosis and the influence of confounding histological factors. NMR Biomed 28:706–714. https://doi.org/10.1002/NBM.3299

32. Chandarana H, Lim RP, Jensen JH, et al (2012) Hepatic Iron Deposition in Patients With Liver Disease: Preliminary Experience With Breath-Hold Multiecho T2*-Weighted Sequence. http://dx.doi.org/102214/AJR081996 193:1261–1267. https://doi.org/10.2214/AJR.08.1996

33. Idilman IS, Celik A, Savas B, et al (2021) The feasibility of T2 mapping in the assessment of hepatic steatosis, inflammation, and fibrosis in patients with non-alcoholic fatty liver disease: a preliminary study. Clin Radiol 76:709.e13-709.e18. https://doi.org/10.1016/J.CRAD.2021.06.014

34. Park HW, Kim DJ, Cho ZH (1987) Gradient reversal technique and its applications to chemical-shift-related NMR imaging. Magn Reson Med 4:526–536. https://doi.org/10.1002/MRM.1910040604

35. Pruessmann KP, Weiger M, Scheidegger MB, Boesiger P (1999) SENSE: Sensitivity Encoding for Fast MRI. Magn Reson Med 42:952–962. https://doi.org/10.1002/(SICI)1522-2594(199911)42:5

36. Hoad CL, Palaniyappan N, Kaye P A study of T1 relaxation time as a measure of liver fibrosis and the influence of confounding histological factors. NMR Biomed 28:706–714

37. Li J, Liu H, Zhang C, et al (2020) Native T1 mapping compared to ultrasound elastography for staging and monitoring liver fibrosis: an animal study of repeatability, reproducibility, and accuracy. Eur Radiol 30:337–345. https://doi.org/10.1007/S00330-019-06335-0/TABLES/3

38. Heye T, Yang SR, Bock M, et al (2012) MR relaxometry of the liver: significant elevation of T1 relaxation time in patients with liver cirrhosis. Eur Radiol 22:1224–1232. https://doi.org/10.1007/S00330-012-2378-5

39. Wu J, Shi Z, Zhang Y, et al (2021) Native T1 Mapping in Assessing Kidney Fibrosis for Patients With Chronic Glomerulonephritis. Front Med (Lausanne) 8:772326. https://doi.org/10.3389/FMED.2021.772326

40. Banerjee R, Pavlides M, Tunnicliffe EM, et al (2014) Multiparametric magnetic resonance for the non-invasive diagnosis of liver disease. J Hepatol 60:69–77. https://doi.org/10.1016/j.jhep.2013.09.002

41. Tunnicliffe EM, Banerjee R, Pavlides M, et al (2017) A model for hepatic fibrosis: the competing effects of cell loss and iron on shortened modified Look-Locker inversion recovery T 1 (shMOLLI-T 1) in the liver. J Magn Reson Imaging 45:450–462. https://doi.org/10.1002/JMRI.25392

42. Mozes FE, Tunnicliffe EM, Pavlides M, Robson MD (2016) Influence of fat on liver T1 measurements using modified Look–Locker inversion recovery (MOLLI) methods at 3T. Journal of Magnetic Resonance Imaging 44:105–111. https://doi.org/10.1002/JMRI.25146

43. Mozes FE, Tunnicliffe EM, Moolla A, et al (2019) Mapping tissue water T1 in the liver using the MOLLI T1 method in the presence of fat, iron and B0 inhomogeneity. NMR Biomed 32:e4030. https://doi.org/10.1002/NBM.4030

44. Wood JC, Enriquez C, Ghugre N, et al (2005) MRI R2 and R2* mapping accurately estimates hepatic iron concentration in transfusion-dependent thalassemia and sickle cell disease patients. Blood 106:1460–1465. https://doi.org/10.1182/blood-2004-10-3982

45. Gardener AG, Francis ST (2010) Multislice perfusion of the kidneys using parallel imaging: image acquisition and analysis strategies. Magn Reson Med 63:1627–1636. https://doi.org/10.1002/MRM.22387

46. Buxton RB, Frank LR, Wong EC, et al (1998) A general kinetic model for quantitative perfusion imaging with arterial spin labeling. Magn Reson Med 40:383–396. https://doi.org/10.1002/MRM.1910400308

47. Dobre MC, Uğurbil K, Marjanska M (2007) Determination of blood longitudinal relaxation time (T1) at high magnetic field strengths. Magn Reson Imaging 25:733–735. https://doi.org/10.1016/J.MRI.2006.10.020

48. Ishak K, Baptista A, Bianchi L, et al (1995) Histological grading and staging of chronic hepatitis. J Hepatol 22:696–699. https://doi.org/10.1016/0168-8278(95)80226-6

49. Chowdhury AH, Cox EF, Francis ST, Lobo DN (2012) A randomized, controlled, double-blind crossover study on the effects of 2-L infusions of 0.9% saline and plasma-lyte® 148 on renal blood flow velocity and renal cortical tissue perfusion in healthy volunteers. Ann Surg 256:18–24. https://doi.org/10.1097/SLA.0B013E318256BE72

50. Lobo DN, Stanga Z, Aloysius MM, et al (2010) Effect of volume loading with 1 liter intravenous infusions of 0.9% saline, 4% succinylated gelatine (Gelofusine) and 6% hydroxyethyl starch (Voluven) on blood volume and endocrine responses: A randomized, three-way crossover study in healthy volunteers. Crit Care Med 38:464–470. https://doi.org/10.1097/CCM.0B013E3181BC80F1

51. Palaniyappan N, Cox E, Bradley C, et al (2016) Non-invasive assessment of portal hypertension using quantitative magnetic resonance imaging. J Hepatol 65:1131–1139. https://doi.org/10.1016/J.JHEP.2016.07.021

52. Hectors SJ, Bane O, Kennedy P, et al (2021) Noninvasive diagnosis of portal hypertension using gadoxetate DCE-MRI of the liver and spleen. Eur Radiol 31:4804–4812. https://doi.org/10.1007/S00330-020-07495-0

53. Wagner M, Hectors S, Bane O, et al (2018) Non-invasive prediction of portal pressure with MR elastography and DCE-MRI of the liver and

spleen: preliminary results. J Magn Reson Imaging 48:1091. https://doi.org/10.1002/JMRI.26026

54. Chouhan MD, Mookerjee RP, Bainbridge A, et al (2017) Caval subtraction 2D phase-contrast MRI to measure total liver and hepatic arterial blood flow. Invest Radiol 52:170–176. https://doi.org/10.1097/RLI.0000000000000328

55. Danielsen KV, Hove JD, Nabilou P, et al (2021) Using MR elastography to assess portal hypertension and response to beta-blockers in patients with cirrhosis. Liver International 41:2149–2158. https://doi.org/10.1111/LIV.14981

56. McGrath DM, Bradley CR, Francis ST (2021) In silico evaluation and optimisation of magnetic resonance elastography of the liver. Phys Med Biol 66:. https://doi.org/10.1088/1361-6560/AC3263

57. Quantitative Imaging Biomarkers Alliance (2017) QIBA Profile : Magnetic Resonance Elastography of the Liver. 1–65

58. Serai SD, Obuchowski NA, Venkatesh SK, et al (2017) Repeatability of MR Elastography of Liver: A Meta-Analysis. Radiology 285:92. https://doi.org/10.1148/RADIOL.2017161398

59. Kim YS, Jang YN, Song JS (2018) Comparison of gradient-recalled echo and spin-echo echo-planar imaging MR elastography in staging liver fibrosis: a meta-analysis. Eur Radiol 28:1709–1718. https://doi.org/10.1007/S00330-017-5149-5/TABLES/4

60. Dennis A, Mouchti S, Kelly M, et al (2020) A composite biomarker using multiparametric magnetic resonance imaging and blood analytes accurately identifies patients with non-alcoholic steatohepatitis and significant fibrosis. Scientific Reports 2020 10:1 10:1–11. https://doi.org/10.1038/s41598-020-71995-8

61. Hubbard Cristinacce PL, Keaveney S, Aboagye EO, et al (2022) Clinical translation of quantitative magnetic resonance imaging biomarkers – An

overview and gap analysis of current practice. Physica Medica 101:165–182. https://doi.org/10.1016/J.EJMP.2022.08.015

7. List of peer reviewed publications from the University of Nottingham with author contribution

7.1 First Author Publications

I) Bradley CR, Cox EF, Scott RA, James MW, Kaye P, Aithal GP, Francis ST, Guha IN. Multi-organ assessment of compensated cirrhosis patients using quantitative magnetic resonance imaging. Journal of Hepatology. 2018 Nov 1;69(5):1015-24.

This paper was the first paper to assess multiple organs in a cohort of patients with liver disease in a single one hour scan session. This work was also the first to show that MRI measures had the power to predict negative liver related outcomes up to 2304 days before the event occurred.

Author contribution – MRI data acquisition (35%), MRI data analysis (50%), statistical analysis (100%), and interpretation (40%), drafting of manuscript including critical review of manuscript (40%).

II) Bradley CR, Cox EF, Palaniyappan N, Aithal GP, Francis ST, Guha IN. Variability of noninvasive MRI and biological markers in compensated cirrhosis: insights for assessing disease progression. European Radiology Experimental. 2022 Oct 24;6(1):52.

This paper was the first to perform multiple organ serial MRI measures 1 year apart in liver disease patients and report on the variability of these MRI measures as well as offering sample size estimations for future studies investigation liver disease progression or regression with respect to intervention.

Author contribution - MRI data acquisition (35%), MRI data analysis (50%), statistical analysis (100%), and interpretation (40%), drafting of manuscript including critical review of manuscript (40%).

III) Bradley CR, Scott RA, Cox E, Palaniyappan N, Thomson BJ, Ryder SD, Irving WL, Aithal GP, Guha IN, Francis S. Short-term changes observed in

multiparametric liver MRI following therapy with direct-acting antivirals in chronic hepatitis C virus patients. European Radiology. 2019 Jun;29(6):3100-7.

This paper was the first paper to show that MRI measures of the liver were sensitive enough to observe changes to liver structure in a short period of time between pre and post direct acting antiviral therapy in a cohort of chronic hepatitis C virus patients who achieved sustained virological response.

Author contribution - MRI data acquisition (90%), MRI data analysis (90%), statistical analysis (100%), interpretation (40%), drafting of manuscript including critical review of manuscript (40%).

IV) Bradley CR, Bragg DD, Cox EF, El-Sharkawy AM, Buchanan CE, Chowdhury AH, Macdonald IA, Francis ST, Lobo DN. A randomized, controlled, double-blind crossover study on the effects of isoeffective and isovolumetric intravenous crystalloid and gelatin on blood volume, and renal and cardiac hemodynamics. Clinical Nutrition. 2020 Jul 1;39(7):2070-9.

This paper showed that MRI measures of the kidney and heart were sensitive enough to detect haemodynamic changes over the time course of different infusion types and that there were no differences between infusion types despite the volume of the crystalloid infusion being three times that of one of the colloid infusion.

Author contribution - MRI data acquisition (70%), MRI data analysis (90%), statistical analysis (100%), interpretation (60%), drafting of manuscript including critical review of manuscript (50%).

7.2 Co-author Publications

V) Palaniyappan N, Cox E, Bradley CR, Scott R, Austin A, O'Neill R, Ramjas G, Travis S, White H, Singh R, Thurley P. Non-invasive assessment of portal hypertension using quantitative magnetic resonance imaging. Journal of hepatology. 2016 Dec 1;65(6):1131-9.

7. List of peer reviewed publications from the University of Nottingham with author contribution

This paper was the first to demonstrate that structural and haemodynamic measures could be used to create a model that predicted portal pressure measurements with the hepatic venous pressure gradient measure in liver disease patients. This model was then applied to a validation cohort as described in this paper.

Author contribution - MRI data acquisition (20%), data analysis and interpretation (25%), drafting of manuscript including critical review of manuscript (10%).

VI) Cox EF, Buchanan CE, Bradley CR, Prestwich B, Mahmoud H, Taal M, Selby NM, Francis ST. Multiparametric renal magnetic resonance imaging: validation, interventions, and alterations in chronic kidney disease. Frontiers in physiology. 2017 Sep 14;8:696.

This paper was the first to describe a multiparametric MRI protocol for the assessment of the kidneys with short term validation of measures.

Author contribution - MRI data acquisition (5%), data analysis and interpretation (5%), statistical analysis (5%), drafting of manuscript including critical review of manuscript (10%).

VII) McGrath DM, Bradley CR, Francis ST. In silico evaluation and optimisation of magnetic resonance elastography of the liver. Physics in Medicine & Biology. 2021 Nov 10;66(22):225005.

This paper used magnetic resonance elastography simulations to evaluate current MRE techniques and offered optimisations to improve accuracy of MRE data.

Author contribution - MRI data acquisition design (30%), data analysis and interpretation (20%), drafting of manuscript including critical review of manuscript (20%).

7. List of peer reviewed publications from the University of Nottingham with author contribution

7.3 Conference proceedings

A) Bradley CR, Buchanan C, Cox EF, Francis ST. Assessment of Optimal Technique for Measurement of Medullary Perfusion. InProc. Intl. Soc. Mag. Reson. Med 2018 (Vol. 26, p. 4600).

B) Bradley CR, Scott R, Cox EF, Palaniyappan N, Guha IN, Aithal GP, Francis ST. Quantitative MRI to assess portal hypertension in cirrhosis patients at 3T. InProc. Intl. Soc. Mag. Reson. Med 2019 (Vol. 27, p. 1738).

C) Bradley CR, McGrath D, Cox EF, Francis ST. Effect of spatial resolution on Gradient Echo Magnetic Resonance Elastography at 3T. InProc. Intl. Soc. Mag. Reson. Med 2020 (Vol. 28, p. 2493).

D) Bradley CR, Scott R, Cox EF, Palaniyappan N, Guha IN, Aithal GP, Francis ST. Quantitative MRI to assess portal hypertension in cirrhosis patients. InProc. Intl. Soc. Mag. Reson. Med 2020 (Vol. 28, p. 0323).

E) Bradley CR, Mcgrath D, Cox EF, Palaniyappan N, Scott R, Guha IN, Aithal GP, Francis ST. The association of Liver Stiffness with Liver tissue T_1 and Superior Mesenteric Artery blood flow across disease severity. InProc. Intl. Soc. Mag. Reson. Med 2022 (Vol. 30, p. 0604).

F) Bradley CR, Cox EF, Francis ST. Translation of a non-contrast quantitative MRI protocol for portal pressure prediction InProc. Intl. Soc. Mag. Reson. Med 2023 (Vol. 31, p. To Be Confirmed).

8. Statements about Joint Authorship

The University of Nottingham recognises that, in many disciplines, jointly authored papers are the norm rather than the exception, The University requires a statement from any joint principal author outlining the candidate's contribution to the publication. Below are signed statements from Joint principal authors regarding **Publications II, III, IV**.

8.1 Joint Principal Author Statements

Regarding **Publication II**, Variability of noninvasive MRI and biological markers in compensated cirrhosis: insights for assessing disease progression. I, Eleanor Cox, was a postdoctoral fellow on the study and was involved in the MRI data collection and analysis for the study from 2010 – 2015. I agree with the following statement on author contribution of Christopher Bradley: MRI data acquisition (35%), MRI data analysis (50%), statistical analysis (100%), and interpretation (40%), drafting of manuscript including critical review of manuscript (40%).

Signed:  Date: 7th February 2023

Regarding **Publication II**, Variability of noninvasive MRI and biological markers in compensated cirrhosis: insights for assessing disease progression. I, Naaventhan Palaniyappan, was an academic clinical lecturer, and was involved in recruiting patients to this study, drafting and critically reviewing the manuscript. I agree with the following statement on author contribution of Christopher Bradley: MRI data acquisition (35%), MRI data analysis (50%), statistical analysis (100%), and interpretation (40%), drafting of manuscript including critical review of manuscript (40%).

8. Statements about Joint Authorship

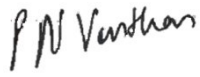

Signed: Date: 7th February 2023

Regarding **Publication III**, Short-term changes observed in multiparametric liver MRI following therapy with direct-acting antivirals in chronic hepatitis C virus patients. I, Robert Scott, was an academic clinical fellow involved in recruiting patients to this study, collating clinical information, drafting and critically reviewing the manuscript. I agree with the following statement on author contribution of Christopher Bradley (reflective of co-operative teamwork): MRI data acquisition (90%), MRI data analysis (90%), statistical analysis (100%), interpretation (40%), drafting of manuscript including critical review of manuscript (40%).

Signed: 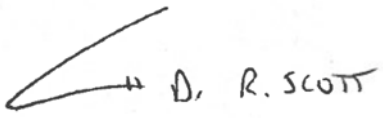 Date: 7th February 2023

Regarding **Publication IV**, A randomized, controlled, double-blind crossover study on the effects of isoeffective and isovolumetric intravenous crystalloid and gelatin on blood volume, and renal and cardiac hemodynamics. I, Damian Bragg was a clinical fellow on this published works, recruiting patients to this study and collecting the clinical data. I agree with the following statement on author contribution of Christopher Bradley: MRI data acquisition (70%), MRI data analysis (90%), statistical analysis (100%), interpretation (60%), drafting of manuscript including critical review of manuscript (50%).

Signed: 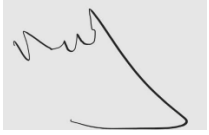 Date: 6th February 2023

9. Reprints of publications

9.1 Publication I: Bradley CR, Cox EF, Scott RA, James MW, Kaye P, Aithal GP, Francis ST, Guha IN. Multi-organ assessment of compensated cirrhosis patients using quantitative magnetic resonance imaging. Journal of Hepatology. 2018 Nov 1;69(5):1015-24.

Research Article
Cirrhosis

JOURNAL
OF HEPATOLOGY

Multi-organ assessment of compensated cirrhosis patients using quantitative magnetic resonance imaging

Graphical abstract

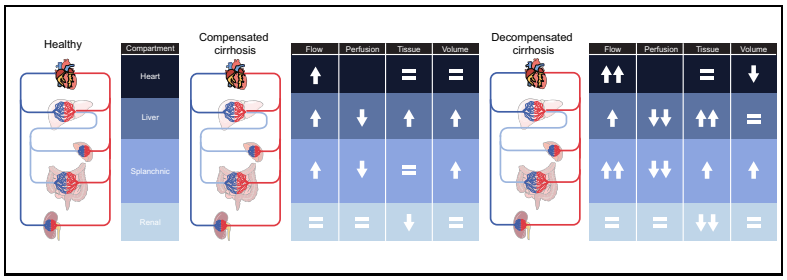

Highlights

- Assessment of MRI parameters in a single scan session.
- Higher liver T_1 and reduced liver perfusion with increasing disease severity and clinical outcomes.
- Reduced renal cortex T_1 linked to disease severity and clinical outcomes.

Authors

Christopher R. Bradley, Eleanor F. Cox, Robert A. Scott, ..., Guruprasad P. Aithal, Susan T. Francis, Indra Neil Guha

Correspondence

Neil.Guha@nottingham.ac.uk
(I.N. Guha)

Lay summary

This study assesses the changes to structure, blood flow and perfusion that occur in the key organs (liver, spleen and kidney) associated with severe liver disease (Compensated Cirrhosis), using magnetic resonance imaging. The magnetic resonance imaging measures which changed with disease severity and were related to negative liver-related clinical outcomes are described.

http://dx.doi.org/10.1016/j.jhep.2018.05.037
 J. Hepatol. 2018, 69, 1015–1024

Research Article
Cirrhosis

JOURNAL OF HEPATOLOGY

Multi-organ assessment of compensated cirrhosis patients using quantitative magnetic resonance imaging

Christopher R. Bradley[1,2], Eleanor F. Cox[1,2], Robert A. Scott[2], Martin W. James[2], Phillip Kaye[2], Guruprasad P. Aithal[2,3], Susan T. Francis[1,2,†], Indra Neil Guha[2,3,*,†]

[1]*Sir Peter Mansfield Imaging Centre, School of Physics and Astronomy, University of Nottingham, Nottingham, UK;* [2]*NIHR Biomedical Research Centre, Nottingham University Hospitals NHS Trust and the University of Nottingham, Nottingham, UK;* [3]*Nottingham Digestive Diseases Centre, School of Medicine, University of Nottingham, Nottingham, UK*

See Editorial, pages 996–998

Background & Aims: Advancing liver disease results in deleterious changes in a number of critical organs. The ability to measure structure, blood flow and tissue perfusion within multiple organs in a single scan has implications for determining the balance of benefit *vs.* harm for therapies. Our aim was to establish the feasibility of magnetic resonance imaging (MRI) to assess changes in Compensated Cirrhosis (CC), and relate this to disease severity and future liver-related outcomes (LROs).

Methods: A total of 60 patients with CC, 40 healthy volunteers and 7 patients with decompensated cirrhosis were recruited. In a single scan session, MRI measures comprised phase-contrast MRI vessel blood flow, arterial spin labelling tissue perfusion, T_1 longitudinal relaxation time, heart rate, cardiac index, and volume assessment of the liver, spleen and kidneys. We explored the association between MRI parameters and disease severity, analysing differences in baseline MRI parameters in the 11 (18%) patients with CC who experienced future LROs.

Results: In the liver, compositional changes were reflected by increased T_1 in progressive disease (p <0.001) and an increase in liver volume in CC (p = 0.006), with associated progressive reduction in liver (p <0.001) and splenic (p <0.001) perfusion. A significant reduction in renal cortex T_1 and increase in cardiac index and superior mesenteric arterial blood flow was seen with increasing disease severity. Baseline liver T_1 (p = 0.01), liver perfusion (p <0.01), and renal cortex T_1 (p <0.01) were significantly different in patients with CC who subsequently developed negative LROs.

Conclusions: MRI enables the contemporaneous assessment of organs in liver cirrhosis in a single scan without the requirement for a contrast agent. MRI parameters of liver T_1, renal T_1, hepatic and splenic perfusion, and superior mesenteric arterial blood flow were related to the risk of LROs.

Lay summary: This study assesses the changes to structure, blood flow and perfusion that occur in the key organs (liver, spleen and kidney) associated with severe liver disease (Compensated Cirrhosis), using magnetic resonance imaging. The magnetic resonance imaging measures which changed with disease severity and were related to negative liver-related clinical outcomes are described.

Introduction

The evolution of liver cirrhosis to clinical liver-related outcomes resulting from portal hypertension is not simply dictated by architectural and haemodynamic changes within the liver. Rather, advancing liver disease results in deleterious changes in a number of critical organs and the understanding of this process is a central aspect in the clinical management of cirrhotic patients.

The hyperdynamic circulation in cirrhosis is characterised by increased cardiac output and decreased systemic vascular resistance with low arterial blood pressure.[1–3] Splanchnic vasodilation, with a resulting decrease in the effective central volume, has been proposed as an important driver of the hyperdynamic circulation.[1,4] Associated with splanchnic vasodilation is an increase in portal vein blood flow which maintains and perpetuates portal hypertension.[5] Further, architectural and haemodynamic changes in the heart, spleen, and kidney have also been shown to occur and have important pathophysiological consequences. For example, cirrhotic cardiomyopathy is characterised by increased cardiac output with a sub-optimal ventricular response to stress, and structural and electrophysiological abnormalities.[2] Cardiac dysfunction associated with cirrhosis has been shown to be an important prognostic determinant of mortality at one year.[6] Renal vasoconstriction, related to splanchnic vasodilation, portal hypertension and activation of compensatory neurohormonal systems, is a precursor for the development of hepatorenal syndrome.[3,6,7] In cirrhosis, splenic enlargement may result from portal venous congestions and/or hyperplasia. In association, the splenic artery is suggested to dilate,[8] and recent data suggests that the splenic artery to hepatic artery diameter ratio can predict the development of

Keywords: Compensated Cirrhosis; Magnetic Resonance Imaging; Arterial Spin Labelling; Phase contrast; Longitudinal T_1 relaxation time.
Received 2 January 2018; received in revised form 29 May 2018; accepted 30 May 2018; available online 08 June 2018

* Corresponding author. Address: National Institute for Health Research (NIHR) Nottingham Biomedical Research Centre, Nottingham University Hospitals NHS Trust and University of Nottingham, E Floor, West Block QMC, Queens Medical Centre, Nottingham NG7 2UH, UK. Tel.: +44 (0) 115 8231162.
E-mail address: Neil.Guha@nottingham.ac.uk (I.N. Guha).
† Joint senior authors.

ascites and varices.[9] Splenic stiffness has also been found to have a strong association with portal hypertension.[10,11] However, there is an incomplete understanding of how changes in the different organs are inter-related, and what temporal relationships exist.

The importance of assessing critical organs in liver cirrhosis in a holistic fashion is illustrated by the current controversy surrounding beta-blockers in liver cirrhosis. The debate regarding the safety of beta-blockers focusses on whether the beneficial effects of beta-blockers in liver cirrhosis, centred around a reduction in cardiac output, splanchnic vasodilation and portal inflow and improvement in intrahepatic resistance (alpha 1 blockade), is counterbalanced by deleterious effects in advanced cirrhosis centred on a reduction in renal perfusion and cardiac output as described previously.[12] A key limitation in being able to define the critical window[6,13] of benefit of beta-blockers *vs.* harm is the lack of robust non-invasive tools to measure changes across organs in a contemporaneous manner. If this could be done, treatment could be individualised more effectively. This does not currently occur in clinical practice, in a consistent manner, as the tools for measurement are blunt (*e.g.* heart rate) or invasive (hepatic venous pressure gradient measurement [HVPG]).

Recent advances in non-invasive magnetic resonance imaging (MRI) techniques allow the assessment of blood flow to organs,[14] tissue perfusion,[15,16] and compositional changes including fibrosis and inflammation,[17–19] in the key organs associated with cirrhosis. Until now, such measures have only been examined in single organs rather than using a comprehensive multi-organ approach in a single scan session.

Our aim was to assess the feasibility of performing MRI to contemporaneously analyse the liver, heart, spleen and kidneys in patients with Compensated Cirrhosis (CC). We aim to describe the differences in quantitative MRI measures within these organs between healthy volunteers, and patients with CC and Decompensated Cirrhosis (DC). As proof of concept, we explore whether differences in MRI parameters are observed in patients with future clinical liver-related outcomes.

Materials and methods

Study population

Sixty patients were consecutively recruited from a CC cohort study, a prospective study initiated in 2010 focussed on tracking liver disease progression. Here, baseline measures collected for this cohort are reported. Institutional and local research approval was gained (10/H0403/10). Patients were recruited with evidence of cirrhosis (confirmed by a combination of biopsy, clinical and radiological criteria) and no evidence of decompensation (ascites, significant jaundice, hepatic encephalopathy and variceal bleeding), hepatocellular carcinoma and portal vein thrombosis. Exclusion criteria included orthotopic liver transplantation, ischaemic heart disease, alcoholic cardiomyopathy (defined by clinical evidence of systolic dysfunction) and valvular heart disease.

For comparator measures, we prospectively recruited two additional groups – a Healthy Volunteer (HV) and Decompensated Cirrhosis (DC) group. Forty HVs were recruited who had no major co-morbidity including cardiovascular or chronic liver disease. Seven ambulatory patients with DC were recruited, defined as Baveno 3 or 4 stage (ascites, encephalopathy or previous variceal bleed); exclusion criteria included portal vein thrombosis, the presence of hepatocellular carcinoma (HCC), and orthotopic liver transplantation. Subjects attended on a single study day following an overnight fast. Statistical power to assess the difference between groups was determined for each MRI parameter at a power of 80% and significance level of 5%.

Patients were invited to return for research visits on a six-monthly basis for assessment of liver-related clinical outcomes as defined by ascites (needing paracentesis or diuretic therapy), grade 3 or grade 4 encephalopathy, variceal haemorrhage requiring endoscopic therapy and emergency admission, HCC (defined by EASL criteria) and liver-related death. For patients who declined follow-up visits, we obtained their consent to access relevant medical records (both family practitioner and hospital records) to record clinical outcomes.

Multi-organ MRI protocol

All participants were scanned following a 6 h fast, with MRI scans carried out between 8 am–12 pm. Imaging was performed on a 1.5 T Philips Achieva MRI scanner (Best, Netherlands) using a 16-element Torso receive coil and body transmit coil. MR measures were collected on four organs: liver – blood flow in the portal vein and hepatic artery, liver perfusion and tissue T_1; spleen and superior mesenteric artery (SMA) – blood flow assessed in the splenic and SMA, splenic tissue perfusion and tissue T_1; renal – blood flow in right renal artery, kidney volume, renal tissue perfusion and tissue T_1; heart – aortic blood flow corrected for body surface area (BSA) to yield cardiac index and left ventricular (LV) wall mass as a measure of cardiac strain. This non-invasive protocol took less than 1 h for hepatic (∼20 min), spleen, SMA and renal (∼15 min), and cardiac (∼10 min) measures. The following describes the acquisition protocol parameters.

Organ volume

First multi-slice balanced turbo-field echo (bTFE) localiser images were acquired in three perpendicular orientations to locate organs and vessels of interest for slice positioning, and from which to estimate organ (liver, kidney and spleen) volume.

Blood flow measures

Phase-contrast (PC)-MRI was used to quantify vessel lumen cross-sectional area (CSA), velocity and bulk blood flow in vessels within each system. A TFE technique (two averages, TFE factor 4–6 dependent on subjects' heart rate) was used with a single slice perpendicular to the vessel of interest. A total of 15 phases were collected across the cardiac cycle using specified velocity encoding for each vessel (portal vein 50 cm/s, hepatic/splenic/renal arteries 100 cm/s, SMA 140 cm/s). Each vessel measurement was acquired during a 15–20 s breath hold.

Perfusion of the liver, spleen and kidney

Respiratory-triggered Flow Alternating Inversion-Recovery Arterial Spin Labelling (FAIR-ASL)[15,16] (post-labelling delay 1,100 ms, balanced fast field echo [bFFE] readout) was used to measure tissue perfusion in the liver, spleen and renal tissue. Liver perfusion data was acquired in three sagittal slices through the right lobe (slice gap 5 mm, 60 ASL pairs in ∼8 min), spleen/renal perfusion data was collected in five contiguous coronal-oblique slices through the spleen and long axis of the kidney (30 ASL pairs in ∼5 mins). An equilibrium base magnetisation M_0 and T_1 image was acquired for each slice orientation for perfusion quantification.

Relaxometry of the liver, spleen and kidney
A modified respiratory-triggered inversion-recovery sequence[16,19,20] was used to measure tissue T_1 in the liver, spleen and kidney, with slices geometrically matched to the ASL data. For liver tissue, a fat suppressed spin-echo echo-planar imaging (SE-EPI) readout was used to ensure no influence of fat on T_1 measures. Data was collected at 13 inversion times (TI) (100–1,200 ms in 100 ms steps, and 1,500 ms) with minimal temporal slice spacing between the three slices (65 ms) collected in a descend slice order, in an acquisition time of ~2 min. For the spleen and kidney, a bFFE readout was used and data acquired at 9 TIs (100–900 ms in 100 ms steps) with minimal temporal slice spacing (144 ms), both ascend and descend slice order acquisitions were acquired to increase the dynamic range of inversion times[16,19,20] in ~3 min. It was confirmed that study participants did not have excess iron.[16,19,20]

Cardiac assessment
Cardiac output was measured using a PC-MRI of the aorta with 30 phases and velocity encoding of 200 cm/s in ~1 min whilst free breathing. Short-axis cine images were acquired to measure LV wall mass using a multi-slice TFE sequence (12 slices, 30 phases, 3 slices acquired per 15–20 s breath hold).

Data analysis

Blood flow measures
'Q-flow' software (Philips Medical Systems) was used to analyse PC-MRI data. For each vessel, a region-of-interest (ROI) was drawn to estimate flow by averaging the flow velocity values within the ROI and multiplying by vessel lumen CSA. Mean flow was calculated by averaging the flow rates for each cardiac phase across the cardiac cycle.

Perfusion
The analysis procedure for ASL data performed using MATLAB and/or IDL routines is shown (Fig. S1). Each ASL label/control image was motion corrected to the base magnetisation M_0 image using in-house software. Individual perfusion-weighted images (control-label) were calculated, inspected for motion (exclude >1 voxel movement) and averaged to create a single perfusion-weighted image (ΔM). ΔM, M_0 and T_1 maps were used in a kinetic model[21] to compute tissue perfusion maps. A binary mask of each organ (see *relaxometry* section) was formed and used to calculate the mean liver, spleen and renal cortex perfusion.

Relaxometry
Inversion-recovery data were fit to a two-parameter model to generate T_1 and M_0 maps. Binary organ masks were formed from the M_0 image, and major blood vessels further segmented by excluding voxels with a T_1 >1,500 ms. Median T_1 values were calculated within liver and spleen masks. For the kidney mask, a histogram of T_1 values was formed to yield two peaks originating from the renal cortex and medulla (Fig. S1A), and the median T_1 values of the renal cortex and medulla calculated.

Volume
Analyze® (Mayo Clinic) was used to draw an ROI around each organ (liver, kidney, spleen) within each slice, and total organ volume calculated by summing across slices.

Cardiac
Cardiac MRI data was analysed using ViewForum software (Philips Medical Systems, Best, Netherlands). PC-MRI data of the aorta was analysed by computing the stroke volume and heart rate, and multiplying these parameters to yield cardiac output. This software was also used to draw wall contours from which LV wall mass was calculated. Both cardiac output and LV wall mass are presented corrected for BSA.[22]

Validation of MR measures

T_1 relaxometry of the liver
We assessed liver histology in a cohort of patients with cirrhosis who previously had T_1 mapping of the liver on a 1.5 T scan,[19,20] all MRI scans were collected within three months of liver biopsy. Liver biopsies were obtained via either the percutaneous or the transjugular route from patients with METAVIR fibrosis stage 4. Patients were fasted overnight before the procedure and biopsies were carried out by experienced operators. Biopsies were stained with hematoxylin and eosin, picrosirius red (PSR) and Perls' Prussian blue stains. All biopsy data were analysed by a single experienced pathologist blinded to MRI data. The percentage of fibrous tissue relative to the total biopsy area was estimated for each biopsy by visual morphometry.[17] A Spearman's rank correlation coefficient (in terms of R value) was computed between the continuous variables of visual morphometry and liver tissue T_1.

All patients with CC had a blood sample to assess non-invasive markers of liver fibrosis (Enhanced Liver Fibrosis [ELF] score). In addition, in all patients with CC, transient elastography evaluation was performed using FibroScan® (Echo-Sens, Paris, France) to provide a liver stiffness measure (LSM) in kPa. The FibroScan® measure was repeated to obtain 10 readings and a median LSM value calculated. Spearman's rank correlation coefficients (R value) are presented between ELF and LSM with a statistical significance threshold of $p < 0.05$.

ASL perfusion of the liver
In all patients, measures of indocyanine green (ICG) were performed and plasma disappearance rate (ICG-PDR, percentage of ICG eliminated in 1 min after an ICG bolus) (%/min), and its retention rate at 15 min (ICGR15, the circulatory retention of ICG during the first 15 min after a bolus injection (%)) computed. A Spearman's rank correlation coefficient was performed between ICG-PDR and ICGR15 and liver perfusion as measured using arterial spin labelling. Correlation coefficients are presented in terms of R value with a statistical significance threshold of $p < 0.05$.

Repeatability of multiparametric MRI measures
To determine the between session repeatability of MRI measures, the intra-subject Coefficient of Variation (CoV) (defined as the standard deviation/mean) of multiparametric MRI measures were assessed. A subset of 10 healthy participants (age 23–37 years, body mass index 20–26 kg/m^2) had three scans, at least one week apart and within four weeks, at the same time of day and after an overnight fast to limit diurnal and dietary variability. The CoV measures are provided (Table S1).

Statistical analysis

All statistical analysis was performed using Prism 6 (GraphPad Software, Inc., La Jolla, CA). A Shapiro-Wilk normality test was applied to data collected on each MRI parameter. Normal data

is expressed as mean (SEM) and non-normal as median (interquartile range, IQR) across each group. Tests between the three patient groups were made using a one-way analysis of variance (one-way ANOVA) with Bonferroni correction for normally distributed data, otherwise a Kruskal-Wallis test was performed to assess probable differences between the groups, with *post hoc* Tukey's test where significant differences were identified.

To compare results between patients with CC who did or did not have a negative liver-related clinical outcome, a two-tailed unpaired *t* test was performed to assess differences in normally distributed parameters, or a Mann-Whitney U test was performed, significance was considered at $p < 0.05$. In addition, to test the probability of organ involvement in outcome, a survival analysis was performed providing Kaplan-Meier curves and significance of difference determined by a log-rank test, using the 1st tertile of MRI parameters as cut-off values.

For further details regarding the materials used, please refer to the CTAT table.

Results

The CC cohort (n = 60) comprised 25 females and 35 males, aged 60 ± 9 years, with a range of aetiologies, the largest being Alcoholic Liver Disease (ALD, 21 patients, 35%), Non-Alcoholic Fatty Liver Disease (NAFLD, 16 patients, 27%), and Hepatitis C Virus (HCV, 12 patients, 20%), with the remaining 18% of patients having primary biliary cirrhosis, Hepatitis B Virus (HBV), primary sclerosing cholangitis, autoimmune hepatitis and haemochromatosis. Mean model for end-stage liver disease (MELD) score, FIB4 and aspartate aminotransferase-to-platelet ratio index (APRI) scores were 7.7 ± 2.1, 3.4 ± 2.3, and 1.2 ± 1.2. Of this group, six patients were on beta-blockers. The healthy volunteer (HV) group (n = 40) comprised 17 female and 23 male patients, aged 59 ± 10 years. The DC (n = 7) group comprised five female and two male patients of 48 ± 13 years, five of whom had ALD, one NAFLD and one HCV, with decompensation type comprising four cases of ascites, two of varices and one encephalopathy. Mean MELD, FIB4 and APRI scores were 9.9 ± 3.3, 3.5 ± 1.6, and 1.4 ± 1.1, respectively.

Validation of MR measures

T_1 relaxometry of the liver

T_1 relaxation time correlated significantly with visual morphometry of percentage fibrosis in advanced F4 fibrosis ($R = 0.62$, $p < 0.001$) (Fig. S2). As a secondary outcome, we show a significant positive correlation of liver tissue T_1 with ELF score, $R = 0.65$ and $p < 0.001$ (Fig. S3). In addition, a highly significant correlation of liver tissue T_1 with the LSM from FibroScan® was demonstrated ($R = 0.68$, $p < 0.001$) (Fig. S3).

ASL perfusion of the liver

In all patients ICG measures were collected and correlated with liver perfusion as measured by ASL. A weak but significant positive correlation was demonstrated between liver perfusion measured using ASL and ICG-PDR ($R = 0.46$, $p = 0.0016$), and negative correlation with ICGR15 ($R = 0.46$, $p = 0.0011$) (Fig. S4).

Repeatability of multiparametric MRI measures

Intra-subject repeatability for all the multiparametric MRI measures is provided (Table S1). Measurement of MR parameters is highly repeatable with a CoV of <10% in assessment of volume, T_1 relaxometry measures, and ASL perfusion.

Changes in compensated and decompensated cirrhosis compared to healthy volunteers

In the following section, MRI measures are provided for each organ studied – liver, spleen and SMA, renal and cardiac – and compared across the stages of disease severity, *i.e.* HV *vs.* CC *vs.* DC.

Liver

The changes measured in the liver across the three groups are shown (Fig. 1). Liver volume was significantly greater in patients with CC compared to both HVs and those with DC ($p = 0.006$). We observed liver tissue T_1 progressively increased with disease severity, from HV to CC and DC ($p < 0.001$), with statistically significant differences between the HV and CC group ($p < 0.001$), and the CC and DC group ($p = 0.01$). Portal vein CSA significantly increased in CC patients compared to HVs ($p < 0.001$). The CSA of the hepatic artery increased with

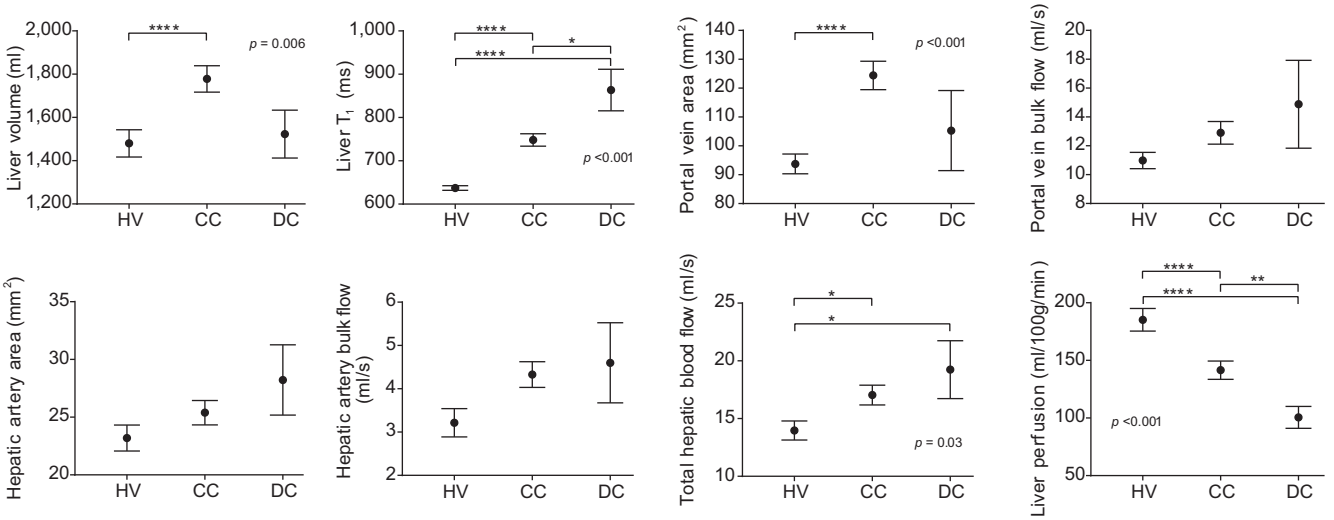

Fig. 1. Changes in the liver in Healthy Volunteers, patients with Compensated Cirrhosis and those with Decompensated Cirrhosis. Data analysed using one-way ANOVA, followed by the Tukey *post hoc* test. *$p < 0.05$, **$p < 0.01$, ***$p < 0.005$, ****$p < 0.001$. CC, Compensated Cirrhosis; CSA, cross-sectional area; DC, Decompensated Cirrhosis; HV, healthy volunteers.

disease severity (though not significant $p = 0.09$). Total hepatic blood flow (portal vein + hepatic artery flow) significantly increased with disease severity ($p = 0.03$). The percentage contribution of portal vein flow to total hepatic flow (portal vein flow + hepatic artery flow) did not significantly change with liver disease severity (77.9 ± 1.2%, 72.8 ± 1.9%, and 74.5 ± 6.7% for HV, CC, and DC respectively). Liver perfusion significantly reduced with disease severity ($p < 0.001$), with statistically significant differences between the HV and CC group ($p < 0.001$), and the CC and DC groups ($p < 0.01$).

Spleen and SMA

Changes in the spleen and SMA across the groups are shown (Fig. 2). Spleen volume was increased in the CC and DC groups compared to HVs ($p < 0.03$; 206 ± 16 ml, 459 ± 34 ml, and 490 ± 112 ml for HV, CC, and DC respectively), with spleen T_1 increasing with disease severity. No significant difference was found in CSA of the splenic artery, whilst splenic artery bulk flow significantly increased with disease severity ($p < 0.001$). SMA bulk flow showed an increase with disease severity. Spleen tissue perfusion significantly decreased with disease severity ($p < 0.001$, 151 ± 7 ml/100 g/min, 120 ± 6 ml/100 g/min, and 82 ± 9 ml/100 g/min for HV, CC, and DC respectively).

Renal

Renal changes across the groups are shown (Fig. 3). No significant difference is seen in total renal volume between the HV, CC and DC groups. A significant reduction in renal cortex T_1 ($p < 0.001$) was demonstrated with disease severity, a trend for reduced T_1 was found in the renal medulla but this was not significant. No significant difference was found in CSA of the renal artery or renal artery bulk flow, but flow per beat reduced with disease severity. No significant difference in renal cortex perfusion was found between the HV, CC, and DC groups.

Cardiac

Differences in cardiac parameters across the groups are shown (Fig. 4). Cardiac index significantly increased with disease severity ($p = 0.005$). This was driven by the increase in heart rate with disease severity ($p < 0.001$, 59.6 ± 1.6, 67.2 ± 1.6, 76.2 ± 3.1 beats

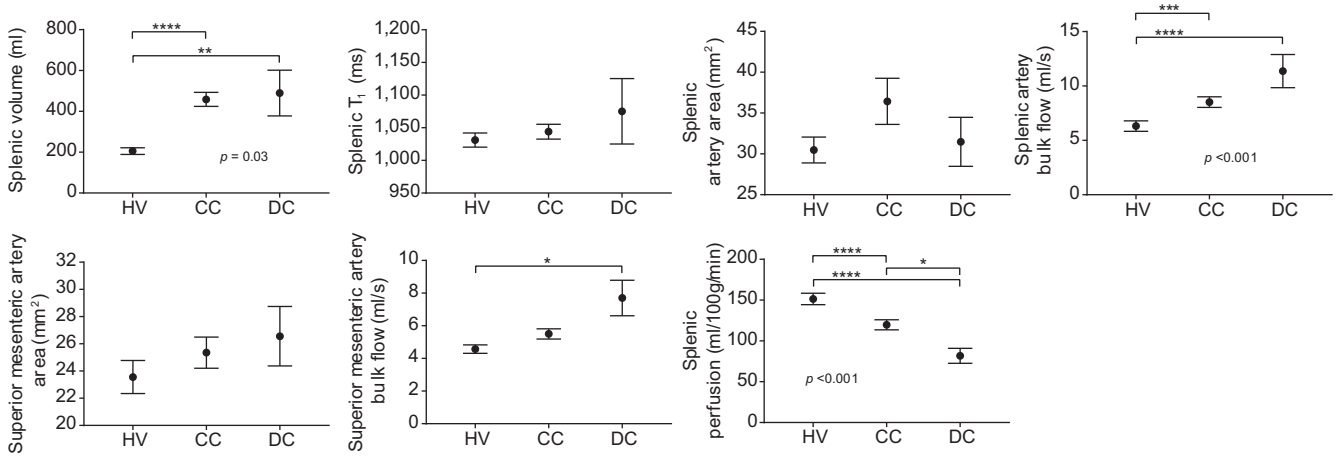

Fig. 2. Changes in the spleen and superior mesenteric artery in Healthy Volunteers, patients with Compensated Cirrhosis and those with Decompensated Cirrhosis. Data analysed using one-way ANOVA, followed by the Tukey *post hoc* test. *$p < 0.05$, **$p < 0.01$, ***$p < 0.005$, ****$p < 0.001$. CC, Compensated Cirrhosis; CSA, cross-sectional area; DC, Decompensated Cirrhosis; HV, Healthy Volunteers.

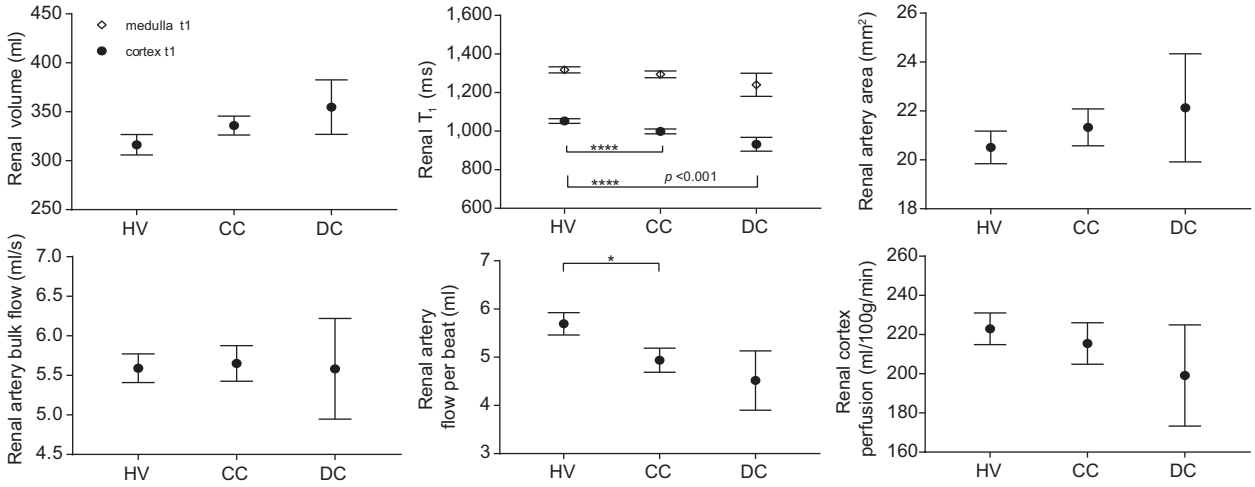

Fig. 3. Changes in the kidney in healthy volunteers, patients with Compensated Cirrhosis and those with Decompensated Cirrhosis. Data analysed using one-way ANOVA, followed by the Tukey *post hoc* test. *$p < 0.05$, **$p < 0.01$, ***$p < 0.005$, ****$p < 0.001$. CC, Compensated Cirrhosis; CSA, cross-sectional area; DC, Decompensated Cirrhosis; HV, Healthy Volunteers.

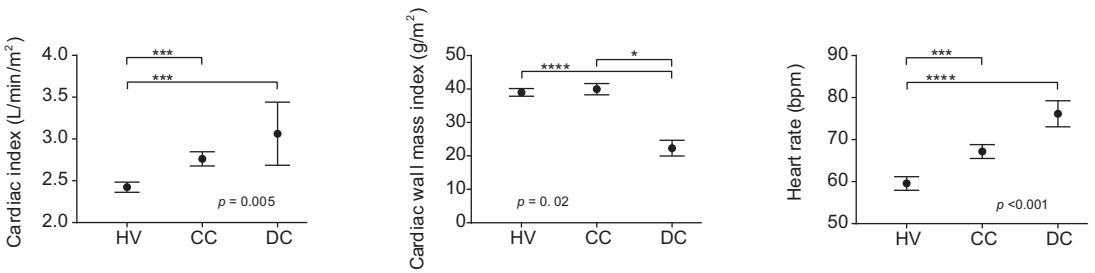

Fig. 4. Changes in the cardiac function between healthy volunteers, patients with Compensated Cirrhosis and those with Decompensated Cirrhosis. Data analysed using one-way ANOVA, followed by the Tukey *post hoc* test. $^{*}p < 0.05$, $^{**}p < 0.01$, $^{***}p < 0.005$, $^{****}p < 0.001$. CC, Compensated Cirrhosis; DC, Decompensated Cirrhosis; HV, Healthy Volunteers.

per minute (bpm) for HV, CC, and DC, respectively), no significant change in stroke volume was found with disease severity. BSA corrected cardiac LV wall mass was significantly different across the groups ($p = 0.02$; 39.0 ± 1.1, 34.0 ± 1.7, 22.3 ± 2.4 g/m^2 for HV, CC, and DC respectively).

Assessment of baseline MR parameters related to a future clinical outcome in patients with compensated cirrhosis at baseline

Here, we present baseline MRI data for those patients with CC who developed a liver-related outcome. Of the 60 patients with CC at baseline (mean MELD score 7.7), 11 patients (18%) developed a future liver-related outcome. The median number of days from MRI scan to a liver-related outcome was 1,001 (range: 59–2,304). Seven had ascites, one developed encephalopathy, one developed a variceal bleed, two had HCC. Of these patients, seven patients died of a liver-related cause after the first liver-related outcome; liver failure (four cases) and HCC (three cases) as listed on the death certificate.

The patients with an outcome were aged 59 ± 6 years, six were male and five female, with aetiologies including four with HCV, five with ALD, one with NAFLD and one with HBV. How the MR parameters found to be significantly different between HVs, CC and DC patients relate to clinical liver-related outcomes is displayed (Fig. 5).

There was no significant difference in liver volume between patients with CC with and without a liver-related outcome. In contrast, liver tissue T_1 was significantly higher ($p = 0.01$) in

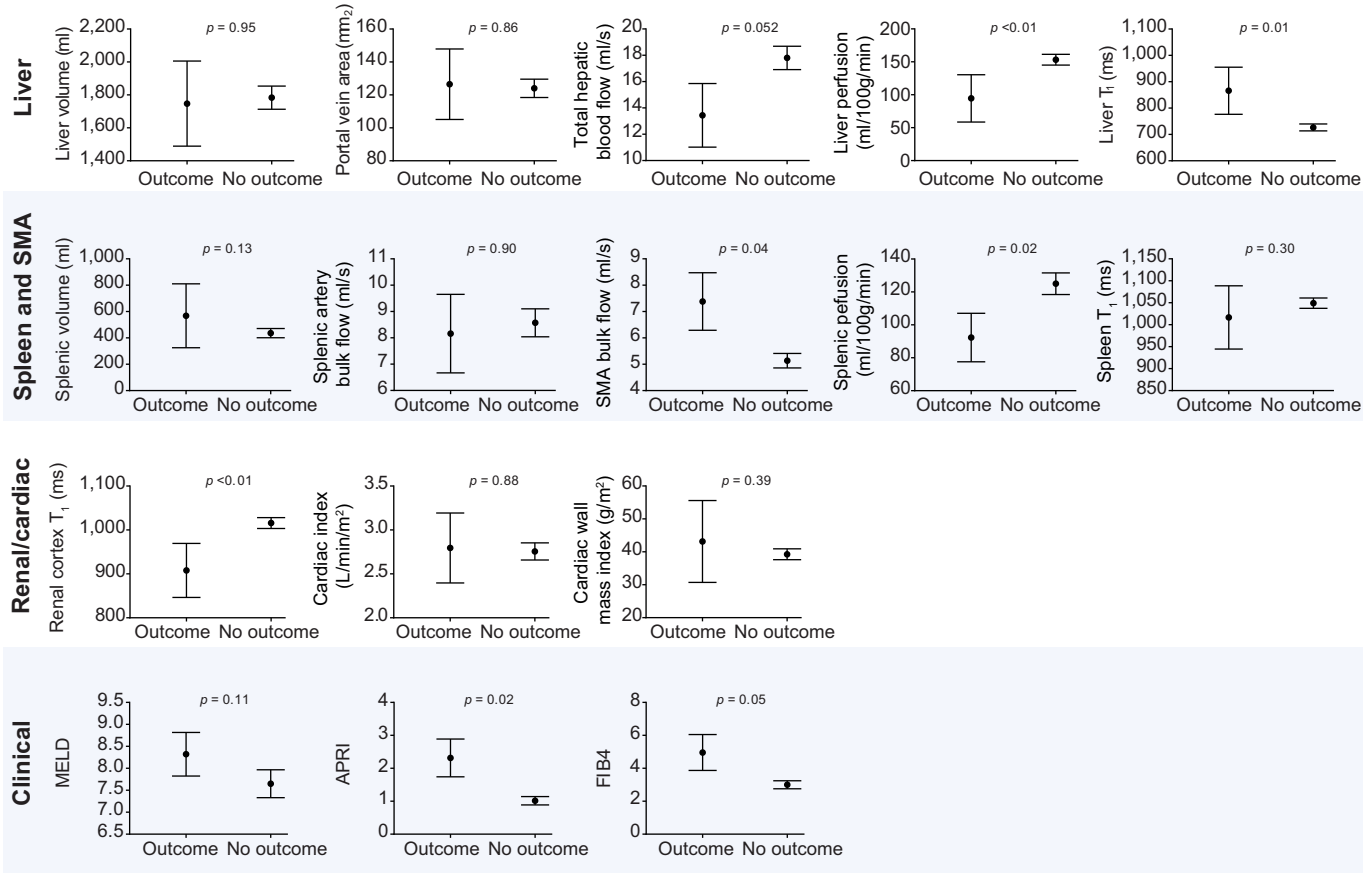

Fig. 5. Baseline MRI parameters in patients with Compensated Cirrhosis, with and without liver-related outcomes. APRI, aspartate aminotransferase-to-platelet ratio index; CC, Compensated Cirrhosis; FIB4, fibrosis 4 score; MELD, model for end-stage liver disease; SMA, superior mesenteric arterial. Statistical analysis performed using two-tailed unpaired t-test.

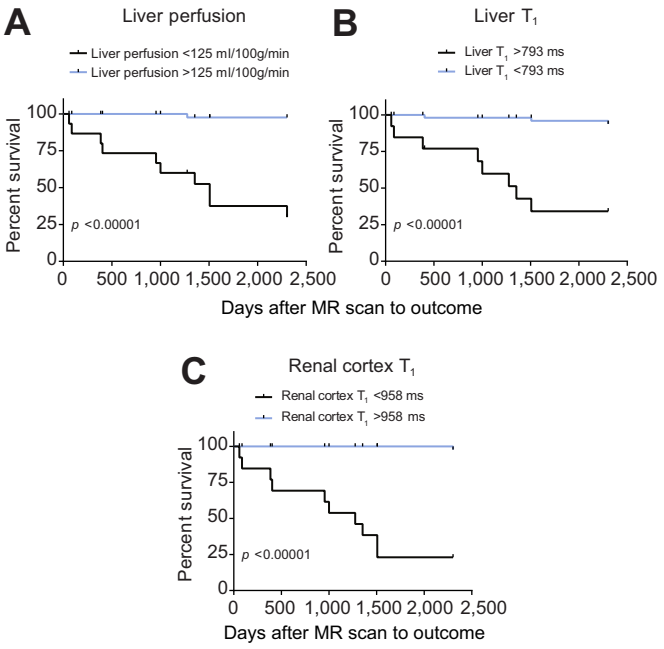

Fig. 6. Kaplan-Meier curves for liver-related outcome survival in patients with Compensated Cirrhosis. (A) There were significant differences between those with Liver T_1 for the 1st tertile T_1 of 793 ms ($p < 0.001$). (B) There was significance between liver perfusion using the 1st tertile of 125 ml/100 g/min ($p < 0.001$). (C) There was a significant difference between renal T_1 using a 1st tertile of 958 ms ($p < 0.001$).

those patients with CC and a clinical outcome (834 ± 36 ms) compared to those without (719 ± 10 ms). The CSA of the portal vein was not significantly different between patients with CC, with and without a clinical outcome. Total hepatic blood flow was significantly ($p = 0.05$) lower in those with outcomes (13.4 ± 7.6 ml/s) compared to those patients with no outcomes (17.8 ± 6.0 ml/s). Perfusion measured in the right lobe of the liver was significantly lower ($p < 0.01$) in those patients with an outcome (clinical liver-related outcome: 95.8 ± 9.5 ml/100 g/min, no liver-related outcome: 160 ± 8.0 ml/100 g/min). No significant difference was found in spleen volume or splenic T_1 between those with and without outcomes, but splenic perfusion was lower and SMA blood flow higher in those with a clinical outcome. Renal cortex T_1 was significantly shorter in the patients with CC and an outcome (919 ± 28 ms) compared to those with no outcome (1,012 ± 11 ms). There was no significant difference in cardiac measures of cardiac index or LV wall mass index between those with and without a clinical outcome. Tertile cut-off points (as used in[23]) of liver perfusion, liver T_1 and renal T_1 were used to compute Kaplan-Meier survival curves (Fig. 6). These MRI parameters were significant predictors of liver-related outcomes.

Discussion

We have shown that it is feasible to study changes in cirrhosis representing the flow, volume, composition and perfusion in critical organs (liver, kidney, spleen and heart) in a contemporaneous fashion in a single scan session using quantitative MRI without requiring the injection of a contrast agent. Individual MR components change with disease severity, as illustrated by Fig. 7, and taken together this data provides a comprehensive evaluation of cirrhosis relating to aspects of structure and haemodynamics. Furthermore, a subset of MRI markers measured at baseline (*i.e.* liver T_1, liver perfusion and renal cortex T_1) differentiate two groups of patients with CC, those who develop or do not develop a future liver-related clinical outcome up to seven years later (Figs. 5, 6).

This study highlights two conceptual aspects that are coherent with our current understanding of how liver disease progresses. Firstly, structural changes as evidenced by changes in organ volume (*i.e.* spleen and liver) and compositional change (*i.e.* increased liver T_1 and splenic T_1) relate to increasing disease progression from the spectrum of HVs to DC. Secondly, changes in haemodynamics, both to and within the organ, evolve with progressive disease. This is exemplified by the reduction in both liver and splenic perfusion. Despite the small size of the DC group, it is interesting to note that the reduction of hepatic perfusion occurs in the context of increased total hepatic blood delivery in the CC and DC group, though this only results in

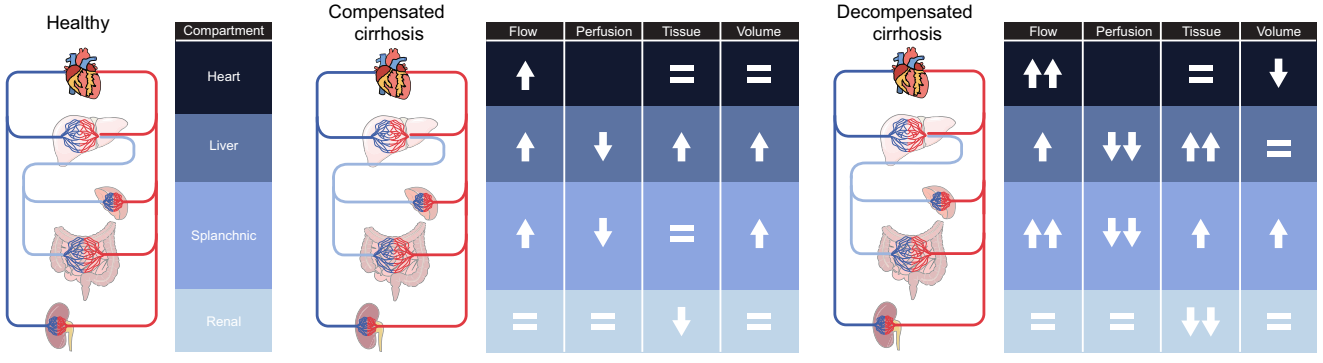

Fig. 7. Multi-organ changes demonstrated in this study in compensated and decompensated liver disease. Infographic to pictorially illustrate the changes in key organs (heart, liver, splanchnic and kidney) demonstrated in this study of contemporaneous MR measures in compensated and decompensated cirrhosis. A hyperdynamic circulation results in increased blood flow in the liver, splanchnic circulation and increased cardiac output in patients with CC, with further increases in spleen blood flow and cardiac index in patients with DC. Here liver and splenic perfusion was shown to be reduced in patients with CC compared to the HV group, and perfusion in these organs is further reduced in those with DC. No significant change in renal perfusion was found between patients with CC and DC, and the HV group. Liver tissue T_1 increased in patients with CC compared to HVs, and further increased in those with DC. Spleen T_1 was only significantly different from the HV group in DC patients. In contrast renal T_1 was reduced in patients with CC and further reduced in those with DC, compared to HVs. LV wall mass was significantly reduced in patients with DC compared to HVs, whilst liver volume was found to increase only in patients with CC, and spleen volume was increased in patients with CC and DC compared to HVs. CC, Compensated Cirrhosis; DC, Decompensated Cirrhosis; HV, Healthy Volunteers.

an increase in normalised hepatic blood flow between the HV and DC group (Fig. S5). The reduction in liver volume that occurs in DC compared to CC patients, as previously shown in,[24] suggests that this is not related to a larger mass of liver tissue to supply. We hypothesise two explanations for this discordance. Firstly, intrahepatic shunting may occur, although using our current MR methods we do not have the spatial resolution to directly visualise shunts. Secondly, in liver disease it is difficult to use normalised hepatic blood flow as a measure of global perfusion due to the underlying changes in liver composition. The deposition of fat, interstitial oedema and inflammatory cells can all potentially increase liver volume. As the liver starts decompensating, these features subside and in addition there is a loss of hepatocyte volume relative to an increasing amount of extracellular matrix.[25] This highlights the importance of measuring perfusion rather than blood flow *per se*.

The increase in splenic artery blood flow is largely compensated for by the increase in spleen volume, with a trend for a reduction in normalised splenic flow (Fig. S5) in agreement with the significant reduction in perfusion. The increase in splenic T_1 also suggests that angio-architectural changes occur within the spleen, perhaps related to fibrosis. Finally, there was a trend for reduced renal perfusion, in the context of maintained renal artery bulk flow and increased kidney volume, in agreement with a reduced normalised renal blood flow (Fig. S5).

Of the 60 patients with CC, six were on beta-blockers, with this sub-group showing a significant reduction in splenic artery CSA, mean velocity and flux, spleen perfusion and portal vein mean velocity, thus increasing the CC cohort group variance in these measures. In addition, the DC sample size is currently underpowered to determine significant incremental changes, except in T_1 relaxometry measures; this remains a work in progress.

The significant difference in baseline MRI parameters in those patients at risk of clinical events, within an average follow-up period of three years and maximum follow-up of seven years, is very encouraging. In this study 18% (11) of patients had a negative clinical outcome, this is a similar sample size to a recent study of events using multiparametric MRI of the liver alone and an associated liver inflammation and fibrosis score in which 10 patients (11%) were studied.[26] In the current study, we had more liver-related outcomes compared with previous studies (4% in a transient elastography study[27] and 13% in an ELF study[28]). The increased liver T_1 (a marker of structural severity) and reduced liver perfusion (a marker of haemodynamic severity) in patients with early compensated liver cirrhosis experiencing future liver-related clinical outcomes has biological plausibility and provides a link between surrogate bio-imaging signals and robust clinical end points. The relevance of the strong relationship of renal cortex T_1 to both disease severity and clinical outcomes is novel. Two studies, in patients with cirrhosis, have suggested changes in T_1 occur within the cortex of the kidney, but until now these studies have been based on signal intensity changes of T_1-weighted images,[29,30] with no quantitative measures of T_1 relaxation times having previously being reported. These previous studies suggest that the mechanism and physiology of reduced renal cortex T_1 is decreased water content in the renal cortex due to renal hypoperfusion. Whilst the overall blood flow to the kidneys was maintained in our study, there was both a trend toward reduced renal perfusion, reduced renal artery flow per beat decreased and kidney volume increased (Fig. 3), with a significant reduction in normalised bulk renal blood between HVs and patients with CC (Fig. S5). Thus, it is intriguing to speculate that regional vasoconstriction, driven by neurohormonal mechanisms, accounted for differential water content and reduced T_1. If this is proven to be the case, this has direct implications for the treatment of hepatorenal syndrome.

The overall picture that emerges from this study is consistent with our current understanding of the hyperdynamic circulation and the peripheral arterial vasodilatation hypothesis.[4] With advancing liver disease, reflected by structural changes within the liver (prolonged liver T_1 values, Fig. 1) and haemodynamic changes in the liver (reduced liver perfusion, Fig. 1), there is a predicted rise in portal pressure (calculated from MRI data as a surrogate measure of HVPG[20] shown in Fig. S6). Pooling of blood in the splanchnic circulation as evidenced by increased SMA bulk flow and splenic artery bulk flow (Fig. 2) perpetuates this raised portal pressure. To accommodate the reduced effective central volume, the cardiac index increases in association with a raised heart rate (Fig. 4). Importantly this compensatory mechanism may be fragile as highlighted by the reduced LV wall mass in DC in our study and by others.[31] The DC group, albeit small in number, were ambulatory in our study. It is plausible that acute insults, including sepsis, that lead to hospitalisation tip the balance of these compensatory mechanisms. Recently, it has been proposed that vasodilation occurs in a differential manner in regional beds. Using PC-MRI angiography, McAvoy and colleagues[32] found a reduction in total renal blood flow in patients with advanced liver disease compared to HVs but an increase in total hepatic blood flow and SMA flow. Our data supports this concept of differential visceral blood flow in cirrhosis.

Here we present validation of our MRI measures against the gold standard, showing the correlation of T_1 with the continuous biopsy variable of visual morphometry in METAVIR fibrosis stage F4, in agreement with previous reports in the literature across a wider range of fibrosis scores obtained from histology.[17,19] Further, we show that liver perfusion assessed in this CC cohort shows a significant correlation with indocyanine green (ICG-PDR and ICGR15). A recent study[33] assessed ICG continuous clearance and HVPG measurement against 2D PC-MRI of portal venous and hepatic arterial flow. They were able to demonstrate useful correlates that suggest that further development of MRI protocols for liver blood flow would be beneficial. We acknowledge ICG-PDR and ICGR15 are surrogates and not true measures of perfusion. Formal ICG clearance would be the optimal method, but this requires invasive transjugular hepatic venous sampling and simultaneous peripheral arterial sampling in patients receiving a continuous peripheral ICG infusion, as such this invasive procedure is far less practical. Doppler ultrasound has been widely used to assess blood flow in liver disease,[34,35] and has the advantage of being widely available. However, disadvantages include intra- and inter-observer variation, with reported intra-class variation of 0.49[36] due to inadequate standardisation of protocols including anatomical site, doppler beam angle and operator experience. Annet *et al.* showed PC-MRI parameters have the sensitivity to detect a significant difference between HV and cirrhotics not reflected in doppler ultrasound.[34] Doppler ultrasound has been shown to underestimate blood flow and be less reproducible in comparison to PC-MRI,[37] here we have shown the CoV of PC-MRI to be less than 5% in HVs,[38] further MRI has been shown to be more reliable with respect to inter-observer variability than

duplex doppler ultrasound.[39] Several studies have used computed tomography to assess portal vein and hepatic artery blood flow, but this is limited by ionising radiation exposure.[40]

There are a number of clinical implications of this study. Firstly, understanding the benefit *vs.* risk of existing and emerging therapeutics. Beta-blockers are used as standard care in the setting of portal hypertension. However, non-selective beta-blockers may be potentially deleterious after a critical threshold or window period has been traversed. It remains unclear when exactly this occurs, but this is likely to be related to diminishing cardiac output and a reduction in renal blood flow.[6] The concept of using MR protocols to assess response to beta-blockers has been explored by the Edinburgh group. They used PC-MRI to show a significant reduction in cardiac output (as measured by superior aorta blood flow) but maintenance of blood flow in other vessels (SMA, portal vein, hepatic artery, azygous vein) four weeks after commencing beta-blocker therapy, though this was in a small cohort of patients who were heart rate responders (n = 9).[13] Furthermore, using MRI protocols to assess novel drug compounds has been highlighted by the recent report of serelaxin providing therapeutic potential in renal dysfunction in cirrhosis. In this study selective renal vasodilation did not appear to be offset by a reduction in systemic blood pressure or hepatic perfusion.[41] Taken together with our findings, the vision should be to use MRI protocols to assess response at an individual level and thus provide tailored therapy which is effective and safe. A further potential application for this MRI protocol could be as a prognostic tool for overall liver outcomes or specific complications. There is a growing body of literature showing the promise of non-invasive markers of liver fibrosis for prognostic performance.[42,43] The ability of two simple scores FIB4 and APRI to differentiate outcomes in early CC, as reproduced in this study (Fig. 5) cautions against positioning MRI as a generic prognostic tool. However, the difference in parameters between patients with/without significant clinical outcomes suggests that there is potential to use these parameters for prediction, which would be an understandable ambition in the era of emerging anti-fibrotic compounds. Larger studies are required to determine clinical utility of these promising multiparametric measures related to liver-related outcomes.[44]

This study was designed as a proof of concept study to assess the feasibility of using MRI to assess different organs in cirrhosis and confirms this is possible. Importantly, the scan time for the present protocol is one hour. Whilst we have obviated the requirement for an intravenous contrast agent, the scan time can now be reduced by omitting parameters which have been found to be non-contributory. This will be important for patient compliance and reducing cost and burden on radiology service provision time for future implementation into clinical practice. Whilst the MR picture obtained provides an overview it is by no means an exclusive assessment of the hyperdynamic circulation. For example, the current protocol does not provide an assessment of systemic vascular resistance nor does it delineate intrahepatic shunts, which we have postulated to underpin the marked reduction in liver perfusion. We deliberately chose aspects of MRI measurements that have been validated previously by our group and others based on comparison to gold standard reference tests including invasive angiography and liver biopsy. The current imaging protocol has been performed on 1.5 T but can easily be applied at 3 T, which provides higher signal-to-noise ratio and spatial resolution. Demonstrating that monitoring of therapy with MRI protocols can change hard clinical outcomes and is cost effective within a multicentred randomised controlled trial will be required before considering implementation into clinical care.

We have shown that quantitative MRI can provide a global picture of cirrhosis by measuring aspects of flow, volume, composition and perfusion in critical organs. The change of key parameters including liver T_1, liver perfusion and renal cortical T_1 in both progressive disease and in liver-related clinical outcomes has tangible utility in the understanding and treatment of the complications of chronic liver disease.

Financial support

Financial support was received from the NIHR Biomedical Research Centre (NIHR BRC); Gastrointestinal and Liver Disorder Theme, Nottingham University Hospitals NHS Trust and University of Nottingham. This article presents independent research funded and supported by the NIHR Nottingham Digestive Diseases Biomedical Research Unit, Nottingham University Hospitals NHS Trust and University of Nottingham. Views expressed are those of the authors and not necessarily those of the NHS, NIHR or Department of Health.

Conflict of interest

The authors declare no conflicts of interest that pertain to this work.

Please refer to the accompanying ICMJE disclosure forms for further details.

Authors' contributions

CRB (Acquisition, analysis and interpretation of data, statistical analysis, drafting of the manuscript), EFC (Acquisition, analysis and interpretation of data, critical revision of the manuscript), RS and PK (Acquisition of data and critical revision of the manuscript), MWJ and GPA (critical revision of the manuscript), STF (Study concept and design, acquisition, analysis, interpretation of data, statistical analysis, drafting of the manuscript), and ING (Study concept and design, interpretation of data, statistical analysis, drafting of the manuscript).

Acknowledgments

We would like to thank the NIHR Nottingham BRC research nurses, including Antonella Ghezi, Andrea Bennett, Tracey Wildsmith and Louise James who conducted patient enrolment and performed clinical measures, and Rubie-Jo Barker who produced illustrations.

Supplementary data

Supplementary data associated with this article can be found, in the online version, at https://doi.org/10.1016/j.jhep.2018.05.037.

References

Author names in bold designate shared co-first authorship

[1] Iwakiri Y, Groszmann RJ. The hyperdynamic circulation of chronic liver diseases: from the patient to the molecule. Hepatology 2006;43(2 Suppl 1):S121–S131.

[2] Møller S, Henriksen JH. Cardiovascular complications of cirrhosis. Gut 2008;57(2):268–278.
[3] Schrier RW, Arroyo V, Bernardi M, Epstein M, Henriksen JH, Rodés J. Peripheral arterial vasodilation hypothesis: a proposal for the initiation of renal sodium and water retention in cirrhosis. Hepatology 1988;8 (5):1151–1157.
[4] Moller S, Bendtsen F. The pathophysiology of arterial vasodilatation and hyperdynamic circulation in cirrhosis. Liver Int 2018;38 (4):570–580.
[5] Taylor CR, McCauley TR. Magnetic resonance imaging in the evaluation of the portal venous system. J Clin Gastroenterol 1992;14(3):268–273.
[6] Krag A, Bendtsen F, Henriksen JH, Moller S. Low cardiac output predicts development of hepatorenal syndrome and survival in patients with cirrhosis and ascites. Gut 2010;59(1):105–110.
[7] Lautt WW. Regulatory processes interacting to maintain hepatic blood flow constancy: vascular compliance, hepatic arterial buffer response, hepatorenal reflex, liver regeneration, escape from vasoconstriction. Hepatol Res 2007;37(11):891–903.
[8] Blendis L, Kreel L, Williams R. The coeliac axis and its branches in splenomegaly and liver disease. Gut 1969;10(2):85–90.
[9] Zeng D, Dai C, Lu S, He N, Wang W, Li H. Abnormal splenic artery diameter/hepatic artery diameter ratio in cirrhosis-induced portal hypertension. World J Gastroenterol 2013;19(8):1292–1298.
[10] Colecchia A, Montrone L, Scaioli E, Bacchi-Reggiani ML, Colli A, Casazza G, et al. Measurement of spleen stiffness to evaluate portal hypertension and the presence of esophageal varices in patients with HCV-related cirrhosis. Gastroenterology 2012;143(3):646–654.
[11] Takuma Y, Nouso K, Morimoto Y, Tomokuni J, Sahara A, Toshikuni N, et al. Measurement of spleen stiffness by acoustic radiation force impulse imaging identifies cirrhotic patients with esophageal varices. Gastroenterology 2013;144(1):92–101, e2.
[12] Reiberger T, Mandorfer M. Beta adrenergic blockade and decompensated cirrhosis. J Hepatol 2017;66(4):849–859.
[13] McDonald N, Lilburn DML, Lachlan NJ, Macnaught G, Patel D, Jayaswal ANA, et al. Assessment of haemodynamic response to nonselective beta-blockers in portal hypertension by phase-contrast magnetic resonance angiography. Biomed Res Int 2017;2017:9281450.
[14] Applegate GR, Thaete FL, Meyers SP, Davis PL, Talagala SL, Recht M, et al. Blood flow in the portal vein: velocity quantitation with phase-contrast MR angiography. Radiology 1993;187(1):253–256.
[15] Gardener AG, Francis ST. Multislice perfusion of the kidneys using parallel imaging: image acquisition and analysis strategies. Magn Reson Med 2010;63(6):1627–1636.
[16] Cox EF, Buchanan CE, Bradley CR, Prestwich B, Mahmoud H, Taal M, et al. Multiparametric renal magnetic resonance imaging: validation, interventions, and alterations in chronic kidney disease. Front Physiol 2017;8:696.
[17] Agrawal S, Hoad CL, Francis ST, Guha IN, Kaye P, Aithal GP. Visual morphometry and three non-invasive markers in the evaluation of liver fibrosis in chronic liver disease. Scand J Gastroenterol 2017;52 (1):107–115.
[18] Heye T, Yang S, Bock M, Brost S, Weigand K, Longerich T, et al. MR relaxometry of the liver: significant elevation of T1 relaxation time in patients with liver cirrhosis. Eur Radiol 2012;22(6):1224–1232.
[19] Hoad CL, Palaniyappan N, Kaye P, Chernova Y, James MW, Costigan C, et al. A study of T(1) relaxation time as a measure of liver fibrosis and the influence of confounding histological factors. NMR Biomed 2015;28 (6):706–714.
[20] Palaniyappan N, Cox EF, Bradley CR, Scott R, Austin A, O'Neill R, et al. Non-invasive assessment of portal hypertension using quantitative magnetic resonance imaging. J Hepatol 2016;65(6):1131–1139.
[21] Buxton RB, Frank LR, Wong EC, Siewert B, Warach S, Edelman RR. A general kinetic model for quantitative perfusion imaging with arterial spin labeling. Magn Reson Med 1998;40(3):383–396.
[22] Natori S, Lai S, Finn JP, Gomes AS, Hundley WG, Jerosch-Herold M, et al. Cardiovascular function in multi-ethnic study of atherosclerosis: normal values by age, sex, and ethnicity. AJR Am J Roentgenol 2006;186(6 Suppl 2):S357–S365.
[23] Banypersad SM, Fontana M, Maestrini V, Sado DM, Captur G, Petrie A, et al. T1 mapping and survival in systemic light-chain amyloidosis. Eur Heart J 2015;36(4):244–251.
[24] Tong C, Xu X, Liu C, Zhang T, Qu K. Assessment of liver volume variation to evaluate liver function. Front Med 2012;6(4):421–427.
[25] Williams MJ, Clouston AD, Forbes SJ. Links between hepatic fibrosis, ductular reaction, and progenitor cell expansion. Gastroenterology 2014;146(2):349–356.
[26] Pavlides M, Banerjee R, Sellwood J, Kelly CJ, Robson MD, Booth JC, et al. Multiparametric magnetic resonance imaging predicts clinical outcomes in patients with chronic liver disease. J Hepatol 2016;64(2):308–315.
[27] Pang JXQ, Zimmer S, Niu S, Crotty P, Tracey J, Pradhan F, et al. Liver stiffness by transient elastography predicts liver-related complications and mortality in patients with chronic liver disease. PLoS One 2014;9(4): e95776.
[28] Parkes J, Roderick P, Harris S, Day C, Mutimer D, Collier J, et al. Enhanced liver fibrosis test can predict clinical outcomes in patients with chronic liver disease. Gut 2010;59(9):1245–1251.
[29] Lee KS, Muñoz A, Báez AB, Ngo L, Rofsky NM, Pedrosa I. Corticomedullary differentiation on T1-Weighted MRI: comparison between cirrhotic and noncirrhotic patients. J Magn Reson Imaging 2012;35(3):644–649.
[30] Yamada F, Amano Y, Hidaka F, Fukushima Y, Kumita S. Pseudonormal corticomedullary differentiation of the kidney assessed on T1-weighted imaging for chronic kidney disease patients with cirrhosis. Magn Reson Med Sci 2015;14(3):165–171.
[31] Merli M, Torromeo C, Giusto M, Iacovone G, Riggio O, Puddu E. Survival at 2 years among liver cirrhotic patients is influenced by left atrial volume and left ventricular mass. Liver Int 2017;37(5):700–706.
[32] McAvoy NC. Editorial: increased cardiac output in cirrhosis - non-invasive assessment of regional blood flow by magnetic resonance angiography. Aliment Pharmacol Ther 2016;43(12):1342–1343.
[33] Chouhan MD, Mookerjee RP, Bainbridge A, Punwani S, Jones H, Davies N, et al. Caval subtraction 2D phase-contrast MRI to measure total liver and hepatic arterial blood flow: proof-of-principle, correlation with portal hypertension severity and validation in patients with chronic liver disease. Invest Radiol 2017;52(3):170–176.
[34] Annet L, Materne R, Danse E, Jamart J, Horsmans Y, Van Beers BE. Hepatic flow parameters measured with MR imaging and Doppler US: correlations with degree of cirrhosis and portal hypertension. Radiology 2003;229(2):409–414.
[35] Popov D, Krasteva R, Ivanova R, Mateva L, Krastev Z. Doppler parameters of hepatic and renal hemodynamics in patients with liver cirrhosis. Int J Nephrol 2012;2012:961654.
[36] Iwao T, Toyonaga A, Shigemori H, Oho K, Sumino M, Sato M, et al. Echo-Doppler measurements of portal vein and superior mesenteric artery blood flow in humans: inter- and intra-observer short-term reproducibility. J Gastroenterol Hepatol 1996;11(1):40–46.
[37] Yzet T, Bouzerar R, Allart JD, Demuynck F, Legallais C, Robert B, et al. Hepatic vascular flow measurements by phase contrast MRI and doppler echography: a comparative and reproducibility study. J Magn Reson Imaging 2010;31(3):579–588.
[38] Chowduhury AH, Cox EF, Francis ST, Lobo DN. A randomized, controlled, double-blind crossover study on the effects of 2-L infusions of 0.9% saline and plasma-lyte(R) 148 on renal blood flow velocity and renal cortical tissue perfusion in healthy volunteers. Ann Surg 2012;256(1):18–24.
[39] Vermeulen MAR, Ligthart-Melis GC, Buijsman R, Siroen MPC, van de Poll MCG, Boelens PG, et al. Accurate perioperative flow measurement of the portal vein and hepatic and renal artery: a role for preoperative MRI? Eur J Radiol 2012;81(9):2042–2048.
[40] Motosugi U, Sou TH, Morisaka H, Sano K, Araki T. Multi-organ perfusion CT in the abdomen using a 320-detector row CT scanner: Preliminary results of perfusion changes in the liver, spleen, and pancreas of cirrhotic patients. Eur J Radiol 2012;81(10):2533–2537.
[41] **Snowdon VK**, **Lachlan NJ**, Hoy AM, Hadoke PWF, Semple SI, Patel D, et al. Serelaxin as a potential treatment for renal dysfunction in cirrhosis: preclinical evaluation and results of a randomized phase 2 trial. PLoS Med 2017;14(2).
[42] Angulo P, Bugianesi E, Bjornsson ES, Charatcharoenwitthaya P, Mills PR, Barrera F, et al. Simple noninvasive systems predict long-term outcomes of patients with nonalcoholic fatty liver disease. Gastroenterology 2013;145(4):782–799, e4.
[43] Vergniol J, Foucher J, Terrebonne E, Bernard PH, Bail B, Merrouche W, et al. Noninvasive tests for fibrosis and liver stiffness predict 5-year outcomes of patients with chronic hepatitis C. Gastroenterology 2011;140(7):1970–1979, e1-3.
[44] Chouhan MD, Ambler G, Mookerjee RP, Taylor SA. Multiparametric magnetic resonance imaging to predict clinical outcomes in patients with chronic liver disease: a cautionary note on a promising technique. J Hepatol 2017;66(2):455–457.

Multi-organ assessment of compensated cirrhosis patients using quantitative magnetic resonance imaging

Christopher R Bradley, Eleanor F Cox, Robert A Scott, Martin W James, Phillip Kaye

Guruprasad P Aithal, Susan T Francis, Indra Neil Guha

Table of contents

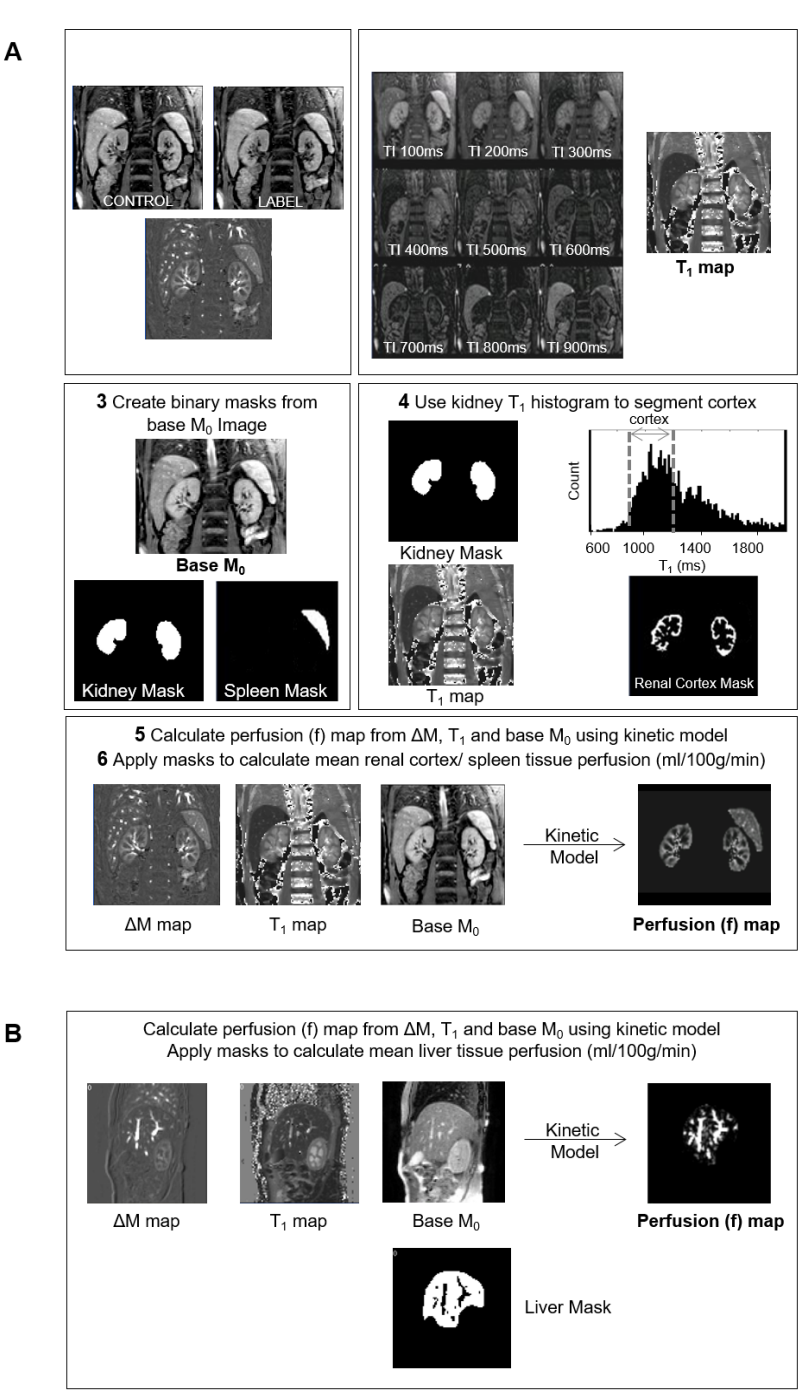

Fig. S1. Analysis pipeline for A) renal and spleen, and B) liver T1 and ASL data. Example image analysis indicating segmentation of the kidneys, definition of cortex and medulla masks using histogram analysis, and the application of the renal cortex mask to an arterial spin labelling perfusion map allowing the interrogation of renal cortex perfusion. Similar steps are performed to assess perfusion and T_1 values in the spleen and liver.

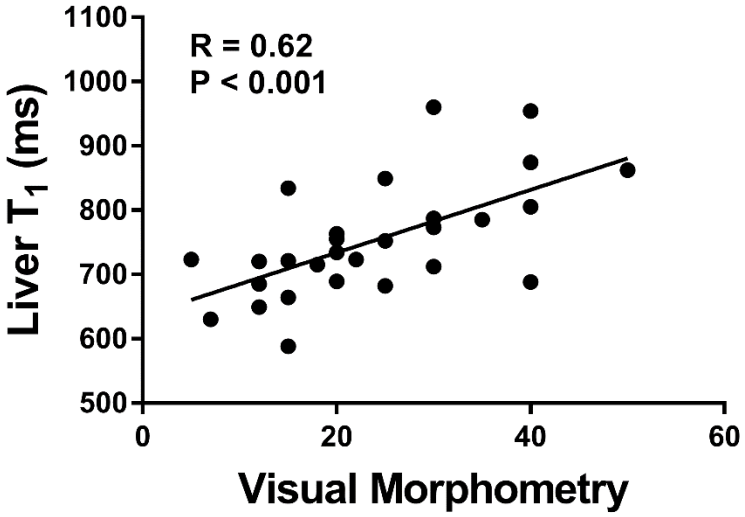

Fig. S2. Liver T_1 relaxation time as a measure of fibrosis as assessed by gold standard liver biopsy. Scatter plot of the distribution of liver T_1 relaxation time with pathologist's estimate of fibrosis in the F4 group, methods based on those described in [17]. Spearman rho and p-value of correlation shown.

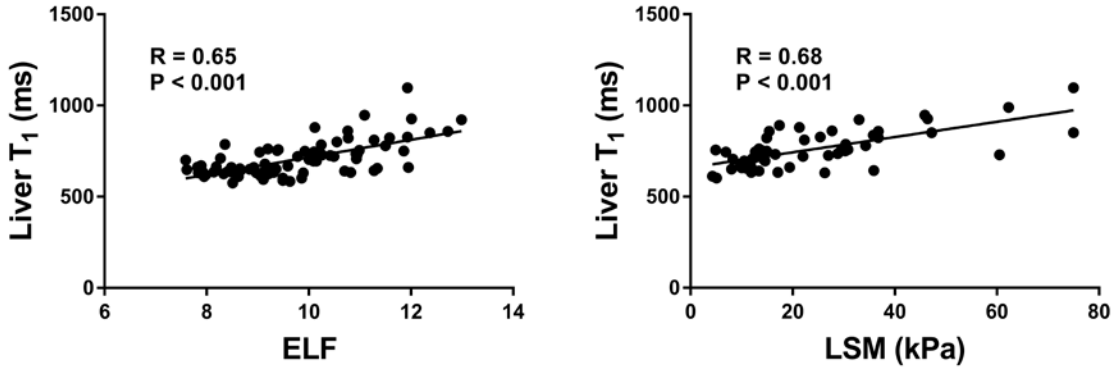

Fig. S3. Liver T_1 relaxation time as a measure of ELF and LSM. Scatter plot of distribution of liver T_1 relaxation time with ELF and LSM as measured from Fibroscan®, with Spearman rho and p-value of correlation shown.

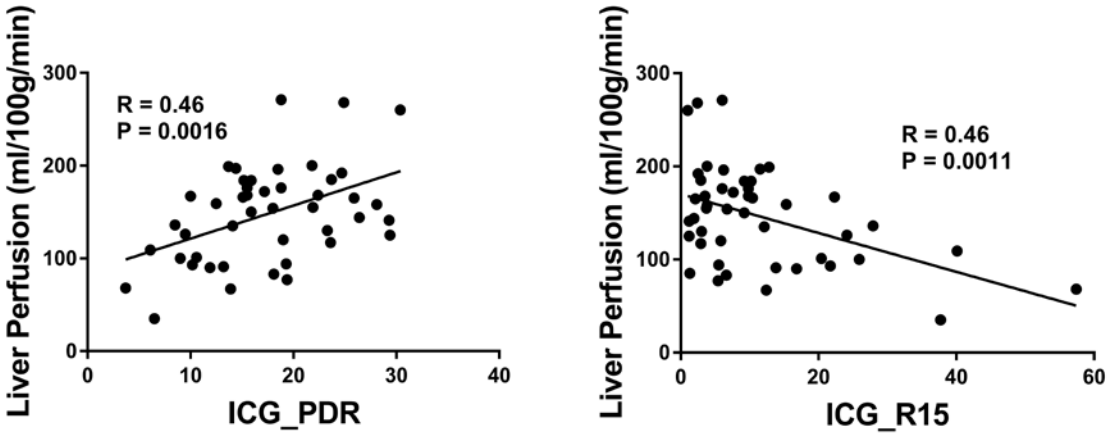

Fig. S4. Liver perfusion as a measure of ICG_PDR and ICG_R15. Scatter plot of distribution of liver T_1 relaxation time with plasma disappearance rate (ICG_PDR) and retention rate at 15 minutes (ICG_R15), with Spearman rho and p-value of correlation shown.

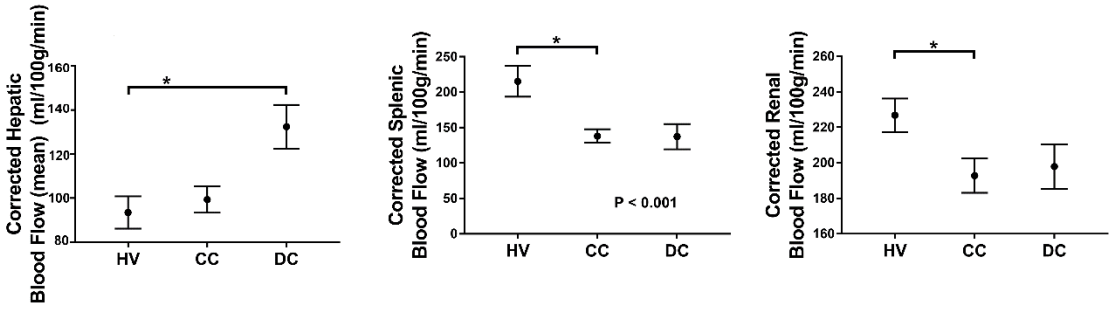

Fig. S5. Organ volume normalised blood flow measures in healthy volunteers (HV), compensated cirrhosis patients (CC) and decompensated patients (DC). Plots show normalised liver blood flow, normalised splenic blood flow, and normalised renal blood flow. Data analyzed using one-way ANOVA, followed by a Tukey *post-hoc* test. *p < 0.05, **p < 0.01, ***p < 0.005, ****p < 0.001.

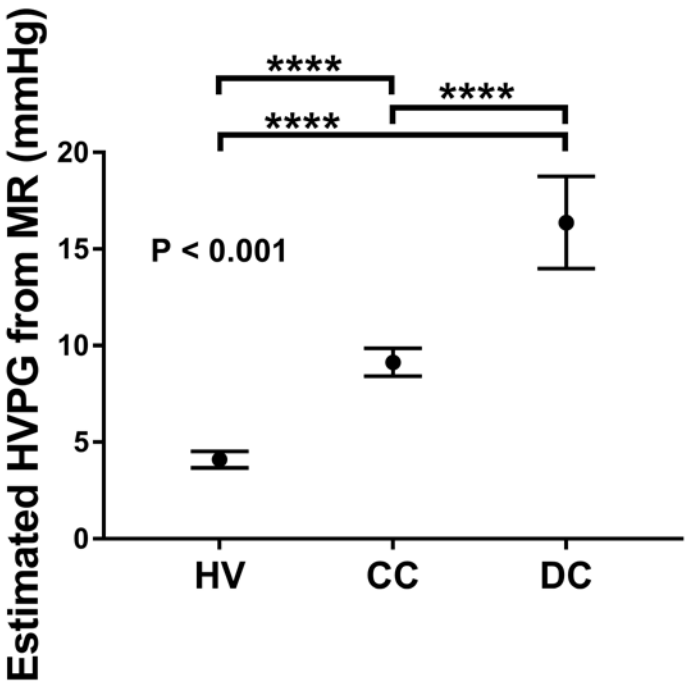

Fig. S6. Estimated HVPG. Estimated HVPG computed using liver T_1 relaxation time and splenic artery velocity measures, based on the model proposed in [20].

Table S1: Intra-subject repeatability of the multiparametric MRI measures. Abbreviations: CoV coefficient of variation; CSA cross sectional area; SMA superior mesenteric artery; T_1 longitudinal relaxation time.

Liver	**CoV (%)**	**Spleen and SMA**	**CoV (%)**	**Renal/Cardiac**	**CoV (%)**
Liver volume	4.6	Spleen volume	5.2	Renal volume	4.2
Liver T_1	1.5	Spleen T_1	1.8	Cortex T_1 Medulla T_1	2.0 1.8
Portal vein flow	18.6	Splenic artery flow	11	Renal Artery Flow	14.4
Portal vein CSA	9.5	Splenic artery CSA	7.3	Renal Artery CSA	11.1
Hepatic artery flow	22.7	SMA flow	7.6	Global single kidney perfusion	14.9
Hepatic artery CSA	13.3	SMA CSA	5.3	ASL renal cortex perfusion	9.3
ASL Perfusion	12	Spleen perfusion	6.9	Cardiac Index	8.2

Table S2: Baseline characteristics of healthy volunteers, and the compensated and decompensated cirrhosis patients.

MR measure	Healthy volunteer	CC Patients	DC patients
Liver volume (ml)	1480 ± 63	1778 ± 61	1523 ± 111
Liver T_1 (ms)	637 ± 5	748 ± 14	864 ± 48
Portal vein flow (ml/s)	11.0 ± 0.6	12.9 ± 0.8	14.9 ± 3.0
Portal vein CSA (mm^2)	93.7 ± 3.4	124.4 ± 4.9	105.3 ± 13.9
Portal vein mean velocity (cm/s)	12.0 ± 0.6	11.0 ± 0.7	13.9 ± 2.0
Portal vein flow per beat (ml)	11.0 ± 0.6	11.9 ± 0.8	11.9 ± 2.2
Hepatic Artery flow (ml/s)	3.21 ± 0.3	4.3 ± 0.3	4.6 ± 0.9
Hepatic Artery CSA (mm^2)	23.3 ± 1.1	25.4 ± 1.1	28.2 ± 3.0
Hepatic Artery mean velocity (cm/s)	13.9 ± 1.1	17.4 ± 1.1	15.7 ± 2.9

Hepatic Artery flow per beat (ml)	3.3 ± 0.3	4.0 ± 0.3	3.7 ± 0.7
Total hepatic flow (ml/s)	14.0 ± 0.8	17.0 ± 0.9	19.2 ± 2.5
Liver perfusion (ml/100g/min)	185.1 ± 9.8	141.5 ± 7.9	100.5 ± 9.5
Splenic volume (ml)	205 ± 16	459 ± 34	489.5 ± 112
Splenic T1 (ms)	1031 ± 11	1044 ± 11	1075 ± 50
Splenic Artery flow (ml/s)	6.3 ± 0.5	8.5 ± 0.5	11.4 ± 1.5
Splenic Artery CSA (mm^2)	30.5 ± 1.6	36.4 ± 2.8	31.5 ± 3.0
Splenic artery mean velocity (cm/s)	21.6 ± 1.4	26.0 ± 1.5	38.6 ± 7.0
Splenic Artery flow per beat (ml)	6.6 ± 0.6	7.9 ± 0.5	9.1 ± 1.2
SMA flow (ml/s)	4.6 ± 0.3	5.5 ± 0.3	7.7 ± 1.1
SMA CSA (mm^2)	23.6 ± 1.2	25.3 ± 1.1	26.6 ± 2.2

SMA mean velocity (cm/s)	19.7 ± 0.7	21.7 ± 0.8	30 ± 4.7
SMA flow per beat (ml)	4.5 ± 0.2	5.0 ± 0.3	6.2 ± 0.8
Splenic perfusion (ml/100g/min)	151 ± 7	120 ± 6	81 ± 9
Renal volume (ml)	316 ± 10	336 ± 10	355 ± 28
Renal T1 (ms)	1318 ± 16	1295 ± 17	1240 ± 60
Renal Artery flow (ml/s)	5.6 ± 0.2	5.7 ± 0.2	5.6 ± 0.6
Renal Artery CSA (mm^2)	20.5 ± 0.7	21.3 ± 0.8	22.1 ± 2.2
Renal artery mean velocity (cm/s)	27.6 ± 0.8	25.9 ± 1.1	26.7 ± 4.0
Renal Artery flow per beat (ml)	5.7 ± 0.2	4.9 ± 0.2	4.5 ± 0.6
Renal cortex perfusion (ml/100g/min)	223 ± 8	215 ± 11	199 ± 26
Cardiac Index ($L/min/m^2$)	2.42 ± 0.06	2.76 ± 0.09	3.06 ± 0.38

Cardiac Wall mass Index (g/m^2)	39.0 ± 1.1	40.0 ± 1.7	22.3 ± 2.4
Heart rate	59.6 ± 1.6	67.2 ± 1.6	76.2 ± 3.1

Table S3: Characteristsics of the compensated cirrhosis patients with and without liver related outcome (LRO). All values shown are mean (standard deviation) except * which indicate median and interquartile range.

MR measure	LRO	No LRO	P value
Liver volume (ml)	1948 (521)	*1728 (740)	0.25
Liver T_1 (ms)	853.7 (125)	720 (73)	<0.001
Portal vein flow (ml/s)	8.7 (6.5)	13.8 (5.7)	0.01
Hepatic Artery flow (ml/s)	3.8 (1.9)	4.1 (2.7)	0.58
Total hepatic flow (ml/s)			
Liver perfusion (ml/100g/min)	93.3 (32.2)	162.5 (46.2)	<0.001
Splenic volume (ml)	550 (331)	432 (224)	0.14
Splenic T1 (ms)	1001 (80)	1048 (74)	0.09
Splenic Artery flow (ml/s)	8.2 (3.3)	8.6 (3.3)	0.79
SMA flow (ml/s)	7.4 (3.6)	*4.6 (2.8)	0.04
Splenic perfusion (ml/100g/min)	92.3 (41.8)	125.1 (39.4)	0.04
Renal volume (ml)	348 (82)	340 (67)	0.76

Renal T1 (ms)			
Cortex	909 (89)	1012 (71)	<0.001
Medulla	1149 (119)	1321 (97)	<0.001
Cortoicomedullary difference	239 (44)	292 (80)	0.003
Renal Artery flow (ml/s)	5.74 (1.8)	5.38 (1.8)	0.56
Renal cortex perfusion (ml/100g/min)	234 (109)	211 (60)	0.437
Cardiac Index (L/min/m^2)	2.8 (0.6)	*2.7(0.7)	0.77
Cardiac Wall mass Index (g/m^2)	41.9 (16.2)	39.8 (11.8)	0.86

9.2 Publication II: Bradley CR, Cox EF, Palaniyappan N, Aithal GP, Francis ST, Guha IN. Variability of noninvasive MRI and biological markers in compensated cirrhosis: insights for assessing disease progression. European Radiology Experimental. 2022 Oct 24;6(1):52.

Bradley *et al.*
European Radiology Experimental (2022) 6:52
https://doi.org/10.1186/s41747-022-00303-y

European Radiology Experimental

ORIGINAL ARTICLE Open Access

Variability of noninvasive MRI and biological markers in compensated cirrhosis: insights for assessing disease progression

Christopher R. Bradley[1,2†], Eleanor F. Cox[1,2†], Naaventhan Palaniyappan[1,3†], Guruprasad P. Aithal[1,3], Susan T. Francis[1,2†] and Indra Neil Guha[1,3*†]

Abstract

Background: We annually monitored stable compensated cirrhosis (CC) patients to evaluate serial variation in blood serum, liver stiffness, and multiparametric magnetic resonance imaging (mpMRI) measures to provide reference change values (RCV) and sample size measures for future studies.

Methods: Patients were recruited from a prospectively followed CC cohort, with assessments at baseline and annually over three years. We report on blood markers, transient elastography liver stiffness measures (LSM) and noninvasive mpMRI (volume, T1 mapping, blood flow, perfusion) of the liver, spleen, kidneys, and heart in a stable CC group and a healthy volunteer (HV) group. Coefficient of variation over time (CoV_T) and RCV are reported, along with hazard ratio to assess disease progression. Sample size estimates to power future trials of cirrhosis regression on mpMRI are presented.

Results: Of 60 CC patients enrolled, 28 with stable CC were followed longitudinally and compared to 10 HVs. CoV_T in mpMRI measures was comparable between CC and HV groups. CoV_T of Enhanced Liver Fibrosis score was low (< 5%) compared to Fibrosis-4 index (17.9%) and Aspartate Aminotransferase-to-Platelet-Ratio Index (19.4%). A large CoV_T (20.7%) and RCV (48.3%) were observed for LSM. CoV_T and RCV were low for liver, spleen, and renal T1 values (CoV_T < 5%, RCV < 8%) and volume (CoV_T < 10%, RCV < 16%); haemodynamic measures were high (CoV_T 12–25%, RCV 16–47%).

Conclusions: Evidence of low CoV_T and RCV in multiorgan T1 values. RCV and sample size estimates are provided for future longitudinal multiorgan monitoring in CC patients.

Trial registration: ClinicalTrials.gov identifier: NCT02037867, Registered: 05/01/2013.

Keywords: Biomarkers, Disease progression, Liver cirrhosis, Multiparametric magnetic resonance imaging, Sample size

Key points

- Liver, kidney, and spleen T1 have low variation over time in stable compensated cirrhosis (CC).
- Multiorgan haemodynamic multiparametric magnetic resonance imaging (mpMRI) measures have high variation over time in stable CC.
- Liver T1, volume, blood flow, and spleen volume were predicted to best detect cirrhosis progression.

†Christopher R. Bradley, Eleanor F. Cox, and Naaventhan Palaniyappan are joint first authors.

†Susan T. Francis and Indra Neil Guha are joint senior authors.

*Correspondence: Neil.Guha@nottingham.ac.uk

[3] Nottingham Digestive Diseases Centre, School of Medicine, University of Nottingham, Nottingham, UK
Full list of author information is available at the end of the article

- Liver T1 and left ventricle wall mass were predicted to best detect decompensation progression.
- Sample size estimates for future multiorgan mpMRI trials of CC regression are provided.

Background

The assessment of chronic liver disease using noninvasive markers is firmly established within clinical practice to study liver fibrosis across aetiology [1–4]. Baseline measures of chronic liver disease have been shown to provide prognostic value in determining clinical outcomes [5], using simple laboratory tests [6, 7], specific fibrosis markers [8], and transient elastography (Fibroscan®) [6, 9]. Recently, novel magnetic resonance imaging (MRI) techniques [10] have been used to study liver disease, for example liver tissue longitudinal relaxation time, *i.e.*, T1, has been shown to correlate with disease severity of liver fibrosis in a cross-sectional study [11]. Liver MRI is now being used in clinical trials of longitudinal change, and the need to study critical organs such as the heart, kidneys and splanchnic circulation is now recognised as a central aspect in the clinical management of cirrhotic patients [12–14]. However, there is limited knowledge of serial variation of multiorgan MRI measures in healthy volunteers and stable patients. It is important to know whether the increase or decrease between two measurements collected serially in time is of clinical significance.

The serial change in a measurement originates from its technical variation (related to the test imprecision) and the biological variation within a subject over time - together this is described by the intra-individual coefficient of variance across time (CoV_T), as well as any change in pathology due to disease progression or regression. For serial measures to reflect clinical improvement or disease progression, any changes over time in the absolute value of a measure should exceed the CoV_T.

The measurement of biomarkers in stable liver disease provides an insight into the temporal variation in the serial, longitudinal measurement of a biomarker, and the required change needed to reflect an alteration in the underlying pathology. Studies reporting the variation in measures in stable patients with liver disease are limited exclusively to blood tests and serum markers [15–17]. In a recent paper, Trivedi et al. [18] assessed the inter- and intra-individual variation in serum alkaline phosphatase and enhanced liver fibrosis (ELF) score over time in patients with primary sclerosing cholangitis. They showed that serum alkaline phosphatase could not associate with disease progression due to a large CoV_T, whilst the ELF score had a lower CoV_T of < 5% and could be used to track fibrosis progression and development of cirrhosis. To date, very few studies have reported the variation of MRI measures in chronic liver disease [19, 20].

The aim of this study is to assess the serial annual variation in blood serum and multiorgan MRI measures of blood flow, perfusion, volume, and T1 mapping in the liver, kidney, and spleen in a stable compensated cirrhosis (CC) patient group who did not develop any clinical outcomes, *i.e.*, in the absence of decompensation and stable validated measures of liver function: model for end-stage liver disease (MELD) and United Kingdom model for end-stage liver disease (UKELD). These data provide reference change values in compensated cirrhosis patients to track disease progression or regression and for intervention assessment in future studies.

Methods

Study design and cohort information

We performed a retrospective analysis of data from individuals enrolled in the Compensated Cirrhosis Cohort in Nottingham (3CN Study), a study focused on tracking liver disease [10] (research approval 10/H0403/10). Inclusion criteria were evidence of cirrhosis based on histology and radiological features and no evidence of decompensation (ascites, significant jaundice, hepatic encephalopathy, and variceal bleeding), hepatocellular carcinoma, and portal vein thrombosis. Exclusion criteria included orthotopic liver transplantation, ischaemic heart disease, alcoholic cardiomyopathy (defined by clinical evidence of systolic dysfunction) and valvular heart disease (defined by echocardiography). CC patients were managed in accordance with standard clinical care guidelines [21]. For alcoholic and non-alcoholic fatty liver disease (NAFLD), lifestyle intervention was offered including referral to an alcohol counsellor and/or dietician, both with a special interest in chronic liver disease. For patients with chronic hepatitis C, the treatment regimens followed the national guidelines appropriate to the specific area (directly acting anti-viral treatment). In addition, patients attended six-monthly clinical research visits (physical examination, blood tests, and Fibroscan®) and an annual research multiparametric MRI (mpMRI).

Patients were assessed at baseline and returned for research visits for up to 3 years. Of the 60 CC patients scanned at baseline, 28 formed our stable control CC group. They did not develop any clinical outcomes (absence of decompensation and stable validated MELD or UKELD measures of liver function) and accepted to take part in longitudinal follow-up are studied in this work. Figure 1 provides an overview of the study protocol and annual research visits, illustrating 28 control CC patients at year 1, with 11 completing their year 3 follow-up. In addition, of the 40 healthy volunteers (HVs) assessed at baseline, 10 HVs who were age, gender, and

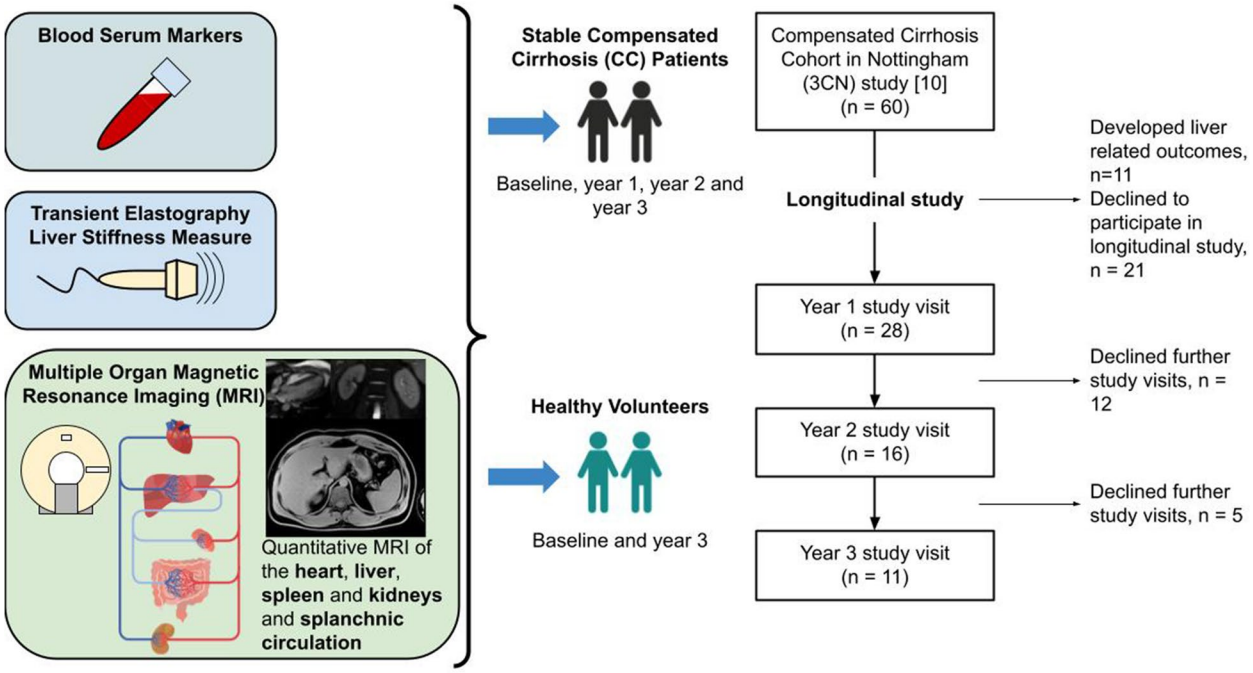

Fig. 1 Schematic of the study and consort diagram. Schematic of blood markers (MELD, UKELD, APRI, FIB4, ELF), Fibroscan® LSM, and multiparametric magnetic resonance imaging (volume, T1-mapping, blood flow, perfusion) of the liver, spleen and kidneys, and cardiac index. Illustration of healthy volunteers (HV) and compensated cirrhosis (CC) patients studied longitudinally as indicated by consort diagram. *MELD* Model for end-stage liver disease, *UKELD* United Kingdom model for end-stage liver disease, *APRI* Aspartate aminotransferase to platelet ratio index, *FIB4* Fibrosis-4, *ELF* Enhanced liver fibrosis, *LSM* Liver stiffness measure, *TE* Transient elastography

body mass index (BMI) matched to the year 3 CC patient group were scanned at baseline and year 3. Decompensated cirrhosis (DC) patients were scanned at baseline only.

At each visit, participants attended following an overnight fast. Blood samples assessed markers of liver fibrosis including Enhanced Liver Fibrosis (ELF), Aspartate aminotransferase to Platelet Ratio Index (APRI) and Fibrosis-4 (FIB4) index. mpMRI measures detailed below were collected. In addition, Fibroscan® liver stiffness measure (LSM) was obtained by an experienced operator. For the HV group, only ELF and MRI measures were collected.

Multiorgan mpMRI protocol

Participants were scanned following a 6-hour fast, between 8 am and 12 pm. All imaging was performed on a 1.5-T Achieva scanner (Philips, Best, The Netherlands) using a 16-element Torso receive coil and the body transmit coil. In each 1-hour scan session, unenhnaced MRI measures were collected on the liver (~20 min), splanchnic organs, and kidneys (~15 min), and heart (~10 min) [10]. Imaging sequence parameters for all MRI measures are shown in detail in Table 1. This comprised: liver-portal vein and hepatic artery blood flow, liver perfusion, and tissue T1 [11, 22]; spleen and superior mesenteric artery–splenic artery and superior mesenteric artery blood flow, splenic tissue perfusion and tissue T1; kidney–right renal artery blood flow, kidney volume, renal tissue perfusion [23, 24], and tissue T1 [24]; heart–cardiac index and left ventricular (LV) wall mass index [25]. Organ volume was measured from high resolution anatomical images. T1 mapping was performed using a respiratory triggered inversion recovery spin echo echo-planar imaging scheme. Blood flow measures were performed using phase-contrast MRI and perfusion using respiratory triggered flow alternating inversion recovery arterial spin labelling (ASL). Due to the longitudinal repeat measures performed in this study, no dynamic contrast-enhanced MRI measures were collected.

Image analysis

Volume of liver, spleen and kidneys

Analyze® (Version 9, Mayo Clinic https://analyzedirect.com/) was used to draw an ROI around each organ (liver, kidney, spleen) for each slice, with total organ volume calculated by summing across slices. Liver and spleen volumes were adjusted for patient body surface area (BSA).

Table 1 Imaging sequence parameters for all magnetic resonance imaging (MRI) measures used in this study

Parameter	Sequence	Readout	Echo time/TR (ms)	FoV (mm^3)	Voxel size (mm^3)		Sequence specific	Scan duration (s)
Volume						Orientation		
Liver, spleen, kidneys	Anatomical	BTFE	1.5/3.3	400 × 400 × 175	1.56 × 1.56 × 7	Coronal		18
Blood flow						VENC (cm/s)	Phases	
Superior mesenteric artery	PC-MRI	TFE	3.7/6.9	150 × 280 × 6	1.17 × 1.17 × 6	140	15	15—20
Hepatic artery	PC-MRI	TFE	3.7/6.9	150 × 280 × 6	1.17 × 1.17 × 6	100	15	15—20
Splenic artery	PC-MRI	TFE	3.7/6.9	150 × 280 × 6	1.17 × 1.17 × 6	100	15	15—20
Right renal artery	PC-MRI	TFE	3.7/0.9	150 × 280 × 6	1.17 × 1.17 × 6	100	15	15—20
Portal vein	PC-MRI	TFE	3.7/6.9	150 × 280 × 6	1.17 × 1.17 × 6	50	15	15—20
Cardiac						VENC (cm/s)	Phases	
Cardiac Output	PC-MRI of ascending aorta	TFE	3.7/6.9	280 × 280 × 6	1.17 × 1.17 × 6	200	30	60
Left ventricle wall mass	Short-axis cine MRI	TFE	1.25/2.5	370 × 370 × 96	2 × 2 × 8	Oblique	30	4′ 15—20 s
Organ Perfusion							ASL parameters	
Liver	FAIR-ASL	BFFE	1.2/2.4	288 × 288 × 39	3 × 3 × 8	Sagittal right lobe	TI 1,100 ms, 60 pairs	~ 360
Spleen and Kidneys	FAIR-ASL	BFFE	1.2/2.4	288 × 288 × 25	3 × 3 × 5	Coronal oblique through kidney long axis	TI 1,100 ms, 30 pairs	~ 180
Microstructure							Inversion times (ms)	
Liver	Inversion recovery T1 mapping	FS SE-EPI	27/8,000	288 × 288 × 39	3 × 3 × 8	Sagittal right lobe	100–1,200 ms in 100 ms steps + 1,500 ms	~120
Spleen and kidneys	Inversion recovery T1 mapping	BFFE	1.2/2.4	288 × 288 × 25	3 × 3 × 5	Coronal oblique through kidney long axis	100–900 ms in 100 ms steps	~120

BFFE Balanced fast field-echo, *BTFE* Balanced turbo-field-echo, *FAIR ASL* Flow alternating inversion-recovery arterial spin labelling, *FoV* Field of view, *FS* Fat-suppressed, *PC-MRI* Phase-contrast MRI, *SE-EPI* Spin-echo echo-planar imaging, *TFE* Turbo field-echo, *TI* Inversion time, *TR* Repetition time, *VENC* Velocity encoding

Blood flow measures

MR Qflow (a plug-in available on the ViewForum Philips Medical Systems, Best, The Netherlands https://www.philips.co.uk/healthcare/product/HCAPP013/-mr-qflow-) was used to analyse phase-contrast MRI data. For each vessel, a region of interest was drawn on each cardiac phase to estimate flow by averaging the flow velocity values and multiplying by vessel lumen cross-sectional area. Mean flow was calculated by averaging flow across cardiac cycle phases.

Cardiac function and structure

Cardiac MRI data was analysed using ViewForum software (Philips Medical Systems, Best, The Netherlands). phase-contrast MRI data of the aorta was analysed by computing stroke volume and heart rate, then multiplying these to yield cardiac output. This software was also used to draw wall contours to calculate end diastolic LV wall mass. Cardiac output and LV wall mass were adjusted for patient BSA[NO_PRINTED_FORM].

Perfusion and T1 relaxation mapping of the liver, spleen and kidneys

Inversion-recovery data were fit to a two-parameter model to generate T1 maps. ASL analysis was performed using MATLAB (2014a, Natick, MA, USA) and/or IDL (version 8.0, Broomfield, CO, USA). Individual perfusion-weighted images (control-label) were calculated, inspected for motion (excluding > 1 voxel) and averaged creating a perfusion-weighted image. Perfusion-weighted image, base equilibrium magnetisation, M_0, image, and T1 maps were used in a kinetic model [26] to compute tissue perfusion maps.

A binary organ mask was formed to calculate mean liver, spleen and renal cortex perfusion. For the liver and spleen, masks were formed from the base M_0 image and applied to T_1 maps to obtain the median T1 (excluding major blood vessels with a T_1 > 1,300 ms) and perfusion. Whole kidney masks were formed by manual segmentation of the T1 map, applied to the T1 and perfusion maps, and the mode of each parameter calculated for each kidney, the mean was then computed across kidneys.

Statistical analysis

In this stable CC control group, we aim to determine the variance over time in blood serum, Fibroscan® LSM and MRI measures of blood flow, structure, and perfusion, and evaluate this in the context of future clinical trials. To address this, we performed the following analyses regarding (1) the changes with disease stage in the baseline cross-sectional data; (2) the coefficient of variation (CoV) within the stable CC control group at baseline (interindividual, groupwise CoV, CoV_G); (3) the CoV across time in annual measurements in individuals in the stable CC control group (intraindividual, CoV_T) and the reference change value (RCV), defined as the percentage change in a measure in an individual that can be attributed to pathological change, (as employed in a recent study of high sensitivity cardiac troponin-T (hs-cTnT) concentration in dialysis patients [27]); (4) the variation in serum and MRI measures collected in HVs to determine whether the results differ between stable CC and HV group; (5) the hazard ratio (HR) of these measures to assess disease progression; (6) sample size estimates for future longer-term clinical trials powered on mpMRI measures to study cirrhosis regression. Details of each of these analyses are provided below.

1. *Cross-sectional multiparametric MRI measures with disease stage.* The percentage change in MRI measures at baseline between the HV, CC, and DC groups was calculated to determine clinically relevant increases or decreases in measures.
2. *Categorical change in clinical and MRI measures in the stable CC control group.* To demonstrate the stability of each clinical and MRI measure in the stable CC control group, the percentage change from baseline was computed for each individual at year 1, year 2, and year 3. After a Shapiro-Wilk test for normality, a paired Wilcoxon test confirmed no significant changes between time-points (Prism 8, GraphPad Software, Inc., La Jolla, CA, USA). The median (interquartile range, IQR) group percentage change from baseline at year 1, year 2, and year 3 was then calculated. For each measure, the CoV within the group at baseline was computed (inter-individual, CoV_G).
3. *Annual intra-individual variability in clinical and MRI measures in the stable CC control group.* The year-to-year intra-individual variation in each measure was assessed by calculating the annual CoV in each of the measures (year 1 *versus* baseline, year 2 *versus* year 1, year 3 *versus* year 2), and computing the median of these CoVs defined to be the CoV_T (intraindividual variance across time). Importantly, this variation combines the effect of the intraindividual biological variation and analytical sample measurement error (from two repeat measurement collected sequentially in time). The RCV was then computed as follows:

$$RCV = 2^1/2 \times Z \times CoV_T$$

For a significant ($p < 0.05$) one-directional change a Z-score (Z) of 1.65 was used, and the log-normal approach was used to compute the asymmetrical limits

for the upward (positive, RCV_{up}) and downward (negative, RCV_{down}) value of the log-normal RCV.

4. *Baseline to Year 3 intra-individual variability in clinical and MRI measures in the stable CC control group and HV group.* To assess whether the timing and frequency of sampling are important factors in CoV_T and RCV measures, CoV_T was also computed for the stable CC control group from the baseline and Year 3 measures only, this was also performed for the HV group. The median intra-individual CoV across each group was then computed for CoV_T. For each measure, RCV and the asymmetrical limits were computed from CoV_T. The coefficient of variance at baseline (CoV_G) was also calculated for each group.
5. *Performance of measures to detect disease progression using MRI.* To evaluate the sensitivity to assess progression from HV to CC, a HR was computed for each MRI measure, defined as the difference in absolute values of a measure between HV and CC groups divided by the RCV in absolute units for that measure in the HV group. We also compute the HR for progression from CC to DC using the absolute value of the RCV of the CC group. A positive HR indicates an increase in the absolute value of a measure, whilst a negative HR indicates a decrease. A HR > 1 or < -1 suggests that the MRI measure could detect a significant pathological change.
6. *Sample size estimation for clinical trials detecting regression of cirrhosis using MRI.* To illustrate how MRI measures could be used in clinical trials, the sample size needed to detect a clinically significant change from compensated cirrhosis (F4) to advanced fibrosis (F3) at a power of 80% and confidence of 0.05 was calculated. For this, we extrapolate from the change in T1 from F4 to F3 reported in our previous work with biopsy-proven measures [11]. This showed a change of 55 ms for T1 from F4 to F3, equivalent to 50% of the change in T1 from CC toward HVs reported in this study. Thus, to represent F4 to F3 in other measures we also report the sample size needed for a 50% change from CC toward HV.

Results

Cross-sectional multiorgan mpMRI measures with disease stage

At baseline, cross-sectional multiorgan MRI measures were collected in 60 CC patients and 40 HVs, and DC

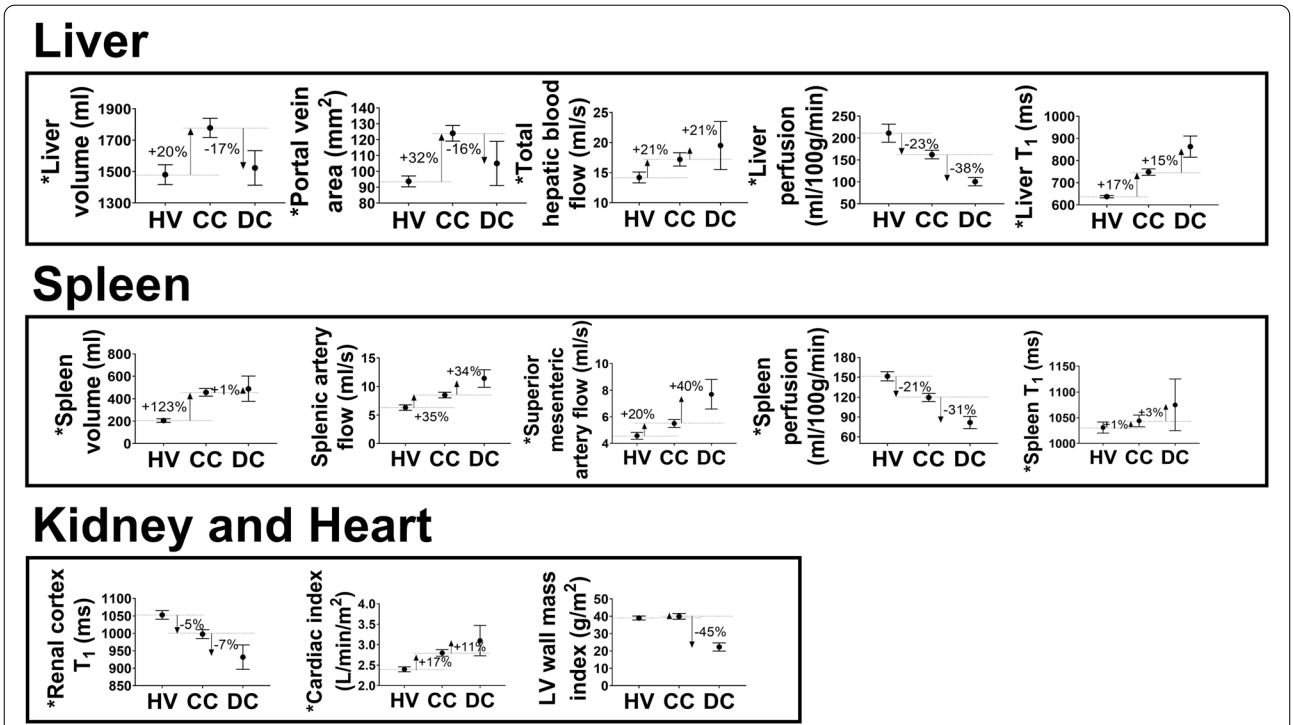

Fig. 2 Baseline magnetic resonance imaging parameters for 40 healthy volunteers (HV), 60 compensated cirrhosis (CC) patients, and 7 decompensated cirrhosis (DC) patients. Baseline measures (mean and standard error of the mean) of the liver (volume, portal vein area, total hepatic blood flow, liver perfusion, liver T1), spleen (volume, splenic artery flow and superior mesenteric artery flow, spleen perfusion, spleen T1), kidney (renal cortex T1), and heart (cardiac index and left ventricle [LV] wall mass index) are shown, with the percentage change between the HV and CC groups, and CC and DC groups shown by arrows. Asterisk indicates measures which are significantly different ($p < 0.05$, independent samples *t*-test) between the CC and HV group [10]

Table 2 Characteristics of the 60 compensated cirrhosis cohort divided into 28 stable control patients followed longitudinally in this paper, and those non-returner patients excluded as they either failed to return for repeat assessments or developed a clinical outcome. Also shown is the 10 healthy volunteer group followed longitudinally

	Compensated cirrhosis		Healthy volunteers
	Stable returners	Non-returners	
N	28	32	10
Gender	17 male (61%)	18 male (56%)	6 male (60%)
Age (years)	59 (8)	59 (13)	63 (4)
Aetiology	29% NALFD/18% ALD/25% HCV/28% other	40% NAFLD/37% ALD/15% HCV/7% other	N/A
BMI (kg/m^2)	27.5 (5.6)	28.5 (4.9)	26 (3.0)
MELD	7.5 (1.6)	6.9 (1.8)	N/A
UKELD	43.1 (2.9)	43.5 (2.3)	N/A
APRI	0.71 (0.61)	0.71 (1.2)	N/A
FIB4	2.5 (1.8)	2.9 (1.9)	N/A
ELF score	10.2 (1.2)	11.5 (1.9)	8.9 (0.8)
Fibroscan® LSM (kPa)	18 (17)	23 (21)	N/A

Numbers in parentheses correspond to the standard deviation in measures unless stated otherwise

NAFLD Non-alcoholic fatty liver disease, *ALD* Alcoholic liver disease, *HCV* Hepatitis C virus, *BMI* Body mass index, *MELD* Model for end-stage liver disease, *UKELD* United Kingdom model for end-stage liver disease, *APRI* Aspartate aminotransferase to platelet ratio index, *FIB4* Fibrosis-4, *ELF* Enhanced liver fibrosis, *LSM* Liver stiffness measure

patients. In patients with CC, a hyperdynamic circulation resulted in increased blood flow in the liver, splanchnic circulation and increased cardiac index, with further increases in spleen blood flow and cardiac index in patients with DC, as summarised in Fig. 2. Liver and splenic perfusion was reduced in patients with CC compared to the HV group, and perfusion in these organs was further reduced in those with DC. No significant change in renal perfusion was found between patients with CC and DC, and the HV group. Liver tissue T1 increased in patients with CC compared to HVs, and further increased in those with DC. Spleen T1 was only significantly different from the HV group in DC patients. In contrast, renal T1 reduced in patients with CC and further reduced in those with DC, compared to HVs. LV wall mass was significantly reduced in patients with DC compared to HVs, whilst liver volume was found to increase only in patients with CC, and spleen volume was increased in patients with CC and DC compared to HVs. Note that with disease progression liver volume and portal vein area first increase from HV to CC and then decrease as patients decompensate. This baseline cross-sectional data has previously been described in detail [10]. These results provide the context for the percentage change in MRI measures between the HV, CC and DC groups, and the increase or decrease in measures that are of clinical relevance when considering longitudinal variance of measures.

Baseline characteristics of the stable CC control group and HV group

Of the 60 CC patients enrolled at baseline, on retrospective analysis, 28 stable CC control patients were followed longitudinally. The baseline characteristics of this 28 stable CC group along with the 32 non-returners are provided in Table 2. The stable CC control group comprised 28 patients at year 1, 16 patients at year 2 and 11 patients at year 3. Of the 28 stable CC control patients, 21 patients (75%) had cirrhosis diagnosed from liver biopsy, 4 (14%) from typical radiological features of cirrhosis (nodular liver and evidence of portal hypertension), and 3 (11%) from clinical findings of cirrhosis including typical clinical history and presence of abdominal collaterals on examination.

There was no significant change in the BMI during the study period, with a median BMI of 28 (IQR 6), 28 (IQR 6), and 27 (IQR 4) kg/m^2 at years 1, 2, and 3 respectively. All patients with chronic hepatitis C achieved sustained virological response prior to the study. In alcohol-related cirrhosis, abstinence from alcohol was noted among all the patients. In addition, 10 age, gender, and BMI-matched healthy volunteers were studied at baseline and year 3, whose baseline characteristics are provided in Table 2.

Annual intra-individual variability in clinical measures in the stable CC control group

Figure 3a shows the year-to-year percentage change in MELD and UKELD scores, APRI, FIB4, ELF, and

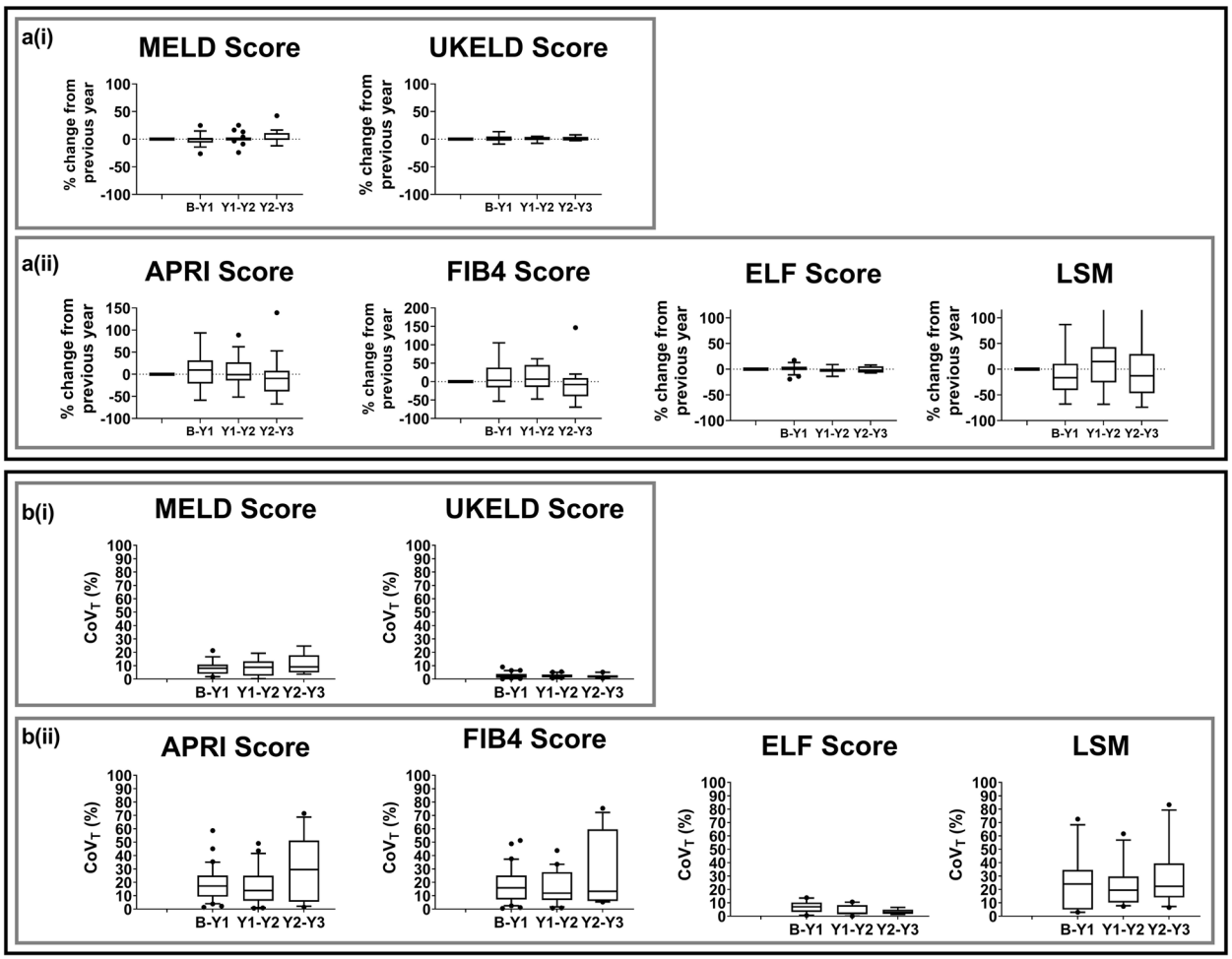

Fig. 3 **a** Year-to-year percentage change in clinical measures in the stable compensated cirrhosis control group. **b** Year-to-year coefficient of variation (CoV_T) in clinical measures in the stable compensated cirrhosis control group. Clinical measures of MELD, UKELD, APRI, FIB4, ELF scores, and Fibroscan® LSM are shown. Bars indicate the interquartile range and the horizontal bold line shows the median, dots represent outliers. *MELD* Model for end-stage liver disease, *UKELD* United Kingdom model for end-stage liver disease, *APRI* Aspartate aminotransferase to platelet ratio index, *FIB4* Fibrosis-4, *ELF* Enhanced liver fibrosis, *LSM* Liver stiffness measure

Fibroscan® LSM. There were no significant ($p \geq 0.23$) changes in MELD, UKELD, APRI, FIB4, ELF score or Fibroscan® LSM over the three years. Figure 3b shows the year-to-year CoV_T and Table 3 summarises the CoV_G, CoV_T, and RCV in the clinical measures in the stable CC control group. For all clinical measures, CoV_T was lower than CoV_G. UKELD and ELF score showed the lowest annual variation with a median CoV_T of 2.2% and 4.0% respectively. Fibroscan® LSM had the largest annual variation with median CoV_T of 20.7%. The RCV values provide the percentage change in a serial measurement that represents a statistically significant ($p < 0.05$) change. The RCV for UKELD and ELF score was 5.1% and 6.8%, respectively, whilst the RCV for Fibroscan® LSM was markedly higher at 48.3%.

Annual intra-individual variability in MRI measures in the stable CC control group

Figure 4 shows the year-to-year percentage change in MRI measures. In this stable CC control group, there was no significant difference in any MRI measure when compared year-to-year. Figure 5 shows the CoV_T of each MRI measure. The annual variation in structural-related MRI measures (volume and T1) is smaller than haemodynamic measures (vessel flow and tissue perfusion). The CoV_T of liver and spleen volume was < 10%, whilst the CoV_T of liver, spleen and renal cortex T1 was < 5%. Contrastingly, flow measurements of splanchnic circulation (splenic artery and superior mesenteric artery) had a median CoV_T of 25% and 16%, respectively. For comparison, in Fig. 5, the technical variation (analytical CoV, CoV_A) measured in HVs from

Table 3 Interindividual baseline variance (CoV_G), intraindividual variance across time (CoV_T), reference change value (RCV), and asymmetrical limits of the log-normal RCV (RCV_{up}/RCV_{down}) for clinical (serum markers MELD, UKELD, APRI, FIB4, ELF); Fibroscan® LSM) and magnetic resonance imaging (MRI) measures

		CoV_G (%)	CoV_T (%)	RCV (%)	RCV_{up}/RCV_{down} (%)
Clinical measures					
MELD (stable CC annual)		26.2	8.6 [7.0]	17.6	19.9/-15.6
UKELD (stable CC annual)		6.6	2.2 [1.7]	5.1	5.5/-5.1
APRI (stable CC annual)		104.3	19.4 [10.0]	39.5	51.8/-30.4
FIB4 (stable CC annual)		78.1	17.9 [10.8]	36.4	46.6/-28.6
ELF score	Stable CC annual	10.4	4.0 [3.2]	6.8	8.3/-7.7
	Stable CC b-Y3	8.4	4.2 [3.0]	8.6	9.1/-8.1
	HV b-Y3	7.6	3.6 [2.1]	7.4	7.0/-7.7
Fibroscan® LSM (Stable CC annual)		59.8	20.7 [21.6]	48.3	93.0/-41.0
MRI measures					
Liver volume	Stable CC annual	26.6	7.5 [3.4]	13.1	16.8/-14.4
	Stable CC b-Y3	21.6	9.4 [8.1]	19.1	21.8/-16.8
	HV b-Y3	9.9	1.8 [5.7]	3.6	3.7/-3.5
Portal vein area	Stable CC annual	31.6	11.0 [9.4]	16.8	22.0/-18.1
	Stable CC b-Y3	22.4	11.0 [9.4]	19.2	21.9/-16.8
	HV b-Y3	22.5	12.4 [8.2]	25.4	21.4/-30.1
Total hepatic blood flow	Stable CC annual	30.2	12.2 [16.8]	26.3	36.9/-26.9
	Stable CC b-Y3	19.9	9.1 [11.5]	18.6	21.1/-16.4
	HV b-Y3	27.8	28.1 [33.4]	65.5	114/-53.4
Liver perfusion	Stable CC annual	31.0	21.0 [14.7]	40.8	61.7/-38.2
	Stable CC b-Y3	16.8	20.6 [22.7]	31.1	42.4/-31.8
	HV b-Y3	29.3	13.1 [20.8]	26.7	32.0/-22.3
Liver T1	Stable CC annual	11.0	4.2 [2.2]	7.3	9.1/-8.4
	Stable CC b-Y3	12.7	5.0 [4.2]	10.2	11.0/-9.6
	HV b-Y3	6.2	2.5 [2.5]	5.1	5.3/-4.9
Spleen volume	Stable CC annual	48.4	9.5 [5.8]	15.3	19.9/-16.6
	Stable CC b-Y3	35.1	11.1 [7.4]	22.6	26.5/-19.4
	HV b-Y3	28.4	14.8 [5.3]	30.1	24.6/-37.0
Splenic artery flow	Stable CC annual	38.6	25.0 [24.5]	46.5	72.9/-42.2
	Stable CC b-Y3	35.2	8.2 [12.5]	16.7	18.7/-14.9
	HV b-Y3	33.4	18.0 [30.2]	36.7	47.1/-28.7
Superior mesenteric artery flow	Stable CC annual	35.3	15.7 [9.7]	31.1	44.5/-30.8
	Stable CC b-Y3	36.8	13.7 [16.9]	28.0	33.9/-23.2
	HV b-Y3	23.1	9.8 [7.9]	20.0	17.4/-22.9
Spleen perfusion	Stable CC annual	31.4	16.0 [9.2]	26.3	36.6/-26.8
	Stable CC b-Y3	36.4	11.4 [21.7]	23.2	27.3/-19.9
	HV b-Y3	27.1	10.4 [3.4]	21.2	18.4/-24.9
Spleen T1	Stable CC annual	7.7	2.8 [3.7]	4.1	5.0/-4.8
	Stable CC b-Y3	5.2	4.2 [3.7]	8.5	9.0/-8.0
	HV b-Y3	5.9	2.3 [2.8]	4.6	4.5/-4.7
Renal cortex T1	Stable CC annual	10.1	3.6 [2.5]	6.6	8.2/-7.6
	Stable CC b-Y3	9.2	3.6 [3.7]	7.4	7.0/-7.7
	HV b-Y3	5.6	2.4 [2.3]	4.9	4.8/-4.7
Cardiac Index	Stable CC annual	26.7	9.5 [7.9]	19.2	25.6/-20.4
	Stable CC b-Y3	27.5	10.9 [10.9]	22.4	26.0/-19.2
	HV b-Y3	20.5	7.4 [9.0]	15.1	16.7/-13.7
LV wall mass index	Stable CC annual	31.8	15.3 [11.2]	33.1	32.4/-47.9
	Stable CC b-Y3	28.3	13.8 [6.9]	28.2	34.1/-23.3
	HV b-Y3	32.6	10.1 [8.9]	20.7	23.8/-18.0

For each parameter, variation indices are given for annual variability in the stable compensated cirrhosis (CC) control group (stable CC annual), and for baseline to year 3 variability in the stable CC control group (Stable CC b-Y3) and the HV group (HV b-Y3)

CoV coefficient of variation, *MELD* model for end-stage liver disease, *UKELD* United Kingdom Model for end-stage liver disease, *APRI* aspartate aminotransferase to platelet ratio index, *FIB4* Fibrosis-4, *ELF* enhanced liver fibrosis, *Fibroscan® LSM* Liver stiffness measure, *LV* left ventricle

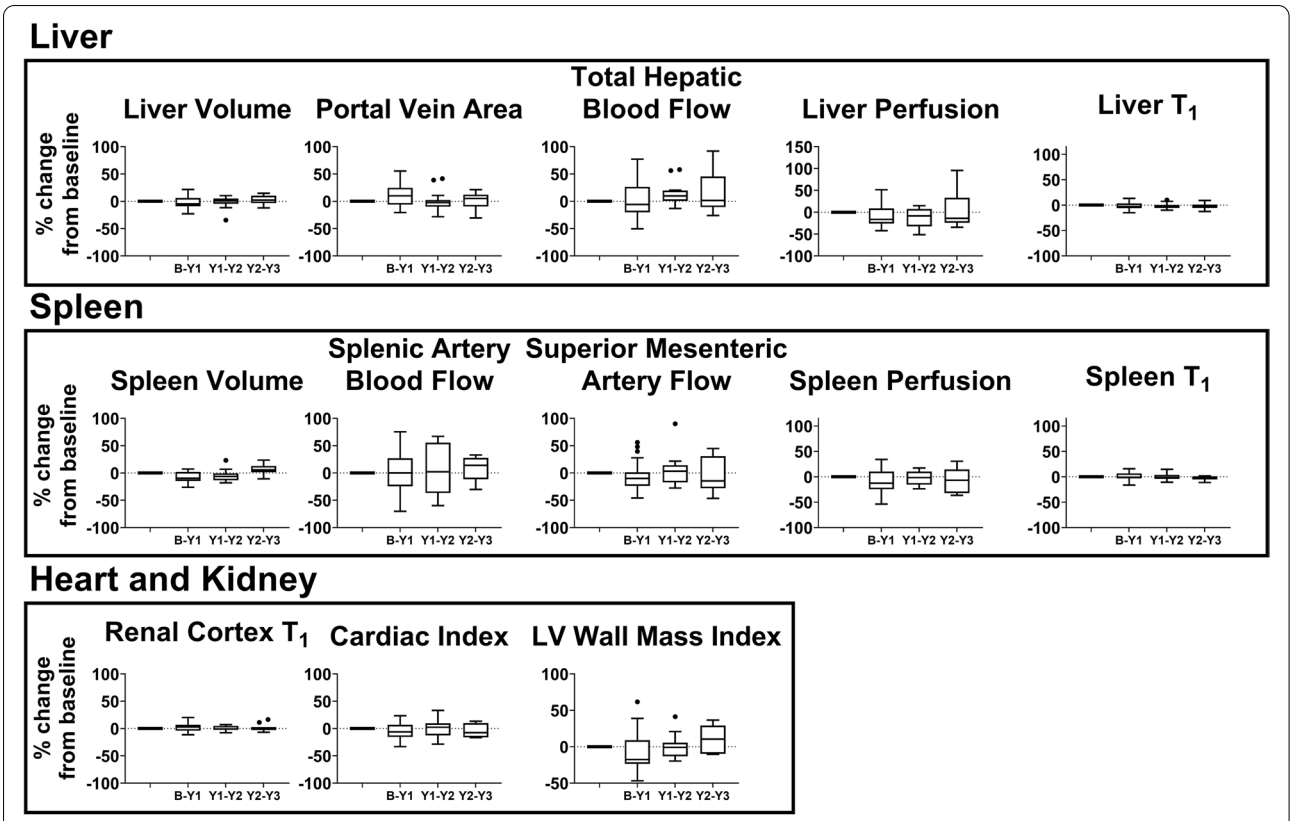

Fig. 4 Year-to-year percentage change in magnetic resonance imaging measures in the stable compensated cirrhosis control group. Measures liver (volume, portal vein area, total hepatic blood flow, liver perfusion, liver T1), spleen (volume, splenic and superior mesenteric artery flow, spleen perfusion, spleen T1), kidney (renal cortex T1), and heart (cardiac index and left ventricle [LV] wall mass index) are shown. Bars indicate interquartile range and horizontal bold line shows the median percentage change, dots represent outliers

triplicate scans 1 week apart [10] is shown. Table 3 summarises CoV_G, CoV_T, and RCV in annual MRI measures in the stable CC control group. The lowest values of RCV were for liver T1 (7.3%), spleen T1 (4.1%), and renal cortex T1 (6.6%), with the highest RCV values, were seen for liver perfusion (40.8%) and splenic artery flow (46.5%).

Since Fibroscan® LSM [28], ELF [29], and liver T1 [11] have each been shown to provide a method to evaluate liver fibrosis, Fig. 6 illustrates the year-to-year percentage change and the CoV_T in these measures for those stable CC control patients who completed all three annual follow-up scans. All individual ELF score and liver T1 show a percentage change < 17.5% and < 14.6%, respectively, and year-to-year CoV_T < 13.8% and < 11.4%, respectively, whilst Fibroscan® LSM had a percentage change of up to 150%, resulting into a CoV_T of 83%.

Baseline to year 3 intraindividual variability in clinical and MRI measures in the stable CC control group and HV group

To assess whether the timing and frequency of sampling are important factors in RCV measures, the CoV_T and RCV in clinical and MRI measures for subjects (stable CC and HV) studied between baseline and year 3 were calculated, as shown in Table 3. There was no noticeable difference in RCV values computed for the different frequency of measures (annual *versus* baseline to year 3) for the stable CC control group. RCVs were similar between the stable CC control group and the HV group for baseline to year 3 measures.

Performance of measures to detect change in disease stage

Figure 7 provides a schematic of the HR for disease progression. Figure 7a (i) shows the progression of HV to CC, for which a HR much higher than 1.0 was found for liver T1, BSA-corrected liver and spleen volume and hepatic blood flow and is ~1.0 for portal vein area, cardiac index, splenic and superior mesenteric artery flow, and ~ -1.0 for liver and spleen perfusion and renal cortex T1. For progression from CC to DC, Fig. 7a(ii) shows that the HR of portal vein area and liver volume changes sign to ~ -1, whilst liver T1 remained much higher than 1.0. Similar HRs were found for other MRI measures between

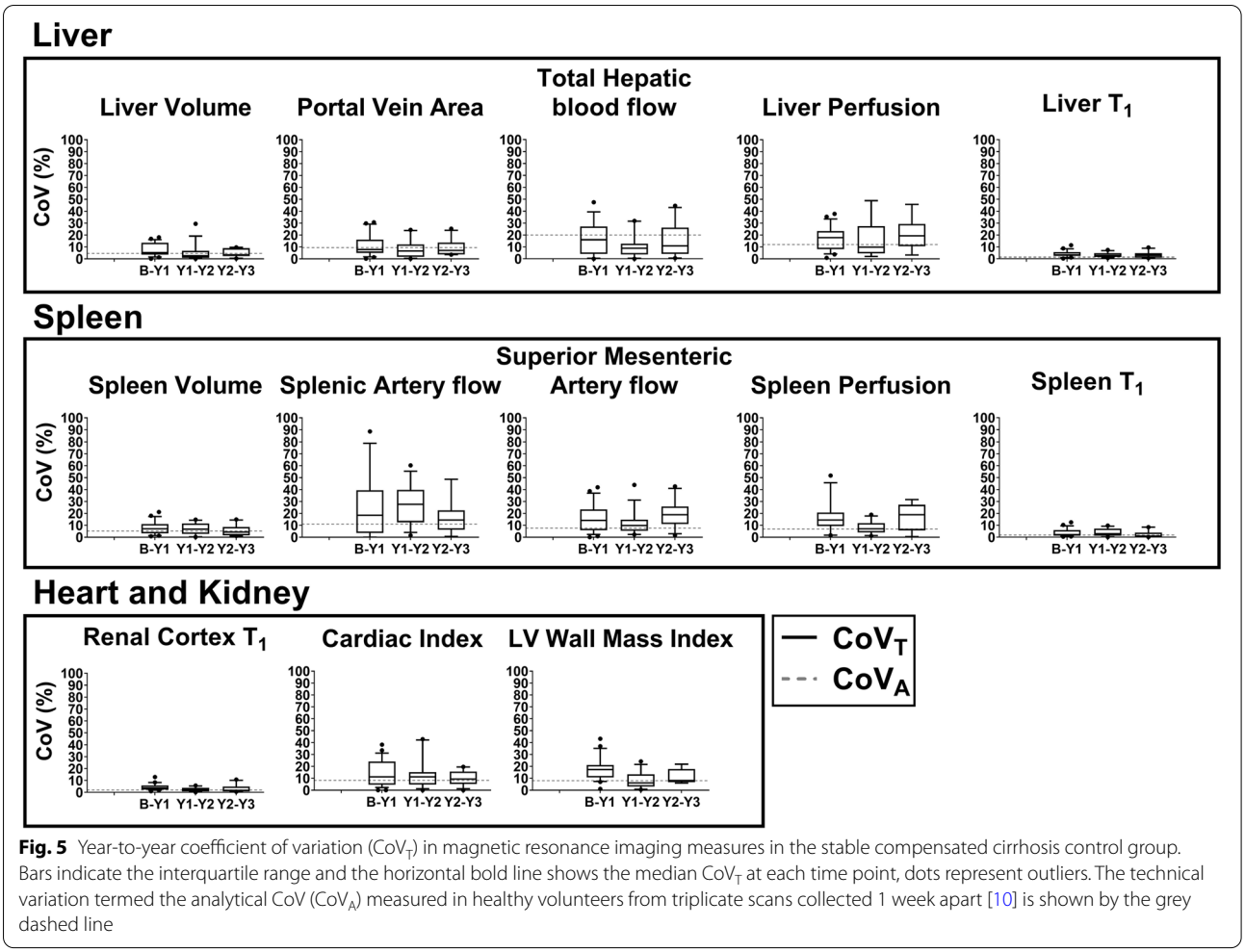

Fig. 5 Year-to-year coefficient of variation (CoV_T) in magnetic resonance imaging measures in the stable compensated cirrhosis control group. Bars indicate the interquartile range and the horizontal bold line shows the median CoV_T at each time point, dots represent outliers. The technical variation termed the analytical CoV (CoV_A) measured in healthy volunteers from triplicate scans collected 1 week apart [10] is shown by the grey dashed line

HV to CC and CC to DC, except for LV wall mass which is lower than -1 for CC to DC.

Estimating sample sizes for clinical trials to predict regression of cirrhosis using multiparametric MRI

Figure 7b shows the sample size of each MRI measure required in a clinical trial to assess cirrhosis regression from F4 toward F3, shown as a percentage change from the mean MRI value in the stable CC group. For a disease state change from F4 to F3, liver T1, spleen and liver volume, and portal volume area require a sample size of lower than 100.

Discussion

Here we evaluate the serial variation of clinical measures and multi-organ (cardiac, kidney, liver and splanchnic circulation) multiparametric MRI measures that have the potential to study disease-related changes in patients with CC and HVs. Repeatability of quantitative MRI measures has generally been assessed in HVs across vendors and field strength over a period of hours or up to 1 week (*e.g.*, liver T1 and T2*, as reported by Bachtiar et al. [30]). To our knowledge, limited long-term reproducibility data has been collected in only healthy control subjects and serial variation has not previously been evaluated in imaging biomarkers in patients with stable CC. Knowledge of such variability is important since many trials are now beginning to study serial annual MRI changes, for example due to drug treatments [20, 31]. The lack of a control group is often stated as a limitation in such longitudinal trials [31]. In this study, stable CC patients who remained compensated for at least 2 years following their final MRI visit were followed annually to determine the variability in clinical and multiorgan MRI measures.

Among the clinical measures, ELF was most consistent with a year-to-year CoV_T < 5% and RCV of 6.8%; in comparison, APRI and FIB4 showed scores with CoV_T of 19% and 18%, and RCV of 36% and 39%, respectively. Fibroscan® LSM had a median (IQR) year-to-year CoV_T of 20.7% (21.6%) resulting into a large RCV of 40.8%. This level of change agrees with Nascimbeni et al. [19], who reported a

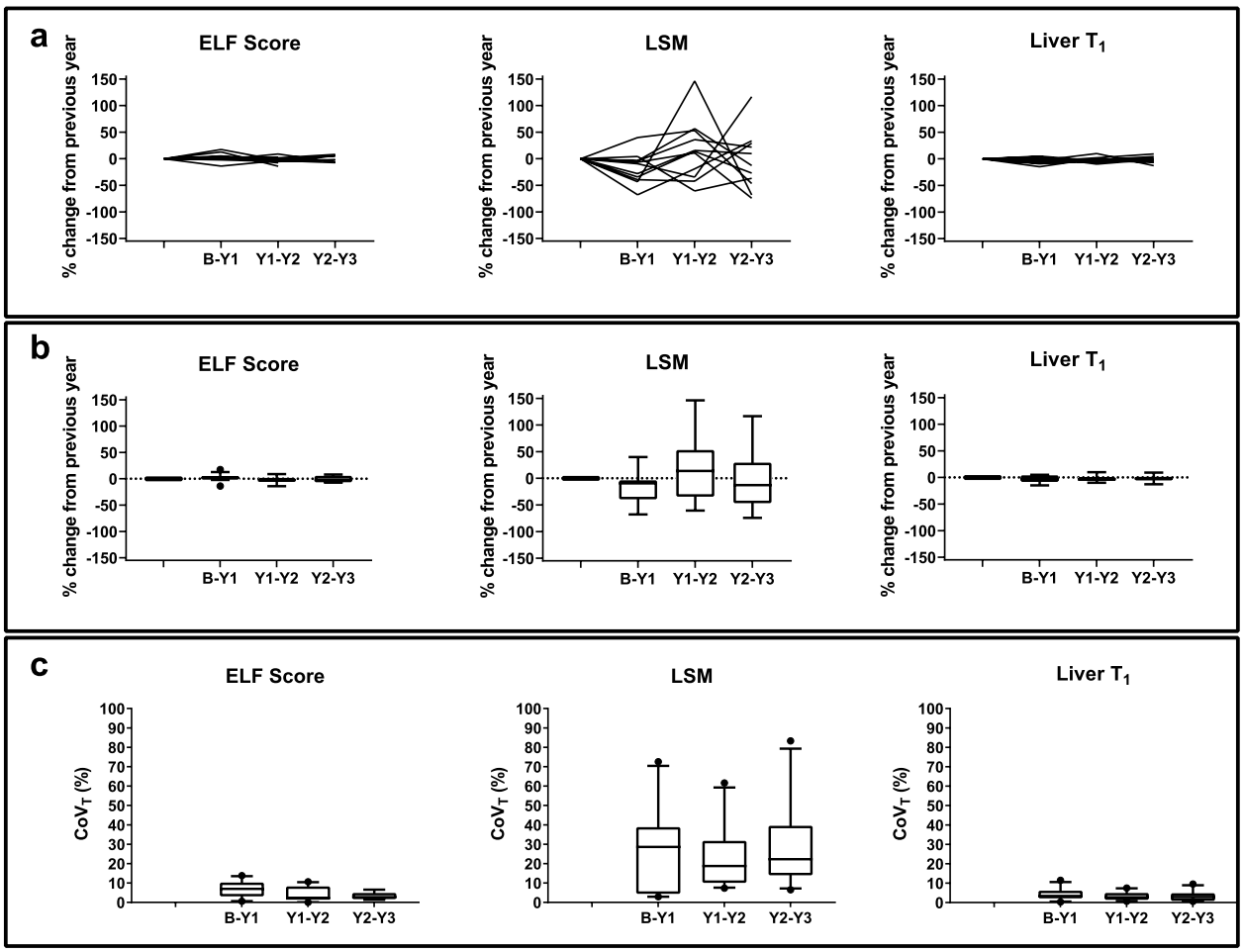

Fig. 6 ELF score, Fibroscan® LSM and liver T1 for the stable compensated cirrhosis control patients who completed all three annual follow-up scans: **a** individual subject percentage change from baseline values at year 1, year 2, and year 3; **b** group percentage change from baseline values at year 1, year 2, and year 3. Bars indicate the interquartile range and bold line shows the median percentage change. There was no significant difference from baseline ($p > 0.05$ Bonferroni-corrected); **c** Year-to-year coefficient of variation (CoV_T) in magnetic resonance imaging measures. Bars indicate the interquartile range and the horizontal bold line shows the median CoV, dots represent outliers. *ELF* Enhanced liver fibrosis, *LSM* Liver stiffness measure

retrospective analysis of 500 paired Fibroscan® LSMs with a variation of over 50% in 61 paired measurements. Thus, an increase in LSM of 33% (*i.e.*, from 15 kPa to 20 kPa) would not reflect a true change, which would have implications on clinical management of this patient. A LSM of less than 20 kPa is the threshold set by Baveno VI guidelines [32] to avoid screening gastroscopy for varices, but if LSM subsequently increases on annual follow-up, endoscopy is recommended. In comparison to previous studies, Vergniol et al. [6] showed that the change from baseline to 3 years in LSM from Fibroscan®, APRI and FIB4 has prognostic value in chronic hepatitis. Siddiqui et al. [33] showed that FIB4, APRI, and NAFLD fibrosis scores can detect fibrosis progression, whilst Hartl et al. [34] performed annual LSMs and showed LSM was a reliable predictor in autoimmune hepatitis.

Liver T1 has been shown to provide a marker of liver disease due to increases in extracellular tissue fluid that occurs in response to inflammation and fibrosis, this had a low annual variance of CoV_T of 2.5% across the 3-year follow-up period in HVs and 4.2% in CC, with a RCV < 7%. Using LiverMultiScan® in a noncirrhotic population, Harrison et al. [10] showed a similar liver T1 CoV_T of 2.3% over an 18-week period. Renal cortex T1, which has been shown to decrease in cirrhosis, and spleen T1 was also consistent over the 3-year period, with a CoVT of 3.6 and 2.8%, and resulting into a RCV < 7%. It should be noted that here we have a fat-suppressed inversion recovery

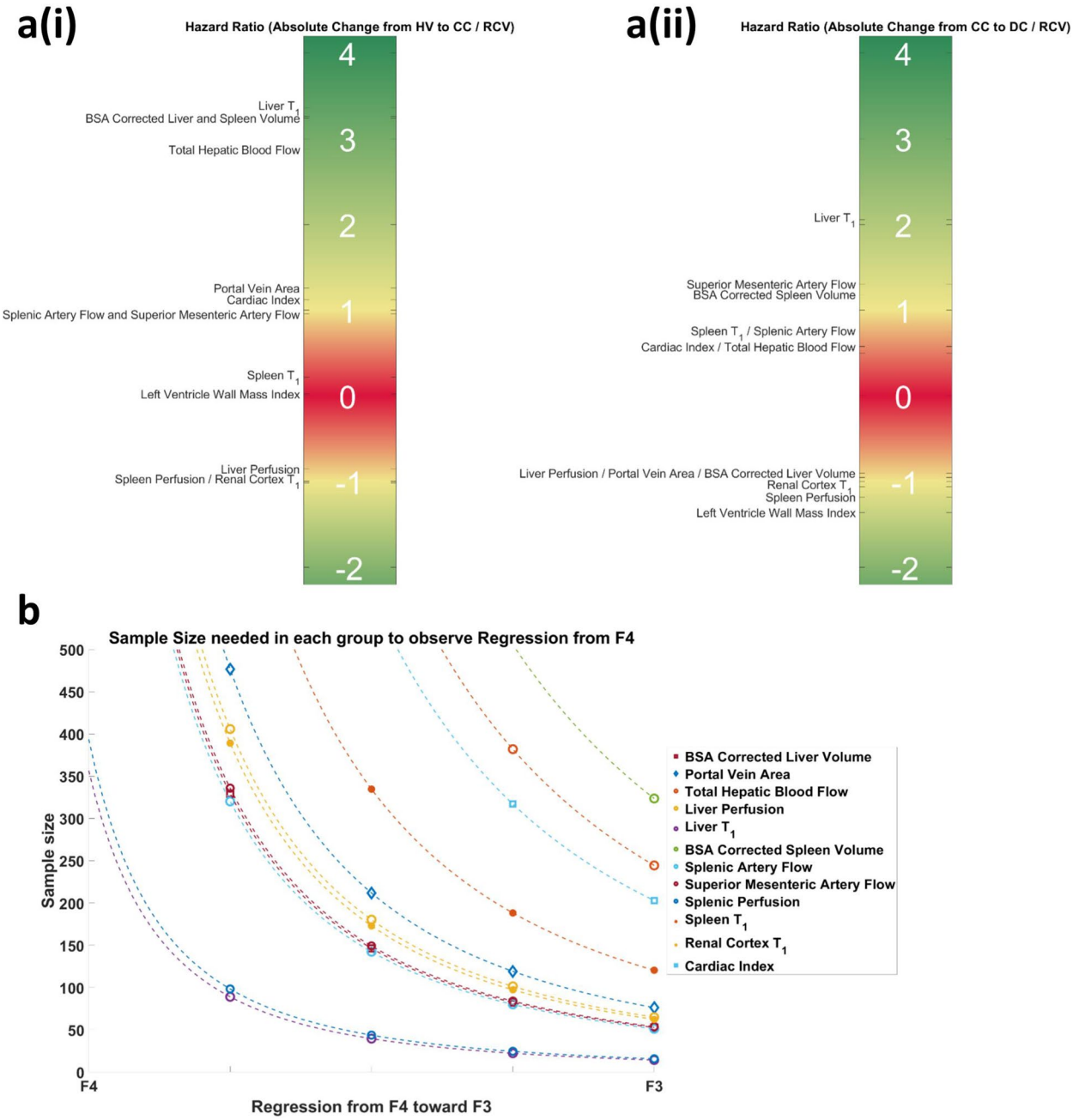

Fig. 7 A schematic of the hazard ratio (HR) for disease progression. Panel **a** (i) shows the progression from healthy volunteer (HV) to compensated cirrhosis (CC), whilst panel **a** (ii) shows that the hazard ratio for progression from CC to decompensated cirrhosis (DC). Positive values indicate an increase in measure and negative values a decrease in measures. If the absolute value of the HR is >1 this indicates the reference change value (RCV) is less than the clinical change. Panel **b** shows sample size estimation for the number of CC patients required in clinical trial to detect a change from stage F4 (compensated cirrhosis, CC) to F3 (advanced cirrhosis) liver disease which has clinical significance; data points are shown for a 25%, 50%, 75%, and 100% regression from F4 to F3. *BSA* Body surface area

spin-echo echo-planar imaging scheme for T1 mapping rather than a modified Look-Locker inversion recovery, MOLLI, scheme, as the former is not confounded by the effect of iron, fat, and frequency offsets [35]. These measures can be compared to the use of gadolinium ethoxybenzyl-diethylenetriaminepentaacetic acid, Gd-EOB-DTPA, pre- and postcontrast images to assess liver function and the degree of liver fibrosis, where a CoV of

7.1% has been reported in cirrhotic patients [36]. However, it should be also noted that the absence of both previous reaction to MRI contrast media and renal failure is necessary to undergo this contrast-enhanced T1 relaxometry.

The CoV_T of haemodynamic measures, which fluctuate with daily physiology, were higher than structural measures, with RCVs of 20–30% for vessel measures and ~50% for organ perfusion. We have previously shown the within-session analytical CoV of phase-contrast MRI measurements of hepatic and splanchnic flow to be 10% [10], and that the RCV includes the biological variation and differences in scan planning. Of note, hepatic and splenic artery flow measurements appear least consistent likely due to the increased difficulty in identifying and planning of these vessels. Here we use a flow alternating inversion recovery-based ASL scheme, which labels both blood from the hepatic artery and portal vein, and accounts for measured T1 in perfusion quantification. The values measured are similar to those reported in dynamic contrast-enhanced studies which show liver perfusion parameters to have a CoV of 39% 1 week apart [37].

The HR plots highlight that those measures which best detect clinical change are liver T1, BSA-corrected liver and spleen volume and total hepatic blood flow for progression from HV to CC, whilst liver T1 and LV wall mass best detected the evolution of CC into DC. Portal vein area and liver volume MRI measures increased from a healthy state to CC, and then decreased as DC occurs, so particular care should be taken when assessing these measures as a reduction in a marker could simultaneously indicate progression or regression. However, these markers used in combination with markers that progress/regress linearly could help provide better individual patient care.

New drugs are now becoming available to study CC regression/nonprogression [38], and here we showed those MRI measures suited to monitor such changes in clinical trials, with liver T1, spleen and liver volume and portal volume being the best candidates.

The main limitations of our study relate to the relatively low sample size and the dropout of patients through the follow-up period. As with all longitudinal studies, we encountered patient attrition which resulted in fewer patients at the end of the study. However, this is the first prospective study to attempt to specifically address the question of the biological variation in non-invasive markers in cirrhosis.

In conclusion, we provided the CoV_G, CoV_T, and RCV for clinical and MRI measures in stable CC patients. This is the first time that detailed serial non-invasive MRI measures have been reported. The RCVs can be used to interpret the change in measures in CC patients. We have used these to estimate sample size to power future clinical trials of cirrhosis regression using multiparametric MRI measures.

Abbreviations

APRI: Aspartate aminotransferase to platelet ratio index; ASL: Arterial spin labelling; BMI: Body mass index; BSA: Body surface area; CC: Compensated cirrhosis; CoV: Coefficient of variation; CoV_A: Analytical coefficient of variation; CoV_G: Groupwise coefficient of variation; CoV_T: Coefficient of Variation across time; DC: Decompensated cirrhosis; ELF: Enhanced liver fibrosis; FIB4: Fibrosis-4; HR: Hazard ratio; HV: Healthy volunteer; IQR: Interquartile range; LSM: Liver stiffness measure; LV: Left ventricle; MELD: Model for end stage liver disease; MRI: Magnetic resonance imaging; mpMRI: Multiparametric MRI; NAFLD: Non-alcoholic fatty liver disease; RCV: Reference change value; UKELD: United Kingdom model for end-stage liver disease.

Acknowledgements

We would like to thank the NIHR Nottingham BRC research nurses, including Antonella Ghezzi, Andrea Bennett, Tracey Wildsmith, and Louise James who conducted patient enrolment and performed clinical measures.

Authors' contributions

CRB (acquisition, analysis, and interpretation of data, statistical analysis, drafting of the manuscript), EFC (acquisition, analysis, and interpretation of data, statistical analysis, drafting of the manuscript), NP (interpretation of data, statistical analysis, drafting of the manuscript), GPA (critical revision of manuscript), STF (acquisition, analysis, study concept and design, interpretation of data, statistical analysis, drafting of the manuscript), and ING (study concept and design, interpretation of data, statistical analysis, drafting of the manuscript). The author(s) read and approved the final manuscript.

Funding

This research was funded by the NIHR Nottingham Biomedical Research Centre and carried out at/supported by the NIHR Nottingham Clinical Research Facilities. The views expressed are those of the author(s) and not necessarily those of the NHS, the NIHR or the Department of Health and Social Care.

Availability of data and materials

The data supporting the findings of this research can be requested by approaching the corresponding author.

Declarations

Ethics approval and consent to participate

Institutional and local research approval was gained by the UK National Research Ethics Service. Patients and healthy volunteers gave signed written informed consent to take part in this research study according to institutional and local research ethics committee approval (10/H0403/10).

Consent for publication

All patients gave written informed consent to publish the results of data collected during this research study.

Competing interests

The authors declare that they have no competing interests.

Author details

[1]NIHR Nottingham Biomedical Research Centre, Nottingham University Hospitals NHS Trust and the University of Nottingham, Nottingham, UK. [2]Sir Peter Mansfield Imaging Centre, School of Physics and Astronomy, University of Nottingham, Nottingham, UK. [3]Nottingham Digestive Diseases Centre, School of Medicine, University of Nottingham, Nottingham, UK.

Received: 8 May 2022 Accepted: 4 August 2022
Published online: 24 October 2022

References

1. Moreno C, Mueller S, Szabo G (2019) Non-invasive diagnosis and biomarkers in alcohol-related liver disease. J Hepatol 70:273–283. https://doi.org/10.1016/J.JHEP.2018.11.025

2. Vilar-Gomez E, Chalasani N (2018) Non-invasive assessment of non-alcoholic fatty liver disease: Clinical prediction rules and blood-based biomarkers. J Hepatol 68:305–315. https://doi.org/10.1016/J.JHEP.2017.11.013
3. Castera L, Friedrich-Rust M, Loomba R (2019) Noninvasive assessment of liver disease in patients with nonalcoholic fatty liver disease. Gastroenterology 156:1264–1281.e4. https://doi.org/10.1053/J.GASTRO.2018.12.036
4. Li Y, Huang YS, Wang ZZ et al (2016) Systematic review with meta-analysis: the diagnostic accuracy of transient elastography for the staging of liver fibrosis in patients with chronic hepatitis B. Aliment Pharmacol Ther 43:458–469. https://doi.org/10.1111/APT.13488
5. Jayaswal ANA, Levick C, Selvaraj EA et al (2020) Prognostic value of multiparametric magnetic resonance imaging, transient elastography and blood-based fibrosis markers in patients with chronic liver disease. Liver Int 40:3071–3082. https://doi.org/10.1111/LIV.14625
6. Vergniol J, Foucher J, Terrebonne E et al (2011) Noninvasive tests for fibrosis and liver stiffness predict 5-year outcomes of patients with chronic hepatitis C. Gastroenterology 140:1970–1979.e3. https://doi.org/10.1053/J.GASTRO.2011.02.058
7. Angulo P, Bugianesi E, Bjornsson ES et al (2013) Simple noninvasive systems predict long-term outcomes of patients with nonalcoholic fatty liver disease. Gastroenterology 145:782–789.e4. https://doi.org/10.1053/J.GASTRO.2013.06.057
8. Parkes J, Roderick P, Harris S et al (2010) Enhanced liver fibrosis test can predict clinical outcomes in patients with chronic liver disease. Gut 59:1245–1251. https://doi.org/10.1136/GUT.2009.203166
9. Bloom S, Kemp W, Nicoll A et al (2018) Liver stiffness measurement in the primary care setting detects high rates of advanced fibrosis and predicts liver-related events in hepatitis C. J Hepatol 69:575–583. https://doi.org/10.1016/J.JHEP.2018.04.013
10. Bradley CR, Cox EF, Scott RA et al (2018) Multi-organ assessment of compensated cirrhosis patients using quantitative magnetic resonance imaging. J Hepatol 69:1015–1024. https://doi.org/10.1016/J.JHEP.2018.05.037
11. Hoad CL, Palaniyappan N, Kaye P et al (2015) A study of T1 relaxation time as a measure of liver fibrosis and the influence of confounding histological factors. NMR Biomed 28:706–714. https://doi.org/10.1002/NBM.3299
12. Iwakiri Y, Groszmann RJ (2006) The hyperdynamic circulation of chronic liver diseases: From the patient to the molecule. Hepatology 43:S121–S131
13. Møller S, Henriksen JH (2009) Cardiovascular complications of cirrhosis. Postgrad Med J 85:44–54. https://doi.org/10.1136/gut.2006.112177
14. Schrier RW, Arroyo V, Bernardi M et al (1988) Peripheral arterial vasodilation hypothesis: a proposal for the initiation of renal sodium and water retention in cirrhosis. Hepatology 8:1151–1157. https://doi.org/10.1002/HEP.1840080532
15. Istaces N, Gulbis B (2015) Study of FibroTest and hyaluronic acid biological variation in healthy volunteers and comparison of serum hyaluronic acid biological variation between chronic liver diseases of different etiology and fibrotic stage using confidence intervals. Clin Biochem 48:652–657. https://doi.org/10.1016/J.CLINBIOCHEM.2015.03.020
16. Rossi E, Adams LA, Ching HL et al (2013) High biological variation of serum hyaluronic acid and hepascore, a biochemical marker model for the prediction of liver fibrosis. Clin Chem Lab Med 51:1107–1114. https://doi.org/10.1515/CCLM-2012-0584/MACHINEREADABLECITATION/RIS
17. Jabor A, Kubíček Z, Fraňková S et al (2018) Enhanced liver fibrosis (ELF) score: reference ranges, biological variation in healthy subjects, and analytical considerations. Clin Chim Acta 483:291–295. https://doi.org/10.1016/J.CCA.2018.05.027
18. Trivedi PJ, Muir AJ, Levy C et al (2021) Inter- and intra-individual variation, and limited prognostic utility, of serum alkaline phosphatase in a trial of patients with primary sclerosing cholangitis. Clin Gastroenterol Hepatol 19:1248–1257. https://doi.org/10.1016/J.CGH.2020.07.032
19. Nascimbeni F, Lebray P, Fedchuk L et al (2015) Significant variations in elastometry measurements made within short-term in patients with chronic liver diseases. Clin Gastroenterol Hepatol 13:763–771.e6. https://doi.org/10.1016/J.CGH.2014.07.037
20. Harrison SA, Dennis A, Fiore MM et al (2018) Utility and variability of three non-invasive liver fibrosis imaging modalities to evaluate efficacy of GR-MD-02 in subjects with NASH and bridging fibrosis during a phase-2 randomized clinical trial. PLoS One 13:e0203054. https://doi.org/10.1371/JOURNAL.PONE.0203054
21. Cirrhosis in over 16s: assessment and management. NICE guideline NG50. https://www.nice.org.uk/guidance/ng50.
22. Palaniyappan N, Cox E, Bradley C et al (2016) Non-invasive assessment of portal hypertension using quantitative magnetic resonance imaging. J Hepatol 65:1131–1139. https://doi.org/10.1016/J.JHEP.2016.07.021
23. Gardener AG, Francis ST (2010) Multislice perfusion of the kidneys using parallel imaging: image acquisition and analysis strategies. Magn Reson Med 63:1627–1636. https://doi.org/10.1002/MRM.22387
24. Cox EF, Buchanan CE, Bradley CR et al (2017) Multiparametric renal magnetic resonance imaging: validation, interventions, and alterations in chronic kidney disease. Front Physiol 8:696. https://doi.org/10.3389/FPHYS.2017.00696/BIBTEX
25. Natori S, Lai S, Finn JP et al (2006) Cardiovascular function in multi-ethnic study of atherosclerosis: normal values by age, sex, and ethnicity. AJR Am J Roentgenol 186. https://doi.org/10.2214/AJR.04.1868
26. Buxton RB, Frank LR, Wong EC et al (1998) A general kinetic model for quantitative perfusion imaging with arterial spin labeling. Magn Reson Med 40:383–396. https://doi.org/10.1002/MRM.1910400308
27. Fahim MA, Hayen AD, Horvath AR et al (2015) Biological variation of high sensitivity cardiac troponin-T in stable dialysis patients: Implications for clinical practice. Clin Chem Lab Med 53:715–722. https://doi.org/10.1515/CCLM-2014-0838/MACHINEREADABLECITATION/RIS
28. Selvaraj EA, Mózes FE, Jayaswal ANA et al (2021) Diagnostic accuracy of elastography and magnetic resonance imaging in patients with NAFLD: a systematic review and meta-analysis. J Hepatol 75:770–785. https://doi.org/10.1016/J.JHEP.2021.04.044/ATTACHMENT/57673770-93F5-4735-AE87-FED4DA98ED9C/MMC3.PDF
29. Vali Y, Lee J, Boursier J et al (2020) Enhanced liver fibrosis test for the non-invasive diagnosis of fibrosis in patients with NAFLD: A systematic review and meta-analysis. J Hepatol 73:252–262. https://doi.org/10.1016/J.JHEP.2020.03.036/ATTACHMENT/CEF13473-AF0E-4523-9A59-1913BBBDB1FB/MMC3.PDF
30. Bachtiar V, Kelly MD, Wilman HR et al (2019) Repeatability and reproducibility of multiparametric magnetic resonance imaging of the liver. PLoS One 14. https://doi.org/10.1371/JOURNAL.PONE.0214921
31. Jayakumar S, Middleton MS, Lawitz EJ et al (2019) Longitudinal correlations between MRE, MRI-PDFF, and liver histology in patients with non-alcoholic steatohepatitis: analysis of data from a phase II trial of selonsertib. J Hepatol 70:133–141. https://doi.org/10.1016/J.JHEP.2018.09.024
32. Kamath PS, Mookerjee RP (2015) Expanding consensus in portal hypertension: Report of the Baveno VI Consensus Workshop: Stratifying risk and individualizing care for portal hypertension. J Hepatol 63:743–752. https://doi.org/10.1016/J.JHEP.2015.05.022
33. Siddiqui MS, Yamada G, Vuppalanchi R et al (2019) Diagnostic accuracy of noninvasive fibrosis models to detect change in fibrosis stage. Clin Gastroenterol Hepatol 17:1877–1885.e5. https://doi.org/10.1016/J.CGH.2018.12.031
34. Hartl J (2020) Liver stiffness in autoimmune hepatitis. In: Liver elastography: clinical use and interpretation, pp 181–186. https://doi.org/10.1007/978-3-030-40542-7_16
35. Mozes FE, Tunnicliffe EM, Moolla A et al (2019) Mapping tissue water T1 in the liver using the MOLLI T1 method in the presence of fat, iron and B0 inhomogeneity. NMR Biomed 32:e4030. https://doi.org/10.1002/NBM.4030
36. Choi JY, Kim H, Sun M, Sirlin CB (2014) Histogram analysis of hepatobiliary phase MR imaging as a quantitative value for liver cirrhosis: preliminary observations. Yonsei Med J 55:651. https://doi.org/10.3349/YMJ.2014.55.3.651
37. Galbraith SM, Lodge MA, Taylor NJ et al (2002) Reproducibility of dynamic contrast-enhanced MRI in human muscle and tumours: comparison of quantitative and semi-quantitative analysis. NMR Biomed 15:132–142. https://doi.org/10.1002/NBM.731
38. Sanyal AJ, Anstee QM, Trauner M et al (2022) Cirrhosis regression is associated with improved clinical outcomes in patients with nonalcoholic steatohepatitis. Hepatology 75:1235–1246. https://doi.org/10.1002/HEP.32204

Publisher's Note

9.3 Publication III: Bradley CR, Scott RA, Cox E, Palaniyappan N, Thomson BJ, Ryder SD, Irving WL, Aithal GP, Guha IN, Francis S. Short-term changes observed in multiparametric liver MRI following therapy with direct-acting antivirals in chronic hepatitis C virus patients. European Radiology. 2019 Jun;29(6):3100-7.

European Radiology (2019) 29:3100–3107
https://doi.org/10.1007/s00330-018-5788-1

GASTROINTESTINAL

Short-term changes observed in multiparametric liver MRI following therapy with direct-acting antivirals in chronic hepatitis C virus patients

C. Bradley[1,2] · R. A. Scott[2] · E. Cox[1,2] · N. Palaniyappan[2] · B. J. Thomson[2] · S. D. Ryder[2] · W. L. Irving[2] · G. P. Aithal[2,3] · I. N. Guha[2,3] · S. Francis[1,2]

Received: 11 July 2018 / Revised: 4 September 2018 / Accepted: 21 September 2018 / Published online: 30 November 2018

Abstract

Methods We applied multiparametric MRI to assess changes in liver composition, perfusion and blood flow in 17 patients before direct-acting antiviral (DAA) therapy and after treatment completion (within 12 weeks of last DAA tablet swallowed).

Results We observed changes in hepatic composition indicated by a reduction in both liver longitudinal relaxation time (T1, 35 ± 4 ms), transverse relaxation time (T2, 2.5 ± 0.8 ms; T2* 3.0 ± 0.7 ms), and liver perfusion (28.1 ± 19.7 ml/100 g/min) which we suggest are linked to reduced pro-inflammatory milieu, including interstitial oedema, within the liver. No changes were observed in liver or spleen blood flow, splenic perfusion, or superior mesenteric artery blood flow.

Conclusion For the first time, our study has shown that treatment of HCV with DAAs in patients with cirrhosis leads to an acute reduction in liver T1, T2 and T2* and an increase in liver perfusion measured using MR parameters. The ability of MRI to characterise changes in the angio-architecture of patients with cirrhosis after intervention in the short term will enhance our understanding of the natural history of regression of liver disease and potentially influence clinical decision algorithms.

Key Points

- *DAAs have revolutionised the treatment of hepatitis C and achieve sustained virological response in over 95% of patients, even with liver cirrhosis.*
- *Currently available non-invasive measures of liver fibrosis are not accurate after HCV treatment with DAAs, this prospective single-centre study has shown that MRI can sensitively measure changes within the liver, which could reflect the reduction in inflammation with viral clearance.*
- *The ability of MRI to characterise changes in structural and haemodynamic MRI measures in the liver after intervention will enhance our understanding of the progression/regression of liver disease and could potentially influence clinical decision algorithms.*

Keywords Hepatitis C · Magnetic resonance imaging · Echo-planar imaging · Sustained virologic response

C. Bradley and R. A. Scott are joint first authors.

✉ S. Francis
susan.francis@nottingham.ac.uk

[1] Sir Peter Mansfield Imaging Centre, School of Physics and Astronomy, University of Nottingham, Nottingham, UK

[2] NIHR Nottingham Biomedical Research Centre, Nottingham University Hospitals NHS Trust and the University of Nottingham, Nottingham, UK

[3] Nottingham Digestive Diseases Centre, School of Medicine, the University Of Nottingham, Nottingham, UK

Abbreviations

DAAs	Direct-acting antiviral treatments
HCV	Hepatitis C virus
HVPG	Hepatic venous portal gradient
NHS	National Health Service
SVR	Sustained virological response

Introduction

Globally, chronic hepatitis C virus (HCV) infection is estimated to affect 71 million people [1]. Direct-acting antivirals

(DAAs) have revolutionised HCV treatment, with sustained virological response (SVR) rates approaching 100% in compensated cirrhosis [2–4], emerging data suggesting excellent SVR in decompensated liver disease [5, 6]. Despite high SVR rates, there is an incomplete understanding of the effect of viral clearance on the liver in the context of DAA therapy. The progression or regression of fibrosis and/or portal hypertension caused by DAA therapy could have implications for each patient wider than chronic HCV management alone. Potential changes include those reflecting liver composition, including volume, inflammation and fibrosis; and hepatosplanchnic haemodynamic changes, including liver perfusion and blood flow.

Improvement in clinical outcomes following HCV eradication with treatment regimens of pegylated interferon and ribavirin is established; large cohort studies show differences in liver decompensation rates between SVR and non-SVR groups: hazard ratio (HR) 0.24 (95% CI 0.14–0.42), $p < 0.001$ [7]; HR 0.26 (95% CI 0.17–0.39), $p < 0.001$ [8]; and HR 0.15 (95% CI 0.06–0.38), $p = 0.04$ [9]. Assessment by invasive liver biopsy in HCV patients with established cirrhosis has shown regression of cirrhosis in 61% and reduction of collagen in 89% of patients at 61 months following an SVR [10]. Further studies using liver biopsy have shown cirrhosis regression rates of 46 to 75% after 3–10 years [11–14]. Although promising, regression was not ubiquitous nor studied in those with the most advanced liver disease due to the known risks of treatment with interferon and ribavirin. It remains unproven whether the regression seen was due to selection bias of those who achieved SVR, aviraemia or an immunomodulatory effect of the interferon itself [15]. Hepatic venous pressure gradient (HVPG), an invasive measure of portal hypertension, also improves with SVR [16–18]. Together, this published data builds a strong case for the concept of regression.

However, individual and invasive techniques for measuring fibrosis and portal hypertension respectively do not assess the complex pathophysiological changes associated with progression and regression of chronic liver injury. Furthermore, ethical and practical constraints limit serial liver biopsy sampling with DAA therapy. A multicentre prospective study, with paired invasive HVPG and non-invasive transient elastography (TE), demonstrated DAA therapy significantly reduced HVPG, but patients continued to have clinically significant portal hypertension and remained at risk of decompensation [19]. Currently available clinical non-invasive markers, including TE, overestimate regression compared to biopsy after SVR [19, 20]. In an era of novel antifibrotic therapy on the horizon, robust non-invasive biomarkers for use in advanced liver disease patients who receive DAA therapy to understand the structural and functional changes in the liver and stratify ongoing risk post SVR and focus interventions are required.

Non-invasive, contrast agent-free, quantitative multiparametric magnetic resonance imaging (MRI) provides the opportunity to assess liver composition (volume, fibrosis/inflammation) and haemodynamics (liver tissue perfusion, blood flow) in a single scan session (< 40 min). Longitudinal relaxation time (T_1) of liver tissue is validated against inflammation/fibrosis on liver biopsy [21–23], and MRI measurements also closely correlate with the invasive HVPG measurement [24]. Inflammation lengthens hepatic transverse relaxation time (T_2) in liver disease [25–27]. More recently, specific MR liver biomarkers, including liver T_1 and liver perfusion, predicted clinical outcomes [28, 29].

Here, we collect quantitative MRI data in patients with liver cirrhosis who underwent DAA therapy from the NHS England expanded access programme [5]. This study describes the early changes in structural and haemodynamic MRI measures in the liver between baseline (pre-treatment) and follow-up to SVR (immediately post-treatment) at a 3–6-month time window following the start of DAA therapy, in patients with advanced end-stage liver disease.

Methods

In this prospective, observational study, patients were recruited through the NHS England expanded access programme, established to prioritise treatment for patients with greatest clinical priority, including compensated and decompensated liver disease. Treatment was with sofosbuvir plus, by clinician choice, ledipasvir or daclatasvir, with or without ribavirin [5, 30]. The study received ethical approval from the NRES Committee East Midlands - Derby 1 (Research Ethics Committee reference 11/EM/0314). Once enrolled in the study, if a subject did not attend a study visit after treatment, they were sent a letter and telephoned twice by the research team and withdrawn from the study if uncontactable.

Patients underwent a detailed MRI study before DAA therapy and after treatment completion (within 12 weeks of last DAA tablet swallowed). Patients followed standard management protocols for DAA therapy and monitoring. Routine clinical information including medical history, clinical examination and laboratory values were recorded for each participant. Laboratory values were used to calculate validated scores of ALT, Fib4 [25] and APRI [26] using freely available online calculators.

MRI measures

MRI data were acquired on a 1.5-T Philips Achieva scanner (Philips Healthcare Systems) in a single 40-min scan session using methods described in [21]. Subjects were scanned feet first supine after an overnight fast, using a body transmit and 16-element SENSEXL torso coil. The MRI protocol comprised a series of non-invasive measures to assess liver

composition and haemodynamics. Multislice balanced fast field echo (bFFE) images were initially acquired in three orthogonal planes (35 slices of 1.75 × 1.75 × 7 mm^3 resolution, single breath holds per orientation) to locate the liver and vessels of interest and to estimate liver volume.

Liver composition

Liver T_1, T_2 and T_2* were mapped in nine axial slices through the liver (field of view (FOV) 288 × 288 mm^2, voxel size 3 × 3 × 8 mm^3, 4-mm slice spacing). A modified respiratory-gated inversion recovery sequence with a fat-suppressed spin echo echo-planar imaging (SE-EPI) readout scheme was used to measure liver T_1 [22, 27, 28] (inversion times for first SE-EPI image slice were 100–1000 ms in 100-ms increments). For all inversion times, SE-EPI imaging slices were collected at end expiration such that the first slice was collected at 1500 ms after the respiratory trigger with subsequent slices collected with a 65-ms temporal slice spacing. The T_1 mapping sequence was acquired with slices collected in ascend and descend slice ordering to increase the dynamic range of inversion times. In total, 20 inversion times were acquired in < 3 min. A respiratory-gated SE-EPI sequence was used to map liver T_2 comprising six echo times (TE = 27, 35, 42, 50, 60, 70 ms) in approximately 2 min. T_2* mapping was collected using a multiecho fast field echo (mFFE) sequence comprising 12 echo times (TE_1 = 5 ms, ΔTE = 2.5 ms) acquired in a ~ 17-s breath hold. T_2 and T_2* datasets were geometrically matched to the T_1 dataset.

In-house software was used to create T_1, T_2 and T_2* maps (MATLAB, The MathWorks Inc.). Prior to data fitting, images affected by motion (due to missing the respiratory trigger) were discarded. To create T_1 and M_0 maps, data at the 20 inversion times were fit using a voxel-by-voxel two-parameter fit. For T_2 and T_2* mapping, a voxel-by-voxel log-linear least-squares method was used to fit the echo intensities to create T_2 and T_2* maps. To assess the quantitative T_1, T_2 and T_2* maps, a region of interest covering the liver was selected and a histogram of values within computed. A Gaussian curve was fitted to the histogram to determine the mode of the T_1, T_2 and T_2* distribution within the liver; this procedure excludes regions where vessels are visible within the liver.

Blood flow

Phase contrast (PC)-MRI assessed blood flow through vessels in the hepatic circulation (portal vein, hepatic artery) as well as vessels critically related to portal hypertension (splenic artery, right renal artery, superior mesenteric artery (SMA)) with reconstructed voxel size of 1.17 × 1.17 × 6 mm^3 [22]. PC-MRI was performed using a single slice turbo field echo (TFE); slice was placed perpendicular to each vessel. Fifteen phases were collected across the cardiac cycle for the portal vein, 20 phases for all other vessels, with velocity encoding in the portal vein of 50 cm/s, in the hepatic, splenic, renal arteries 100 cm/s, and 140 cm/s in the SMA. Each measurement was acquired in a single < 20-s breath hold. Using Q-flow software (Philips Medical Systems), mean artery cross-sectional area (mm^2), mean velocity (cm/s), and hence mean bulk flow (ml/s) over the cardiac cycle were calculated for each vessel.

Liver perfusion

Respiratory-triggered flow-sensitive alternating inversion recovery arterial spin labelling (FAIR-ASL) data (288 × 288 mm^2 field of view, 3 × 3 × 8 mm^3 voxel, 3 sagittal slices, slice gap 5 mm) were collected with a balanced fast field echo (bFFE) readout in approximately 5 min. A base (M_0) equilibrium scan and T_1 map were also acquired for quantification of hepatic tissue perfusion using a kinetic model. In-house software was used to motion correct the images and perform automatic outlier rejection of images affected by movement prior to quantification of tissue perfusion [29].

Statistical analysis

Statistical analysis was performed with *GraphPad Prism7* software. Continuous variables are expressed as mean ± standard deviation for normal data otherwise median (interquartile range), while categorical variables are reported as number of patients with (proportion of patients with) the certain characteristic.

Paired Student's *t* test is used for comparisons between pre- and post-treatments for normally distributed data and Wilcoxon matched pairs signed-rank test when not normally distributed. All statistical analysis is Bonferroni corrected for multiple comparisons.

Repeatability of multiparametric MRI measures

To determine between session repeatability of MRI measures, the intra-subject coefficient of variation (CoV) (defined as the standard deviation/mean) of multiparametric MRI measures was assessed. A subset of ten healthy participants (age 23–37 years, body mass index 20–26 kg/m^2) had three scans, at least 1 week apart and within 4 weeks, at the same time of day and after an overnight fast to limit diurnal and dietary variability. This healthy participant study was approved by the University of Nottingham Ethics committee.

Results

Seventeen HCV patients with advanced liver disease underwent DAA therapy within 1 week of their pre-treatment MRI scan (Table 1). Patients returned for their

Table 1 Pre-treatment characteristics of the 17 hepatitis C virus patients consented to this study

Demographic table	
Variable	All patients
Age, mean (SD)	53 (8)
Male (%)	14 (82%)
Transplant (%)	3 (18%)
Cirrhosis (%)	15 (88%)
MELD (IQR)	8 (7–8.25)
Compensated (%)	7 (41%)
Decompensated (%)	8 (47%)
Previous variceal haemorrhage	4 (23%)
Ascites	2 (12%)
Jaundice	2 (12%)
Diabetes (%)	2 (12%)
Body mass index median (IQR)	25.6 kg/m^2(24.0–27.9)
HCV genotype	
1 (%)	9 (53%)
2 (%)	1 (6%)
3 (%)	7 (41%)

Table 2 Coefficient of variance of MRI measures

MRI Measure	CoV (%)
Liver volume	4.6
Liver T_1	1.5
Liver T_2	4.3
Liver T2*	3.7
Portal vein flow	13.6
Hepatic artery flow	22.7
Liver perfusion	12
Spleen volume	5.2
Spleen T_1	1.8
Splenic artery flow	11
SMA flow	7.6

post-treatment MRI scan at a median of 22 days (3–79 days) after the last DAA taken. Study demographics are provided in Table 1. Sixteen of 17 patients (94%) achieved SVR, defined as undetectable serum viral RNA 12 weeks after treatment completion. Validated serum clinical liver markers of ALT, Fib4 and APRI were collected at pre- and post-MRI time points. The majority of patients had significantly improved liver function test scores post-treatment compared to pre-treatment (Fig. 1), with a significant group reduction in ALT, Fib4 and APRI.

Table 2 shows that all MR volume and relaxometry measures had a CoV < 5%, and all haemodynamic measures < 15%, apart from hepatic artery blood flow. There were significant changes in the liver microstructure as assessed by MR relaxation times with DAA therapy, with a significant reduction in liver T_1, T_2 and T_2* after treatment; however, no change was observed in splenic T_1 (Fig. 2). Figure 3 shows the example of liver T_1, T_2 and T_2* maps pre- and post-DAA therapy. No significant differences were observed in liver or spleen volume. No significant changes were observed in any blood flow measure (hepatic artery, splenic artery, superior mesenteric artery or portal vein); however, there was an increase in liver perfusion following DAA therapy (Fig. 4). Paired perfusion data is presented for $n = 9$ participants, all of whom achieved SVR. The remaining subjects had inadequate paired data due to insufficient anatomical matching between visits.

Discussion

Using multiparametric MRI in patients with HCV-related cirrhosis pre- and post-DAA therapy, we have demonstrated significant changes in the liver composition (T_1, T_2 and T_2*) and haemodynamics over a short time period following clearance of HCV infection. We did not observe any changes in bulk hepatic or splanchnic blood flow in the short time frame between MRI scans.

To our knowledge, this is the first study to document changes in MR parameters following DAA therapy. Few previous studies have assessed the effect of HCV treatment on MRI measures. One previous study assessed the effect of HCV treatment (pegylated interferon, ribavirin, telaprevir) on liver diffusion, demonstrating reduced liver apparent diffusion coefficient suggested to be associated with ultrastructural changes such as cell necrosis/apoptosis and inflammatory cell infiltration [31]. A recent study showed a small increase in liver volume following antiviral treatment, which was larger

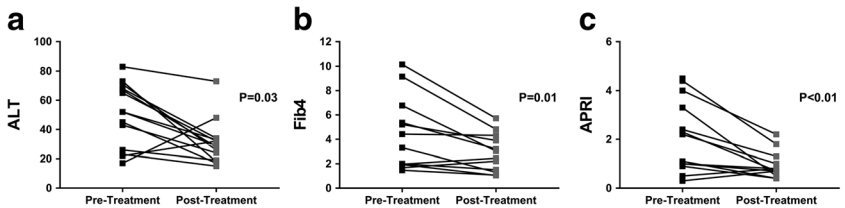

Fig. 1 Liver function test markers of all 17 participants (16 of whom achieved SVR) pre-treatment and post-treatment. **a** A significant reduction in ALT of 54 ± 25. **b** Fib4 reduced by 1.6 ± 0.5.**c** APRI score showed a significant reduction of 31.0 ± 0.3

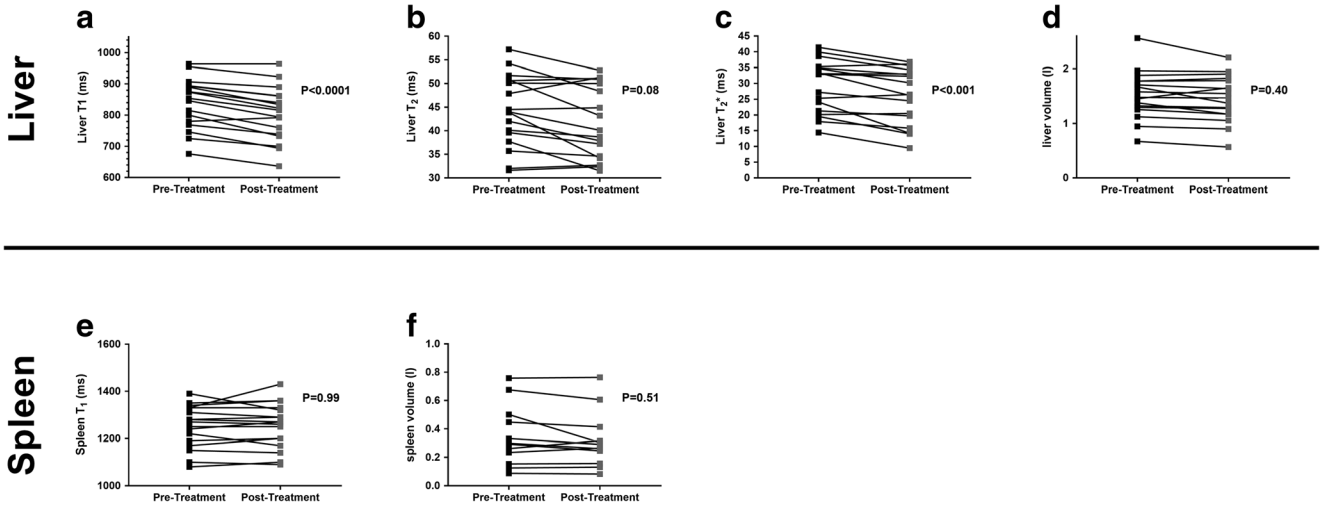

Fig. 2 Post-treatment with DAA therapy showed (**a**) a reduction in liver T_1 of 35 ± 4 ms, (**b**) a reduction in liver T_2 of 2.5 ± 0.8 ms and (**c**) a reduction in liver T_2* by 3 ± 0.7 ms. **d**–**f** No significant difference is observed in spleen T_1, liver volume or spleen volume between pre- and post-DAA treatments

in patients with SVR [31], interpreted to indicate liver regeneration and/or recovery and reduced fibrotic load of the liver.

The strengths of this current study are the prospective recruitment and phenotyping of the patients. The quantitative MRI parameters have previously been validated against "gold standard" measures including liver biopsy [19, 20] and HVPG [22]. More recently, specific MR liver biomarkers, including liver T_1, liver perfusion and haemodynamic measures, were associated with clinical outcomes in independent cohorts of patients [28, 29]. Liver T_1 acquisition and analysis have been shown to be highly repeatable [19], with an intra-subject CoV < 1.8% and a low inter- and intra-observer variability with intra-class correlation coefficient > 0.99 [22]. Here, we demonstrate the intra-subject variability in MR relaxation time is low, with a CoV of 1.5, 4.3 and 3.7% for liver T_1, T_2 and T_2* respectively, considerably lower than inter-subject variability. Capturing data pre- and post-treatment enables direct intra-individual comparisons, strengthening the validity of the data, since each subject is their own control. We show that in response to DAA therapy, the reduction in T_1 is more significant compared to that of T_2 and T_2*; this could be attributed to the smaller CoV. However, there is also variability within the literature in terms of a T_2 change, with pre-clinical models of liver fibrosis shown to result in an increase as well as decrease in T_2 [32]. It is hypothesised that increased T_2 is related to hepatic inflammation associated with the development of fibrosis or the proliferation of small biliary ducts in models of bile duct ligation [27].

The limitations of this study are the small sample size from a single UK centre, with some variation in patient disease

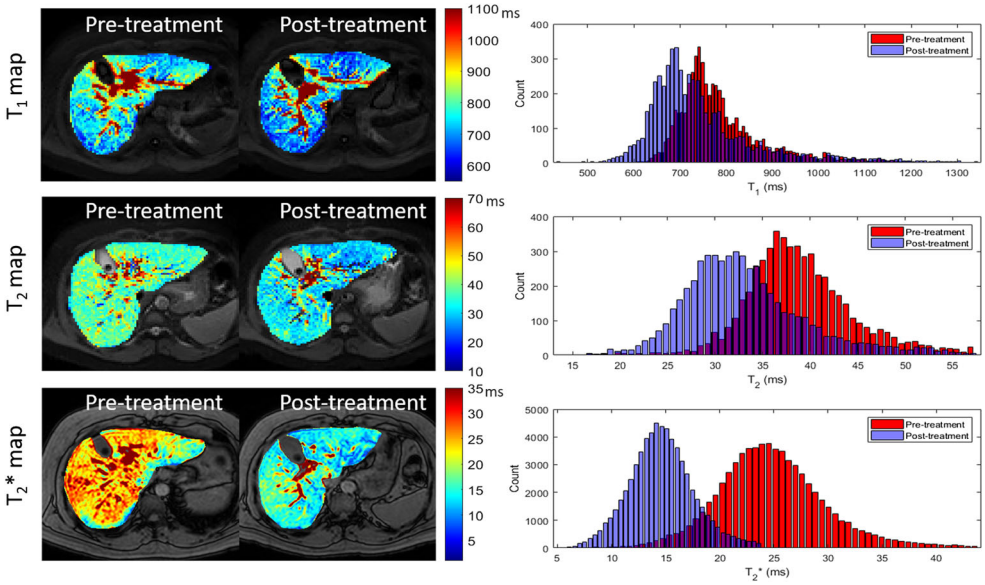

Fig. 3 Example axial T_1 map, T_2 map and T_2* map showing the liver pre- and post-DAA treatment

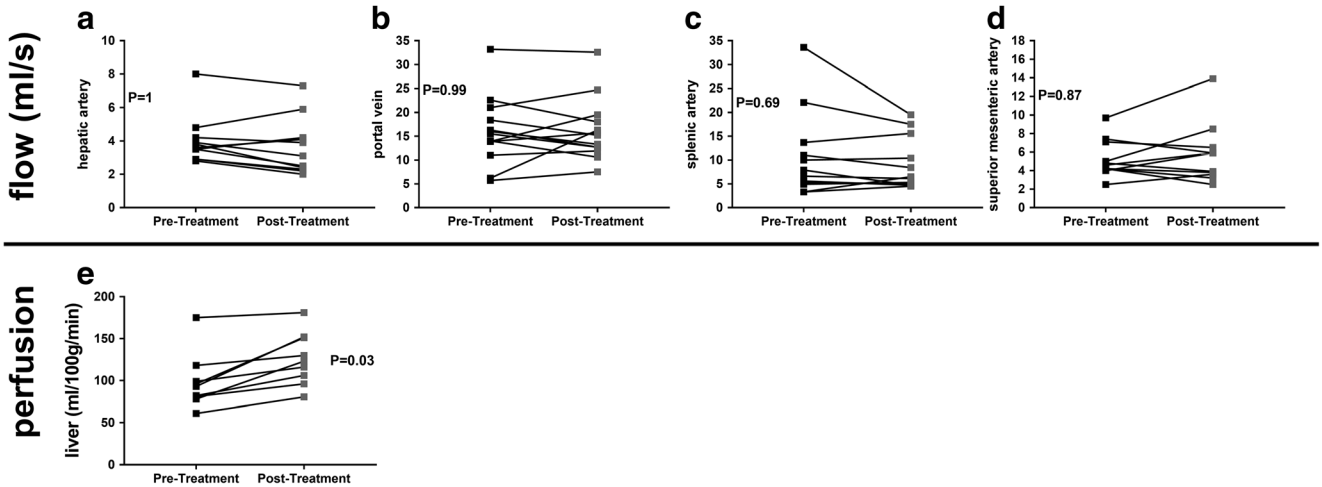

Fig. 4 Bulk flow to the liver in the (**b**) portal vein and (**a**) hepatic artery as well as (**d**) superior mesenteric and (**c**) splenic artery flow shows no significant changes between pre- and post-DAA therapies. **e** An increase in liver perfusion of mean change 28.1 ± 19.7 ml/100 g/min is observed following DAA therapy

severity. Due to practical constraints, we were unable to perform parallel invasive assessments of liver biopsy or HVPG. The timing of the MRI scans in close proximity to drug therapy enabled characterisation of changes at an early time point in subjects who achieve SVR at a later time point.

The observation that only few specific MR parameters changed in the study time period is relevant. Notwithstanding the possibility of type 1 and type 2 errors, the lack of significant changes in liver bulk blood flow potentially indicates the natural history of "regression". Reversal of fibrotic and vascular networks, which of course may be incomplete [33], is thought to occur over years. To date, there is limited data showing histological changes associated with DAA treatment in HIV coinfection [34] and post-transplant populations [35], both demonstrating a significant reduction in necroinflammation with SVR. It is widely recognised that both TE and serum markers of fibrosis are influenced by necroinflammation [20, 36–38]. Moreover, short-term studies have shown that TE dynamically changes during treatment with DAA therapy, and long-term studies have shown that both TE and serum fibrosis markers may overestimate regression in the long term [19, 33].

Pegylated interferon and ribavirin ameliorate portal hypertension in patients with HCV monoinfection [16–18] and HIV/HCV coinfection [39]. Multiple studies similarly show that DAA treatment results in statistically significant reductions in HVPG [19, 34, 40, 41] but interestingly may not alter clinically significant portal hypertension [19].

We speculate our key findings of reduced liver T_1, T_2 and T_2* and increased liver perfusion are linked by a reduction in the pro-inflammatory milieu within the liver, including interstitial oedema, aligned with a reduction in serum ALT. We hypothesise that DAA treatment reduces necroinflammation which may improve liver function over a longer period of time [30] and can be a treatment for portal hypertension provided treatment in the early stage of portal hypertension [19], and we believe this also underlies the reported change in TE [20]. A reduction in necroinflammation on liver biopsy in the short term, even when associated with a short duration of viral suppression using interferon-based treatment, has a positive impact on future clinical outcomes at 6 years and fibrosis regression [42]. Chronic inflammation might be expected to increase perfusion but is unknown in the context of advanced liver disease. A recent MRI study showed reduced perfusion is associated with progressive liver disease and linked to adverse outcomes [29], and CT has shown worsening perfusion with progressive fibrosis in HCV [43]. This is consistent with our finding of a significant increase in liver perfusion with the likely acute resolution of chronic necroinflammation after DAA treatment in advanced liver disease caused by HCV.

A multimodal technique including MRI that captures how the different aspects of liver composition, perfusion and blood flow change over time could provide additional confidence for clinical decision-making. In addition, robust non-invasive tests that are specific to the liver would be valuable to drug development for antifibrotic compounds as they can be repeated at multiple time points to evaluate drug efficacy. MRI has the potential to be a key non-invasive tool to evaluate the efficacy of interventions in chronic liver disease and stratify patients according to the potential clinical outcomes.

In summary, for the first time, our MRI study has shown that treatment of HCV with DAAs in patients with cirrhosis leads to an acute reduction in liver T_1, T_2 and T_2* and increase in liver perfusion measured. The ability of MRI to characterise changes in the angio-architecture of patients with cirrhosis after intervention at such short intervals will enhance our understanding of the progression/regression of chronic liver disease and potentially assist clinical decision-making. The sensitivity of these MR measures should be exploited to

accelerate early phase of clinical development of novel antifibrotic agents.

In future work, our intention is to use quantitative MRI measures to observe the long-term effects of DAA therapy on liver composition, perfusion and surrounding haemodynamics to characterise the extent of fibrosis regression, vascular remodelling and reduction in portal hypertension that may occur after DAA therapy. Furthermore, we aim to assess whether MRI changes correspond to, or are predictive of, histological regression of fibrosis, as described in long-term studies with interferon and ribavirin [10, 44, 45].

Funding The authors state that this work has received funding from the National Institute for Health Research (NIHR) Nottingham Biomedical Research Centre, Nottingham University Hospitals NHS Trust and University of Nottingham. The views expressed in this paper are those of the authors and not necessarily those of the NHS, the NIHR or the Department of Health.

Compliance with ethical standards

Guarantor The scientific guarantor of this publication is Professor Susan Francis.

Conflict of interest The authors of this manuscript declare no relationships with any companies, whose products or services may be related to the subject matter of the article.

Statistics and biometry No complex statistical methods were necessary for this paper.

Informed consent Written informed consent was obtained from all subjects (patients) in this study.

Ethical approval The HCV MRI study received ethical approval by the NRES Committee East Midlands - Derby 1 (Research Ethics Committee reference 11/EM/0314).

Methodology
- Prospective
- Observational
- Performed at one institution

References

1. Polaris Observatory HCV Collaborators (2017) Global prevalence and genotype distribution of hepatitis C virus infection in 2015: a modelling study. Lancet Gastroenterol Hepatol 2:161–176
2. Afdhal N, Zeuzem S, Kwo P et al (2014) Ledipasvir and sofosbuvir for untreated HCV genotype 1 infection. N Engl J Med 370:1889–1898
3. Poordad F, Hezode C, Trinh R et al (2014) ABT-450/r-ombitasvir and dasabuvir with ribavirin for hepatitis C with cirrhosis. N Engl J Med 370:1973–1982
4. Lawitz E, Sulkowski MS, Ghalib R et al (2014) Simeprevir plus sofosbuvir, with or without ribavirin, to treat chronic infection with hepatitis C virus genotype 1 in non-responders to pegylated interferon and ribavirin and treatment-naive patients: the COSMOS randomised study. Lancet 384:1756–1765
5. Foster GR, Irving WL, Cheung MC et al (2016) Impact of direct acting antiviral therapy in patients with chronic hepatitis C and decompensated cirrhosis. J Hepatol 64:1224–1231
6. Charlton M, Everson GT, Flamm SL et al (2015) Ledipasvir and sofosbuvir plus ribavirin for treatment of HCV infection in patients with advanced liver disease. Gastroenterology 149:649–659
7. Innes HA, McDonald SA, Dillon JF et al (2015) Toward a more complete understanding of the association between a hepatitis C sustained viral response and cause-specific outcomes. Hepatology 62:355–364
8. Nahon P, Bourcier V, Layese R et al (2017) Eradication of hepatitis C virus infection in patients with cirrhosis reduces risk of liver and non-liver complications. Gastroenterology 152:142–156 e142
9. Morgan TR, Ghany MG, Kim HY et al (2010) Outcome of sustained virological responders with histologically advanced chronic hepatitis C. Hepatology 52:833–844
10. D'Ambrosio R, Aghemo A, Rumi MG et al (2012) A morphometric and immunohistochemical study to assess the benefit of a sustained virological response in hepatitis C virus patients with cirrhosis. Hepatology 56:532–543
11. Pol S, Carnot F, Nalpas B et al (2004) Reversibility of hepatitis C virus-related cirrhosis. Hum Pathol 35:107–112
12. Mallet V, Gilgenkrantz H, Serpaggi J et al (2008) Brief communication: the relationship of regression of cirrhosis to outcome in chronic hepatitis C. Ann Intern Med 149:399–403
13. George SL, Bacon BR, Brunt EM, Mihindukulasuriya KL, Hoffmann J, Di Bisceglie AM (2009) Clinical, virologic, histologic, and biochemical outcomes after successful HCV therapy: a 5-year follow-up of 150 patients. Hepatology 49:729–738
14. Poynard T, McHutchison J, Manns M et al (2002) Impact of pegylated interferon alfa-2b and ribavirin on liver fibrosis in patients with chronic hepatitis C. Gastroenterology 122:1303–1313
15. Koretz RL, Lin KW, Ioannidis JP, Lenzer J (2015) Is widespread screening for hepatitis C justified? BMJ 350:g7809
16. Burroughs AK, Groszmann R, Bosch J et al (2002) Assessment of therapeutic benefit of antiviral therapy in chronic hepatitis C: is hepatic venous pressure gradient a better end point? Gut 50:425–427
17. Rincon D, Ripoll C, Lo Iacono O et al (2006) Antiviral therapy decreases hepatic venous pressure gradient in patients with chronic hepatitis C and advanced fibrosis. Am J Gastroenterol 101:2269–2274
18. Roberts S, Gordon A, McLean C et al (2007) Effect of sustained viral response on hepatic venous pressure gradient in hepatitis C-related cirrhosis. Clin Gastroenterol Hepatol 5:932–937
19. Lens S, Alvarado-Tapias E, Mariño Z et al (2017) Effects of all-oral anti-viral therapy on HVPG and systemic hemodynamics in patients with hepatitis C virus-associated cirrhosis. Gastroenterology. https://doi.org/10.1053/j.gastro.2017.07.016
20. D'Ambrosio R, Aghemo A, Fraquelli M et al (2013) The diagnostic accuracy of Fibroscan for cirrhosis is influenced by liver morphometry in HCV patients with a sustained virological response. J Hepatol 59:251–256
21. Hoad CL, Palaniyappan N, Kaye P et al (2015) A study of T(1) relaxation time as a measure of liver fibrosis and the influence of confounding histological factors. NMR Biomed 28:706–714
22. Agrawal S, Hoad CL, Francis ST, Guha IN, Kaye P, Aithal GP (2017) Visual morphometry and three non-invasive markers in the

evaluation of liver fibrosis in chronic liver disease. Scand J Gastroenterol 52:107–115
23. Banerjee R, Pavlides M, Tunnicliffe EM et al (2014) Multiparametric magnetic resonance for the non-invasive diagnosis of liver disease. J Hepatol 60:69–77
24. Palaniyappan N, Cox E, Bradley C et al (2016) Non-invasive assessment of portal hypertension using quantitative magnetic resonance imaging. J Hepatol 65:1131–1139
25. Chow AM, Gao DS, Fan SJ et al (2012) Measurement of liver T(1) and T(2) relaxation times in an experimental mouse model of liver fibrosis. J Magn Reson Imaging 36:152–158
26. Guimaraes AR, Siqueira L, Uppal R et al (2016) T2 relaxation time is related to liver fibrosis severity. Quant Imaging Med Surg 6:103–114
27. Anderson SW, Jara H, Ozonoff A, O'Brien M, Hamilton JA, Soto JA (2012) Effect of disease progression on liver apparent diffusion coefficient and T2 values in a murine model of hepatic fibrosis at 11.7 Tesla MRI. J Magn Reson Imaging 35:140–146
28. Pavlides M, Banerjee R, Sellwood J et al (2016) Multiparametric magnetic resonance imaging predicts clinical outcomes in patients with chronic liver disease. J Hepatol 64:308–315
29. Bradley CR, Cox EF, Scott RA et al (2018) Multi organ assessment of compensated cirrhosis patients using quantitative magnetic resonance imaging. J Hepatol. https://doi.org/10.1016/j.jhep.2018.05.037
30. Cheung MC, Walker AJ, Hudson BE et al (2016) Outcomes after successful direct-acting antiviral therapy for patients with chronic hepatitis C and decompensated cirrhosis. J Hepatol 65:741–747
31. Gurcan NI, Sakçı Z, Akhan S et al (2016) Liver apparent diffusion coefficient changes during telaprevir-based therapy for chronic hepatitis C. Balkan Med J 33:602–606
32. Aube C, Moal F, Oberti F et al (2007) Diagnosis and measurement of liver fibrosis by MRI in bile duct ligated rats. Dig Dis Sci 52:2601–2609
33. Desmet VJ, Roskams T (2004) Cirrhosis reversal: a duel between dogma and myth. J Hepatol 40:860–867
34. Schwabl P, Mandorfer M, Steiner S et al (2017) Interferon-free regimens improve portal hypertension and histological necroinflammation in HIV/HCV patients with advanced liver disease. Aliment Pharmacol Ther 45:139–149
35. Mauro E, Crespo G, Montironi C et al (2018) Portal pressure and liver stiffness measurements in the prediction of fibrosis regression after sustained virological response in recurrent hepatitis C. Hepatology 67:1683–1694
36. Bachofner JA, Valli PV, Kröger A et al (2017) Direct antiviral agent treatment of chronic hepatitis C results in rapid regression of transient elastography and fibrosis markers fibrosis-4 score and aspartate aminotransferase-platelet ratio index. Liver Int 37:369–376
37. Knop V, Hoppe D, Welzel T et al (2016) Regression of fibrosis and portal hypertension in HCV-associated cirrhosis and sustained virologic response after interferon-free antiviral therapy. J Viral Hepat 23:994–1002
38. Poynard T, Moussalli J, Munteanu M et al (2013) Slow regression of liver fibrosis presumed by repeated biomarkers after virological cure in patients with chronic hepatitis C. J Hepatol 59:675–683
39. Reiberger T, Payer BA, Ferlitsch A et al (2012) A prospective evaluation of pulmonary, systemic and hepatic haemodynamics in HIV-HCV-coinfected patients before and after antiviral therapy with pegylated interferon and ribavirin. Antivir Ther 17:1327–1334
40. Afdhal N, Everson GT, Calleja JL et al (2017) Effect of viral suppression on hepatic venous pressure gradient in hepatitis C with cirrhosis and portal hypertension. J Viral Hepat. https://doi.org/10.1111/jvh.12706
41. Mandorfer M, Kozbial K, Schwabl P et al (2016) Sustained virologic response to interferon-free therapies ameliorates HCV-induced portal hypertension. J Hepatol 65:692–699
42. Morishima C, Shiffman ML, Dienstag JL et al (2012) Reduction in hepatic inflammation is associated with less fibrosis progression and fewer clinical outcomes in advanced hepatitis C. Am J Gastroenterol 107:1388–1398
43. Ronot M, Asselah T, Paradis V et al (2010) Liver fibrosis in chronic hepatitis C virus infection: differentiating minimal from intermediate fibrosis with perfusion CT. Radiology 256:135–142
44. D'Ambrosio R, Degasperi E, Aghemo A et al (2016) Serological tests do not predict residual fibrosis in hepatitis C cirrhotics with a sustained virological response to interferon. PLoS One 11:e0155967
45. Shiffman ML, Sterling RK, Contos M et al (2014) Long term changes in liver histology following treatment of chronic hepatitis C virus. Ann Hepatol 13:340–349

9.4 Publication IV: Bradley CR, Bragg DD, Cox EF, El-Sharkawy AM, Buchanan CE, Chowdhury AH, Macdonald IA, Francis ST, Lobo DN. A randomized, controlled, double-blind crossover study on the effects of isoeffective and isovolumetric intravenous crystalloid and gelatin on blood volume, and renal and cardiac hemodynamics. Clinical Nutrition. 2020 Jul 1;39(7):2070-9.

Clinical Nutrition 39 (2020) 2070–2079

Contents lists available at ScienceDirect

Clinical Nutrition

journal homepage: http://www.elsevier.com/locate/clnu

Randomized Control Trials

A randomized, controlled, double-blind crossover study on the effects of isoeffective and isovolumetric intravenous crystalloid and gelatin on blood volume, and renal and cardiac hemodynamics

Christopher R. Bradley [a, b, 1], Damian D. Bragg [a, 1], Eleanor F. Cox [a, b], Ahmed M. El-Sharkawy [a], Charlotte E. Buchanan [b], Abeed H. Chowdhury [a], Ian A. Macdonald [c, d], Susan T. Francis [a, b], Dileep N. Lobo [a, d, *]

[a] Gastrointestinal Surgery, Nottingham Digestive Diseases Centre and National Institute for Health Research (NIHR) Nottingham Biomedical Research Centre, Nottingham University Hospitals NHS Trust and University of Nottingham, Queen's Medical Centre, Nottingham, NG7 2UH, UK
[b] Sir Peter Mansfield Imaging Centre, University Park, University of Nottingham, NG7 2RD, UK
[c] School of Life Sciences, University of Nottingham, Queen's Medical Centre, Nottingham, NG7 2UH, UK
[d] MRC Versus Arthritis Centre for Musculoskeletal Ageing Research, University of Nottingham, Queen's Medical Centre, Nottingham, NG7 2UH, UK

ARTICLE INFO

Article history:
Received 24 July 2019
Accepted 30 September 2019

Keywords:
Balanced crystalloids
Balanced gelatin solution
Magnetic resonance imaging
Randomized controlled study
Cardiac output
Renal blood flow

SUMMARY

Background & aims: Blood volume expanding properties of colloids are superior to crystalloids. In addition to oncotic/osmotic properties, the electrolyte composition of infusions may have important effects on visceral perfusion, with infusions containing supraphysiological chloride causing hyperchloremic acidosis and decreased renal blood flow. In this non-inferiority study, a validated healthy human subject model was used to compare effects of colloid (4% succinylated gelatin) and crystalloid fluid regimens on blood volume, renal function, and cardiac output.

Methods: Healthy male participants were given infusions over 60 min > 7 days apart in a randomized, crossover manner. Reference arm (A): 1.5 L of Sterofundin ISO, isoeffective arm (B): 0.5 L of 4% Gelaspan®, isovolumetric arm (C): 0.5 L of 4% Gelaspan® and 1 L of Sterofundin ISO (all B. Braun, Melsungen, Germany). Participants were studied over 240 min. Changes in blood volume were calculated from changes in weight and hematocrit. Renal volume, renal artery blood flow (RABF), renal cortex perfusion and diffusion, and cardiac index were measured with magnetic resonance imaging.

Results: Ten of 12 males [mean (SE) age 23.9 (0.8) years] recruited, completed the study. Increase in body weight and extracellular fluid volume were significantly less after infusion B than infusions A and C, but changes in blood volume did not significantly differ between infusions. All infusions increased renal volume, with no significant differences between infusions. There was no significant difference in RABF across the infusion time course or between infusion types. Renal cortex perfusion decreased during the infusion (mean 18% decrease from baseline), with no significant difference between infusions. There was a trend for increased renal cortex diffusion (4.2% increase from baseline) for the crystalloid infusion. All infusions led to significant increases in cardiac index.

Conclusions: A smaller volume of colloid (4% succinylated gelatin) was as effective as a larger volume of crystalloid at expanding blood volume, increasing cardiac output and changing renal function. Significantly less interstitial space expansion occurred with the colloid.

Trial registration: The protocol was registered with the European Union Drug Regulating Authorities Clinical Trials Database (https://eudract.ema.europa.eu) (EudraCT No. 2013-003260-32).

1. Introduction

Restoration of blood volume in the perioperative period or in critically ill patients can be achieved with infusions of either crystalloids or colloids. However, it is clear that for a given volume of

* Corresponding author. Gastrointestinal Surgery, Nottingham Digestive Diseases Centre, Nottingham University Hospitals, Queen's Medical Centre, Nottingham, NG7 2UH, UK. Fax: +44 115 8231160.
E-mail address: dileep.lobo@nottingham.ac.uk (D.N. Lobo).
[1] Joint first authors.

https://doi.org/10.1016/j.clnu.2019.09.011

Abbreviations used

ADC	Apparent diffusion coefficient
ASL	Arterial spin labelling
β-NAG	N-acetyl-beta-glucosaminidase
BSA	Body surface area
CV	Coefficient of variance
DWI	Diffusion weighted imaging
ELISA	Enzyme-linked immunosorbent assay
GDFT	Goal-directed fluid therapy
IQR	Interquartile range
KIM-1	Kidney injury molecule 1
MR	Magnetic resonance
MRCP	Magnetic resonance cholangiopancreatography
MRI	Magnetic resonance imaging
NGAL	Neutrophil gelatinase-associated lipocalin
PC MRI	Phase contrast magnetic resonance imaging
RABF	Renal artery blood flow
RARE	Rapid acquisition with relaxation enhancement
SEM	Standard error of the mean
SID_a	Apparent strong ion difference

infusate, the blood volume expanding properties of colloids are superior to crystalloids. Work performed in healthy participants comparing the effects of 0.9% saline, 4% succinylated gelatin and 6% hydroxyethyl starch on blood volume expansion showed that colloids were three times as effective as crystalloids for this purpose [1]. Although the blood volume expanding efficacy of colloids is approximately 70% in patients undergoing laparoscopic cholecystectomy [2], in critically ill patients, volume for volume, colloids may be only up to 1.3 times as effective as crystalloids [3].

Colloids distribute predominantly in the intravascular compartment and this property may have important consequences for visceral blood supply and, thus, function. Crystalloids tend to distribute mainly in the interstitial fluid space, giving rise to tissue edema, and when given in excess, may have adverse effects on gastrointestinal function and wound healing [4–7]. Colloid boluses have also been used intraoperatively to increase stroke volume (goal directed fluid therapy − GDFT), and, thereby, improve tissue perfusion and outcome [8]. A recent study has, however, demonstrated that crystalloids may be as effective as colloids for GDFT [9].

In addition to oncotic properties, the electrolyte composition of infusions may have important effects on visceral perfusion. Data derived from both healthy participant and patient studies have shown that infusions which contain a supraphysiological concentration of chloride can cause significant hyperchloremic acidosis [1,10–17], and reduce renal arterial blood flow and perfusion [10].

The use of balanced crystalloids such as Hartmann's solution, Ringer's lactate, PlasmaLyte 148 (all Baxter Healthcare, Deerfield, IL, USA) and Sterofundin® ISO (B. Braun, Melsungen, Germany), with a sodium and chloride content closer to that of plasma, may achieve better acid-base balance and renal function, less tissue edema, nausea and vomiting, and possibly better survival [11]. Nevertheless, most of the older colloids are suspended in 0.9% saline and this is accompanied by the risk of hyperchloremic acidosis and its sequelae. It is only recently that colloids suspended in balanced solutions have become available.

Our group has previously used magnetic resonance imaging (MRI) to assess renal hemodynamics non-invasively during fluid delivery [10,18]. Phase contrast MRI (PC-MRI) is used to quantify renal artery blood flow (RABF), and Arterial Spin Labeling (ASL) is used to non-invasively map renal perfusion spatially without the need for contrast agents. We showed that when crystalloids were studied, the hyperchloremic acidosis caused by the infusion of 2 L 0.9% saline was associated with a decrease in renal artery flow velocity and renal cortical tissue perfusion when compared with the infusion of a balanced crystalloid [10]. However, in another study we demonstrated that while renal cortical tissue perfusion increased after infusion of 1 L 6% hydroxyethyl starch suspended in a balanced crystalloid, it did not change from baseline after the infusion of 6% hydroxyethyl starch suspended in 0.9% saline, suggesting that the effects of colloids are different from that of crystalloids [18].

Hence, in this non-inferiority study, we aimed to use a validated healthy male participant model previously developed by us [1,10–12,14,18] to compare the effects of colloid (4% gelatin) and crystalloid regimens on RABF and renal cortex perfusion [10,18] as well as renal volume and renal cortex diffusion [apparent diffusion coefficient (ADC)] using diffusion weighted imaging (DWI). In addition, we assessed cardiac index.

The primary objective was to determine the differential impact of isoeffective [using different volumes of crystalloid (1.5 L) and colloid (0.5 L) with a similar plasma volume expanding capacity [1]] and isovolumetric infusions of crystalloid and colloid (1.5 L crystalloid *vs.* 1 L crystalloid + 0.5 L colloid) on blood volume expansion. Secondary endpoints included changes in weight, hematological and serum biochemical parameters, urinalysis, aortic blood flow and cardiac output, as well as renal volume, RABF, and renal cortex perfusion and diffusion.

2. Methods

This non-inferiority randomized, double-blind, crossover study was performed at a university teaching hospital. Twelve healthy males (aged 20–28 years, BMI 20–25 kg/m^2) were recruited after obtaining written informed consent. Those with abnormal blood parameters on the day before each study, acute illness in the preceding 6 weeks, taking regular medication, a history of substance abuse, hypersensitivity to gelatin solutions or to any of the other infusion ingredients or having factors contraindicating MRI were excluded. It was decided to withdraw participants developing adverse events from the study. An adverse event was defined as any unfavorable and unintended sign, symptom, syndrome or illness that develops or worsens during the period of observation in the study. The UK National Research Ethics Service Committee East Midlands (Ref. 13/EM/0363) and the Medicines and Healthcare Products Regulatory Agency granted approvals. The protocol was registered with the European Union Drug Regulating Authorities Clinical Trials Database (https://eudract.ema.europa.eu) (EudraCT No. 2013-003260-32).

2.1. Baseline assessment

Participants reported 24 h prior to the study day to provide a blood and urine sample, and were asked to collect a 24-h urine sample for baseline creatinine clearance. Urine was analyzed for osmolality, neutrophil gelatinase-associated lipocalin (NGAL), N-acetyl-beta-glucosaminidase (β-NAG) and kidney injury molecule-1 (KIM-1), blood was analyzed for blood chemistry parameters to ensure that no concurrent electrolyte abnormalities were present. Height and weight was also recorded. Participants were instructed to abstain from alcohol, caffeine and nicotine for at least 24 h prior to each arm of the study. On the study day, participants presented to the MRI center at 8:00 am having fasted from the previous night. After providing a baseline urine sample, the baseline weight was recorded and a 16-G venous cannula inserted into each antecubital fossa. Blood sampling was performed after lying supine for at least

10 min for blood chemistry parameters including hemoglobin, hematocrit, serum electrolytes, urea, creatinine, albumin, and osmolality.

2.2. Infusions

All the study participants received the following infusions over 60 min on separate occasions at least 7 days apart and in a random order (Table 1).

A) 1.5 L of Sterofundin ISO – 217.5 mmol sodium and 190.5 mmol chloride (reference arm).
B) 0.5 L of 4% Gelaspan® – 75.5 mmol sodium and 51.5 mmol chloride (isoeffective arm).
C) 0.5 L of 4% Gelaspan® and 1 L of Sterofundin ISO – 220.5 mmol sodium and 178.5 mmol chloride (isovolumetric arm).

All infusions were manufactured by B. Braun, Melsungen, Germany.

2.3. Measurements and end points

Blood was sampled at 0 (baseline), 30, 60, 90, 120, 180 and 240 min after commencing the infusion. Subjects voided their bladder on arrival at the MRI center at 8:00 am. After commencement of the infusions they were allowed to void urine at will and had to void again at 240 min, with all of the urine voided being collected. An aliquot of the urine pooled over the 4-h period was analyzed for osmolality and concentrations of urea, creatinine, sodium, potassium, chloride, total proteins, microalbuminuria and urinary NGAL, β-NAG and KIM-1. A further 24-h urine collection was performed from 8:00 am on the study day until 24 h post infusion on the following day. The urine collected over the 240 min of the study was then pooled with urine collected from then until the first voided sample on the next morning to constitute a 24-h urine collection. Urine pooled over the 24-h period was analyzed for the previously mentioned parameters. Weight was recorded at baseline, 100, 120, 180 and 240 min.

2.4. Hematological and biochemical blood analyses

All analyses were performed according to standard methods [1,10–12,14,18]. Assays for NGAL (Human Lipocalin-2/NGAL Quantikine ELISA Kit, R&D Systems Inc., Minneapolis, USA), KIM-1 (Human TIM-1/KIM-1/HAVCR Quantikine ELISA Kit, R&D Systems Inc., Minneapolis, USA) and β-NAG (NAG test kit, PPR Diagnostics Ltd., London, UK) were performed using ELISA in accordance with the instructions provided by the manufacturers.

Table 1
Composition of infusions.

	4% Gelaspan®	Sterofundin ISO®
Colloid molecular weight	26 500 Da	
Sodium (mmol/L)	151	145
Chloride (mmol/L)	103	127
Potassium (mmol/L)	4	4
Calcium (mmol/L)	1	2.5
Magnesium (mmol/L)	1	1
Acetate (mmol/L)	24	24
Malate (mmol/L)		5
Strong ion difference (mmol/L)	52	22
Sodium supplied as	NaCl, 5.55 g/L	NaCl, 6.8 g/L
pH	7.4	5.1–5.9
Theoretical osmolarity, mOsm/L	284	309

Both infusions manufactured by B. Braun, Melsungen, Germany.

2.5. Derived values

Blood volume at time 0 was estimated according to the method described by Nadler et al. [19] and changes in blood volume after the infusions were calculated from changes in hematocrit, using formulae we have described previously [1,2,10,18]. The apparent strong ion difference (SID_a) was calculated as described by Stewart ($SID_a = [Na^+]+[K^+]-[Cl^-]$) [20]. Change in interstitial fluid volume was calculated by subtracting change in blood volume from change in weight.

2.6. MRI protocol

Cardiac and renal MRI measurements were collected on a 3.0 T Philips Achieva MR scanner (Philips Healthcare Systems, Best, Netherlands). The MRI protocol consisted of a series of non-invasive MR measurements to assess cardiac and renal function.

Cardiac MRI data were collected using phase contrast (PC)-MRI to assess cardiac output. Data were then corrected for body surface area (BSA) to compute cardiac index (CI). Renal MRI data were collected using structural images to assess total renal volume, PC-MRI was acquired to determine left RABF, Arterial Spin Labelling (ASL) was used to determine renal cortex tissue perfusion incorporating an estimation of renal T_1 in the quantification of perfusion [21]. Diffusion Weighted Imaging (DWI) was used to determine renal cortex apparent diffusion coefficient (ADC).

Each series of cardiac and renal images were collected in 10 min, with the cardiac and renal scans being interleaved throughout the infusion. In total there were three repeats of the cardiac and three renal scans collected during the infusion, and a further repeat of each post-infusion to assess the time-course of the response (Fig. 1).

Bladder volume was measured using MR cholangiopancreatography (MRCP) with a Rapid Acquisition with Relaxation Enhancement (RARE) sequence at baseline and <40 min after the end of the infusion. Details of the MRI scanning protocols and analysis methods are described in the Supplementary Methods.

2.7. Sample size

This was a pilot study and we assumed that the blood volume expanding effects of the three fluid regimens would be equivalent (non-inferiority). Based on our previous work [10,18], we determined that a sample size of 10 would be adequate to obtain meaningful data for a pilot study. Assuming a drop-out rate of 15%, we sought to recruit 12 participants.

2.8. Randomization, allocation concealment and blinding

A randomization sequence was created using http://www.randomization.com by the Nottingham Clinical Trials Pharmacy. Randomization was performed using sequentially numbered paired sealed opaque envelopes. A nurse not involved in the study was responsible for blinding the investigational products. The infusion bags were covered with opaque bags and the data shown on the screen of the automated infusion pump was masked from the investigators. The randomization code was broken after completion of data analysis.

2.9. Statistical analysis

Statistical analysis was performed using GraphPad Prism (v 7.03) for Windows statistical software package (GraphPad Software

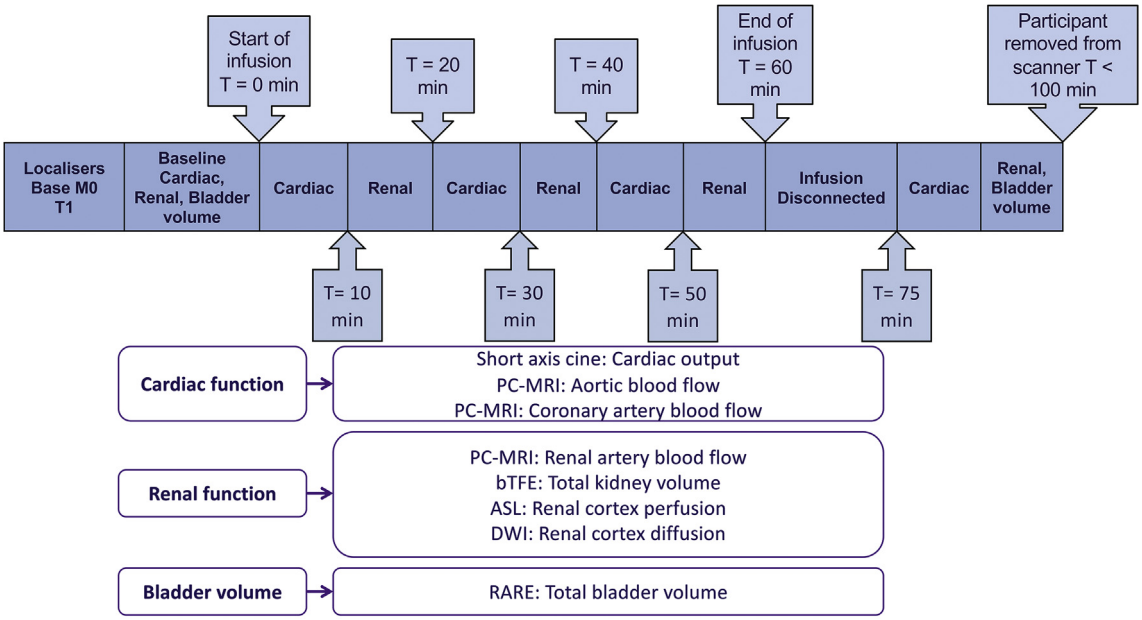

Fig. 1. Diagram showing the protocol for MRI scan collection in each of the infusion sessions to assess cardiac and renal function. The protocol comprised scans to be collected at baseline, repeated at 20-min intervals over the 60 min infusion, and repeated once post-infusion to assess the time-course of the renal and cardiac response. Note, acquired timings may deviate slightly from this protocol timing due to blood sampling and infusion technicalities, timings provided in Figures in the Results section show the actual scan acquisition time (mean time across participants).

Inc., La Jolla, CA). A Shapiro–Wilk test was used to test the normality of the data. Normally distributed group data quantitative variables were expressed as mean [standard error of mean (SEM)], and skewed data as median and interquartile range. A two-way ANOVA with Bonferroni correction was used for comparing two groups with multiple time point comparisons. A one-way ANOVA with Kruskal–Wallis test was used for single comparisons across all three groups. Comparisons between two groups for non-parametric data were analyzed using a Wilcoxon signed-rank test. A student paired t-test was used for comparing two groups where the distribution was normal. The differences were considered statistically significant at $P < 0.05$.

3. Results

Twelve participants, with a mean (SEM) age of 23.9 (0.8) years were recruited to the study over a 13-month period. Two participants were withdrawn from the study due to adverse events. One participant developed persistent tachycardia up to 115 beats per minute during one of the infusions (0.5 L colloid), this settled shortly after terminating the infusion with no further adverse effects. One participant was excluded from analysis due to excessive sweating during two of the infusion sessions and was biochemically more dehydrated following infusion, he required no medical attention. Analysis was performed on data obtained from the remaining 10 participants. Baseline clinical and MRI parameters prior to each infusion arm, and the coefficient of variation in MRI measures are summarized in Table 2.

3.1. Changes in weight, hematocrit, hemoglobin, blood volume, interstitial fluid volume and biochemical parameters

Changes in body weight, hematocrit, hemoglobin, calculated blood volume and interstitial fluid volume, as well as serum biochemistry are shown in Fig. 2. As expected, increase in body weight and extracellular fluid volume were significantly less after the colloid infusion (B) when compared with the crystalloid (A) and crystalloid + colloid infusions (C). For most other parameters, there was no statistically significant difference when the groups were compared. Changes in urinary parameters are summarized in Table 3.

3.2. Urinary NGAL, KIM-1, β-NAG

Although some differences were noted in urinary NGAL, KIM-1 and β-NAG at the measured time points, all values remained in the normal range (data not shown).

3.3. Changes in renal volume, renal artery blood flow, renal global and cortical tissue perfusion, and renal cortex diffusion determined by MRIs

The percentage change in renal MRI parameters, as measured from baseline are shown in Fig. 3. All infusions increased renal volume, this increase was statistically significant at 90 min when compared with baseline for each infusion [A ($P < 0.001$), B ($P = 0.02$), C ($P = 0.004$)]. However, there were no statistically significant differences between the infusions. There was no significant difference in RABF from baseline for any time point across the infusions or any difference between infusions. However, when left RABF was corrected for renal volume change yielding a measure of global perfusion of the left kidney at each time point, a significant decrease was observed between baseline and 95 min after the start of the 0.5 L colloid infusion ($P = 0.037$). No significant change in global perfusion of the left kidney was observed for the crystalloid or combined crystalloid and colloid infusion. Renal cortex perfusion across both kidneys, as determined by ASL, decreased from baseline to 93 min after the crystalloid infusion [with a 23% decrease from baseline ($P = 0.005$)] and the colloid infusion [with a 14% decrease from baseline ($P = 0.048$)]. No significant difference was found in renal cortex perfusion for the combined crystalloid and colloid infusion, or between infusions. There was a significant increase in

Table 2
Baseline clinical and MRI parameters prior to each infusion.

	Before infusion A (1.5 L crystalloid) n = 10	Before infusion B (0.5 L colloid) n = 10	Before infusion C (1 L crystalloid + 0.5 L colloid) n = 10	Coefficient of Variation of baseline MR measures across treatment
Clinical Parameters				
Weight (kg)	74.5 (1.8)	74.1 (1.6)	73.9 (1.6)	
Height (m)	1.81 (0.02)	1.81 (0.02)	1.81 (0.02)	
Body mass index (kg/m^2)	22.7 (0.5)	22.6 (0.5)	22.5 (0.4)	
Hemoglobin (g/L)	150.1 (2.4)	147.8 (2.9)	147.2 (3.0)	
Hematocrit (L/L)	0.439 (0.006)	0.432 (0.007)	0.431 (0.007)	
Serum chloride (mmol/L)	102.9 (0.4)	103.6 (0.6)	103.8 (0.8)	
Serum apparent strong ion difference (mmol/L)	41.2 (0.8)	39.9 (0.6)	40.5 (0.5)	
Serum bicarbonate (mmol/L)	28.2 (0.7)	27.5 (0.5)	27.3 (0.6)	
Serum albumin (g/L)	42.4 (0.8)	41.7 (1.0)	42.8 (0.5)	
Serum osmolality (mOsm/kg)	291 (0.8)	291 (1.0)	291 (0.9)	
Serum creatinine (μmol/L)	78.6 (2.7)	77.6 (2.6)	76.4 (3.2)	
Creatinine clearance (ml/min)	139.6 (13.0)	131.8 (18.6)	127.3 (8.2)	
Calculated blood volume (L)	5.2 (0.1)	5.2 (0.1)	5.2 (0.1)	
MRI Parameters				
Aortic flux (ml/s)	91 (4)	91 (4)	93 (4)	8.2 (2.8)
Cardiac index from aortic flow (L/min/m^2)	2.82 (0.1)	2.83 (0.1)	2.89 (0.1)	8.2 (3.6)
Cardiac index from short axis cine (L/min/m^2)	1.55 (0.1)	1.55 (0.1)	1.52 (0.1)	16 (9)
Renal artery blood flow velocity (cm/s)	6.3 (0.6)	8.0 (0.6)	7.0 (0.4)	12 (5)
Renal cortical tissue perfusion (ml/100 g/min)	215 (14)	235 (17)	235 (9)	9.1 (4.4)
Left global renal perfusion (ml/100 g/min)	215 (20)	262 (14)	231 (13)	12 (5)
Total kidney volume (ml)	351 (25)	365 (23)	359 (24)	4.2 (2.8)
Cortex T_1 (ms)	1026 (9)	1021 (9)	1020 (11)	2.3 (1.1)
Medulla T_1 (ms)	1340 (12)	1327 (13)	1335 (21)	2.9 (2.4)
Bladder volume (ml)	37 (9)	51 (23)	51 (12)	40 (32)

All values mean (SEM). There were no statistically significant differences ($p > 0.05$) between the groups when baseline parameters were compared.

renal cortex ADC from baseline to 95 min after the crystalloid infusion [4.2% increase from baseline ($P = 0.033$)], and a trend for an increase in the combined crystalloid and colloid infusion ($P = 0.09$), whilst no significant change was observed in the colloid infusion.

3.4. Changes in heart rate, stroke volume, aortic flow and cardiac index

Changes in cardiac MRI measures are shown in Fig. 4. All infusions led to a significant increase at 83 min after baseline in aortic flow [crystalloid ($P = 0.035$), colloid ($P < 0.005$), combined crystalloid and colloid ($P = 0.039$)], and a significant increase in cardiac index [crystalloid ($P = 0.036$), colloid ($P < 0.001$), combined crystalloid and colloid ($P = 0.04$)]. Aortic stroke volume significantly increased for the colloid infusion ($P = 0.045$) with a trend for increase in the combined crystalloid and colloid infusion ($P = 0.062$), no significance was observed in the crystalloid infusion. Heart rate significantly increased at 83 min for the crystalloid infusion ($P = 0.007$) and the colloid infusion ($P = 0.004$), no significant difference was observed for the combined crystalloid and colloid infusion.

4. Discussion

4.1. Main findings

This study has confirmed our previous work, showing that the blood volume expanding potential of 0.5 L of colloid (gelatin) is similar to that of 1.5 L of crystalloid in healthy participants [1]. In addition, it has shown that the blood volume expansion produced by a combination of 1 L of crystalloid with 0.5 L of colloid was not statistically different from that produced by separate infusions of either 1.5 L of crystalloid or 0.5 L of colloid. Significant changes in response to the infusions were seen at final measurement compared to baseline with an increase in renal volume, a decrease in global renal perfusion as measured by PC-MRI corrected for renal volume and renal cortex perfusion as assessed by ASL. Perfusion measured using ASL was deemed to be the more robust method of renal hemodynamics, providing a smaller CV than estimating global perfusion by correcting renal artery blood flow by kidney volume. This finding has also been shown in a previous study [21]. The significant increase in renal cortex ADC following the crystalloid infusion could be explained by the increase in the amount of water in the interstitial space of the kidney with crystalloids, which could be a result of decreased glomerular filtration and is consistent with the change in renal volume for the crystalloid infusion [22].

The changes in renal hemodynamics were, however, of a smaller magnitude when compared with our previous work where we induced mean serum chloride concentrations in excess of 108 mmol/L [10]. In addition, markers of acute kidney injury remained in the normal range. All three infusions produced >10% time-related increase in heart rate, stroke volume and cardiac index, but there was no statistically significant difference between the effects of the three infusions.

4.2. Results in context of published literature

The results of this study have also further validated the reproducibility of the model we have developed to study responses of healthy participants to intravenous fluid infusions [1,10–12,14,18]. As shown previously [1,10–12,14,18], all the infusion regimens used

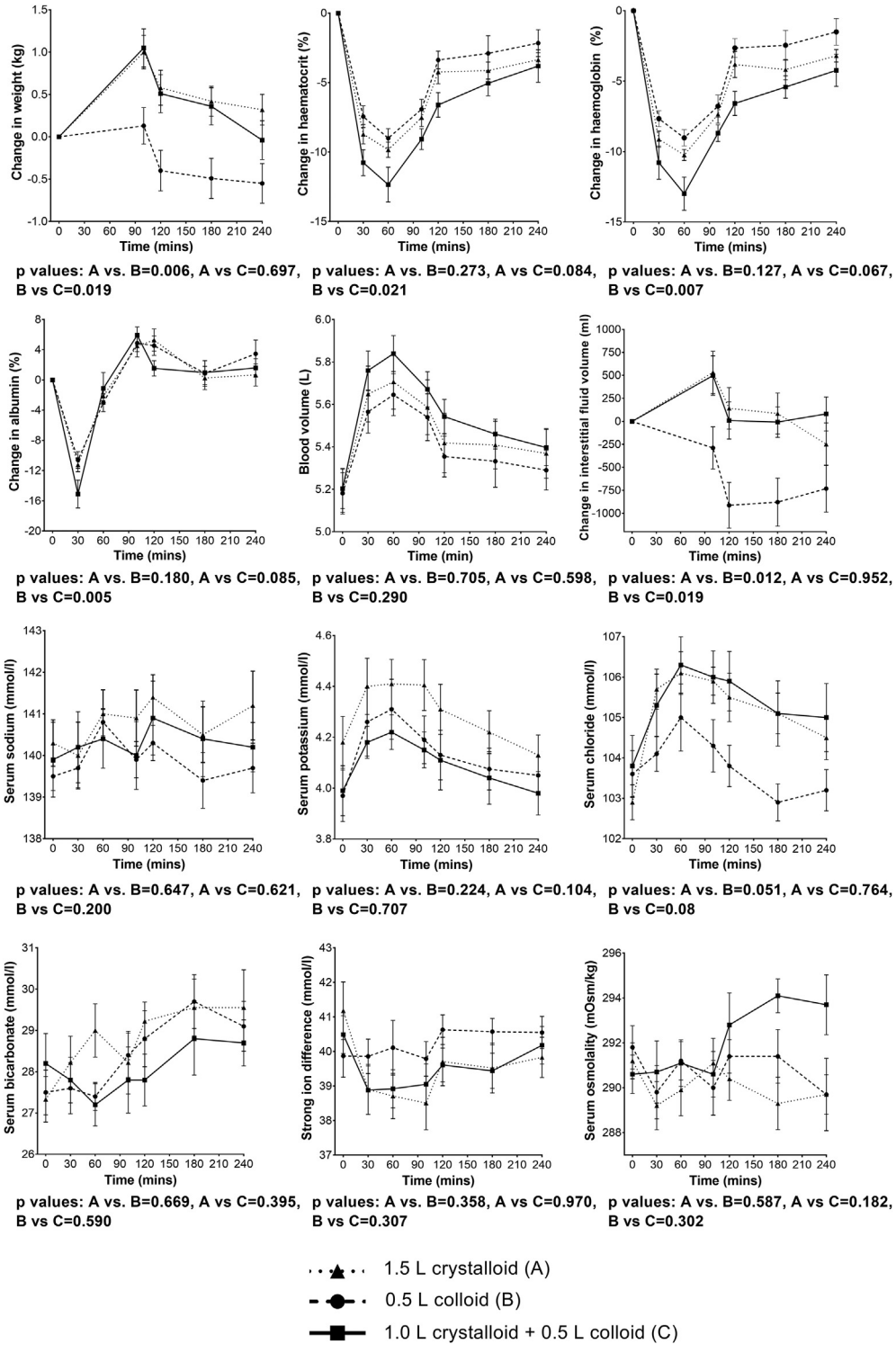

Fig. 2. Changes in body weight, hematocrit, hemoglobin, calculated blood volume and interstitial fluid volume, as well as serum biochemistry. Note weight was recorded at baseline and post MRI scanning.

in the present study produced a dilutional effect on hematocrit, hemoglobin and serum albumin concentration that was reversed as the fluid was excreted in the urine. The crystalloid (1.5 L) and crystalloid + colloid (1 L + 0.5 L respectively) infusions expanded the calculated interstitial fluid space to the same extent, indicating the propensity to produce edema. In contrast, the colloid infusion produced a contraction of the interstitial space, suggesting that the increased colloid oncotic pressure helps draw fluid from the interstitial into the intravascular space. Urine output during the study period was very similar after the infusion of 1.5 L of crystalloid and 0.5 L of colloid, but was slightly greater after the combined crystalloid and colloid infusion.

Compared with infusions of 0.9% saline [1,10,14], all infusions used in this study produced only a small elevation in serum

Table 3
Urinary responses.

	Infusion A (1.5 L crystalloid)	Infusion B (0.5 L colloid)	Infusion C (1.0 L crystalloid + 0.5 L colloid)	*p* (A *vs.* B)	*p* (A *vs.* C)	*p* (B *vs.* C)
Time to first micturition after start of infusion (min)	106 (4)	106 (5)	123 (14)	0.89	0.27	0.17
Postinfusion urinary volume at 240 min (ml)	621 (99)	517 (68)	826 (97)	0.20	0.13	**<0.05**
Preinfusion urinary osmolality (mOsm/kg)	689 (48)	634 (76)	712 (56)	0.21	0.79	0.28
Postinfusion urinary osmolality at 240 min volume (mOsm/kg)	466 (56)	473 (60)	378 (30)	0.88	0.26	0.19
Total postinfusion urinary sodium over 24 h (mmol)	242 (21)	157 (27)	186 (28)	**0.02**	0.06	0.19
Total postinfusion urinary sodium at 240 min (mmol)	69 (12)	49 (7)	72 (10)	0.12	0.87	**<0.05**
Urine sodium at 240 min as percentage of sodium infused	32 (6)	64 (10)	33 (5)	**<0.05**	0.92	**<0.05**
Total postinfusion urinary potassium over 24 h (mmol)	86 (9)	69 (12)	63 (9)	0.09	0.07	0.89
Total postinfusion urinary chloride at 240 min (mmol)	78 (13)	63 (12)	75 (11)	0.34	0.87	0.07
Urine chloride at 240 min as percentage of chloride infused	41 (7)	122 (24)	42 (6)	**<0.05**	0.86	**<0.05**

n = 10, all values mean (SEM). Student paired t test. p values in bold indicate statistically significant differences.

chloride concentration and a 2 mmol/L fall in the strong ion difference, reflecting the reduced chloride concentration of the infusions when compared with 0.9% saline. The changes in serum bicarbonate and potassium concentrations and serum osmolality were also relatively small and for all these measures there were no statistically significant differences between the three infusions. In our previous study [10], we showed that the elevation of serum chloride concentration to >108 mmol/L after the infusion of 2 L 0.9% saline led to a significant fall in both renal artery flow velocity and renal cortical tissue perfusion. However, in the present study, the chloride content of all the infusions was less than that of 0.9% saline and the maximum that the serum chloride concentration reached was around 106 mmol/L (Fig. 2). In addition, there was no significant difference in the fall in strong ion difference between the three infusions. This strengthens the hypothesis that it is the hyperchloremic (≥108 mmol/L) acidosis produced by large chloride loads that has an adverse effect on renal hemodynamics [10,11,23,24]. A hypothesis for the mechanisms of hyperchloremia on reducing renal blood flow and glomerular filtration rate, and ultimately decreasing urinary output and sodium excretion has been proposed [11]. This involves chloride from the high chloride concentration filtrate in the distal tubule of the nephron crossing the basement membrane and causing depolarization of the macula densa and release of adenosine, which acts on the A_1 receptors of the renal vasculature causing vasoconstriction. This phenomenon probably does not occur at a chloride concentration of around 106 mmol/L, and may, thereby, explain the results of our study. Although there was an increase in renal volume by about 5% after all three infusions, indicating some renal edema, there was probably not a high enough increase in intraorgan tissue pressure to disrupt RABF significantly. Interestingly, we have also demonstrated that the infusion of colloid in the form of 4% succinylated gelatin had no adverse effect on renal hemodynamics or markers of kidney injury such as NGAL, β-NAG and KIM-1.

There was a steady increase in heart rate and cardiac index after the three infusions. There was a >10% increase in these parameters when the values at the end of the infusions were compared with baseline. This suggests that even in relatively "euvolemic" healthy participants, infusions of colloids and crystalloids increase stroke volume and cardiac index. To some extent, this response in healthy euvolemic participants may explain why, in some studies using "flow directed fluid therapy", patients received excessive amounts of fluids intraoperatively [9]. Moreover, as the differences seen after crystalloids and colloids were similar, it is possible that crystalloids may have the same effect as colloids when used for "flow-directed fluid therapy" [9]. However, crystalloids are more likely to cause interstitial edema than colloids.

We have demonstrated that infusions containing higher amounts of sodium and chloride lead to a disproportionately higher retention of sodium (Table 3). This effect is believed to be due to an increase in serum chloride concentrations [10,11].

Renal perfusion decreased across all arms of the study. These changes are believed to be a reflection of the action of hyperchloremia leading to a decrease in RABF and an increase in renal volume. This, however, merits some clarification in light of previous work [10,18]. The hyperchloremic acidosis caused by the infusion of 2 L 0.9% saline was associated with a decrease in renal artery flow velocity and renal cortical tissue perfusion when compared with the infusion of a balanced crystalloid [10]. Using 1 L infusions of colloids, we have previously demonstrated that while renal cortical tissue perfusion increased after infusion of 6% hydroxyethyl starch suspended in a balanced crystalloid, it did not change from baseline after the infusion of 6% hydroxyethyl starch suspended in 0.9% saline, suggesting that the effects of colloids are different from that of crystalloids [18]. More importantly, in the previous studies [10,18], the peak serum chloride concentrations were higher (>108 mmol/L) after 0.9% saline and hydroxyethyl starch suspended in 0.9% saline than after any of the infusions studied in the present study.

4.3. Strengths of the study

This experiment has used a well validated model and state of the art MRI techniques that have been shown to have low coefficients of variance (<10%) [21] (Table 2) to study the effects of intravenous fluid infusions on serum and urinary biochemistry and renal and cardiac hemodynamics in healthy human participants. The age and body weight of the participants were within a narrow range, ensuring homogeneity. The fact that the baseline parameters were very similar prior to each infusion (Table 2), indicates that the participants were studied under similar conditions. Coefficients of Variation on MR parameters over 3 weeks assessed were lower than 10% for most MR measures including aortic flow; total kidney

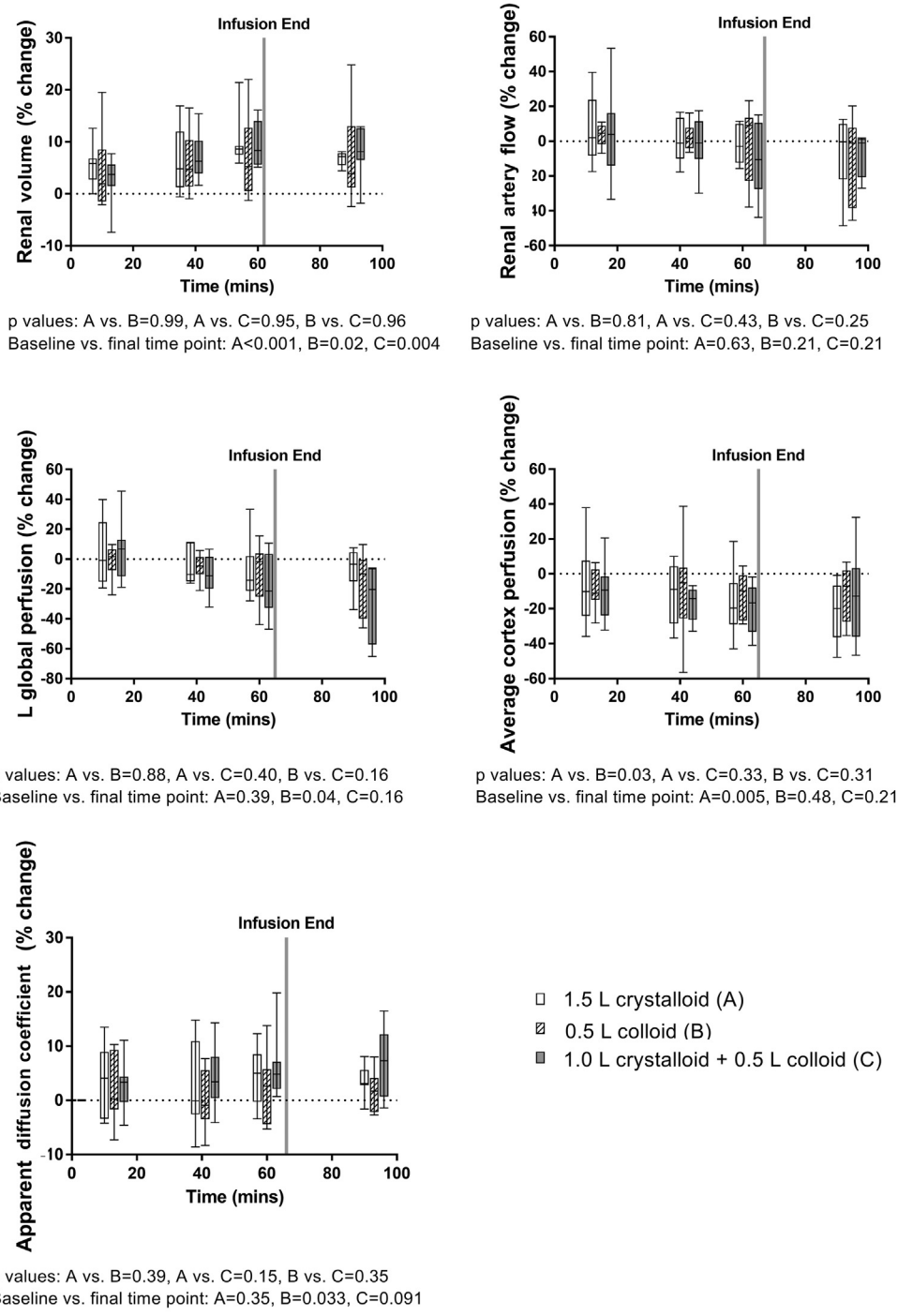

Fig. 3. Percentage change in renal MRI parameters (renal volume, renal artery flow, left renal global perfusion, average cortex perfusion and apparent diffusion coefficient) during each infusion.

volume; renal cortex perfusion estimated with ASL; and apparent diffusion coefficient estimated with DWI.

4.4. Limitations of the study

This study has a few limitations. Healthy participants who were not hypovolemic were studied, and although the study yields valuable data in this group, the results may be different in patients who are hypovolemic or critically ill. Although state of the art MRI techniques were used, the nature of the protocol resulted in cardiac and renal measurements being made at different time points. Although there was little variability in the blood and urinary measurements, there was some variability in the MRI results. We would advise that future studies are conducted to also gather MR data at later time points post-infusion in order to observe measures as they return to a baseline state. In order to gather the five data points across the infusion, the participants in this cohort were supine and on the scanner bed for approaching 3 h, we would advise that future studies collect a similar amount of time points spread over a longer period of time in order to allow for bladder voiding,

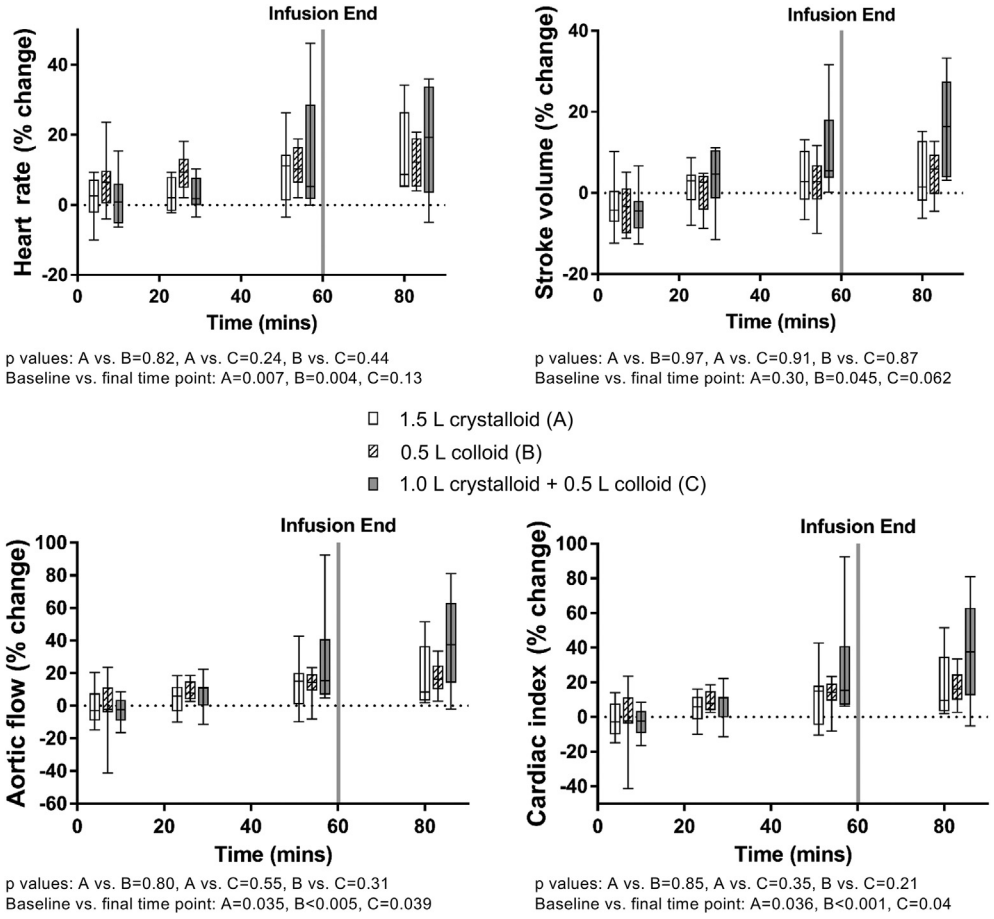

Fig. 4. Percentage change in cardiac MRI parameters (heart rate, stroke volume, aortic flow and cardiac index) during each infusion.

this would also allow the study of larger infusions similar to the amounts patients actually receive perioperatively.

5. Conclusion

MRI provides quantitative measures that are sensitive enough to observe dynamic changes in cardiac function as well as renal structure and function in response to intravenous infusions. A smaller volume of colloid (0.5 L) was as effective as a larger volume of crystalloid (1.5 L) at expanding the blood volume and increasing cardiac output. Significantly less expansion of the interstitial space was associated with an isoeffective volume of colloid. A significant increase in renal volume was associated with all infusions, renal cortex ADC increased significantly only for the crystalloid infusion which showed the most significant renal volume increase. A decrease in global renal cortex perfusion renal cortex perfusion as assessed by ASL was shown for both crystalloid and colloids, with the former driven solely by renal volume change and the later likely by both a reduction in RABF and increase in renal volume. Non-inferiority of the treatment with colloid (4% succinylated gelatin) was also confirmed. The results also indicate that a serum chloride concentration $\geq$108 mmol/L may be necessary to demonstrate adverse effects of hyperchloremia.

Author contributions

CRB – study design, literature search, data collection, data analysis, data interpretation, writing of the manuscript and final approval.

DDB – study design, literature search, data collection, data analysis, data interpretation, writing of the manuscript and final approval.

EFC – study design, literature search, data collection, data analysis, data interpretation, writing of the manuscript and final approval.

AME-S – study design, literature search, data interpretation, writing of the manuscript and final approval.

CEB – study design, literature search, data collection, writing of the manuscript and final approval.

AHC – study design, literature search, data interpretation, writing of the manuscript and final approval.

IAM – study design, data interpretation, writing of the manuscript, critical review, and final approval.

STF – study design, literature search, data interpretation, writing of the manuscript, critical review, supervision and final approval.

DNL – study design, literature search, data interpretation, writing of the manuscript, critical review, supervision and final approval.

Funding

This study was supported by the Medical Research Council [grant number MR/K00414X/1]; and Arthritis Research UK [grant number 19891]. This study was an investigator-initiated project funded by an unrestricted grant from B. Braun, Melsungen, Germany. Support was also received from the National Institute for

Health Research Nottingham Digestive Diseases Biomedical Research Unit.

Role of funding bodies

The funders had no role in the study design, conduct of the study, data collection or analysis or interpretation, and writing of the paper or the decision to submit for publication. No payment has been received from any other source or agency. The corresponding author has full access to all the data in the study and has final responsibility for the decision to submit for publication.

This paper presents independent research funded by the National Institute for Health Research (NIHR). The views expressed are those of the authors and not necessarily the views of the NHS, the NIHR or the Department of Health.

Conflict of Interest

CRB and DDB received travel grants from B. Braun for presentation of the data. IAM has received research funding from Mars Inc. and serves on the advisory board of IKEA for unrelated work. DNL has received unrestricted research funding and speaker's honoraria from Fresenius Kabi, B. Braun, Shire and Baxter Healthcare. None of the other authors have any conflicts of interest to declare.

Appendix A. Supplementary data

Supplementary data to this article can be found online at https://doi.org/10.1016/j.clnu.2019.09.011.

References

[1] Lobo DN, Stanga Z, Aloysius MM, Wicks C, Nunes QM, Ingram KL, et al. Effect of volume loading with 1 liter intravenous infusions of 0.9% saline, 4% succinylated gelatine (Gelofusine) and 6% hydroxyethyl starch (Voluven) on blood volume and endocrine responses: a randomized, three-way crossover study in healthy volunteers. Crit Care Med 2010;38:464–70.

[2] Awad S, Dharmavaram S, Wearn CS, Dube MG, Lobo DN. Effects of an intraoperative infusion of 4% succinylated gelatine (Gelofusine(R)) and 6% hydroxyethyl starch (Voluven(R)) on blood volume. Br J Anaesth 2012;109:168–76.

[3] Myburgh JA, Finfer S, Bellomo R, Billot L, Cass A, Gattas D, et al. Hydroxyethyl starch or saline for fluid resuscitation in intensive care. N Engl J Med 2012;367:1901–11.

[4] Brandstrup B, Tonnesen H, Beier-Holgersen R, Hjortso E, Ording H, Lindorff-Larsen K, et al. Effects of intravenous fluid restriction on postoperative complications: comparison of two perioperative fluid regimens: a randomized assessor-blinded multicenter trial. Ann Surg 2003;238:641–8.

[5] Lobo DN. Fluid overload and surgical outcome: another piece in the jigsaw. Ann Surg 2009;249:186–8.

[6] Lobo DN, Bostock KA, Neal KR, Perkins AC, Rowlands BJ, Allison SP. Effect of salt and water balance on recovery of gastrointestinal function after elective colonic resection: a randomised controlled trial. Lancet 2002;359:1812–8.

[7] Varadhan KK, Lobo DN. A meta-analysis of randomised controlled trials of intravenous fluid therapy in major elective open abdominal surgery: getting the balance right. Proc Nutr Soc 2010;69:488–98.

[8] Rollins KE, Lobo DN. Intraoperative goal-directed fluid therapy in elective major abdominal surgery: a meta-analysis of randomized controlled trials. Ann Surg 2016;263:465–76.

[9] Yates DR, Davies SJ, Milner HE, Wilson RJ. Crystalloid or colloid for goal-directed fluid therapy in colorectal surgery. Br J Anaesth 2014;112:281–9.

[10] Chowdhury AH, Cox EF, Francis ST, Lobo DN. A randomized, controlled, double-blind crossover study on the effects of 2-L infusions of 0.9% saline and plasma-lyte(R) 148 on renal blood flow velocity and renal cortical tissue perfusion in healthy volunteers. Ann Surg 2012;256:18–24.

[11] Lobo DN, Awad S. Should chloride-rich crystalloids remain the main stay of fluid resuscitation to prevent “pre-renal” acute kidney injury?: con. Kidney Int 2014;86:1096–105.

[12] Lobo DN, Stanga Z, Simpson JAD, Anderson JA, Rowlands BJ, Allison SP. Dilution and redistribution effects of rapid 2-litre infusions of 0.9% (w/v) saline and 5% (w/v) dextrose on haematological parameters and serum biochemistry in normal subjects: a double-blind crossover study. Clin Sci (Lond) 2001;101:173–9.

[13] McCluskey SA, Karkouti K, Wijeysundera D, Minkovich L, Tait G, Beattie WS. Hyperchloremia after noncardiac surgery is independently associated with increased morbidity and mortality: a propensity-matched cohort study. Anesth Analg 2013;117:412–21.

[14] Reid F, Lobo DN, Williams RN, Rowlands BJ, Allison SP. (Ab)normal saline and physiological Hartmann's solution: a randomized double-blind crossover study. Clin Sci (Lond) 2003;104:17–24.

[15] Scheingraber S, Rehm M, Sehmisch C, Finsterer U. Rapid saline infusion produces hyperchloremic acidosis in patients undergoing gynecologic surgery. Anesthesiology 1999;90:1265–70 [see comments].

[16] Williams EL, Hildebrand KL, McCormick SA, Bedel MJ. The effect of intravenous lactated Ringer's solution versus 0.9% sodium chloride solution on serum osmolality in human volunteers. Anesth Analg 1999;88:999–1003 [see comments].

[17] Yunos NM, Bellomo R, Hegarty C, Story D, Ho L, Bailey M. Association between a chloride-liberal vs chloride-restrictive intravenous fluid administration strategy and kidney injury in critically ill adults. JAMA 2012;308:1566–72.

[18] Chowdhury AH, Cox EF, Francis ST, Lobo DN. A randomized, controlled, double-blind crossover study on the effects of 1-l infusions of 6% hydroxyethyl starch suspended in 0.9% saline (Voluven) and a balanced solution (Plasma Volume Redibag) on blood volume, renal blood flow velocity, and renal cortical tissue perfusion in healthy volunteers. Ann Surg 2014;259:881–7.

[19] Nadler SB, Hidalgo JH, Bloch T. Prediction of blood volume in normal human adults. Surgery 1962;51:224–32.

[20] Stewart PA. Modern quantitative acid-base chemistry. Can J Physiol Pharmacol 1983;61:1444–61.

[21] Cox EF, Buchanan CE, Bradley CR, Prestwich B, Mahmoud H, Taal M, et al. Multiparametric renal magnetic resonance imaging: validation, interventions, and alterations in chronic kidney disease. Front Physiol 2017;8:696.

[22] Sigmund EE, Vivier PH, Sui D, Lamparello NA, Tantillo K, Mikheev A, et al. Intravoxel incoherent motion and diffusion-tensor imaging in renal tissue under hydration and furosemide flow challenges. Radiology 2012;263:758–69.

[23] Hansen PB, Jensen BL, Skott O. Chloride regulates afferent arteriolar contraction in response to depolarization. Hypertension 1998;32:1066–70.

[24] Wilcox CS. Regulation of renal blood flow by plasma chloride. J Clin Invest 1983;71:726–35.

Supplementary methods

A series of scout images were initially acquired in three orthogonal planes to locate the kidneys, heart and vessels of interest to aid subsequent slice positioning. Baseline cardiac and renal MRI data were then collected comprising structural images to assess kidney volume, phase contrast (PC)-MRI to determine cardiac output and renal artery bulk flow, Arterial Spin Labelling (ASL) data to determine renal cortex tissue perfusion, and Diffusion Weighted Imaging (DWI) to determine the renal cortex apparent diffusion coefficient (ADC). These scans were repeated at 20 minute intervals over the course of the 60 min infusion and at 20 minutes post-infusion to assess the time-course of the response. Bladder volume was measured using MR cholangiopancreatography (MRCP) before and approximately 20 minutes after infusion end.

Cardiac output

PC-MRI was collected using an imaging plane placed perpendicular to the ascending aorta. Acquisition parameters comprised a single slice TFE sequence with 30 phases collected across the cardiac cycle with TE/TR 2.4/3.8ms, FA 15^{o}, number of excitations 3, reconstructed resolution $1.05 \times 1.05 \times 10$ mm^3, velocity encoding 200 cm/s. The TFE factor depended on the subjects' heart rate, data was acquired free breathing in approximately 1 minute. Analysis was performed using ViewForum software (Philips Medical Systems, Best, Netherlands). Arterial flow velocity (cm/s), area (mm^2) and, hence flow (ml/s) were calculated over the cardiac cycle. Cardiac output (L/min) was computed by multiplying stroke volume (i.e. the area under the flow curve within one cardiac cycle) and heart rate. Data were then body surface area (BSA) corrected to compute cardiac index (CI).

Renal volume

Coronal multi-slice balanced-Turbo-Field-Echo (bTFE) images were used to estimate renal volume, these comprised 30 slices of 1.75 x 1.75 x 7 mm^3, with data collected in single breath hold. Analyze9® software (Mayo Clinic) was used to draw a region of interest (ROI) to determine left and right kidney volume within each bTFE image slice. Total renal volume was then calculated from the sum of the volume measures computed across all the slices across both kidneys.

Renal artery blood flow (RABF) and global perfusion

PC-MRI was performed using a single slice TFE technique with the imaging plane placed perpendicular to the left renal artery. Imaging parameters were: echo time (TE)/repetition time (TR) 3.4/7.5 ms, FA 25°, number of excitations 2, reconstructed resolution 1.17 × 1.17 × 6 mm^3, velocity encoding 100 cm/s, with 20 phases collected across the cardiac cycle. Each renal artery measurement was acquired during a single 15-20 s breath hold. Analysis was performed using ViewForum software to compute mean arterial flow velocity (cm/s), mean area (mm^2) and thus mean flux (ml/s) over the cardiac cycle for the left renal artery. Global perfusion of the left kidney was then calculated by correcting left renal artery blood flow by left kidney volume.

Renal cortex perfusion

Respiratory-triggered Arterial Spin Labelling (ASL) data (288 × 300 mm^2 field of view (FOV), 3 × 3 × 8 mm^3 voxel size) were collected using a balanced fast field echo (bFFE) readout scheme [TE/TR 2.1/4.1 ms, SENSE 2, flip angle (FA) 60°, low-high acquisition, and half-Fourier acquisition] with 25 ASL pairs collected in approximately 5 minutes. A base M_0 equilibrium scan and T_1 longitudinal relaxation time map (collecting 13 inversion times of

200, 300, 400, 500, 600, 700, 800, 900, 1000, 1100, 1200, 1300 and 1500 ms using a modified respiratory triggering scheme in a total scan time of less than 3 minutes [1] were acquired for quantification of renal tissue perfusion [2]. Individual perfusion weighted difference images (control-label pairs) were computed, inspected for motion (exclude >1 voxel movement) and realigned, and averaged to create a single perfusion-weighted (PWI) map. Mean renal cortical perfusion was calculated across both kidneys from the PWI maps, T_1 maps and M_0 scans in a kinetic model to calculate tissue perfusion (f) maps (in ml/100 g tissue/min) [1].

Renal cortex diffusion

To obtain specific information on water diffusion in the kidney, diffusion weighted images were acquired with a spin-echo–echo planar imaging (SE-EPI) sequence. Imaging acquisition parameters were a 288 $\times$ 288 mm^2 FOV, 3 $\times$ 3 $\times$ 8 mm^3 voxel size, and TE of 56 ms. Eleven diffusion weighting factors (b-values) were acquired of 0, 5, 20, 60, 120, 190, 270, 370, 470, 580, 700 s/mm^2 to allow estimation of the apparent diffusion coefficient (ADC) and pure tissue molecular diffusion coefficient (D). To compute ADC maps, data was fit to the log of the exponential signal [1].

Bladder volume assessment

Bladder volume was measured using a single shot, fast spin echo sequence (similar to that used for MR cholangiopancreatography- MRCP, effective TE 283 ms) with 30 axial contiguous slices (reconstructed resolution 2 $\times$ 2 x 7 mm^3) acquired free breathing. Volumes were assessed by manually tracing ROIs around the bladder on each slice using Analyze9® software (Mayo Clinic) and summing across the slices.

References

1. Cox EF, Buchanan CE, Bradley CR, et al. Multiparametric renal magnetic resonance Imaging: validation, interventions, and alterations in chronic kidney disease. Front Physiol 2017;8:696.
2. Gardener AG, Francis ST. Multislice perfusion of the kidneys using parallel imaging: image acquisition and analysis strategies. Magn Reson Med 2010; 63: 1627-1636.

9.5 Publication V: Palaniyappan N, Cox E, Bradley CR, Scott R, Austin A, O'Neill R, Ramjas G, Travis S, White H, Singh R, Thurley P. Non-invasive assessment of portal hypertension using quantitative magnetic resonance imaging. Journal of hepatology. 2016 Dec 1;65(6):1131-9.

Research Article

JOURNAL OF HEPATOLOGY

Non-invasive assessment of portal hypertension using quantitative magnetic resonance imaging

Naaventhan Palaniyappan[1,†], Eleanor Cox[2,†], Christopher Bradley[2], Robert Scott[1], Andrew Austin[3], Richard O'Neill[4], Greg Ramjas[4], Simon Travis[4], Hilary White[4], Rajeev Singh[3], Peter Thurley[3], Indra Neil Guha[1], Susan Francis[2], Guruprasad Padur Aithal[1,*]

[1]*National Institute for Health Research (NIHR) Nottingham Digestive Diseases Biomedical Research Unit, Nottingham University Hospitals NHS Trust and University of Nottingham, United Kingdom;* [2]*Sir Peter Mansfield Imaging Centre, University of Nottingham, Nottingham, United Kingdom;* [3]*Royal Derby Hospital, Derby, United Kingdom;* [4]*Department of Radiology, Nottingham University Hospitals NHS Trust, Nottingham, United Kingdom*

See Editorial, pages 1079–1080

Background & Aims: Hepatic venous pressure gradient (HVPG) measurement is currently the only validated technique to accurately evaluate changes in portal pressure. In this study, we evaluate the use of non-contrast quantitative magnetic resonance imaging (MRI) as a surrogate measure of portal pressure.

Methods: Thirty patients undergoing HVPG measurement were prospectively recruited. MR parameters of longitudinal relaxation time (T_1), perfusion of the liver and spleen (by arterial spin labelling), and blood flow in the portal, splanchnic and collateral circulation (by phase contrast MRI) were assessed. We estimated the liver stiffness measurement (LSM) and enhanced liver fibrosis (ELF) score. The correlation of all non-invasive parameters with HVPG was evaluated.

Results: The mean (range) HVPG of the patients was 9.8 (1–22) mmHg, and 14 patients (48%) had clinically significant portal hypertension (CSPH, HVPG $\geqslant$10 mmHg). Liver T_1 relaxation time, splenic artery and superior mesenteric artery velocity correlated significantly with HVPG. Using multiple linear regression, liver T_1 and splenic artery velocity remained as the two parameters in the multivariate model significantly associated with HVPG ($R = 0.90$, $p < 0.001$). This correlation was maintained in patients with CSPH ($R = 0.85$, $p < 0.001$). A validation cohort (n = 10) showed this linear model provided a good prediction of HVPG. LSM and ELF score correlated significantly with HVPG in the whole population but the correlation was absent in CSPH.

Conclusions: MR parameters related to both hepatic architecture and splanchnic haemodynamics correlate significantly with HVPG. This proposed model, confirmed in a validation cohort, could replace the invasive HVPG measurement.

Lay summary: In patients with cirrhosis, the development and progression of portal hypertension is related to worse outcomes. However, the standard technique of assessing portal pressure is invasive and not widely used in clinical practice. Here, we have studied the use of non-invasive MRI in evaluating portal pressure. The MRI measures of liver architecture and blood flow in the splenic artery correlated well with portal pressure. Therefore, this non-invasive method can potentially be used to assess portal pressure in clinical trials and monitoring treatment in practice.

Introduction

The majority of complications in patients with cirrhosis result from the development and progression of portal hypertension characterised by increased intrahepatic resistance and progressive splanchnic vasodilation. Distortion of hepatic architecture resulting from fibrogenesis and nodule formation results in 'static' hepatic vascular resistance, whilst a 'dynamic' component results from the active contraction of myofibroblasts and increased hepatic vascular tone [1]. The rise of portal pressure is perpetuated by the excessive release of endogenous vasodilators resulting in splanchnic vasodilation and increased portal blood flow.

Hepatic venous pressure gradient (HVPG) measurement [2] is the only validated technique to accurately evaluate changes in portal pressure. An HVPG threshold of 10 mmHg is termed clinically significant portal hypertension (CSPH) as it predicts the risk of formation of oesophageal varices [3], clinical decompensation [4] and development of hepatocellular carcinoma [5]. An HVPG >12 mmHg is associated with the risk of variceal bleeding [6] and an HVPG >16 mmHg correlates with increased mortality [7,8], whilst in acute variceal bleeding an HVPG $\geqslant$20 mmHg is an independent prognostic marker [9]. However, HVPG measurements are invasive and available only in specialised hepatology units, precluding its use in routine clinical practice. Thus, the development of non-invasive markers of portal pressure is highly desirable.

Keywords: Portal hypertension; Hepatic venous pressure gradient; Magnetic resonance imaging; Longitudinal T_1 relaxation time.

Received 21 December 2015; received in revised form 19 July 2016; accepted 21 July 2016; available online 27 July 2016

* Corresponding author. Address: NIHR Nottingham Digestive Diseases Biomedical Research Unit at the Nottingham University Hospitals NHS Trust and the University of Nottingham, Queens Medical Centre Campus, E Floor, West Block, Derby Road, Nottingham NG7 2UH, United Kingdom. Tel.: +44 115 746 5124.

E-mail address: guru.aithal@nottingham.ac.uk (G.P. Aithal).

† These authors contributed equally as joint first authors.

Liver stiffness measurement (LSM) as assessed with transient elastography (TE) has been suggested as an alternative measurement to HVPG. LSM is thought to reflect hepatic fibrosis and the resulting intrahepatic resistance. A significant correlation of LSM with HVPG has been demonstrated at an HVPG <10 mmHg, but no statistical significance at an HVPG >12 mmHg [10]. This has led to the suggestion that LSM can identify clinically significant or severe portal hypertension, but is not a good marker of its subsequent progression. This is likely due to extrahepatic factors, such as splanchnic vasodilation and a hyperdynamic circulation, that perpetuate the rise in portal pressure but do not affect the liver tissue stiffness [11]. TE has also been used to measure spleen stiffness which is able to identify the presence of varices and a linear model of spleen and liver stiffness predicting HVPG with a high accuracy [12]. However, there are significant technical challenges related to spleen size and an upper detection limit for tissue stiffness that limit the applicability of this technique. Magnetic resonance elastography (MRE) has the theoretical advantage over TE of assessing liver and splenic stiffness across a larger tissue area. In 36 patients with cirrhosis, MRE-measured loss modulus of the liver and spleen correlated well with HVPG ($R = 0.44$, $p = 0.02$, and $R = 0.57$, $p = 0.002$, respectively) [13]. However, the accessibility of this technique due to hardware availability and cost, and the feasibility of MRE in some patients, can limit its clinical translation.

The ratio of liver to spleen volume as measured by computed tomography has also been shown to predict HVPG, however this measure has the disadvantage of requiring ionising radiation [14]. Using Doppler ultrasound, changes in hepatic and splanchnic flow in portal hypertension have been studied, but results have been inconsistent [15], limiting wider use of this technique [16]. To date, all of these imaging modalities have investigated individual pathophysiological components of portal hypertension.

Recent advances in magnetic resonance imaging (MRI) have made it possible to measure multiple parameters associated with structural [17], blood flow [18] and perfusion [19] changes in the liver in a single scan session. Further, since MRI is non-invasive, repeated assessments are feasible and acceptable. The aim of this current study is to develop quantitative MRI as a surrogate of portal pressure. The MRI parameters of interest relate to the size, architecture and perfusion of the liver and spleen, and changes in portal and splanchnic blood flow. Specifically, we aim to study the correlation of these MRI variables with HVPG.

Materials and methods

Study population

Consecutive patients undergoing HVPG measurement for clinical indications at Nottingham University Hospitals NHS Trust and Derby Teaching Hospitals NHS Foundation Trust between April 2013 and June 2016 were prospectively screened and included in the study, providing a broad range of HVPG values. We excluded patients with hepatocellular carcinoma, portal or hepatic vein thrombosis, absolute contraindications for MR, abdominal/waist circumference larger than 112 cm (due to MR scanner bore constraints), age <18 years and pregnancy.

Thirty-four patients were enrolled for the derivation cohort. Four patients were excluded from the final analysis; three patients did not complete the MR scanning protocol due to claustrophobia, one patient had liver histology compatible with non-cirrhotic portal hypertension. MRI and LSM with TE were performed on the same day and within 6 weeks of the HVPG measurement. Patients received no therapeutic interventions between the HVPG measurement and MRI session.

The study protocol was approved by Staffordshire Research Ethics Committee (Ref 12/WM/0288). Patients gave written informed consent in accordance with the principles of the Declaration of Helsinki (revision of Edinburgh 2000).

HVPG measurement

HVPG measurements were carried out by interventional radiologists. HVPG was measured according to established standards [2] following an overnight fast. Under ultrasonographic guidance, the right internal jugular vein was cannulated and a 9-French vascular sheath placed by the modified Seldinger technique. A 6-French compliant balloon-tipped catheter (Berenstein occlusion catheter, Boston Scientific, UK) was guided into the right hepatic vein for the measurement of wedged and free hepatic venous pressures as recommended [8]. All measurements were obtained in triplicate and recorded via a pre-calibrated Philips IntelliVue MP50 patient monitor (Philips Healthcare, UK). HVPG was calculated from the difference between wedged hepatic pressure and free hepatic pressure, and the mean of triplicate measurements computed.

Liver stiffness measurement (LSM)

LSM was performed prior to the MRI scan, following an overnight fast, using FibroScan® (Echosens, Paris, France) by experienced operators [20]. Due to technical reasons, LSM values were not available on 2 patients, and measurements on 6 patients were unreliable (median LSM >7.1 kPa and interquartile range/median ratio >0.30).

Enhanced liver fibrosis (ELF) score

Blood samples were obtained prior to the MRI scan session. Serum samples were analysed for levels of tissue inhibitor of matrix metalloproteinase-1 (TIMP1), hyaluronic acid (HA) and aminoterminal peptide of procollagen III (P3NP) at an independent reference laboratory (iQur Limited, London, UK). The ELF score was calculated using an established algorithm [21].

MR data acquisition

All patients were scanned following an overnight fast on a 1.5 Tesla scanner (Achieva, Philips Medical Systems) with body transmit coil and 16-channel SENSE torso receive coil. All MR measures were acquired in a 1 h scan session.

Liver and spleen volume

Multi-slice balance turbo field echo (bTFE) localiser images were initially acquired in three orthogonal directions to locate the anatomy of organs and blood vessels of interest, and to estimate liver and spleen volume.

Longitudinal relaxation time (T_1) of liver and spleen

A modified respiratory triggered inversion recovery sequence with spin-echo echo planar imaging (SE-EPI) readout ($3 \times 3 \times 8\ mm^3$ voxel size, 4 mm slice gap (33%), 96×96 image matrix, SENSE factor 2, echo time 27 ms) and fat suppression [17] was acquired to estimate the tissue longitudinal relaxation time (T_1) in the liver from 13 inversion times (100–1200 ms in 100 ms steps and 1500 ms). Three sagittal SE-EPI slices were acquired through the right lobe of the liver with minimal temporal slice spacing (65 ms) in approximately 2 min, dependent on the patients' respiratory rate.

In addition, T_1 maps of the liver and spleen were acquired using a modified respiratory triggered inversion recovery sequence with a balanced steady state free precession (bSSFP, also termed bFFE (balanced fast field echo)) readout (echo/repetition time = 1.75/3.5 ms, flip angle (FA) 60°, linear k-space acquisition, SENSE 2, resolution $3 \times 3 \times 8\ mm^3$). These maps were primarily collected to yield voxel wise T_1 values for the quantification of perfusion measures (see tissue perfusion section), but also provided an alternative T_1 measure from a bSSFP readout scheme as used by others for liver T_1 mapping [22]. This readout scheme results in an apparent recovery time (T_1^*), shorter than the actual longitudinal recovery time T_1 due to the influence of T_2/T_2^* [23]. For coverage of the liver and spleen, 5 coronal-oblique bFFE slices were collected at 9 inversion times (100–900 ms in 100 ms steps) with minimal temporal slice spacing (144 ms) in both ascend and descend slice acquisition order, thus increasing the dynamic range of inversion time values to (100–1500 ms), with data collected in 3 min.

Splanchnic and portal flow measurements

Phase contrast (PC)-MRI was used to quantify the velocity and cross-sectional area of the portal vein and hepatic artery (hepatic inflow), and the right, middle, left hepatic veins (hepatic outflow), as well as the splenic artery (SA) and superior mesenteric artery (SMA) (flow in splanchnic circulation) and azygous vein (collateral flow). Blood flow in each vessel was measured using a vectorcardiogram (VCG) gated 2D PC-MR on a single slice perpendicular to each targeted vessel of interest (echo/repetition time = 4.2/7.5 ms, FA 25°, field of view 280 × 146 mm^2, reconstructed resolution 1.5 × 1.5 × 6 mm^3, SENSE 3, 2 averages). 15 phases were collected for vein measurements and 20 phases for the arteries across the cardiac cycle, with defined velocity encoding (V_{ENC}) for each vessel (portal/hepatic/azygous veins V_{ENC} = 50 cms^{-1}, hepatic/splenic arteries V_{ENC} = 100 cms^{-1}, and SMA V_{ENC} = 140 cms^{-1}). If aliasing occurred, the V_{ENC} was increased and the measure repeated. A flow measurement in each vessel was obtained in triplicate and the mean calculated. Each measurement was acquired during a 15–20 s breath-hold, dependent on the subjects' heart rate.

Tissue perfusion

A multiphase flow alternating inversion recovery arterial spin labelling (ASL) sequence [24] using a bFFE readout (echo/repetition time = 1.75/3.5 ms, FA 45°, linear k-space acquisition, SENSE 2, resolution 3 × 3 × 8 mm^3) was used to quantify tissue perfusion in the liver and spleen. Data were collected with patients breathing freely by introducing a respiratory trigger delay of 200 ms prior to ASL labelling. Labelling was followed by a multiphase Look-Locker sampling scheme with an initial delay of 100 ms and subsequent readout spacing of 371 ms with 6 readout phases collected. Liver ASL data was acquired for a sagittal slice through the right lobe of the liver (50 ASL label/control pairs), whilst spleen data was acquired for a coronal-oblique slice through the spleen (30 ASL label/control pairs). In addition, equilibrium base magnetisation (M_0) images were acquired for each slice orientation as well as a T_1 map (see Longitudinal relaxation time (T_1) of liver and spleen section) to allow quantification of perfusion.

MR data analysis

The investigators analysing the MR data were blind to the HVPG measurements.

Liver and spleen volume

Analyze® software (Mayo Clinic) was used to draw a region of interest around the liver and spleen within each bTFE image slice. Total liver and spleen organ volume was calculated from the sum of the volume measures across all slices.

Longitudinal relaxation time (T_1) of liver and spleen

Inversion recovery data were fit to $S(t) = M_0{}^*abs\ (1–2exp(–t/T_1))$ to generate T_1 and M_0 maps for the SE-EPI data, and estimate apparent T_1 relaxation time ($T_1{}^*$) for the bFFE data. Binary organ masks were formed from the M_0 image by manual segmentation. Histogram analysis was used to assess the distribution of relaxation time values within the liver and spleen. For the liver and spleen in each subject, and for each readout, a histogram of voxel values was fit to a Gaussian function and the peak (distribution mode) used to represent the T_1 or $T_1{}^*$ tissue relaxation time. This method provides an automated method to eliminate voxels containing blood in vessels [17]. In addition, the full-width-half-maximum (FWHM) of the Gaussian function was calculated to reflect the degree of heterogeneity of relaxation time values. All subjects were confirmed to have liver tissue $T_2{}^*$ >22.6 ms [17].

Splanchnic and portal flow measurements

PC-MR data were analysed using Qflow software (Philips Medical System). For each vessel, a region of interest was drawn manually around the vessel lumen on each phase contrast image, with contour detection used. The mean signal intensity within each region of interest reflects flow velocity in the vessel of interest (cm/s) for each cardiac phase, and the mean velocity across the cardiac cycle was computed. The cross-sectional area of each vessel lumen was multiplied by the mean velocity, to compute mean blood flow (ml/s) in each vessel. From triplicate measures, the mean and coefficient of variation (CoV) in all flow measures was estimated.

Liver tissue perfusion

Individual perfusion-weighted difference images (control–label) were calculated for each of the 6 ASL readout phases. These were inspected for motion (excluding control/label pairs with movement of >1 voxel) and averaged to create a single perfusion-weighted (ΔM) map for each phase. Mean values of ΔM, the base equilibrium magnetisation M_0 and T_1 were used in an iterative model [19] to calculate tissue perfusion (ml/100 g/min) and tissue arrival time of the label (ms), assuming a T_1 of blood at 1.5 T of 1.36 s.

Statistical analysis

Statistical analysis was performed using SPSS software version 21(IBM©). Quantitative variables were expressed as mean ± standard deviation (SD), and qualitative variables as absolute and relative frequencies. Shapiro-Wilk test was used to test the normality of the data. HVPG was used as a continuous parameter, and correlations between variables and HVPG were computed using Pearson's or Spearman Rho correlation coefficient (R) as guided by the normal distribution of the data. MR measures that significantly correlated with HVPG in the univariate analyses were included in a multivariate linear regression analysis. In all analyses, p <0.05 was considered statistically significant. Due to the exploratory nature of this study, no adjustments were made for multiple comparisons.

Results

Patient characteristics

All major clinical and biochemical parameters of the initial patient group are presented in Table 1. Eighteen patients (60%) had histological evidence of cirrhosis and 4 patients (13%) had advanced fibrosis. In those with cirrhosis, 14 patients underwent oesophagogastroduodenoscopy (OGD) and oesophageal varices were present in five. In the whole population, nine patients (30%) had no portal hypertension (HVPG ⩽5 mmHg), 21 patients (70%) had portal hypertension of which 14 patients (47%) had clinically significant portal hypertension (HVPG >10 mmHg).

Table 1. Clinical and laboratory features of the study population.

Variable	All patients (n = 30)
Age, years	55 ± 13
Gender M/F	14/16
BMI	27.0 ± 5.2
Aetiology (%)	
Alcohol	9 (30%)
NAFLD	13 (43%)
Autoimmune liver disease	5 (17%)
Histological fibrosis staging	
No fibrosis	4 (13%)
Pericellular fibrosis	4 (13%)
Bridging fibrosis	4 (13%)
Cirrhosis	18 (60%)
Aspartate transaminase (AST), U/L	59.6 ± 40.0
Alanine transaminase (ALT), U/L	49.4 ± 38.4
Bilirubin, μmol/L	25.2 ± 26.7
Alkaline phosphatase (ALP), U/L	141.0 ± 106.8
Albumin, g/L	37.7 ± 5.9
Prothrombin time, seconds	11.7 ± 2.1
Platelet count, x10^9/L	155.7 ± 81.3
Serum sodium, mmol/L	137.8 ± 2.7
Serum creatinine, μmol/L	65.8 ± 23.6
Time between HVPG and MRI, days	25 ± 12
Liver stiffness, kPa	17.5 ± 15.5
HVPG, mmHg	9.8 ± 6.1
HVPG >5 mmHg, n (%)	21 (70%)
CSPH, HVPG ≥10 mmHg, n (%)	14 (47%)

ELF markers and LSM as predictors of HVPG

The ELF score correlated significantly with HVPG (Pearson $R = 0.758$, $p < 0.001$). There was a significant correlation between each of the individual components of the ELF score with HVPG; HA (Spearman $R = 0.752$, $p < 0.001$), P3NP (Spearman $R = 0.607$, $p = 0.001$) and TIMP1 (Pearson $R = 0.512$, $p = 0.006$) (Fig. 1). Valid LSM, as measured by TE, were available in 22 patients. LSM correlated significantly with HVPG (Spearman $R = 0.791$, $p < 0.001$) (Fig. 2A). However, for both ELF scores and LSM, there was no significant correlation in the subgroup of patients with portal hypertension and CSPH at HVPG >10 mmHg.

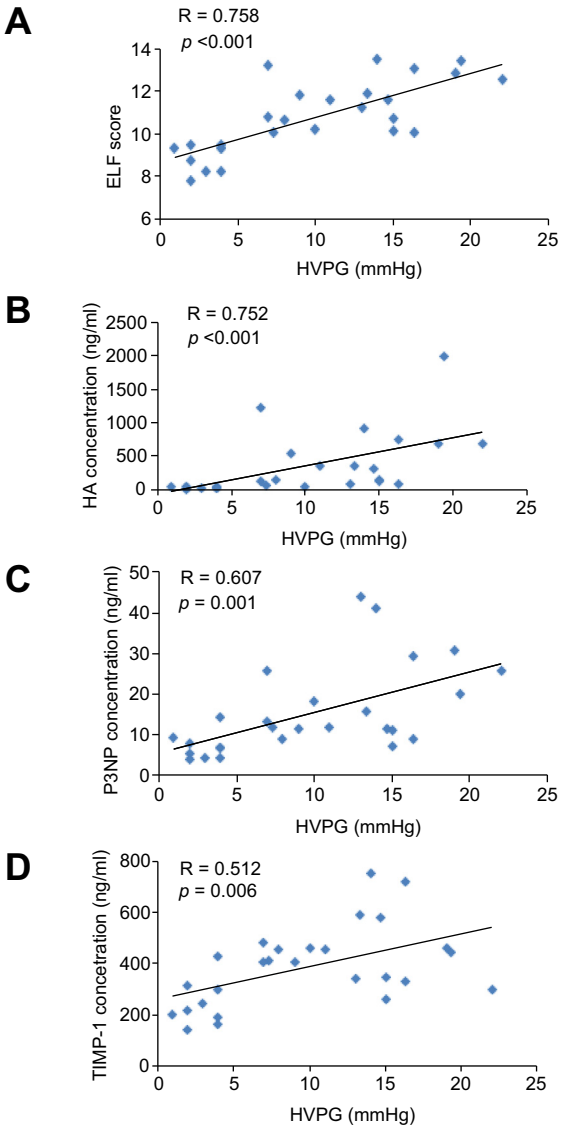

Fig. 1. Correlation between HVPG and serum markers of liver fibrosis. (A) Enhanced Liver Fibrosis (ELF) score, (B) hyaluronic acid (HA), (C) aminoterminal peptide of procollagen III (P3NP) and (D) tissue inhibitor of matrix metalloproteinase 1 (TIMP-1) concentrations.

Longitudinal relaxation time (T_1) as a predictor of HVPG

Considering the whole patient group, there was a statistically significant positive correlation between HVPG and SE-EPI liver T_1 relaxation time (Pearson $R = 0.835$, $p < 0.001$; Predicted HVPG = 585 + 15*(Liver SE-EPI T_1)) (Fig. 2B). This relationship was maintained in patients with portal hypertension with HVPG >5 mmHg (Pearson $R = 0.683$, $p = 0.001$) as well as CSPH with HVPG $\geqslant$10 mmHg (Pearson $R = 0.651$, $p = 0.012$). The mean (± SD) number of voxels in the mask for liver T_1 measurements was 3911(± 1463). The FWHM of the liver SE-EPI T_1 Gaussian distribution showed a significant positive correlation with HVPG (Spearman $R = 0.611$, $p < 0.001$) (Fig. 2C), reflecting the increased heterogeneity in liver T_1 with increased severity of portal hypertension.

The apparent liver relaxation time (T_1^*) measured from bFFE maps was also a predictor of HVPG. As expected, the bFFE readout T_1^* relaxation time was highly correlated with the SE-EPI T_1 value (Pearson $R = 0.890$, $p < 0.001$), but was lower than that of the true T_1 measured using a SE-EPI readout, (Liver SE-EPI T_1) = 141 + 0.92*(Liver bFFE T_1^*) (median Gaussian distribution values). A significant positive correlation of the bFFE T_1^* relaxation time with HVPG was found (Pearson $R = 0.780$, $p < 0.001$), which was significant for HVPG >5 mmHg (Pearson $R = 0.524$, $p = 0.018$).

Spleen T_1^*, estimated from the bFFE readout scheme, correlated with HVPG in the whole patient group (Pearson $R = 0.40$, $p = 0.028$) but this relationship was not significant in patients with portal hypertension and CSPH with HVPG $\geqslant$10 mmHg. Fig. 3 illustrates example coronal bFFE T_1^* maps for patients with increasing HVPG measures.

Splanchnic and portal flow measures in predicting the HVPG

There was no significant relationship between inflow (portal vein, hepatic artery or total hepatic inflow) and outflow (right, middle and left or total hepatic veins) of the liver with HVPG (Table 2). Whilst in the splanchnic circulation, velocity of the blood flow in the SMA and SA correlated significantly with HVPG (Pearson $R = 0.534$, $p = 0.002$, $R = 0.584$, $p = 0.003$ respectively, Fig. 4A-B). A significant positive correlation of SA velocity with HVPG was found for HVPG >5 mmHg (Pearson $R = 0.555$, $p = 0.032$), no significant correlation with SMA velocity was found for HVPG >5 mmHg or HVPG $\geqslant$10 mmHg. No significant correlations were found between SMA or SA velocity at HVPG <10 mmHg, highlighting the haemodynamic changes associated with CSPH. In the azygous vein, velocity and flow correlated significantly with HVPG (Spearman $R = 0.515$, $p = 0.004$ and $R = 0.656$, $p < 0.001$ respectively) (Fig. 4C). In patients with CSPH, no MR flow parameters correlated significantly with HVPG. The within session CoV for PC-MR vessel measures are shown in Table 2.

Tissue perfusion and relationship with HVPG

Valid liver perfusion measurements were obtained in 28 patients and spleen perfusion measurements in 26 patients. Liver tissue perfusion correlated positively with HVPG (Spearman $R = 0.38$, $p = 0.046$) and tissue arrival time negatively correlated with HVPG (Spearman $R = -0.467$, $p = 0.021$). However, this relationship was not present in patients with portal hypertension and CSPH. Spleen tissue perfusion was not related to HVPG.

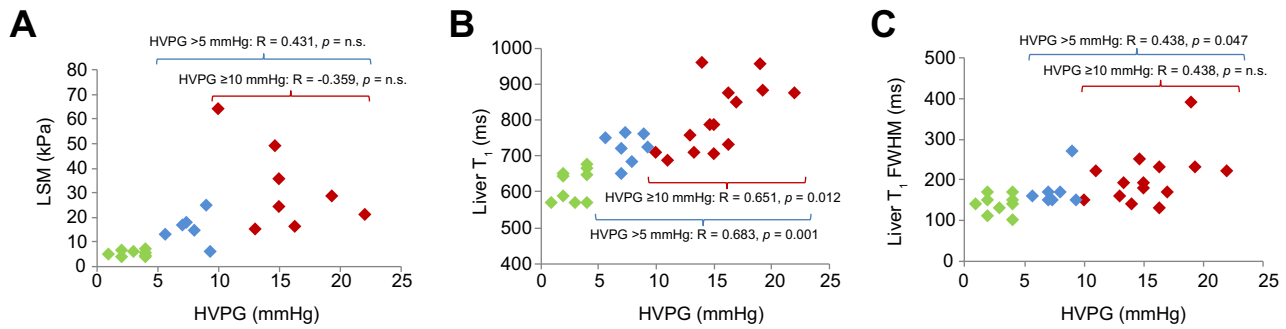

Fig. 2. Correlation of HVPG with imaging markers of liver fibrosis. (A) liver stiffness measurement (LSM), (B) liver SE-EPI T_1 relaxation time (ms) and (C) the full-width-half-maximum (FWHM) of liver SE-EPI T_1 Gaussian distribution (ms).

Spleen and liver volume and their ratio to predict HVPG

Liver volume and spleen volume did not independently correlate with HVPG. The ratio of liver/spleen volume negatively correlated significantly with HVPG (Pearson $R = -0.40$, $p = 0.028$), but this relationship was absent in patients with portal hypertension and CSPH.

Predictive MR model of HVPG

Table 3 shows those MR parameters that correlated with HVPG in the univariate analysis. The best predictive model for HVPG (that provides the minimum sum-of-squares between measured and predicted HVPG) included liver SE-EPI T_1 relaxation time and SA velocity:

HVPG = $-28 + 0.04^{*}$(Liver SE-EPI T_1) + 0.27^{*}(SA velocity) (Spearman $R = 0.90$, $p < 0.001$),

This correlation was maintained in patients with CSPH ($R = 0.85$, $p < 0.001$).

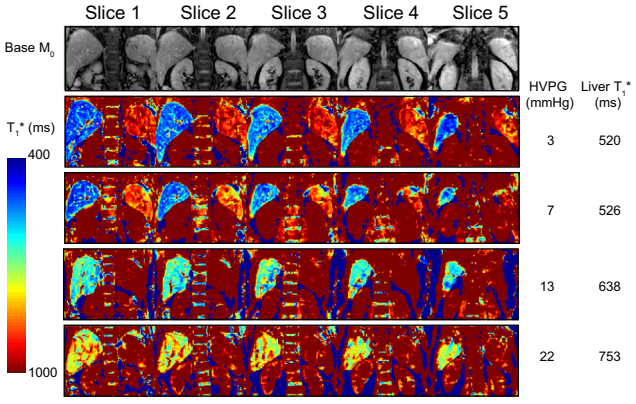

Fig. 3. Example of T_1 relaxation maps. Top row shows example image quality of the coronal-oblique imaging slices for base equilibrium M_0 data acquired from a patient with HVPG of 3 mmHg. Subsequent rows show example coronal-oblique bFFE T_1* maps showing the liver and spleen, together with HVPG (mmHg) and mode of the liver T_1* value (ms) across a range of HVPG from 3–22 mmHg, with columns showing each of the five slices collected for the T_1* map.

Validation cohort

Additionally, 10 patients were enrolled to the study as a validation cohort, which included 4 with non-alcoholic fatty liver disease, 4 with alcoholic liver disease, 1 each with primary biliary cholangitis and autoimmune hepatitis. Of these, 4 patients had portal hypertension, of which 2 had CSPH. In this cohort, there was a statistically significant positive correlation between HVPG and the SE-EPI T_1 relaxation time of the liver (Pearson $R = 0.83$, $p = 0.003$). Fig. 5 illustrates a Bland-Altman plot showing predicted HVPG using liver SE-EPI T_1 alone, and the combined model of liver SE-EPI T_1 and the haemodynamic measure of SA velocity. The combined model can be seen to yield an improved estimation of HVPG, particularly in CSPH.

Discussion

In liver cirrhosis, the disruption of sinusoidal architecture with progressive fibrogenesis and intrahepatic vasoconstriction leads to an increase in intrahepatic resistance resulting in the rise of portal pressure. This is further accentuated by splanchnic vasodilation and increased portal blood flow. In the present study we have demonstrated that a combination of non-invasive quantitative MR measures of liver SE-EPI T_1 relaxation time and SA velocity can provide a non-invasive estimation of portal pressure. The combined model of structural and haemodynamic MR measures identified in this study provides the best predictor to accurately reflect the portal pressures through its full range from normal to CSPH (Fig. 5).

The relationship between the degree of hepatic fibrosis and portal pressure has been reported from studies comparing histological changes in liver biopsy with HVPG. For example, quantitative liver biopsy analysis with collagen proportionate area measurement correlated significantly with HVPG [25]. However, histological analyses are limited by the inherent sampling variability associated with liver biopsies [26,27]. We have previously shown that liver T_1 relaxation time is associated with the degree of fibrosis and inflammation in the liver [17]. This acquisition and analysis approach has been shown to be highly repeatable in healthy subjects [17], with a CoV between visits of 1.8%, and a low inter- and intra-observer variability with intra-class

Table 2. Correlation coefficient and *p* value of portal, splanchnic and collateral circulation flow parameters as measured by phase contrast MR with HVPG, and the intra-session coefficient of variation (CoV) of flow measures.

		All patient group		CSPH, HVPG ≥10 mmHg		CoV, % (Mean ± SD)
		Correlation coefficient, R	*p* value	Correlation coefficient, R	*p* value	
Portal vein n = 30	Area	0.141	0.464	0.182	0.533	3.0 ± 2.0
	Velocity	-0.028	0.882	-0.158	0.589	6.3 ± 4.5
	Flow	0.105	0.581	0.114	0.698	6.0 ± 3.5
	Fraction of total inflow	-0.322	0.102	-0.217	0.477	
Hepatic artery n = 28	Area	0.104	0.605	-0.167	0.585	11.5 ± 6.8
	Velocity	0.295	0.128	0.327	0.275	12.5 ± 8.3
	Flow	0.240	0.218	0.095	0.759	12.5 ± 7.9
	Fraction of total inflow	0.322	0.102	0.217	0.477	
Total hepatic inflow		0.166	0.407	0.065	0.834	
Right hepatic vein n = 30	Area	-0.138	0.482	0.022	0.943	12.3 ± 11
	Velocity	0.114	0.548	-0.02	0.947	11.4 ± 9.4
	Flow	-0.296	0.112	-0.237	0.415	9.5 ± 7.4
Middle hepatic vein n = 27	Area	-0.270	0.183	0.05	0.872	11.8 ± 8.8
	Velocity	0.263	0.185	-0.018	0.955	10.4 ± 9.2
	Flow	0.016	0.936	-0.358	0.229	11.2 ± 8.3
Left hepatic vein n = 22	Area	-0.001	0.996	-0.067	0.854	12.7 ± 9.4
	Velocity	0.060	0.789	0.186	0.607	15.1 ± 11.8
	Flow	0.158	0.483	0.232	0.520	11.3 ± 11.4
Total hepatic outflow		-0.311	0.131	-0.356	0.233	
Superior mesenteric artery n = 30	Area	-0.402*	0.031	-0.156	0.595	5.8 ± 4.6
	Velocity	0.534**	0.002	-0.253	0.384	4.8 ± 3.4
	Flow	0.265	0.156	-0.250	0.389	6.2 ± 4.4
Splenic artery n = 24	Area	-0.107	0.636	-0.201	0.531	9.6 ± 6.0
	Velocity	0.584**	0.003	0.572	0.052	8.8 ± 5.6
	Flow	0.244	0.250	0.172	0.594	11.1 ± 6.6
Azygous vein n = 30	Area	0.341	0.065	0.484	0.079	7.9 ± 7.8
	Velocity	0.515**	0.004	-0.290	0.314	10 ± 7.4
	Flow	0.656**	<0.001	0.273	0.345	10.6 ± 7.5

correlation coefficients of more than 0.99. Here, SE-EPI T_1 data were acquired with fat suppression, removing the effect of fat on the calculated liver T_1 value, which results from the water liver tissue compartment. In contrast, T_1^* data acquired with a bFFE readout is affected by the hepatic fat content in a manner dependent on the phase between the fat and water signal (as determined by field strength and repetition time) [28]. Further since our T_1 measurement method is both respiratory triggered and multi-slice, it allows a large volume of the liver to be sampled [mean (± SD) of 3911 (± 1463) voxels covering 281 (± 106) cm^3] in a reasonable imaging time without the need for breath-hold, making this imaging scheme ideal for patient studies. Previous studies using a modified look-locker inversion recovery (MOLLI) T_1 mapping method with bFFE readout have shown a correlation with fibrosis [22]. However, this technique requires a breath-hold for each slice acquired, and it has been shown that hepatic fat content can be large enough to cause severe MOLLI T_1 alterations [28]. The distribution of liver T_1 values (Gaussian FWHM) was also shown to increase with the worsening portal hypertension, reflecting the increasing heterogeneity of T_1 values across the liver volume. This emphasises the sampling variability associated with liver biopsy and potentially TE, and highlights the need for architectural changes to be studied across the whole liver. In the subgroup of patients with portal hypertension and CSPH, the correlation between liver SE-EPI T_1 relaxation time and HVPG remained significant, demonstrating its applicability in assessing portal pressure in patients with severe portal hypertension. There was no corresponding correlation between LSM and HVPG over this higher HVPG range in patients with portal hypertension and CSPH. Our findings are similar to those of Vizutti and colleagues who also report that LSM did not correlate with HVPG >10 mmHg and it is likely that LSM does not reflect the extrahepatic haemodynamic changes in advanced portal hypertension. The correlation between the ELF score and HVPG has not been previously reported. However, similar to the LSM, the correlation was lost in patients with portal hypertension and CSPH. A previous study has demonstrated the correlation of MRE-measured liver loss modulus with HVPG ($r = 0.44$, $p = 0.02$) [13], a lower correlation than using T_1 alone. It would be of interest to use T_1 measures in conjunction with MRE-derived assessment of liver stiffness to assess the prediction of HVPG.

We show a significant correlation between blood flow velocity in the splanchnic circulation, in SMA and SA with HVPG, which is likely to represent the hyperdynamic state in portal hypertension. Previous Doppler ultrasound studies have reported increased flow in the SMA and SA in patients with cirrhosis [29] but no direct comparisons with HVPG have been made. Doppler ultrasound has also been widely used to assess the changes in portal and splanchnic blood flow in liver disease. However, the reproducibility of Doppler ultrasound has been questionable with high intra- and inter-observer variation [16,30]. PC-MR is a non-invasive flow measurement technique without intravenous

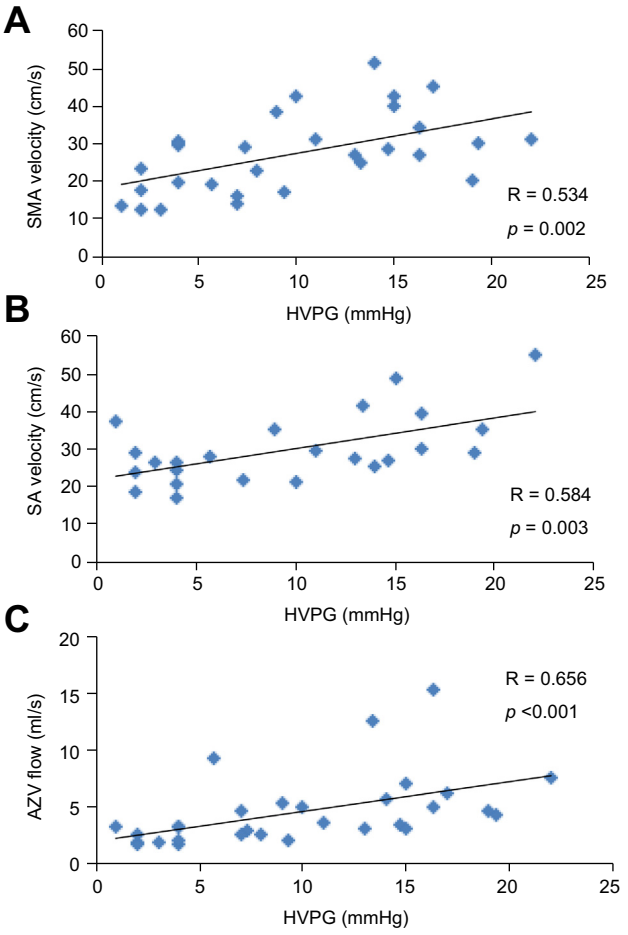

Fig. 4. Correlation of HVPG with splanchnic and collateral flow. (A) superior mesenteric artery (SMA) velocity, (B) splenic artery (SA) velocity and (C) azygous vein (AZV) flow.

Table 3. Correlation coefficient and *p* value of MR variables included in univariate analysis.

Variable	Univariate		Multivariate
	Correlation coefficient, R	*p* value	*p* value
Liver SE-EPI T^1	0.835	<0.001	<0.001
Liver bFFE T^{1*}	0.780	<0.001	<0.001
Spleen bFFE T^{1*}	0.400	0.028	
Splenic artery velocity	0.584	0.003	0.002
SMA velocity	0.534	0.002	
Azygous vein flow	0.656	<0.001	
Liver arrival time	-0.572	0.004	
Ln (liver/spleen volume)	-0.400	0.028	

contrast, whereby the phase shift of flowing blood is proportional to the velocity. Yzet and colleagues reported that PC-MR was a more reliable measure of hepatic blood flow compared to Doppler ultrasound with lower variability and higher reproducibility [18]. In this study, we have shown that within session CoV of the

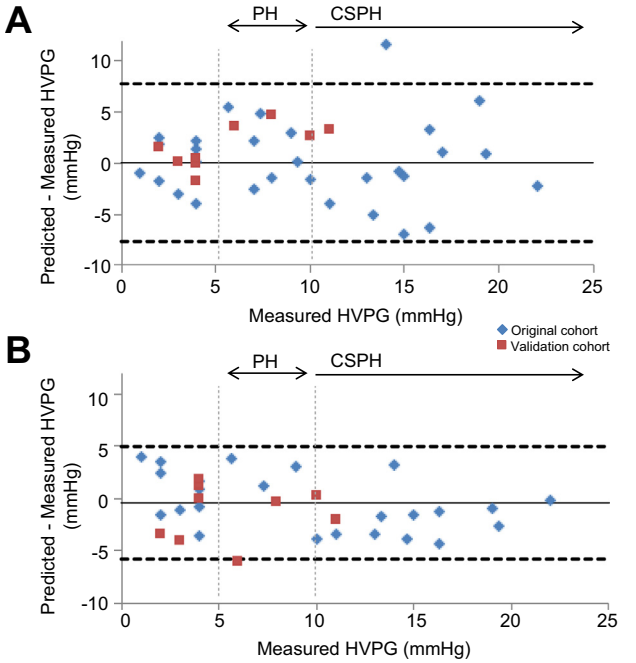

Fig. 5. Predictive MRI model for HVPG. Bland-Altman plot showing the difference between measured and predicted HVPG against the measured HVPG using (A) liver SE-EPI T_1 relaxation time alone, and (B) predictive MR model of liver SE-EPI T_1 relaxation time and splenic artery velocity. Data shown for original (blue diamonds) and validation cohort (red squares), with mean difference (solid line) and ±1.96 standard deviations (broken line) shown.

velocity measurement of SMA and SA by PC-MR is less than 10%, in agreement with a previous study [31].

It is an interesting observation that HVPG can potentially be assessed non-invasively using a simple linear model of MRI parameters of liver SE-EPI T_1 relaxation time and SA velocity. Fig. 5 highlights that this linear model provides good prediction of HVPG across the span of HVPG values from normal to CSPH, better than SE-EPI liver T_1 relaxation time (or SA velocity) alone. The scan time required to collect the data for this model (Liver T_1 and triplicate SA data) is 5–10 min, dependent on breathing rate of the patient, with PC-MR data being planned whilst the respiratory triggered T_1 sequence is acquired.

Various non-invasive markers of HVPG, including LSM, have been reported as being accurate as a binary predictor of the presence or absence of CSPH [32]. However, we believe that the MR measures of hepatic architecture and splanchnic haemodynamics do have the advantage of being able to accurately estimate HVPG values on a continuous scale as identification of the progression of portal hypertension beyond the threshold of CSPH (HVPG $\geqslant$10 mmHg), and this has prognostic implications in patients with cirrhosis [7,9]. We could potentially utilise this MR model to monitor the HVPG response in portal hypertensive patients. For example, MRE has been used for the first time in a recent clinical trial [33], and this proposed algorithm could now be used in future trials in cirrhosis patients to potentially demonstrate and assess diagnostic test characteristics, for example to assess beta-blocker therapy for lowering of HVPG (HVPG to <12 mmHg or reduction of 20% from baseline).

Here, we have included all patients who were undergoing HVPG measurements for clinical suspicion of portal hypertension

in our study population. Although patients without cirrhosis and portal hypertension were included in the study, this reflects the use of HVPG and the potential for non-invasive alternatives in clinical practice. Moreover, the patients included ranged from those with normal portal pressures to severe portal hypertension which enabled the MR measures to be evaluated over a wide range of HVPG values.

In conclusion, in a well characterised patient population, we have shown that a combination of quantitative MR measures of liver T_1 and SA velocity correlate significantly with HVPG; this was replicated in our second cohort. If these results are confirmed by external validation, this non-invasive model including both architectural (liver T_1 relaxation time) and haemodynamic (SA velocity) measures could be used as a surrogate measure of HVPG in clinical trials of portal hypertension as well as monitoring treatment in clinical practice.

Financial support

The authors acknowledge the financial support from NIHR Nottingham Digestive Diseases Biomedical Research Unit, Nottingham University Hospitals NHS Trust and University of Nottingham, and CORE charity. This paper presents independent research funded by the National Institute for Health Research (NIHR). The views expressed are those of the authors and not necessarily those of the NHS, the NIHR or the Department of Health.

Conflict of interest

The authors who have taken part in this study declared that they do not have anything to disclose regarding funding or conflict of interest with respect to this manuscript.

Authors' contributions

NP (Acquisition, analysis and interpretation of data, statistical analysis, drafting of the manuscript); EC (Acquisition, analysis and interpretation of data, critical revision of the manuscript); SF (Study concept and design, interpretation of data, drafting and critical revision of the manuscript); CB, (Acquisition and analysis of data), RS, RON, GR, ST, HW, RS, PT (Acquisition of data); AA, ING, GPA (Study concept and design, critical revision of the manuscript).

Supplementary data

Supplementary data associated with this article can be found, in the online version, at http://dx.doi.org/10.1016/j.jhep.2016.07.021.

References

[1] Reynaert H, Thompson MG, Thomas T, Geerts A. Hepatic stellate cells: role in microcirculation and pathophysiology of portal hypertension. Gut 2002;50:571–581.
[2] Groszmann RJ, Wongcharatrawee S. The hepatic venous pressure gradient: Anything worth doing should be done right. Hepatology 2004;39:280–282.
[3] Groszmann RJ, Garcia-Tsao G, Bosch J, Grace ND, Burroughs AK, Planas R, et al. Beta-blockers to prevent gastroesophageal varices in patients with cirrhosis. N Engl J Med 2005;353:2254–2261.
[4] Ripoll C, Groszmann R, Garcia-Tsao G, Grace N, Burroughs A, Planas R, et al. Hepatic venous pressure gradient predicts clinical decompensation in patients with compensated cirrhosis. Gastroenterology 2007;133:481–488.
[5] Ripoll C, Groszmann RJ, Garcia-Tsao G, Bosch J, Grace N, Burroughs A, et al. Hepatic venous pressure gradient predicts development of hepatocellular carcinoma independently of severity of cirrhosis. J Hepatol 2009;50:923–928.
[6] Garciatsao G, Groszmann RJ, Fisher RL, Conn HO, Atterbury CE, Glickman M. Portal pressure, presence of gastroesophageal varices and variceal bleeding. Hepatology 1985;5:419–424.
[7] Merkel C, Bolognesi M, Bellon S, Zuin R, Noventa F, Finucci G, et al. Prognostic usefulness of hepatic vein catheterization in patients with cirrhosis and esophageal-varices. Gastroenterology 1992;102:973–979.
[8] Silva-Junior G, Baiges A, Turon F, Torres F, Hernandez-Gea V, Bosch J, et al. The prognostic value of HVPG in patients with cirrhosis is highly dependent on the accuracy of the technique. Hepatology 2015;62:1584–1592.
[9] Moitinho E, Escorsell N, Bandi JC, Salmeron JM, Garcia-Pagan JC, Rodis J, et al. Prognostic value of early measurements of portal pressure in acute variceal bleeding. Gastroenterology 1999;117:626–631.
[10] Vizzutti F, Arena U, Romanelli RG, Rega L, Foschi M, Colagrande S, et al. Liver stiffness measurement predicts severe portal hypertension in patients with HCV-related cirrhosis. Hepatology 2007;45:1290–1297.
[11] Garcia-Pagan JC, Gracia-Sancho J, Bosch J. Functional aspects on the pathophysiology of portal hypertension in cirrhosis. J Hepatol 2012;57:458–461.
[12] Colecchia A, Montrone L, Scaioli E, Bacchi-Reggiani ML, Colli A, Casazza G, et al. Measurement of spleen stiffness to evaluate portal hypertension and the presence of esophageal varices in patients with HCV-related cirrhosis. Gastroenterology 2012;143:646–654.
[13] Ronot M, Lambert S, Elkrief L, Doblas S, Rautou PE, Castera L, et al. Assessment of portal hypertension and high-risk oesophageal varices with liver and spleen three-dimensional multifrequency MR elastography in liver cirrhosis. Eur Radiol 2014;24:1394–1402.
[14] Iranmanesh P, Vazquez O, Terraz S, Majno P, Spahr L, Poncet A, et al. Accurate computed tomography-based portal pressure assessment in patients with hepatocellular carcinoma. J Hepatol 2014;60:969–974.
[15] Baik SK. Haemodynamic evaluation by Doppler ultrasonography in patients with portal hypertension: a review. Liver Int 2010;30:1403–1413.
[16] Sacerdoti D, Gaiani S, Buonamico P, Merkel C, Zoli M, Bolondi L, et al. Interobserver and interequipment variability of hepatic, splenic, and renal arterial Doppler resistance indices in normal subjects and patients with cirrhosis. J Hepatol 1997;27:986–992.
[17] Hoad CL, Palaniyappan N, Kaye P, Chernova Y, James MW, Costigan C, et al. A study of T1 relaxation time as a measure of liver fibrosis and the influence of confounding histological factors. NMR Biomed 2015;28:706–714.
[18] Yzet T, Bouzerar R, Allart JD, Demuynck F, Legallais C, Robert B, et al. Hepatic vascular flow measurements by phase contrast MRI and doppler echography: a comparative and reproducibility study. J Magn Reson Imaging 2010;31:579–588.
[19] Francis ST, Bowtell R, Gowland PA. Modeling and optimization of Look-Locker spin labeling for measuring perfusion and transit time changes in activation studies taking into account arterial blood volume. Magn Reson Med 2008;59:316–325.
[20] McCorry RB, Palaniyappan N, Chivinge A, Kaye P, James MW, Aithal GP. Development and evaluation of a nurse-led transient elastography service for the staging of hepatic fibrosis in patients with suspected chronic liver disease. QJM 2012;105:749–754.
[21] Rosenberg WMC, Voelker M, Thiel R, Becka M, Burt A, Schuppan D, et al. Serum markers detect the presence of liver fibrosis: A cohort study. Gastroenterology 2004;127:1704–1713.
[22] Banerjee R, Pavlides M, Tunnicliffe EM, Piechnik SK, Sarania N, Philips R, et al. Multiparametric magnetic resonance for the non-invasive diagnosis of liver disease. J Hepatol 2014;60:69–77.
[23] Schmitt P, Griswold MA, Jakob PM, Kotas M, Gulani V, Flentje M, et al. Inversion recovery TrueFISP: Quantification of T-1, T-2 and spin density. Magn Reson Med 2004;51:661, 698–698.
[24] Liss P, Cox EF, Eckerbom P, Francis ST. Imaging of intrarenal haemodynamics and oxygen metabolism. Clin Exp Pharmacol Physiol 2013;40:158–167.
[25] Calvaruso V, Burroughs AK, Standish R, Manousou P, Grillo F, Leandro G, et al. Computer-assisted image analysis of liver collagen: relationship to

ishak scoring and hepatic venous pressure gradient. Hepatology 2009;49:1236–1244.
[26] Ratziu V, Charlotte F, Heurtier A, Gombert S, Giral P, Bruckert E, et al. Sampling variability of liver biopsy in nonalcoholic fatty liver disease. Gastroenterology 2005;128:1898–1906.
[27] Bedossa P, Dargere D, Paradis V. Sampling variability of liver fibrosis in chronic hepatitis C. Hepatology 2003;38:1449–1457.
[28] Mozes FE, Tunnicliffe EM, Pavlides M, Robson MD. Influence of fat on liver T1 measurements using modified Look-Locker inversion recovery (MOLLI) methods at 3T. J Magn Reson Imaging 2016;44:105–111.
[29] Zwiebel WJ, Mountford RA, Halliwell MJ, Wells PNT. Splanchnic blood-flow in patients with cirrhosis and portal-hypertension – Investigation with duplex-doppler us. Radiology 1995;194:807–812.
[30] Sabba C, Weltin GG, Cicchetti DV, Ferraioli G, Taylor KJ, Nakamura T, et al. Observer variability in echo-Doppler measurements of portal flow in cirrhotic patients and normal volunteers. Gastroenterology 1990;98:1603–1611.
[31] Cox EF, Smith JK, Chowdhury AH, Lobo DN, Francis ST, Simpson J. Temporal assessment of pancreatic blood flow and perfusion following secretin stimulation using noninvasive MRI. J Magn Reson Imaging 2015;42:1233–1240.
[32] Berzigotti A, Seijo S, Arena U, Abraldes JG, Vizzutti F, Garcia-Pagan JC, et al. Elastography, spleen size, and platelet count identify portal hypertension in patients with compensated cirrhosis. Gastroenterology 2013;144:102–111 e1.
[33] Loomba R, Sirlin CB, Ang B, Bettencourt R, Jain R, Salotti J, et al. Ezetimibe for the treatment of nonalcoholic steatohepatitis: assessment by novel magnetic resonance imaging and magnetic resonance elastography in a randomized trial (MOZART trial). Hepatology 2015;61:1239–1250.

9.6 Publication VI: Cox EF, Buchanan CE, Bradley CR, Prestwich B, Mahmoud H, Taal M, Selby NM, Francis ST. Multiparametric renal magnetic resonance imaging: validation, interventions, and alterations in chronic kidney disease. Frontiers in physiology. 2017 Sep 14;8:696.

frontiers in Physiology

ORIGINAL RESEARCH
published: 14 September 2017
doi: 10.3389/fphys.2017.00696

Multiparametric Renal Magnetic Resonance Imaging: Validation, Interventions, and Alterations in Chronic Kidney Disease

*Eleanor F. Cox[1], Charlotte E. Buchanan[1], Christopher R. Bradley[1], Benjamin Prestwich[1], Huda Mahmoud[2], Maarten Taal[2], Nicholas M. Selby[2] and Susan T. Francis[1]**

[1] Sir Peter Mansfield Imaging Centre, University of Nottingham, Nottingham, United Kingdom, [2] Centre for Kidney Research and Innovation, Royal Derby Hospital, University of Nottingham, Derby, United Kingdom

Background: This paper outlines a multiparametric renal MRI acquisition and analysis protocol to allow non-invasive assessment of hemodynamics (renal artery blood flow and perfusion), oxygenation (BOLD T_2*), and microstructure (diffusion, T_1 mapping).

Methods: We use our multiparametric renal MRI protocol to provide (1) a comprehensive set of MRI parameters [renal artery and vein blood flow, perfusion, T_1, T_2*, diffusion (ADC, D, D*, f_p), and total kidney volume] in a large cohort of healthy participants (127 participants with mean age of 41 ± 19 years) and show the MR field strength (1.5 T vs. 3 T) dependence of T_1 and T_2* relaxation times; (2) the repeatability of multiparametric MRI measures in 11 healthy participants; (3) changes in MRI measures in response to hypercapnic and hyperoxic modulations in six healthy participants; and (4) pilot data showing the application of the multiparametric protocol in 11 patients with Chronic Kidney Disease (CKD).

Results: Baseline measures were in-line with literature values, and as expected, T_1-values were longer at 3 T compared with 1.5 T, with increased T_1 corticomedullary differentiation at 3 T. Conversely, T_2* was longer at 1.5 T. Inter-scan coefficients of variation (CoVs) of T_1 mapping and ADC were very good at <2.9%. Intra class correlations (ICCs) were high for cortex perfusion (0.801), cortex and medulla T_1 (0.848 and 0.997 using SE-EPI), and renal artery flow (0.844). In response to hypercapnia, a decrease in cortex T_2* was observed, whilst no significant effect of hyperoxia on T_2* was found. In CKD patients, renal artery and vein blood flow, and renal perfusion was lower than for healthy participants. Renal cortex and medulla T_1 was significantly higher in CKD patients compared to healthy participants, with corticomedullary T_1 differentiation reduced in CKD patients compared to healthy participants. No significant difference was found in renal T_2*.

Conclusions: Multiparametric MRI is a powerful technique for the assessment of changes in structure, hemodynamics, and oxygenation in a single scan session. This protocol provides the potential to assess the pathophysiological mechanisms in various etiologies of renal disease, and to assess the efficacy of drug treatments.

Keywords: magnetic resonance imaging, hemodynamics, oxygenation, renal function, arterial spin labeling

OPEN ACCESS

Edited by:
Maarten Koeners, University of Bristol, United Kingdom

Reviewed by:
Samuel Heyman, Hadassah Hebrew University Hospitals, Israel
Menno Pruijm, Centre Hospitalier Universitaire Vaudois (CHUV), Switzerland

****Correspondence:***
Susan T. Francis
susan.francis@nottingham.ac.uk

Specialty section:
This article was submitted to Renal and Epithelial Physiology, a section of the journal Frontiers in Physiology

Received: *15 February 2017*
Accepted: *30 August 2017*
Published: *14 September 2017*

Citation:
Cox EF, Buchanan CE, Bradley CR, Prestwich B, Mahmoud H, Taal M, Selby NM and Francis ST (2017) Multiparametric Renal Magnetic Resonance Imaging: Validation, Interventions, and Alterations in Chronic Kidney Disease. Front. Physiol. 8:696. doi: 10.3389/fphys.2017.00696

INTRODUCTION

Magnetic Resonance Imaging (MRI) offers the possibility to non-invasively assess the structure of the kidney as well as renal function in a single scan session. This article outlines the development of a quantitative functional multiparametric renal MRI protocol to probe hemodynamics (total and regional blood flow, perfusion), oxygenation [Blood Oxygen Level Dependent (BOLD) T_2* imaging], and microstructure (diffusion weighted imaging, longitudinal relaxation time T_1 mapping) and describes associated analysis methods. This multiparametric MRI protocol is applied in healthy participants, to assess both reproducibility and the field strength dependence of MRI parameters between 1.5 and 3 Tesla (T). In addition, studies are performed in healthy participants to evaluate the possibility of using hypercapnia and hyperoxia to monitor changes in renal BOLD and T_1 reactivity. Finally, pilot data demonstrating the feasibility of this multiparametric protocol in Chronic Kidney Disease (CKD) is shown.

The kidney is an intricate organ which regulates electrolytes, acid-base balance, and blood pressure and filters blood to remove water soluble waste products (Skorecki et al., 2016). Regulation of renal tissue oxygenation is complex, because renal blood flow is not only needed to prevent hypoxic injury but is inextricably linked to the requirement for glomerular filtration. The kidney's response to hypoxia cannot simply be an increase in renal blood flow, as this would also increase oxygen demand; a number of hemodynamic mechanisms are required to regulate the fine balance between oxygen delivery and consumption, and these can be measured using multiparametric MRI.

Oxygen delivery is determined by arterial blood flow, which is regulated by arterial blood pressure and intrarenal vascular resistance, local tissue perfusion and blood oxygen content (Evans et al., 2008). Arterial blood is supplied to the kidney via the renal artery, and blood flow can be estimated from phase contrast MR. The renal artery sequentially divides into segmental, interlobar, arcuate, and interlobular arteries before finally reaching the afferent arterioles that supply the glomeruli. The renal microcirculation varies depending on the location of each nephron within the cortex. In the outer cortex, glomerular efferent arterioles give rise to a capillary network that surrounds the tubules, important for reabsorption of water and electrolytes. In contrast, the efferent arterioles supply the medulla and give rise to the vasa recta, the long unbranched capillary loops that run into the inner medulla associated with the loop of Henle, as well as capillaries in the outer medulla. This facilitates concentration of urine in the medulla, but also has consequences for oxygenation.

The majority of arterial blood delivered to the kidney is directed toward the renal cortex, which primarily is responsible for filtration and tubular reabsorption; 5–15% is delivered to the medulla, whose purpose is concentration of the urine by maintaining a hypertonic environment. Despite the much lower proportional blood flow, the absolute blood flow to the medulla is still significant, reflecting large total renal blood flow (∼20% of cardiac output), and a number of physiological and pathological conditions can produce significant redistribution of renal blood flow. However, a significant cortico-medullary oxygen gradient exists, with the inner medulla having a tissue oxygenation (pO_2) as low as 10 mmHg, compared to 50 mmHg in the cortex. MR potentially provides a non-invasive method to assess this change in tissue oxygenation.

Tubular epithelial transport allows the kidney to regulate volume and composition of urine, but has significant energy and oxygen requirements. Reabsorption of sodium is the main determinant of oxygen consumption (Blantz et al., 2007; Thomson and Blantz, 2008), so that oxygen consumption is related to renal function, with reductions in glomerular filtration rate (GFR) resulting in a lower filtered load and lower requirement for sodium reabsorption. Renal perfusion is driven primarily by the need to maintain glomerular filtration rather than oxygenation, and therefore arteriovenous shunting of oxygen occurs to prevent hyperoxic tissue injury (via peri-glomerular shunts and between arterial and venous limbs of the vasa recta).

Although the kidney can reduce oxygen consumption in response to hypoxia, the lower pO_2 in the medulla increases its propensity to ischemic damage, which is considered a key pathogenic event in acute kidney injury (AKI) and CKD (Venkatachalam et al., 2010). Since multiple interacting mechanisms operate in concert to provide tight regulation of intrarenal oxygenation, dysfunction of these mechanisms may contribute to the pathogenesis of kidney disease. For example, vascular morphologic changes may occur such as, capillary rarefaction as well as factors that affect regional blood flow and oxygen diffusion e.g., upregulation of the renin-angiotensin or sympathetic nervous systems (Adler et al., 2004). Alternatively, other changes may impact regional oxygen utilization such as alterations in global and single nephron GFR, drugs interfering with glomerular hemodynamics or tubular transport and hydration status. In addition to the complexity of kidney function, renal diseases such as CKD are diverse in terms of pathophysiological processes, etiology and outcomes, highlighting the need for multiparametric MRI measures. Renal perfusion and tissue oxygenation appear central integrating factors in kidney disease, highlighting the need to perform a combined assessment of these parameters, and regardless of the nature of initial insult, fibrosis is the final common pathway.

The potential use of complementary MRI techniques to non-invasively assess multiple parameters to provide a wealth of information on renal blood flow and regional perfusion, tissue oxygenation, and degree of fibrosis, as well as behavior in low or high oxygen or carbon dioxide, will undoubtedly aid the understanding of kidney disease. Prior to the use of MRI in kidney disease, the reproducibility of MRI measures and their dependence on different factors must be understood in normal tissue.

Here, we assess the inter-subject variability, repeatability, and field strength dependence of multiparametric MRI measures in healthy participants. Physiological modulations such as, hyperoxia and hypercapnia are performed, and pilot data are shown to illustrate the feasibility of detecting changes in MR measures in CKD.

MATERIALS AND METHODS

Study Design

Studies were carried out according to the principles of the Declaration of Helsinki. Healthy participant studies were approved by the Local Ethics Committee and patient studies were approved by the East Midlands Research Ethics Committee. Written informed consent was obtained from all participants.

Imaging was performed on either a 1.5 or 3 T Philips whole body MR scanner. Data is presented from studies that use the multiparametric renal MRI protocol, comprising quantification of renal blood flow and perfusion, renal oxygenation, and markers of renal microstructural change due to fibrosis/inflammation. All data was collected with subjects fasted for at least 2 h prior to their scan.

Variability, Repeatability, and Field Strength Dependence in Healthy Participants

Here, we evaluate the variation in MRI measures within normal tissue of a healthy participant cohort, specifically we assess renal artery and renal vein blood flow [as measured with phase contrast (PC)-MRI], kidney perfusion [as measured with arterial spin labeling (ASL)], T_1 measures [and a comparison of readout schemes: spin echo–echo planar imaging (SE-EPI) and balanced fast field echo (bFFE)], tissue oxygenation (from BOLD T_2*), diffusion weighted imaging (DWI), and total kidney volume. Data collated across a number of studies are first shown, giving a cohort of 127 participants (88 male) with mean age of 41 ± 19 years. This data is then divided into two groups comprising healthy participants <40 years and >40 years [see Section Application in Chronic Kidney Disease (CKD)]. In addition the field strength dependence of MR relaxation times is assessed. Since clinical MR scanners at both 1.5 and 3 T are now widely available, the field dependence of MR relaxation time measures of T_1 (using both SE-EPI and bFFE) and T_2* for renal cortex and renal medulla was assessed.

A subset of 11 participants (age 20–28 years, body mass index 20–26 kg/m^2) had two/three repeat 3 T scans at the same time of day and after an overnight fast to limit diurnal and dietary variability. To determine the between session repeatability of MRI measures, the intra-subject Coefficient of Variation (CoV; defined as the standard deviation/mean) and intra class correlation (ICC, average measures, two-way random, absolute agreement) were assessed.

Physiological Modulation in Healthy Participants

Physiological modulations, such as gas enrichment by hypercapnia, hyperoxia, or carbogen (hypercapnic-hyperoxia; Milman et al., 2013) may provide a more sensitive marker to assess changes in renal oxygenation and microcirculation reactivity and functionality, and changes in these parameters associated with pathology. Here, we assess the change in MRI parameters in healthy participants in response to hypercapnia and hyperoxia. We induced hypercapnia and hyperoxia using a sequential gas delivery breathing circuit and a prospective, feed-forward gas delivery system (Respiract^{TM}, Thornhill Research Inc., Toronto, Canada) to control and monitor end-tidal oxygen ($P_{ET}O_2$) and carbon dioxide ($P_{ET}CO_2$) partial pressures. Hypercapnia was targeted at $P_{ET}CO_2$ ∼6 mmHg above the subjects' baseline value whilst keeping $P_{ET}O_2$ constant at the subjects' resting value, the paradigm comprised 5 min normoxia and 5 min of hypercapnia. Hyperoxia was targeted at $P_{ET}O_2$ ∼500 mmHg with $P_{ET}CO_2$ targeted to remain constant at the subjects' resting value. The paradigm comprised 5 min normoxia and 5 min of hyperoxia, $P_{ET}O_2$ was increased/decreased over a 1 min transition period.

BOLD T_2* was measured at 3 T using a multi-gradient echo Fast Field Echo (mFFE) sequence in six healthy participants (3 male, mean age 25 years, range 22–28 years) during the hyperoxia and hypercapnia challenge. T_1 was measured during a hyperoxic challenge in five healthy participants (3 male, mean age 26 years, range 22–31 years) using an inversion recovery sequence with modified respiratory triggering and a bFFE readout at 3 T.

Application in Chronic Kidney Disease (CKD)

To demonstrate the feasibility of use of the multiparametric MR protocol in patients, 11 patients with CKD Stage 3 or 4 were scanned (inclusion criteria: estimated GFR 15–66 ml/min/1.73 m^2, age 18–85 years). Baseline blood pressure and estimated GFR of the patients was recorded. The complete multiparametric protocol was performed comprising of localizer scans, PC-MRI, ASL, T_1, T_2*, and DWI data as described below. All scans were acquired in approximately 45 min.

The Multiparametric MRI Protocol

Figure 1 outlines the key MRI parameters within the multiparametric protocol, these measures can all be performed within a 45 min scan session. All mapping data are collected with matched geometry with slices in a coronal-oblique plane through the long axis of the kidneys, allowing automated interrogation of the resulting multiparametric maps. All data is acquired using respiratory triggering or an end-expiration breath hold to ensure data is acquired at the same point in the respiratory cycle. Each of the parameters within this protocol are outlined below.

Localizers and Kidney Volume Assessment

Balanced turbo field echo (bTFE) scans are acquired in three orthogonal planes (30 slices of 1.75 × 1.75 × 7 mm^3 resolution, data collected in single breath hold per orientation). These scans provide a localizer to allow accurate planning of subsequent images, and segmentation of these images yields total kidney volume.

Phase Contrast (PC)-MRI to Assess Renal Artery and Vein Blood Flow

Prior to the PC-MRI acquisition, an angiogram is acquired to plan the placement of the PC-MRI renal artery slice to ensure that it is positioned prior to any bifurcations of the artery.

PC-MRI is then used for the measurement of blood flow in the renal arteries and veins (Debatin et al., 1994; Schoenberg et al., 1997; Bax et al., 2005; Park et al., 2005; Dambreville et al., 2010). PC-MRI is performed using a single slice TFE image placed perpendicular to the vessel of interest. Multiple phases are collected across the cardiac cycle when imaging the renal

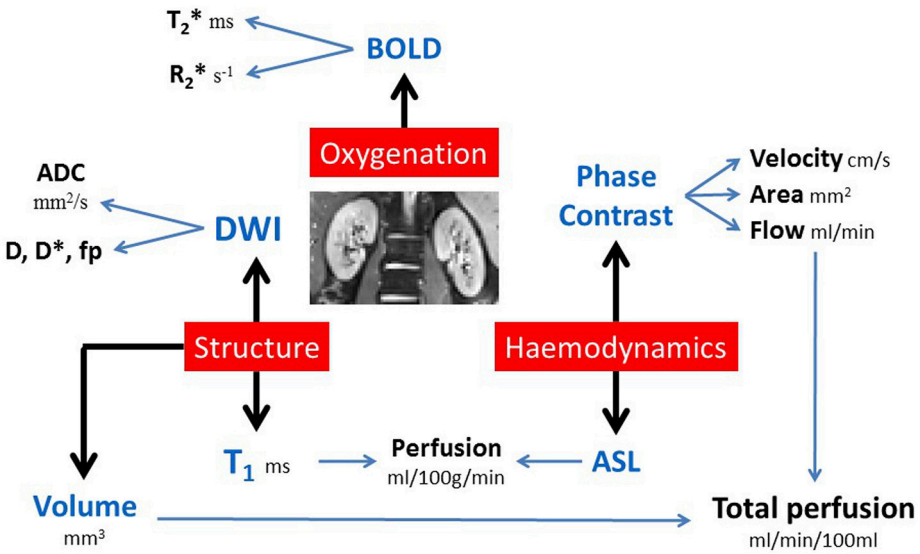

FIGURE 1 | Multiparametric non-invasive renal MRI protocol.

artery (20 phases) and renal vein (15 phases). Imaging parameters use a flip angle of 25°, reconstructed resolution 1.2 × 1.2 × 6 mm^3, and velocity encoding of 100/50 cm/s for renal artery and vein, respectively. Each measurement is acquired during a single 15–20 s breath hold, dependent on the subjects' heart rate.

Arterial Spin Labeling (ASL) to Assess Renal Cortex Perfusion

ASL uses magnetically labeled water protons in blood that act as a diffusible tracer, providing an internal endogenous contrast. By subtracting labeled images (radiofrequency magnetic labeling) from control images (no labeling applied), perfusion maps can be quantified using a kinetic model (Buxton et al., 1998). Renal tissue perfusion assessed by ASL has been implemented in healthy (Karger et al., 2000; Martirosian et al., 2004; Boss et al., 2005; Kiefer et al., 2009; Gardener and Francis, 2010; Cutajar et al., 2012, 2014; Park et al., 2013; Gillis et al., 2014; Tan et al., 2014; Hammon et al., 2016), transplanted (Artz et al., 2011a,b; Niles et al., 2016) and diseased (Michaely et al., 2004; Boss et al., 2005; Fenchel et al., 2006; Ritt et al., 2010; Rossi et al., 2012; Dong et al., 2013; Heusch et al., 2013; Tan et al., 2014) kidneys.

To measure renal cortex perfusion, we have implemented a respiratory-triggered FAIR (Flow-sensitive Alternating Inversion Recovery) ASL scheme. For imaging, we use either a SE-EPI or bFFE readout. Typical imaging parameters at 3 T are a post label delay (PLD) time of 1,800 ms (depending on choice of readout scheme and field strength Buchanan et al., 2015), 40 label/control pairs, 288 × 288 mm field of view, 3 × 3 × 5 mm^3 voxel resolution. A SE-EPI readout provides good spatial coverage, allowing multiple slices to be acquired in a short acquisition time over the ASL signal curve (five slices in ∼ 300 ms at 3 T). A bFFE readout provides the benefit of high spatial resolution, typically 1.5 mm in-plane spatial resolution and 5 mm slice thickness, however this can limit slice coverage due to the increased acquisition time per slice (∼ 250 ms slice spacing at 3 T). Since ASL is a subtraction technique, we use respiratory triggering to minimize the effects of respiratory motion leading to misalignment or blurring. It is important to take into account the arrival time of the blood to the tissue when quantifying perfusion, particularly in disease where the arrival time can be increased, resulting in an apparent reduction in perfusion. A separate scan to assess the arrival time of the blood to the tissue is acquired, by collecting ∼4 label/control pairs at shorter PLD times (500, 700, 900, 1,100 ms). A base equilibrium M_0 scan and T_1 map are also required for accurate perfusion quantification. Depending on respiratory rate, scan time for 40 label/control pairs of ASL data is approximately 6 min, with a further 2 min for assessment of arrival time and collection of a base M_0 scan.

Longitudinal Relaxation Time T_1 Mapping

The assessment of the longitudinal relaxation time T_1 of tissue is essential for the quantification of ASL perfusion. Recently, T_1 mapping alone has been shown to provide an important parameter by which to evaluate fibrosis (due to the association of collagen with supersaturated hydrogel) or inflammation (interstitial edema, cellular swelling). T_1 has been shown to correlate well with fibrosis and edema in the myocardium (Iles et al., 2008; Jellis and Kwon, 2014), liver (Hoad et al., 2015; Tunnicliffe et al., 2017), and more recently in the kidney (Friedli et al., 2016).

Here, an inversion recovery sequence with a modified respiratory triggering scheme (**Figure 2**) has been developed to minimize respiratory-induced abdominal motion between images of differing contrast collected across the range of inversion times required to compute a T_1 map. The respiratory trigger is applied at the peak of inspiration in the respiratory cycle and the image is then acquired at a constant time following this trigger, during the flat end-expiration period of the respiratory

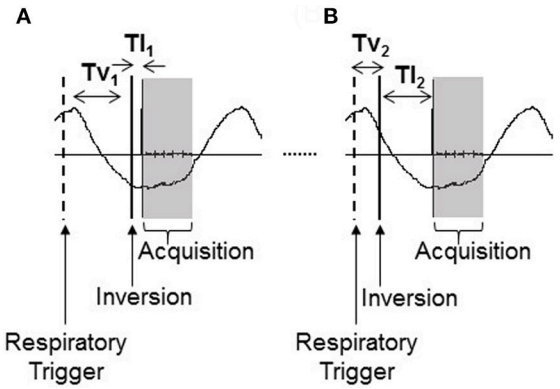

FIGURE 2 | Modified respiratory triggered inversion recovery sequence shown for **(A)** short (TI_1) and **(B)** long (TI_2) inversion time. By altering the variable delay, Tv, each image acquisition is collected at a constant time (Tv + TI) following the respiratory trigger. First arrow indicates the respiratory trigger ("Respiratory Trigger"), second the inversion pulse ("Inversion"), and the shaded block indicates the image acquisition readout ("Acquisition").

cycle. A variable delay, Tv, is introduced between the respiratory trigger and the inversion pulse which is followed by the inversion time, TI, between the inversion pulse and image acquisition. By holding the total time period Tv + TI constant, this results in all image readouts for all inversion times being collected at a constant time of (Tv + TI) following the respiratory trigger and as such all images are aligned across the inversion times. The time (Tv + TI) is chosen to be at the end-expiration period of the respiratory cycle to minimize any potential motion artifacts.

Here, we use either a SE-EPI or bFFE readout scheme for T_1 mapping. In general, the same readout scheme as is used for the ASL acquisition is chosen. Importantly, the chosen image readout scheme has an impact on the measured T_1 value. A SE-EPI readout scheme provides a "true" T_1 value, whereas a bFFE readout scheme results in an "apparent" T_1, shorter than the "true" T_1 due to the influence of transverse relaxation rates (T_2/T_2^*; Schmitt et al., 2004). At 3 T, we typically collect 13 inversion times of 200, 300, 400, 500, 600, 700, 800, 900, 1,000, 1,100, 1,200, 1,300, and 1,500 ms in a total scan time of <3 min. For a multi-slice bFFE readout, the temporal slice spacing is longer (∼250 ms at 3 T) than for a SE-EPI (∼60 ms at 3 T) readout, and therefore the dynamic range of TIs can be increased by acquiring the scans ascend, descend and interleaved slice order.

An alternative scheme for T_1 mapping is to use a modified look-locker inversion recovery (MOLLI) sequence originally developed for cardiac T_1 mapping. This typically involves the acquisition of a cardiac-gated single-shot MOLLI sequence using a bFFE readout [23] with a 3(3)3(3)5 sampling pattern collected in a breath hold. However, this acquisition scheme is not best suited to the kidney, since it is cardiac triggered, requires a number of breath holds for complete coverage of the kidneys, and does not match the ASL acquisition readout scheme, and so it is not implemented in our multiparametric protocol.

Diffusion Weighted Imaging (DWI)

DWI assesses the thermally induced Brownian motion of water within tissues, which can be quantified from the Apparent Diffusion Coefficient (ADC). ADC may also be affected by factors such as tubular flow and capillary perfusion, which can be better distinguished using the IntraVoxel Incoherent Motion (IVIM) model to quantify pure diffusion (D; Le Bihan et al., 1988). In DWI, at least two single-shot echo-planar images are acquired without and with diffusion weighting gradients (b-values) from which molecular diffusion can be quantified and spatially mapped. It is important to note that the quantification of the ADC is affected by the b-values acquired. In this multiparametric protocol, DWI data is acquired with a SE-EPI readout at multiple b-values (for example, 11 b-values of 0, 5, 10, 20, 30, 50, 100, 200, 300, 400, 500 s/mm^2). The highest b-value is chosen such that the echo time (TE) does not become so long as to limit the signal-to-noise ratio (SNR) of the image. Typically a 288 × 288 mm field of view is used with 3 × 3 × 5 mm^3 voxel resolution which has a minimum TE of 56 ms. This sequence is acquired with respiratory triggering such that the image readouts are collected at the end-expiration period. For 11 b-values, the acquisition time is approximately 8 min.

Blood Oxygenation Level Dependent (BOLD) Imaging to Assess Tissue Oxygenation

BOLD MRI exploits the paramagnetic properties of deoxygenated blood, which acts to shorten the transverse relaxation time constant (T_2^*)—alternatively expressed as the relaxation rate R_2^* ($1/T_2^*$)—a measure which provides an indirect non-invasive assessment of oxygen content. Higher R_2^* (or lower T_2^*) is an indicator of lower tissue pO_2. BOLD MRI is more sensitive at detecting changes in medullary compared to cortical pO_2 due to their relative positions on the oxygen dissociation curve—cortical pO_2 lies near the plateau of the hemoglobin oxygenation curve and medullary pO_2 lies on the linear part of the curve, thus a large change in local pO_2 is needed to cause a similar change in R_2^* for the cortex compared to the medulla. The use of BOLD MRI to measure renal oxygenation has been extensively studied. However, it should be highlighted that a number of other factors, such as, hydration status, dietary sodium intake, and susceptibility effects also alter BOLD R_2^* (Pruijm et al., 2017), this can make it difficult to draw definite conclusions from its independent use. For a review of this technique, see Pruijm et al. (2017). In this multiparametric protocol, BOLD T_2^* data is acquired using a mFFE sequence with multiple slices. Typical imaging parameters are 1.5 mm in-plane resolution, 5 mm slice thickness, initial TE 5 ms, TE spacing 3 ms, 12 echoes, flip angle 30°. Each measurement is acquired in a single ∼17 s breath hold.

Analysis of Multiparametric MRI

Kidney Volume Assessment

Analyze9 software (AnalyzeDirect, Overland Park, KS) is used to define a region of interest around the kidneys on each bTFE localizer image slice. Total kidney volume can then be calculated by summing across all slices, typically the coronal slices are

used for organ volume measures. Analysis time is approximately 10 min.

PC-MRI Renal Blood Flow Assessment

A region of interest is placed over the vessel using Q-flow software (Philips Medical Systems, Best, NL). Mean flow velocity (cm/s), mean cross-sectional area of the lumen (mm^2), and hence mean bulk renal blood flow (ml/s) over the cardiac cycle, are calculated for each vessel. Total perfusion of each kidney can then be calculated by correcting the renal blood flow to kidney volume. Analysis time is approximately 2 min per vessel.

Multiparametric Interpretation

Combining multiparametric MRI maps adds considerable insight into the underlying physiology. We have developed a multiparametric image analysis program (MATLAB, The Mathworks Inc., Natick, MA) that generates and combines the parametric ASL perfusion, T_1, diffusion, and BOLD T_2* maps in the same data space. The multiparametric maps can then be used to perform multivariate analysis of structural and hemodynamic measures in automated regions of interest in the cortex and medulla.

Mapping perfusion from ASL data

Individual perfusion weighted difference images (control-label) are calculated, inspected for motion (exclude >1 voxel movement) or realigned, and averaged to create a single perfusion-weighted (ΔM) map. ΔM, T_1 maps (see below), and M_0 maps are then used in a kinetic model (Equation 1; Buxton et al., 1998) to calculate tissue perfusion (f) maps (in ml/100 g tissue/min). $T_{1,blood}$ is assumed to be 1.55 s at 3 T and 1.36 s at 1.5 T (Dobre et al., 2007), whilst λ, the blood-tissue partition coefficient, is assumed to be 0.8 ml/g for kidney. Analysis time is approximately 10 min.

$$\Delta M\,(PLD) = 2M_0 \frac{f}{\lambda} \frac{e^{PLD/T_{1,app-e}}\; PLD/T_{1,blood}}{1/T_{1,blood} - 1/T_{1,app}} \text{ where}$$
$$1/T_{1,app} = 1/T_1 + f/\lambda \quad (1)$$

Longitudinal relaxation time (T_1) mapping

Inversion recovery data is fit on a voxel-by-voxel basis to Equation (2) to generate a "true" T_1 map for the SE-EPI readout, for the bFFE readout an "apparent" T_1 map is obtained. Analysis time is approximately 3 min of user intervention, and up to 1 h processing time on a standard pc.

$$S\,(\mathrm{TI}) = S_0\left(1 - 2e^{-\mathrm{TI}/T_1}\right) \quad (2)$$

Mapping ADC, D, D, and f_p from DWI data*

DWI data are fit to form ADC maps (in mm^2/s) by taking the log of the exponential signal decay (Equation 3). In addition, since the DWI data is collected at a number of b-values, it is possible to model the bi-exponential IVIM model (Equation 4). In the IVIM model, D (in mm^2/s) is the pure tissue molecular diffusion coefficient representing the diffusion coefficient of slow or non-perfusion-based molecular diffusion, D* (in mm^2/s) is the pseudodiffusion coefficient which is the fast or perfusion-based molecular diffusion representing intravoxel microcirculation or perfusion, and f_p is the perfusion fraction (%) of the voxel (Le Bihan et al., 1988; Koh et al., 2011). To fit data to the IVIM model, D was first fit to Equation (3) for b-values of >200 s/mm^2, this assumes that the pseudodiffusion component D* can be neglected above this value. Second, f_p was determined from the zero intercept of this fit. Finally, D* was obtained from the monoexponential fit using the precalculated values of D and f_p (Suo et al., 2015). Analysis time is approximately 5 min of user intervention, and up to 5 min processing time on a standard pc.

$$S(b) = S_0 e^{-b.ADC} \quad (3)$$
$$S\,(b) = f_p S_0 e^{-b.D^*} + (1 - f_p)\, S_0 e^{-b.D} \quad (4)$$

BOLD MRI to map T_2/R_2**

mFFE data are fit voxelwise using a weighted echo time (TE) fit to form T_2*/R_2* maps from the log of the exponential signal decay (Equation 5). Analysis time is approximately 5 min.

$$S(TE) = S_0 e^{-TE/T_2^*} \quad (5)$$

Interpretation of multiparametric maps

Binary whole kidney masks are formed from the manual segmentation of the base equilibrium M_0 scan or T_1 map. To distinguish renal cortex and medulla, a histogram of T_1 values across both kidneys is formed (with a bin size of 20 ms). Two peaks in the histogram, originating from the renal cortex and medulla, can be identified from which to form separate renal cortex and renal medulla masks. This segmentation procedure is illustrated for both a healthy participant and CKD patient in **Figure 3**. It should be noted that T_1 values are elevated in CKD [see Section Application in Chronic Kidney Disease (CKD)], but sufficient corticomedullary differentiation remains to segment the cortex from medulla. These binary cortex and medulla masks can then be applied to each parametric map (perfusion, T_1, ADC, D, D*, and f_p) to interrogate identical regions of interest in which to assess mean values of each parameter. Importantly, to assess heterogeneity of measures and remove bias, a Gaussian curve fit can be applied to the histogram to determine both the mode and full-width-at-half-maximum (FWHM) of renal cortex and medulla parameter values across one or both kidneys (Rossi et al., 2012). The assessment of corticomedullary differentiation (medulla-cortex) in MRI parameters also provides important information. Analysis time is approximately 10 min.

RESULTS

All results given are the mean and standard deviation across participants.

Variability, Repeatability, and Field Strength Dependence in Healthy Participants

Figure 4 shows example multiparametric MRI maps for a single healthy participant collected at 3 T, illustrating that the maps can be combined in the same data space and allow assessment of heterogeneity across the kidney. **Table 1** provides the mean

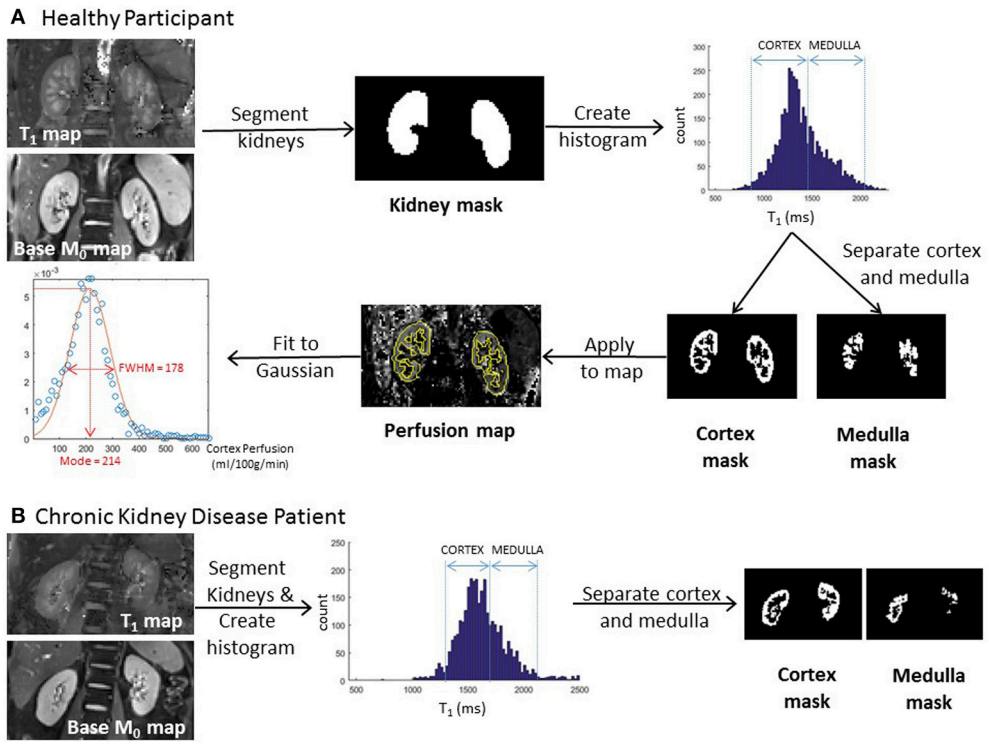

FIGURE 3 | (A) Example image analysis for a healthy participant indicating segmentation of the kidneys from the T_1 map, definition of cortex and medulla masks from the histogram, and the application of the renal cortex mask to an arterial spin labeling perfusion map allowing the interrogation of a histogram [for mode and full-width-at-half-maximum (FWHM)] of renal cortex perfusion values. **(B)** Example image analysis for a chronic kidney disease patient indicating definition of cortex and medulla masks from the T_1 histogram of the kidneys.

and associated standard deviation for MRI parameters collected across the cohort of healthy participants, with the number of subjects included in each analysis provided, and a comparison to literature values.

Table 2 shows the field strength dependence of longitudinal (T_1) and transverse (T_2*) relaxation times. As expected, T_1-values are longer at 3 T compared with 1.5 T for both the SE-EPI and bFFE readout schemes. It should be noted that the "apparent" T_1 measured using a bFFE readout scheme is shorter than the "true" T_1 measured using a SE-EPI readout. The corticomedullary differentiation of T_1 can be seen to be greater at 3 T compared with 1.5 T. Conversely, the transverse relaxation time (T_2*) is longer at 1.5 T.

Table 3 provides the CoV and ICCs for the repeatability study at 3 T. The CoV is low for T_1 (< 2.9%), ADC (2.9%), T_2* (4.1%), and kidney volume (4.2%). The ICCs were high for cortex perfusion (0.801), cortex and medulla T_1 (0.848 and 0.997 using SE-EPI), renal artery flow (0.844) and total kidney volume (0.985).

Physiological Modulation in Healthy Participants

Figure 5A shows the T_2* mode and FWHM in renal cortex and medulla at normoxia and during hypercapnia or during hyperoxia. During hypercapnia, there was a trend for a decrease in the T_2* mode in the renal cortex ($P = 0.098$, paired t-test), but the T_2* FWHM did not change. The T_2* mode in the renal medulla did not change, but the T_2* FWHM was found to increase ($P = 0.02$, paired t-test). During hyperoxia, there was no change in T_2* mode or FWHM in either the renal cortex or renal medulla.

Figure 5B shows the "apparent" T_1 mode and FWHM for renal cortex and medulla at normoxia and during hyperoxia. During hyperoxia, there was no significant change in the "apparent" T_1 mode of renal cortex or medulla, but the FWHM increased in the renal cortex ($P = 0.009$, paired t-test) and medulla ($P = 0.092$, paired t-test).

Application in Chronic Kidney Disease (CKD)

All 11 CKD patients had glomerular kidney disease, **Table 4** provides demographic details of the patients and divides the healthy participants into young (<40 years) and older (>40 years) age groups for comparison. **Table 5** provides the MRI results for each of these groups.

Renal artery blood flow was significantly reduced in the older healthy participants compared to the young healthy participants, though no difference is seen between the older participants and CKD patients. In CKD, renal cortex perfusion and renal vein

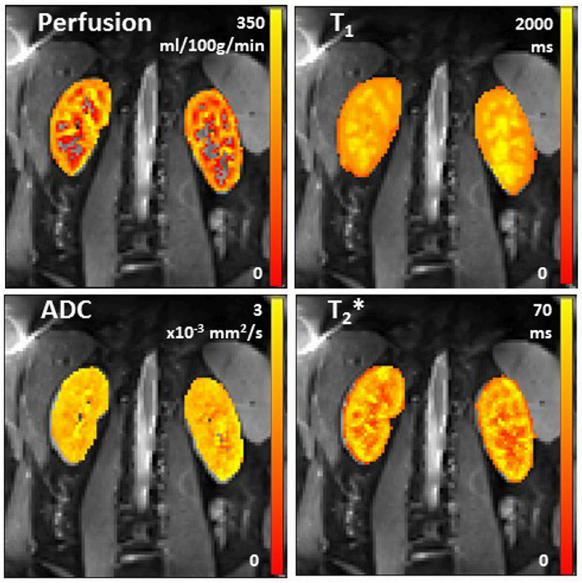

FIGURE 4 | Example arterial spin labeling perfusion, longitudinal relaxation time T_1, ADC (apparent diffusion coefficient), and transverse relaxation time T_2* maps in a healthy participant.

blood flow were lower than in older healthy participants. T_1 SE-EPI in the renal cortex was significantly higher in CKD patients compared to older healthy participants, and corticomedullary T_1 differentiation was reduced in CKD patients compared to older healthy participants. T_2* measured in the renal cortex and medulla was not significantly different in CKD patients compared with healthy participants. In this patient cohort, renal cortex ADC, D and total kidney volume in CKD patients were also not significantly different to healthy participants.

DISCUSSION

This article has demonstrated acquisition and analysis methods to perform multiparametric assessment of the kidneys in healthy participants and CKD patients.

Variability, Repeatability, and Field Strength Dependence in Healthy Participants

We provide a comprehensive summary of MRI parameter values for healthy participants, results are in agreement with values reported across separate studies in the literature (**Table 1**). When comparing T_1 measures for the renal cortex and medulla to literature values, it is important to consider the MR field strength and readout scheme used for the image acquisition. Here, we show the expected T_1 increase with field strength (**Table 2**). Further, the computed T_1 value is dependent on the image readout scheme, with a shorter "apparent" T_1 measured for a bFFE readout compared to a SE-EPI readout, due to the influence of transverse relaxation on the bFFE readout. The T_1 of the medulla was higher than that of the cortex, resulting in clearly visualized corticomedullary differentiation.

The CoV of T_1 measures is very low, <3% for cortex and medulla (**Table 3**). Cutajar et al. reported CoVs of between 0.3 and 11.5% for repeatability of renal cortex T_1 measures on the same day (Cutajar et al., 2012). Gillis et al. showed no significant difference between visits for repeated measures of renal cortex T_1 using a MOLLI method (Gillis et al., 2014). However, MOLLI has some compromises, it is a cardiac gated scheme which provides poor sampling of the inversion recovery curve, requires a breath hold per slice, and since it uses a bFFE readout, its "apparent" T_1 value is also affected by tissue fat content at 3 T (Mozes et al., 2016).

PC-MRI measures of renal artery and vein blood flow have a reasonably high CoV, as previously described (Bax et al., 2005; Khatir et al., 2014). This is likely a result of placement of the imaging slice. In contrast, ASL renal cortex perfusion is a voxel-wise measure and this is shown to have a low CoV and high ICC. Cutajar et al. reported CoVs of between 1.8 and 12.1% for repeatability of renal cortex perfusion measures on the same day (Cutajar et al., 2012) and Chowdhury et al. reported a within session CoV of 3.3% (Chowdhury et al., 2012), but to our knowledge there have been no CoVs reported for measures collected between visits. Gillis et al. showed no significant differences between visits for repeated measures of renal cortex perfusion (Gillis et al., 2014).

Thoeny et al. showed that the measured value of ADC is affected by the choice of b-values (Thoeny et al., 2005). Using only low b-values (0–100 s/mm^2) will result in a high calculated ADC, whilst high b-values (500–1,000 s/mm^2) will result in a low calculated ADC. Using a wide range of b-values provides the least variation in ADC between healthy participants. Here, we use b-values of between 0 and 500 s/mm^2 and show comparable results to Thoeny et al. (2005). Cutajar et al. found no significant difference in ADC between sessions, their ADC values were higher than we report, likely due to their acquisition using only two b-values (Cutajar et al., 2011). The value of both ADC and D had a low CoV, whilst D* and f_p had poor repeatability.

A wide range of renal cortex and medulla T_2* (R_2*) values are reported in the literature. T_2* decreases with increasing field strength and is longer in the renal cortex compared to the renal medulla, indicating the hypoxic state of the medulla. The T_2*/R_2* values we present are in agreement with several studies (Li et al., 2004a; Ding et al., 2013; Khatir et al., 2014; Piskunowicz et al., 2015; van der Bel et al., 2016), whilst others give lower (Simon-Zoula et al., 2006; Park et al., 2012) or higher (Li et al., 2004b) R_2*-values. Khatir et al. (2014) measured similar between session CoVs to those we present here.

Physiological Modulations in Healthy Participants

Here, we assess the change in T_2* on hypercapnia and on hyperoxia, and the change in T_1 in response to hyperoxia. T_2* and T_1 relaxation times of tissues have been suggested to be a potential biomarker for renal tissue oxygenation (Jones et al., 2002; O'Connor et al., 2009; Winter et al., 2011; Donati et al., 2012; Khatir et al., 2014; Ganesh et al., 2016). Changes in T_2* arise from local field inhomogeneities created

TABLE 1 | Between-subject variability for multiparametric MRI measures in healthy participants and associated literature values.

Parameter		Between subject variability		Literature values
		Mean ± std. dev.	Number of subjects	
Single renal artery flow		373 ± 105 ml/min	73	583 ± 164 ml/min (Bax et al., 2005) 443 (404–481) ml/min (Khatir et al., 2015) 365 ± 119 ml/min (Khatir et al., 2014) 0.48 ± 0.13 L/min (Steeden and Muthurangu, 2015)
Single renal vein flow		410 ± 134 ml/min	28	
Total perfusion to single kidney		222 ± 60 ml/min/100 ml	11	3.6 (3.2–4.0) ml/min/cm^3 (Khatir et al., 2015)
Cortex perfusion		255 ± 70 ml/100 g/min	85	204 ml/min/100 g (Cutajar et al., 2012) 355 ± 71 ml/100 g/min (Gardener and Francis, 2010) 321 ± 63 ml/min/100 g (Gillis et al., 2014) 200–260 ml/100 g/min (Martirosian et al., 2004) 367 ± 41 ml/100 g/min (Wang et al., 2012)
Cortex T_1 (at 3 T)	SE-EPI	1367 ± 79 ms	21	1,376 ± 104 ms (MOLLI) (Gillis et al., 2014)
	bFFE	1124 ± 114 ms	26	1,142 ± 154 ms (FSE) (de Bazelaire et al., 2004)
Medulla T_1 (at 3 T)	SE-EPI	1655 ± 76 ms	20	1,651 ± 86 ms (MOLLI) (Gillis et al., 2014)
	bFFE	1389 ± 126 ms	25	1,545 ± 142 ms (FSE) (de Bazelaire et al., 2004)
Cortex T_2^* (at 3 T)		49.6 ± 6.6 ms (R_2* 20.6 ± 3.3 s^{-1})	18	51 ± 8 ms (Ding et al., 2013) 21.8 ± 1.2 s^{-1} (Li et al., 2004b) 11.1 ± 3.8 s^{-1} (Park et al., 2012) 18.2 ± 1.7 s^{-1} (Piskunowicz et al., 2015) 17.4 ± 1.1 s^{-1} (van der Bel et al., 2016)
Medulla T_2^* (at 3T)		29.7 ± 5.4 ms (R_2* 34.9 ± 6.9 s^{-1})	18	37.4 ± 1.2 s^{-1} (Li et al., 2004b) 36 ± 7 ms (Ding et al., 2013)
Cortex ADC		2.3 ± 0.3 ×10^{-3} mm^2/s	39	2.4 ± 0.1 ×10^{-3} mm^2/s (Zhang et al., 2010) 2.63 ± 0.08 × 10^{-3} mm^2/s (Cutajar et al., 2011) 2.4 ± 0.2 × 10^{-3} mm^2/s (Sigmund et al., 2012) 2.00 ± 0.07 × 10^{-3} mm^2/s (Thoeny et al., 2005) 2.4 ± 0.1 × 10^{-3} mm^2/s (Wittsack et al., 2010)
Cortex D		1.7 ± 0.3 ×10^{-3} mm^2/s	38	1.8 ± 0.1 × 10^{-3} mm^2/s (Zhang et al., 2010) 1.96 ± 0.09 × 10^{-3} mm^2/s (Sigmund et al., 2012) 1.5 ± 0.1 × 10^{-3} mm^2/s (Wittsack et al., 2010) 2.44 ± 0.12 × 10^{-3} mm^2/s (Notohamiprodjo et al., 2015)
Cortex D*		10.7 ± 4.5 × 10^{-3} mm^2/s	29	14.2 ± 0.8 × 10^{-3} mm^2/s (Zhang et al., 2010) 24.56 ± 6.10 × 10^{-3} mm^2/s (Sigmund et al., 2012) 13.1 ± 2.2 × 10^{-3} mm^2/s (Wittsack et al., 2010) 22.7 ± 10.6 × 10^{-3} mm^2/s (Notohamiprodjo et al., 2015)
Cortex f_p		28 ± 10%	29	31 ± 2% (Zhang et al., 2010) 18.7 ± 3.5% (Sigmund et al., 2012) 52 ± 10% (Wittsack et al., 2010) 26.6 ± 6.1% (Notohamiprodjo et al., 2015)
Total kidney volume		367 ± 58 ml (Mean 184 ± 29 ml)	22	Mean across kidneys: 141.6 ± 28.5 ml (Seuss et al., 2017) 167 (97–307) ml (Cohen et al., 2009) 196 (136–295) ml (van den Dool et al., 2005)

T_1, longitudinal relaxation time; SE-EPI, spin echo-echo planar imaging; bFFE, balanced fast field echo; T_2, transverse relaxation time; ADC, Apparent Diffusion Coefficient; D, pure Diffusion coefficient; D*, pseudodiffusion coefficient; f_p, perfusion fraction.*

TABLE 2 | Field strength variability in T_1 and T_2*/R_2* in renal cortex and renal medulla, and corticomedullary differentiation (medulla-cortex) for healthy participants.

Parameter	Field strength (T)	Renal cortex		Renal medulla		Corticomedullary differentiation (medulla-cortex)	
		Mean ± std.dev.	Number of subjects	Mean ± std.dev.	Number of subjects	Mean ± std.dev.	Number of subjects
T_1 SE-EPI	1.5	1,024 ± 71 ms	8	1,272 ± 140 ms	8	248 ± 68 ms	8
	3	1,367 ± 79 ms	21	1,655 ± 76 ms	20	286 ± 58 ms	20
T_1 bFFE	1.5	1,053 ± 72 ms	58	1,318 ± 98 ms	38	265 ± 38 ms	38
	3	1,124 ± 114 ms	26	1,388 ± 126 ms	25	268 ± 80 ms	25
T_2*	1.5	70.7 ± 2.4 ms	8	40.7 ± 2.8 ms	8	−30.0 ± 5.2 ms	8
	3	49.6 ± 6.6 ms	18	29.7 ± 5.4 ms	18	−19.9 ± 5.1 ms	18
R_2*	1.5	14.2 ± 0.5 s^{-1}	8	24.6 ± 1.7 s^{-1}	2	10.5 ± 2.2 s^{-1}	8
	3	20.6 ± 3.3 s^{-1}	18	34.9 ± 6.9 s^{-1}	18	14.3 ± 5.0 s^{-1}	18

T_1, longitudinal relaxation time; SE-EPI, spin echo-echo planar imaging; bFFE, balanced fast field echo; T_2, transverse relaxation time; R_2*, transverse relaxation rate.*

TABLE 3 | Intra subject repeatability for the multiparametric MRI measures in healthy participants.

Parameter		Repeatability measures			
		CoV (%)	ICC	Number of subjects	Number of visits
Single renal artery flow		14.4 ± 4.3	0.844	11	3
Single renal vein flow		18.8 ± 10.3	0.649	11	3
Total perfusion to single kidney		14.9 ± 3.8	0.611	10	3
Cortex perfusion		9.3 ± 4.4	0.801	11	3
Cortex T_1 (at 3 T)	SE-EPI	2.0 ± 1.5	0.848	9	2
	bFFE	2.3 ± 1.3	0.616	11	3
Medulla T_1 (at 3 T)	SE-EPI	1.8 ± 1.5	0.997	9	2
	bFFE	2.9 ± 2.4	0.239	11	3
Cortex T_2* (at 3 T)		4.1 ± 3.0	0.718	4	2
Cortex ADC		2.9 ± 2.0	0.745	10	3
Cortex D		9.5 ± 4.8	0.307	10	3
Cortex D*		38.8 ± 19.6	0.210	10	3
Cortex f_p		21.5 ± 10.6	0.102	10	3
Total kidney volume		4.2 ± 2.6	0.985	11	3

CoV, coefficient of variation; ICC, intra class correlation; T_1, longitudinal relaxation time; SE-EPI, spin echo-echo planar imaging; bFFE, balanced fast field echo; T_2, transverse relaxation time; ADC, apparent diffusion coefficient; D, pure diffusion coefficient; D*, pseudodiffusion coefficient; f_p, perfusion fraction.*

by deoxyhemoglobin (Hb) molecules. Increasing the inspired oxygen increases the ratio of diamagnetic oxyhemoglobin to paramagnetic deoxyhemoglobin (HbO_2/Hb) leading to longer T_2*. Increasing inspired carbon dioxide reduces the oxygen affinity of hemoglobin, thus leading to increases in the levels of deoxygenated Hb in venous blood and a reduction in T_2* (Milman et al., 2013). Changes in T_1 arise from changes in levels of dissolved O_2 in plasma and tissue, since oxygen is weakly paramagnetic (Young et al., 1981), thus increasing levels of oxygen acts to shorten T_1.

There is discrepancy in the literature of the effect of breathing 100% oxygen on T_2*. Some studies have shown no change in T_2* in the renal cortex (Jones et al., 2002; O'Connor et al., 2009; Khatir et al., 2014; Niendorf et al., 2015) or medulla (Jones et al., 2002), whilst a small number of studies show a small increase in T_2* in the renal cortex (Winter et al., 2011; Ganesh et al., 2016) and medulla (Donati et al., 2012; Khatir et al., 2014). At normal levels of inspired oxygen, the body maintains hemoglobin levels in arterial blood near to saturation level. During hyperoxia, a higher fraction of HbO_2/Hb and a reduction in blood volume could both be expected to contribute to a small increase in T_2*. As an alternative, hypercapnic-hyperoxia has been shown to cause a marked 50% increase in renal T_2*-weighted signal intensity, suggesting this method provides enhanced sensitivity (Milman et al., 2013).

For T_1, previous studies have shown a decrease in the renal cortex on breathing 100% oxygen, which is equivalent to ∼600 mmHg (Jones et al., 2002; O'Connor et al., 2007, 2009; Ganesh et al., 2016). Here, we used our modified respiratory triggered scheme to measure T_1 and independently controlled end-tidal concentrations of oxygen and carbon dioxide (constant to ∼0.1 mmHg). No significant difference in the mode of T_1 was found between hypercapnia and normoxia. The controlled gas delivery was equivalent to breathing ∼80% oxygen, and this may explain the smaller T_1 change seen in our data. It should be noted that breathing 100% oxygen can lead to hypocapnia (Becker et al., 1996) resulting in a reduction in flow.

To our knowledge, no studies of human kidneys have used hypercapnia. Winter et al. showed no change in T_2* at 1.5 T in the rabbit renal cortex when inspiring 10% carbon dioxide (balance air; Winter et al., 2011), whilst Ganesh et al. show a decrease in T_2* at 3 T when inspiring 10–30% carbon dioxide (21% oxygen, balance nitrogen; Ganesh et al., 2016). Milman et al. showed that hypercapnia induced by 5% CO_2 inhalation caused a marked decline in hemodynamic response imaging maps, based on changes in the signal intensity of a T_2*-weighted image, resembling results of studies in the liver (Milman et al., 2013). The level of inspired carbon dioxide in this work is significantly lower than 10%, this may explain why our T_2* decrease did not reach significance.

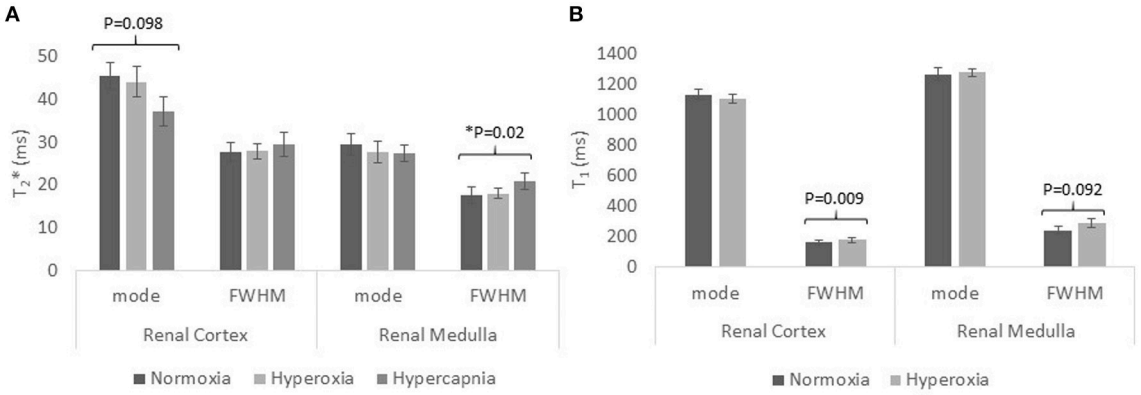

FIGURE 5 | The mode and FWHM (full-width-at-half-maximum) in the renal cortex and medulla of healthy participants for **(A)** transverse relaxation time T_2^* during normoxia, hyperoxia, and hypercapnia; **(B)** longitudinal relaxation time T_1 during normoxia and hyperoxia.

TABLE 4 | Characteristics of healthy participants, split according to age, <40 years and >40 years, and the chronic kidney disease patient cohort.

	Healthy participants <40 years	Healthy participants >40 years	CKD
Male/Female	53/16	34/24	8/3
Age (years)	25 ± 4	60 ± 9	52 ± 14
Height (m)	1.76 ± 0.09	1.71 ± 0.09	1.74 ± 0.06
Weight (kg)	72.4 ± 10.0	76.0 ± 11.7	89.7 ± 10.5
BMI (kg/m^2)	23 ± 2	26 ± 3	30 ± 4
eGFR (ml/min/1.73 m^2)	–	–	51 ± 15
Systolic BP (mmHg)	–	–	132 ± 8
Diastolic BP (mmHg)	–	–	82 ± 8
Hypertension Medication yes/no	–	–	8/3

CKD, Chronic Kidney Disease; BMI, body mass index; eGFR, estimated glomerular filtration rate; BP, blood pressure.

Alternative mechanisms of physiological modulation to assess renal oxygenation and microcirculation reactivity and functionality include water loading, sodium loading, or drug administration (e.g., angiotensin, furosemide, saline). Studies have shown that water loading results in an increase in BOLD T_2^* in the medulla (Prasad et al., 1996; Prasad and Epstein, 1999; Tumkur et al., 2006a; Vivier et al., 2013; Ding et al., 2015), this is thought to be due to the production of endogenous prostaglandin PGE2 in the medulla which decreases deoxyhemoglobin (Hb) levels, but it is not possible to distinguish between changes in oxygen supply and oxygen consumption. Similar more pronounced results have been shown following administration of furosemide (a sodium pump inhibitor; Prasad et al., 1996; Li et al., 2004a; Tumkur et al., 2006b; Vivier et al., 2013), coupled with a larger increase in urinary output (Vivier et al., 2013). Interestingly, T_2^* is not altered in older subjects after water loading (Prasad and Epstein, 1999) or furosemide administration (Epstein and Prasad, 2000).

Chronic Kidney Disease

The standard clinical assessment of renal function is the estimated GFR (eGFR) calculated from serum creatinine concentration. However, this is a late marker of renal dysfunction, is often discordant with tissue damage, is subject to hemodynamic fluctuation, and cannot be used to assess individual kidney function. Kidney biopsy has sampling error associated with the small specimen size, and comes with associated risks of an invasive procedure. This pilot study has assessed the use of multiparametric MRI in CKD patients, potentially providing a number of techniques by which to assess kidney structure and function. Renal blood flow and renal cortex perfusion was lower in CKD patients compared with healthy participants. T_1 values were increased in both renal cortex and medulla compared to healthy participants, though primarily in cortex, resulting in a loss of corticomedullary differentiation.

There have been a number of previous studies assessing changes in individual MRI parameters related to hemodynamics and structure in CKD patients (Inoue et al., 2011; Michaely et al., 2012; Xin-Long et al., 2012; Khatir et al., 2014, 2015; Milani et al., 2016). Studies have compared perfusion in CKD patients with healthy participants and found perfusion to be lower in CKD patients (Rossi et al., 2012; Tan et al., 2014). Gillis et al. showed that the T_1 relaxation time was longer in CKD patients compared to healthy participants (Gillis et al., 2016). Further, ADC values have been shown to be reduced in CKD compared to healthy participants (Goyal et al., 2012). A recent study using DWI and T_1 mapping has demonstrated changes in both kidney ADC and T_1 in animal models and humans with CKD (Friedli et al., 2016). Prior studies have shown conflicting changes in measures of oxygenation in CKD, with some groups reporting a reduction in oxygenation in CKD, whilst others report no differences in cortical or medullary R_2^* (Pruijm et al., 2014). Khatir et al. showed similar cortical and medulla R_2^* values at baseline between patients and controls. But on inspiring 100% oxygen, R_2^* significantly decreased in the renal cortex of CKD patients with no change in R_2^* was observed in healthy participants. Medullary R_2^* increased in both patients and controls on

TABLE 5 | Multiparametric MRI measures in healthy participants split according to age and Chronic Kidney Disease patients.

Parameter	Healthy participants <40 years		Healthy participants >40 years		CKD mean ± SD ($N = 11$)	*P*-value		
	Mean ± SD	N	Mean ± SD	N		ANOVA between groups	<40 years vs. >40 years	>40 years vs. CKD
Renal artery flow (ml/min)	427 ± 117	33	329 ± 69	40	314 ± 148	0.0001	<0.0001	ns
Renal vein flow (ml/min)	437 ± 142	21	334 ± 76	7	212 ± 90	0.0002	0.0773	0.0134
Cortex perfusion (ml/100 g/min)	279 ± 75	42	232 ± 57	43	83 ± 68	<0.0001	0.0019	<0.0001
SE-EPI T_1 (ms) (at 3 T) Cortex	1,347 ± 65	13	1,399 ± 93	8	1,530 ± 99	<0.0001	ns	0.0099
Medulla	1,635 ± 66	12	1,685 ± 84	8	1,726 ± 78	0.0254	ns	ns
ΔT_1	286 ± 28	12	286 ± 89	8	196 ± 45	0.0006	ns	0.0095
T_2^* (ms) (at 3 T) Cortex	48.9 ± 7.4	10	50.4 ± 5.8	8	54.6 ± 7.7	0.0860	ns	ns
Medulla	29.8 ± 5.4	10	29.5 ± 5.7	8	33.0 ± 9.0	ns	ns	ns
Cortex ADC ($\times 10^{-3}$ mm^2/s)	2.3 ± 0.4	23	2.4 ± 0.2	16	2.1 ± 0.3	ns	ns	ns
Cortex D ($\times 10^{-3}$ mm^2/s)	1.7 ± 0.2	23	1.6 ± 0.4	15	1.8 ± 0.4	ns	ns	ns
Total kidney volume (ml)	361 ± 62	15	382 ± 51	7	409 ± 153	ns	ns	ns
Kidney volume, BSA corrected (ml/m^2)	184 ± 29	15	190 ± 25	7	202 ± 86	ns	ns	ns

CKD, Chronic Kidney Disease; T_1, longitudinal relaxation time; SE-EPI, spin echo-echo planar imaging; T_2^*, transverse relaxation time; ADC, apparent diffusion coefficient; D pure diffusion coefficient; BSA body surface area; ns, not significant.

inspiring 100% oxygen (Khatir et al., 2015). Pruijm et al. (2014) assessed patients with CKD and arterial hypertension (Pruijm et al., 2014), no difference in R_2^* was seen between the patient group and healthy participants at baseline. However, following administration of furosemide, a blunted R_2^* decrease was seen in patients compared with healthy participants. Xin-Long et al. (2012) measured the corticomedullary differentiation in R_2^* in healthy participants and CKD patients and found an increased differentiation in CKD patients compared to healthy participants (Xin-Long et al., 2012).

Limitations

It is important to consider the different factors which can impact on reported MR measures. Inconsistent BOLD results have been widely documented between published studies, whilst Michaely et al. showed that in a study of 280 subjects, R_2^* correlated poorly with eGFR (Michaely et al., 2012). This is likely since R_2^* is only an estimator of oxygenation, and is confounded by many other factors, with it being suggested that changes in the blood volume fraction considerably influences renal T_2^* (Niendorf et al., 2015). Estimates of total renal blood flow need to consider kidney volume to also compute total perfusion, and in CKD patients the shrinkage of the kidney should be considered, which can mean that blood flow per kidney is preserved. However, this correction does not take into account that the cortex and medulla may not lose volume at the same rate.

ICC's are high for some MRI parameters presented—T_1, perfusion, renal artery flow and ADC—but other values are relatively low, presently hampering the introduction of these methods in clinical practice. Currently, MRI is expensive and multiple breath hold methods cannot be used in older, frail patients. Here, our multiparametric protocol includes a limited number of breath holds, with ASL, T_1, and DWI data collected using respiratory triggered acquisitions. In this study, inter-observer variability was not assessed since the post-processing is automated, including ROI placement. Further automation of this pipeline could be included and with the introduction of greater processing power, maps could be computed online at the scanner. In future, functional sodium technology to provide information on renal concentrating capacity will provide a further additional measure for multiparametric protocols (Maril et al., 2006). At this point, studies showing that MRI parameters can predict hard outcomes, such as, end stage renal disease, death or rapid decline of kidney function are necessary. For ultimate use in the clinic, MRI protocols need to be time efficient, and so it will be important to define key MRI parameters of high ICC which can be used for clinical assessment.

CONCLUSIONS

This paper has outlined a multiparametric MRI acquisition and analysis protocol for assessment of renal structure, hemodynamics and oxygenation. No other modality can combine non-invasive techniques to provide such a comprehensive evaluation of renal function as MRI. Studies showing that MRI has added value to simply monitoring serum creatinine and proteinuria in kidney disease, and that MRI can provide similar information as a kidney biopsy are now eagerly awaited. The ability of early identification of patients at risk of progressing to end-stage kidney disease and protocols to assess the efficacy of treatments would improve clinical outcome, be of cost benefit for society and improve life quality for the patients.

AUTHOR CONTRIBUTIONS

EC: study design, acquisition, analysis and interpretation of data, statistical analysis, drafting of manuscript, final

approval of manuscript, accountable for all aspects of the work; CEB: study design, acquisition, analysis and interpretation of data, critical revision of manuscript, final approval of manuscript, accountable for all aspects of the work; CRB: acquisition, analysis and interpretation of data, critical revision of manuscript, final approval of manuscript, accountable for all aspects of the work; BP: acquisition, analysis and interpretation of data, final approval of manuscript, accountable for all aspects of the work; HM: study design, interpretation of data, final approval of manuscript, accountable for all aspects of the work; MT: study design, interpretation of data, final approval of manuscript, accountable for all aspects of the work; NS: study design, interpretation of data, critical revision of manuscript, final approval of manuscript, accountable for all aspects of the work; SF: study design, acquisition, analysis and interpretation of data, drafting of manuscript, final approval of manuscript, accountable for all aspects of the work.

FUNDING

The authors acknowledge the financial support from the National Institute for Health Research Nottingham Digestive Diseases Biomedical Research Unit, Nottingham University Hospitals NHS Trust and University of Nottingham, the Medical Research Council Confidence in Concept Award and the Dr. Hadwen Trust. The Dr. Hadwen Trust (DHT) is the UK's leading non-animal biomedical research charity that exclusively funds and promotes human-relevant research that replaces the use of animals whilst supporting the progress of medicine.

ACKNOWLEDGMENTS

The authors acknowledge the support of the Sir Peter Mansfield Imaging Centre (SPMIC), the NIHR Nottingham Digestive Diseases Biomedical Research Unit (NDDBRU) and the Centre for Kidney Research and Innovation (CKRI), University of Nottingham.

REFERENCES

Adler, S., Huang, H., Wolin, M. S., and Kaminski, P. M. (2004). Oxidant stress leads to impaired regulation of renal cortical oxygen consumption by nitric oxide in the aging kidney. *J. Am. Soc. Nephrol.* 15, 52–60. doi: 10.1097/01.ASN.0000101032.21097.C5

Artz, N. S., Sadowski, E. A., Wentland, A. L., Djamali, A., Grist, T. M., Seo, S., et al. (2011a). Reproducibility of renal perfusion MR imaging in native and transplanted kidneys using non-contrast arterial spin labeling. *J. Magn. Reson. Imaging* 33, 1414–1421. doi: 10.1002/jmri.22552

Artz, N. S., Sadowski, E. A., Wentland, A. L., Grist, T. M., Seo, S., Djamali, A., et al. (2011b). Arterial spin labeling MRI for assessment of perfusion in native and transplanted kidneys. *Magn. Reson. Imaging* 29, 74–82. doi: 10.1016/j.mri.2010.07.018

Bax, L., Bakker, C. J., Klein, W. M., Blanken, N., Beutler, J. J., and Mali, W. P. (2005). Renal blood flow measurements with use of phase-contrast magnetic resonance imaging: normal values and reproducibility. *J. Vasc. Intervent. Radiol.* 16, 807–814. doi: 10.1097/01.RVI.0000161144.98350.28

Becker, H. F., Polo, O., McNamara, S. G., Berthon-Jones, M., and Sullivan, C. E. (1996). Effect of different levels of hyperoxia on breathing in healthy subjects. *J. Appl. Physiol.* 81, 1683–1690.

Blantz, R. C., Deng, A., Miracle, C. M., and Thomson, S. C. (2007). Regulation of kidney function and metabolism: a question of supply and demand. *Trans. Am. Clin. Climatol. Assoc.* 118, 23–43.

Boss, A., Martirosian, P., Graf, H., Claussen, C. D., Schlemmer, H. P., and Schick, F. (2005). High resolution MR perfusion imaging of the kidneys at 3 Tesla without administration of contrast media. *RoFo* 177, 1625–1630. doi: 10.1055/s-2005-858761

Buchanan, C. E., Cox, E. F., and Francis, S. T. (eds.). (2015). *Evaluation of Readout Schemes for Arterial Spin Labelling in the Human Kidney*. Toronto, ON: Int Soc Mag Reson.

Buxton, R. B., Frank, L. R., Wong, E. C., Siewert, B., Warach, S., and Edelman, R. R. (1998). A general kinetic model for quantitative perfusion imaging with arterial spin labeling. *Magn. Reson. Med.* 40, 383–396. doi: 10.1002/mrm.1910400308

Chowdhury, A. H., Cox, E. F., Francis, S. T., and Lobo, D. N. (2012). A randomized, controlled, double-blind crossover study on the effects of 2-L infusions of 0.9% saline and plasma-lyte(R) 148 on renal blood flow velocity and renal cortical tissue perfusion in healthy volunteers. *Ann. Surg.* 256, 18–24. doi: 10.1097/SLA.0b013e318256be72

Cohen, E. I., Kelly, S. A., Edye, M., Mitty, H. A., and Bromberg, J. S. (2009). MRI estimation of total renal volume demonstrates significant association with healthy donor weight. *Eur. J. Radiol.* 71, 283–287. doi: 10.1016/j.ejrad.2008.03.006

Cutajar, M., Clayden, J. D., Clark, C. A., and Gordon, I. (2011). Test-retest reliability and repeatability of renal diffusion tensor MRI in healthy subjects. *Eur. J. Radiol.* 80, e263–e268. doi: 10.1016/j.ejrad.2010.12.018

Cutajar, M., Thomas, D. L., Banks, T., Clark, C. A., Golay, X., and Gordon, I. (2012). Repeatability of renal arterial spin labelling MRI in healthy subjects. *Magma* 25, 145–153. doi: 10.1007/s10334-011-0300-9

Cutajar, M., Thomas, D. L., Hales, P. W., Banks, T., Clark, C. A., and Gordon, I. (2014). Comparison of ASL and DCE MRI for the non-invasive measurement of renal blood flow: quantification and reproducibility. *Eur. Radiol.* 24, 1300–1308. doi: 10.1007/s00330-014-3130-0

Dambreville, S., Chapman, A. B., Torres, V. E., King, B. F., Wallin, A. K., Frakes, D. H., et al. (2010). Renal arterial blood flow measurement by breath-held MRI: accuracy in phantom scans and reproducibility in healthy subjects. *Magn. Reson. Med.* 63, 940–950. doi: 10.1002/mrm.22278

de Bazelaire, C. M., Duhamel, G. D., Rofsky, N. M., and Alsop, D. C. (2004). MR imaging relaxation times of abdominal and pelvic tissues measured *in vivo* at 3.0 T: preliminary results. *Radiology* 230, 652–659. doi: 10.1148/radiol.2303021331

Debatin, J. F., Ting, R. H., Wegmuller, H., Sommer, F. G., Fredrickson, J. O., Brosnan, T. J., et al. (1994). Renal artery blood flow: quantitation with phase-contrast MR imaging with and without breath holding. *Radiology* 190, 371–378. doi: 10.1148/radiology.190.2.8284383

Ding, J., Xing, W., Wu, D., Chen, J., Pan, L., Sun, J., et al. (2015). Evaluation of renal oxygenation level changes after water loading using susceptibility-weighted imaging and T2* mapping. *Korean J. Radiol.* 16, 827–834. doi: 10.3348/kjr.2015.16.4.827

Ding, Y., Mason, R. P., McColl, R. W., Yuan, Q., Hallac, R. R., Sims, R. D., et al. (2013). Simultaneous measurement of tissue oxygen level-dependent (TOLD) and blood oxygenation level-dependent (BOLD) effects in abdominal tissue oxygenation level studies. *J. Magn. Reson. Imaging* 38, 1230–1236. doi: 10.1002/jmri.24006

Dobre, M. C., Ugurbil, K., and Marjanska, M. (2007). Determination of blood longitudinal relaxation time (T1) at high magnetic field strengths. *Magn. Reson. Imaging* 25, 733–735. doi: 10.1016/j.mri.2006.10.020

Donati, O. F., Nanz, D., Serra, A. L., and Boss, A. (2012). Quantitative BOLD response of the renal medulla to hyperoxic challenge at 1.5 T and 3.0 T. *NMR Biomed.* 25, 1133–1138. doi: 10.1002/nbm.2781

Dong, J., Yang, L., Su, T., Yang, X., Chen, B., Zhang, J., et al. (2013). Quantitative assessment of acute kidney injury by noninvasive arterial spin labeling perfusion MRI: a pilot study. *Sci. China Life Sci.* 56, 745–750. doi: 10.1007/s11427-013-4503-3

Epstein, F. H., and Prasad, P. (2000). Effects of furosemide on medullary oxygenation in younger and older subjects. *Kidney Int.* 57, 2080–2083. doi: 10.1046/j.1523-1755.2000.00057.x

Evans, R. G., Gardiner, B. S., Smith, D. W., and O'Connor, P. M. (2008). Intrarenal oxygenation: unique challenges and the biophysical basis of homeostasis. *Am. J. Physiol. Renal Physiol.* 295, F1259–F1270. doi: 10.1152/ajprenal.90230.2008

Fenchel, M., Martirosian, P., Langanke, J., Giersch, J., Miller, S., Stauder, N. I., et al. (2006). Perfusion MR imaging with FAIR true FISP spin labeling in patients with and without renal artery stenosis: initial experience. *Radiology* 238, 1013–1021. doi: 10.1148/radiol.2382041623

Friedli, I., Crowe, L. A., Berchtold, L., Moll, S., Hadaya, K., de Perrot, T., et al. (2016). New Magnetic resonance imaging index for renal fibrosis assessment: a comparison between diffusion-weighted imaging and T1 mapping with histological validation. *Sci. Rep.* 6:30088. doi: 10.1038/srep30088

Ganesh, T., Estrada, M., Duffin, J., and Cheng, H. L. (2016). T2* and T1 assessment of abdominal tissue response to graded hypoxia and hypercapnia using a controlled gas mixing circuit for small animals. *J. Magn. Reson. Imaging* 44, 305–316. doi: 10.1002/jmri.25169

Gardener, A. G., and Francis, S. T. (2010). Multislice perfusion of the kidneys using parallel imaging: image acquisition and analysis strategies. *Magn. Reson. Med.* 63, 1627–1636. doi: 10.1002/mrm.22387

Gillis, K. A., McComb, C., Foster, J. E., Taylor, A. H., Patel, R. K., Morris, S. T., et al. (2014). Inter-study reproducibility of arterial spin labelling magnetic resonance imaging for measurement of renal perfusion in healthy volunteers at 3 Tesla. *BMC Nephrol.* 15:23. doi: 10.1186/1471-2369-15-23

Gillis, K. A., McComb, C., Patel, R. K., Stevens, K. K., Schneider, M. P., Radjenovic, A., et al. (2016). Non-contrast renal magnetic resonance imaging to assess perfusion and corticomedullary differentiation in health and chronic kidney disease. *Nephron* 133, 183–192. doi: 10.1159/000447601

Goyal, A., Sharma, R., Bhalla, A. S., Gamanagatti, S., and Seth, A. (2012). Diffusion-weighted MRI in assessment of renal dysfunction. *Indian J. Radiol. Imaging* 22, 155–159. doi: 10.4103/0971-3026.107169

Hammon, M., Janka, R., Siegl, C., Seuss, H., Grosso, R., Martirosian, P., et al. (2016). Reproducibility of kidney perfusion measurements with arterial spin labeling at 1.5 Tesla MRI combined with semiautomatic segmentation for differential cortical and medullary assessment. *Medicine* 95:e3083. doi: 10.1097/MD.0000000000003083

Heusch, P., Wittsack, H. J., Heusner, T., Buchbender, C., Quang, M. N., Martirosian, P., et al. (2013). Correlation of biexponential diffusion parameters with arterial spin-labeling perfusion MRI: results in transplanted kidneys. *Invest. Radiol.* 48, 140–144. doi: 10.1097/RLI.0b013e318277bfe3

Hoad, C. L., Palaniyappan, N., Kaye, P., Chernova, Y., James, M. W., Costigan, C., et al. (2015). A study of T(1) relaxation time as a measure of liver fibrosis and the influence of confounding histological factors. *NMR Biomed.* 28, 706–714. doi: 10.1002/nbm.3299

Iles, L., Pfluger, H., Phrommintikul, A., Cherayath, J., Aksit, P., Gupta, S. N., et al. (2008). Evaluation of diffuse myocardial fibrosis in heart failure with cardiac magnetic resonance contrast-enhanced T1 mapping. *J. Am. Coll. Cardiol.* 52, 1574–1580. doi: 10.1016/j.jacc.2008.06.049

Inoue, T., Kozawa, E., Okada, H., Inukai, K., Watanabe, S., Kikuta, T., et al. (2011). Noninvasive evaluation of kidney hypoxia and fibrosis using magnetic resonance imaging. *J. Am. Soc. Nephrol.* 22, 1429–1434. doi: 10.1681/ASN.2010111143

Jellis, C. L., and Kwon, D. H. (2014). Myocardial T1 mapping: modalities and clinical applications. *Cardiovasc. Diagn. Ther.* 4, 126–137. doi: 10.3978/j.issn.2223-3652.2013.09.03

Jones, R. A., Ries, M., Moonen, C. T., and Grenier, N. (2002). Imaging the changes in renal T1 induced by the inhalation of pure oxygen: a feasibility study. *Magn. Reson. Med.* 47, 728–735. doi: 10.1002/mrm.10127

Karger, N., Biederer, J., Lusse, S., Grimm, J., Steffens, J., Heller, M., et al. (2000). Quantitation of renal perfusion using arterial spin labeling with FAIR-UFLARE. *Magn. Reson. Imaging* 18, 641–647. doi: 10.1016/S0730-725X(00)00155-7

Khatir, D. S., Pedersen, M., Jespersen, B., and Buus, N. H. (2014). Reproducibility of MRI renal artery blood flow and BOLD measurements in patients with chronic kidney disease and healthy controls. *J. Magn. Reson. Imaging* 40, 1091–1098. doi: 10.1002/jmri.24446

Khatir, D. S., Pedersen, M., Jespersen, B., and Buus, N. H. (2015). Evaluation of renal blood flow and oxygenation in CKD using magnetic resonance imaging. *Am. J. Kidney Dis.* 66, 402–411. doi: 10.1053/j.ajkd.2014.11.022

Kiefer, C., Schroth, G., Gralla, J., Diehm, N., Baumgartner, I., and Husmann, M. (2009). A feasibility study on model-based evaluation of kidney perfusion measured by means of FAIR prepared true-FISP arterial spin labeling (ASL) on a 3-T MR scanner. *Acad. Radiol.* 16, 79–87. doi: 10.1016/j.acra.2008.04.024

Koh, D. M., Collins, D. J., and Orton, M. R. (2011). Intravoxel incoherent motion in body diffusion-weighted MRI: reality and challenges. *Am. J. Roentgenol.* 196, 1351–1361. doi: 10.2214/AJR.10.5515

Le Bihan, D., Breton, E., Lallemand, D., Aubin, M. L., Vignaud, J., and Laval-Jeantet, M. (1988). Separation of diffusion and perfusion in intravoxel incoherent motion MR imaging. *Radiology* 168, 497–505. doi: 10.1148/radiology.168.2.3393671

Li, L. P., Storey, P., Pierchala, L., Li, W., Polzin, J., and Prasad, P. (2004a). Evaluation of the reproducibility of intrarenal R2* and DeltaR2* measurements following administration of furosemide and during waterload. *J. Magn. Reson. Imaging* 19, 610–616. doi: 10.1002/jmri.20043

Li, L. P., Vu, A. T., Li, B. S., Dunkle, E., and Prasad, P. V. (2004b). Evaluation of intrarenal oxygenation by BOLD MRI at 3.0 T. *J. Magn. Reson. Imaging* 20, 901–904. doi: 10.1002/jmri.20176

Maril, N., Margalit, R., Rosen, S., Heyman, S. N., and Degani, H. (2006). Detection of evolving acute tubular necrosis with renal 23Na MRI: studies in rats. *Kidney Int.* 69, 765–768. doi: 10.1038/sj.ki.5000152

Martirosian, P., Klose, U., Mader, I., and Schick, F. (2004). FAIR true-FISP perfusion imaging of the kidneys. *Magn. Reson. Med.* 51, 353–361. doi: 10.1002/mrm.10709

Michaely, H. J., Metzger, L., Haneder, S., Hansmann, J., Schoenberg, S. O., and Attenberger, U. I. (2012). Renal BOLD-MRI does not reflect renal function in chronic kidney disease. *Kidney Int.* 81, 684–689. doi: 10.1038/ki.2011.455

Michaely, H. J., Schoenberg, S. O., Ittrich, C., Dikow, R., Bock, M., and Guenther, M. (2004). Renal disease: value of functional magnetic resonance imaging with flow and perfusion measurements. *Invest. Radiol.* 39, 698–705. doi: 10.1097/00004424-200411000-00008

Milani, B., Ansaloni, A., Sousa-Guimaraes, S., Vakilzadeh, N., Piskunowicz, M., Vogt, B., et al. (2016). Reduction of cortical oxygenation in chronic kidney disease: evidence obtained with a new analysis method of blood oxygenation level-dependent magnetic resonance imaging. *Nephrol. Dial. Transplant.* doi: 10.1093/ndt/gfw362. [Epub ahead of print].

Milman, Z., Heyman, S. N., Corchia, N., Edrei, Y., Axelrod, J. H., Rosenberger, C., et al. (2013). Hemodynamic response magnetic resonance imaging: application for renal hemodynamic characterization. *Nephrol. Dial. Transplant.* 28, 1150–1156. doi: 10.1093/ndt/gfs541

Mozes, F. E., Tunnicliffe, E. M., Pavlides, M., and Robson, M. D. (2016). Influence of fat on liver T1 measurements using modified Look-Locker inversion recovery (MOLLI) methods at 3T. *J. Magn. Reson. Imaging* 44, 105–111. doi: 10.1002/jmri.25146

Niendorf, T., Pohlmann, A., Arakelyan, K., Flemming, B., Cantow, K., Hentschel, J., et al. (2015). How bold is blood oxygenation level-dependent (BOLD) magnetic resonance imaging of the kidney? Opportunities, challenges and future directions. *Acta Physiol.* 213, 19–38. doi: 10.1111/apha.12393

Niles, D. J., Artz, N. S., Djamali, A., Sadowski, E. A., Grist, T. M., and Fain, S. B. (2016). Longitudinal assessment of renal perfusion and oxygenation in transplant donor-recipient pairs using arterial spin labeling and blood oxygen level-dependent magnetic resonance imaging. *Invest. Radiol.* 51, 113–120. doi: 10.1097/RLI.0000000000000210

Notohamiprodjo, M., Chandarana, H., Mikheev, A., Rusinek, H., Grinstead, J., Feiweier, T., et al. (2015). Combined intravoxel incoherent motion and diffusion tensor imaging of renal diffusion and flow anisotropy. *Magn. Reson. Med.* 73, 1526–1532. doi: 10.1002/mrm.25245

O'Connor, J. P., Jackson, A., Buonaccorsi, G. A., Buckley, D. L., Roberts, C., Watson, Y., et al. (2007). Organ-specific effects of oxygen and carbogen gas inhalation on tissue longitudinal relaxation times. *Magn. Reson. Med.* 58, 490–496. doi: 10.1002/mrm.21357

O'Connor, J. P., Naish, J. H., Jackson, A., Waterton, J. C., Watson, Y., Cheung, S., et al. (2009). Comparison of normal tissue R1 and R2* modulation by oxygen and carbogen. *Magn. Reson. Med.* 61, 75–83. doi: 10.1002/mrm.21815

Park, J. B., Santos, J. M., Hargreaves, B. A., Nayak, K. S., Sommer, G., Hu, B. S., et al. (2005). Rapid measurement of renal artery blood flow with ungated spiral phase-contrast MRI. *J. Magn. Reson. Imaging* 21, 590–595. doi: 10.1002/jmri.20325

Park, S. H., Wang, D. J., and Duong, T. Q. (2013). Balanced steady state free precession for arterial spin labeling MRI: initial experience for blood flow mapping in human brain, retina, and kidney. *Magn. Reson. Imaging* 31, 1044–1050. doi: 10.1016/j.mri.2013.03.024

Park, S. Y., Kim, C. K., Park, B. K., Huh, W., Kim, S. J., and Kim, B. (2012). Evaluation of transplanted kidneys using blood oxygenation level-dependent MRI at 3 T: a preliminary study. *Am. J. Roentgenol.* 198, 1108–1114. doi: 10.2214/AJR.11.7253

Piskunowicz, M., Hofmann, L., Zuercher, E., Bassi, I., Milani, B., Stuber, M., et al. (2015). A new technique with high reproducibility to estimate renal oxygenation using BOLD-MRI in chronic kidney disease. *Magn. Reson. Imaging* 33, 253–261. doi: 10.1016/j.mri.2014.12.002

Prasad, P. V., and Epstein, F. H. (1999). Changes in renal medullary pO2 during water diuresis as evaluated by blood oxygenation level-dependent magnetic resonance imaging: effects of aging and cyclooxygenase inhibition. *Kidney Int.* 55, 294–298. doi: 10.1046/j.1523-1755.1999.00237.x

Prasad, P. V., Edelman, R. R., and Epstein, F. H. (1996). Noninvasive evaluation of intrarenal oxygenation with BOLD MRI. *Circulation* 94, 3271–3275. doi: 10.1161/01.CIR.94.12.3271

Pruijm, M., Hofmann, L., Piskunowicz, M., Muller, M. E., Zweiacker, C., Bassi, I., et al. (2014). Determinants of renal tissue oxygenation as measured with BOLD-MRI in chronic kidney disease and hypertension in humans. *PLoS ONE* 9:e95895. doi: 10.1371/journal.pone.0095895

Pruijm, M., Milani, B., and Burnier, M. (2017). Blood oxygenation level-dependent MRI to assess renal oxygenation in renal diseases: progresses and challenges. *Front. Physiol.* 7:667. doi: 10.3389/fphys.2016.00667

Ritt, M., Janka, R., Schneider, M. P., Martirosian, P., Hornegger, J., Bautz, W., et al. (2010). Measurement of kidney perfusion by magnetic resonance imaging: comparison of MRI with arterial spin labeling to para-aminohippuric acid plasma clearance in male subjects with metabolic syndrome. *Nephrol. Dial.* 25, 1126–1133. doi: 10.1093/ndt/gfp639

Rossi, C., Artunc, F., Martirosian, P., Schlemmer, H. P., Schick, F., and Boss, A. (2012). Histogram analysis of renal arterial spin labeling perfusion data reveals differences between volunteers and patients with mild chronic kidney disease. *Invest. Radiol.* 47, 490–496. doi: 10.1097/RLI.0b013e318257063a

Schmitt, P., Griswold, M. A., Jakob, P. M., Kotas, M., Gulani, V., Flentje, M., et al. (2004). Inversion recovery TrueFISP: quantification of T1, T2, and spin density. *Magn. Reson. Med.* 51, 661–667. doi: 10.1002/mrm.20058

Schoenberg, S. O., Just, A., Bock, M., Knopp, M. V., Persson, P. B., and Kirchheim, H. R. (1997). Noninvasive analysis of renal artery blood flow dynamics with MR cine phase-contrast flow measurements. *Am. J. Physiol.* 272, H2477–H2484.

Seuss, H., Janka, R., Prummer, M., Cavallaro, A., Hammon, R., Theis, R., et al. (2017). Development and evaluation of a semi-automated segmentation tool and a modified ellipsoid formula for volumetric analysis of the kidney in non-contrast T2-weighted MR images. *J. Digit. Imaging* 30, 244–254. doi: 10.1007/s10278-016-9936-3

Sigmund, E. E., Vivier, P. H., Sui, D., Lamparello, N. A., Tantillo, K., Mikheev, A., et al. (2012). Intravoxel incoherent motion and diffusion-tensor imaging in renal tissue under hydration and furosemide flow challenges. *Radiology* 263, 758–769. doi: 10.1148/radiol.12111327

Simon-Zoula, S. C., Hofmann, L., Giger, A., Vogt, B., Vock, P., Frey, F. J., et al. (2006). Non-invasive monitoring of renal oxygenation using BOLD-MRI: a reproducibility study. *NMR Biomed.* 19, 84–89. doi: 10.1002/nbm.1004

Skorecki, K., Chertow, G. M., Marsden, P. A., Taal, M. W., and Yu, A. S. L. (2016). *Brenner and Rector's The Kidney, 10th Edn*. Philadelphia, PA: Elsevier.

Steeden, J. A., and Muthurangu, V. (2015). Investigating the limitations of single breath-hold renal artery blood flow measurements using spiral phase contrast MR with R-R interval averaging. *J. Magn. Reson. Imaging* 41, 1143–1149. doi: 10.1002/jmri.24638

Suo, S., Lin, N., Wang, H., Zhang, L., Wang, R., Zhang, S., et al. (2015). Intravoxel incoherent motion diffusion-weighted MR imaging of breast cancer at 3.0 Tesla: comparison of different curve-fitting methods. *J. Magn. Reson. Imaging* 42, 362–370. doi: 10.1002/jmri.24799

Tan, H., Koktzoglou, I., and Prasad, P. V. (2014). Renal perfusion imaging with two-dimensional navigator gated arterial spin labeling. *Magn. Reson. Med.* 71, 570–579. doi: 10.1002/mrm.24692

Thoeny, H. C., De Keyzer, F., Oyen, R. H., and Peeters, R. R. (2005). Diffusion-weighted MR imaging of kidneys in healthy volunteers and patients with parenchymal diseases: initial experience. *Radiology* 235, 911–917. doi: 10.1148/radiol.2353040554

Thomson, S. C., and Blantz, R. C. (2008). Glomerulotubular balance, tubuloglomerular feedback, and salt homeostasis. *J. Am. Soc. Nephrol.* 19, 2272–2275. doi: 10.1681/ASN.2007121326

Tumkur, S. M., Vu, A. T., Li, L. P., Pierchala, L., and Prasad, P. V. (2006a). Evaluation of intra-renal oxygenation during water diuresis: a time-resolved study using BOLD MRI. *Kidney Int.* 70, 139–143. doi: 10.1038/sj.ki.5000347

Tumkur, S., Vu, A., Li, L., and Prasad, P. V. (2006b). Evaluation of intrarenal oxygenation at 3.0 T using 3-dimensional multiple gradient-recalled echo sequence. *Invest. Radiol.* 41, 181–184. doi: 10.1097/01.rli.0000187166.43871.fb

Tunnicliffe, E. M., Banerjee, R., Pavlides, M., Neubauer, S., and Robson, M. D. (2017). A model for hepatic fibrosis: the competing effects of cell loss and iron on shortened modified Look-Locker inversion recovery T1 (shMOLLI-T1) in the liver. *J. Magn. Reson. Imaging* 45, 450–462. doi: 10.1002/jmri.25392

van den Dool, S. W., Wasser, M. N., de Fijter, J. W., Hoekstra, J., and van der Geest, R. J. (2005). Functional renal volume: quantitative analysis at gadolinium-enhanced MR angiography–feasibility study in healthy potential kidney donors. *Radiology* 236, 189–195. doi: 10.1148/radiol.2361021463

van der Bel, R., Coolen, B. F., Nederveen, A. J., Potters, W. V., Verberne, H. J., Vogt, L., et al. (2016). Magnetic resonance imaging-derived renal oxygenation and perfusion during continuous, steady-state angiotensin-II infusion in healthy humans. *J. Am. Heart Assoc.* 5:e003185. doi: 10.1161/JAHA.115.003185

Venkatachalam, M. A., Griffin, K. A., Lan, R., Geng, H., Saikumar, P., and Bidani, A. K. (2010). Acute kidney injury: a springboard for progression in chronic kidney disease. *Am. J. Physiol. Renal Physiol.* 298, F1078–F1094. doi: 10.1152/ajprenal.00017.2010

Vivier, P. H., Storey, P., Chandarana, H., Yamamoto, A., Tantillo, K., Khan, U., et al. (2013). Renal blood oxygenation level-dependent imaging: contribution of R2 to R2* values. *Invest. Radiol.* 48, 501–508. doi: 10.1097/RLI.0b013e3182823591

Wang, J., Zhang, Y., Yang, X., Wang, X., Zhang, J., Fang, J., et al. (2012). Hemodynamic effects of furosemide on renal perfusion as evaluated by ASL-MRI. *Acad. Radiol.* 19, 1194–1200. doi: 10.1016/j.acra.2012.04.021

Winter, J. D., Estrada, M., and Cheng, H. L. (2011). Normal tissue quantitative T1 and T2* MRI relaxation time responses to hypercapnic and hyperoxic gases. *Acad. Radiol.* 18, 1159–1167. doi: 10.1016/j.acra.2011.04.016

Wittsack, H. J., Lanzman, R. S., Mathys, C., Janssen, H., Modder, U., and Blondin, D. (2010). Statistical evaluation of diffusion-weighted imaging of the human kidney. *Magn. Reson. Med.* 64, 616–622. doi: 10.1002/mrm.22436

Xin-Long, P., Jing-Xia, X., Jian-Yu, L., Song, W., and Xin-Kui, T. (2012). A preliminary study of blood-oxygen-level-dependent MRI in patients with chronic kidney disease. *Magn. Reson. Imaging* 30, 330–335. doi: 10.1016/j.mri.2011.10.003

Young, I. R., Clarke, G. J., Bailes, D. R., Pennock, J. M., Doyle, F. H., and Bydder, G. M. (1981). Enhancement of relaxation rate with paramagnetic contrast agents in NMR imaging. *J. Comput. Tomogr.* 5, 543–547. doi: 10.1016/0149-936X(81)90089-8

Zhang, J. L., Sigmund, E. E., Chandarana, H., Rusinek, H., Chen, Q., Vivier, P. H., et al. (2010). Variability of renal apparent diffusion coefficients: limitations of the monoexponential model for diffusion quantification. *Radiology* 254, 783–792. doi: 10.1148/radiol.09090891

Conflict of Interest Statement: The authors declare that the research was conducted in the absence of any commercial or financial relationships that could be construed as a potential conflict of interest.

9.7 Publication VII: McGrath DM, Bradley CR, Francis ST. In silico evaluation and optimisation of magnetic resonance elastography of the liver. Physics in Medicine & Biology. 2021 Nov 10;66(22):225005.

PAPER • OPEN ACCESS

In silico evaluation and optimisation of magnetic resonance elastography of the liver

To cite this article: Deirdre M McGrath *et al* 2021 *Phys. Med. Biol.* **66** 225005

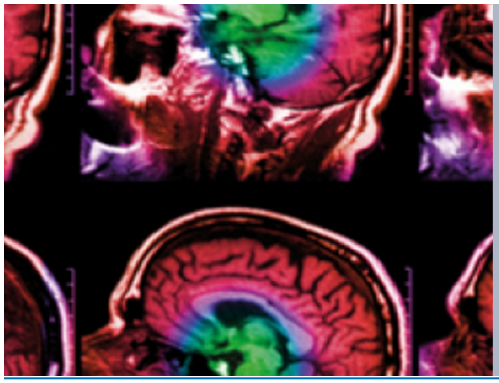

IOP Publishing Phys. Med. Biol. 66 (2021) 225005 https://doi.org/10.1088/1361-6560/ac3263

Physics in Medicine & Biology

IPEM Institute of Physics and Engineering in Medicine

OPEN ACCESS

RECEIVED
12 May 2021

REVISED
7 September 2021

ACCEPTED FOR PUBLICATION
22 October 2021

PUBLISHED
10 November 2021

PAPER

In silico evaluation and optimisation of magnetic resonance elastography of the liver

Deirdre M McGrath[1,2], **Christopher R Bradley**[1,2] and **Susan T Francis**[1,2]

[1] Sir Peter Mansfield Imaging Centre, University of Nottingham, University Park, Nottingham NG7 2RD, United Kingdom
[2] NIHR Nottingham Biomedical Research Centre, Radiological Sciences, Division of Clinical Neuroscience, Queens Medical Centre, Nottingham, NG7 2UH, United Kingdom

E-mail: Deirdre.McGrath@nottingham.ac.uk

Keywords: magnetic resonance elastography, simulation, finite element modelling, liver, fibrosis, cirrhosis

Supplementary material for this article is available online

Abstract

Objective. Magnetic resonance elastography (MRE) is widely adopted as a biomarker of liver fibrosis. However, *in vivo* MRE accuracy is difficult to assess. *Approach.* Finite element model (FEM) simulation was employed to evaluate liver MRE accuracy and inform methodological optimisation. MRE data was simulated in a 3D FEM of the human torso including the liver, and compared with spin-echo echo-planar imaging MRE acquisitions. The simulated MRE results were compared with the ground truth magnitude of the complex shear modulus ($|G^*|$) for varying: (1) ground truth liver $|G^*|$; (2) simulated imaging resolution; (3) added noise; (4) data smoothing. Motion and strain-based signal-to-noise (SNR) metrics were evaluated on the simulated data as a means to select higher-quality voxels for preparation of acquired MRE summary statistics of $|G^*|$. *Main results.* The simulated MRE accuracy for a given ground truth $|G^*|$ was found to be a function of imaging resolution, motion-SNR and smoothing. At typical imaging resolutions, it was found that due to under-sampling of the MRE wave-field, combined with motion-related noise, the reconstructed simulated $|G^*|$ could contain errors on the scale of the difference between liver fibrosis stages, e.g. 54% error for ground truth $|G^*| = 1$ kPa. Optimum imaging resolutions were identified for given ground truth $|G^*|$ and motion-SNR levels. *Significance.* This study provides important knowledge on the accuracy and optimisation of liver MRE. For example, for motion-SNR $\leqslant 5$, to distinguish between liver $|G^*|$ of 2 and 3 kPa (i.e. early-stage liver fibrosis) it was predicted that the optimum isotropic voxel size is 4–6 mm.

1. Introduction

Magnetic resonance elastography (MRE) (McGrath 2018) is a powerful diagnostic tool to determine the biomechanical properties of biological tissue. Through its sensitivity to pathology-driven changes in tissue biomechanics, MRE can detect disease such as fibrosis (Yin *et al* 2007, Singh *et al* 2015). There are two broad classes of MRE, dynamic (Muthupillai *et al* 1995) and static (or 'quasi-static') methods (McGrath *et al* 2012). In the former, mechanical waves are delivered, while the latter involves applying a compressive force to the whole tissue volume. For both, the resulting displacement field is measured using motion encoding gradients (MEGs) and the biomechanical properties are estimated from the measurements using an inversion algorithm to produce an 'elastogram'. Dynamic MRE has been widely adopted for the detection and staging of hepatic fibrosis and cirrhosis (Singh *et al* 2015, Mathew and Venkatesh 2018). However, a number of questions remain with regard to MRE validation.

Crucially, it is difficult to determine the true accuracy of clinical MRE. Comparison with mechanical bench-top testing of surgically-resected tissue is usually not possible in human studies. Biopsy cores can be removed to assess liver fibrosis via histological analysis (Morisaka *et al* 2018). However, the biomechanical properties of

ex vivo tissue do not match the *in vivo* state due to loss of hydration and blood pressure, removal from the tissue matrix, and potential damage and loss of structural integrity.

Commonly physical phantoms are built to test MRE and benchmark accuracy. However it is difficult to make anthropomorphic phantoms that reproduce the *in vivo* MRE motion field; although some work has been done on breast phantoms (Madsen *et al* 1988, Madsen *et al* 2006). In liver MRE, the vibrations delivered to the skin undergo multiple reflections and refractions at anatomical interfaces, e.g. the ribs. Hence, the *in vivo* wave pattern is more complex than that of a geometric and homogeneous phantom, and an inversion algorithm that performs well for a phantom will not necessarily be optimal for *in vivo* tissue. Furthermore, the ground truth mechanical properties of the phantom material might be difficult to determine. For water-based materials, e.g. gelatine, the properties may be temperature-dependent, or change over time with dehydration. Moreover, non-water-based materials, e.g. acrylics, might not include sufficient viscosity to model biological tissue.

The determination of *in vivo* MRE accuracy is challenging, as it is influenced by multiple factors. One solution is to validate MRE methods using computational modelling, as demonstrated for brain (McGrath *et al* 2016, McGrath *et al* 2017). The advantage of this approach is that the ground truth mechanical properties are known *a priori* and can be compared with the inversion-reconstructed properties to measure accuracy. Anthropomorphic *in silico* models can be generated from anatomical imaging data and used to simulate MRE motion fields in the body. The computed data can be compared with MRE data measured from the same individual, to evaluate the realism of the simulation. Further, *in silico* data can be used to validate and optimise MRE acquisition methodology and inversion algorithms.

This work presents finite element model (FEM) based MRE simulations to optimise MRE acquisitions and assess the accuracy of MRE to measure liver biomechanical properties. The purpose of this initial study is to investigate the potential of simulation-based MRE evaluation, starting with the model of a healthy individual; while future studies with models of other volunteers and patients will be needed to fully examine this technique. It should be recognised that the realism of simulations is necessarily limited in various aspects, which might influence the accuracy of absolute simulated values. But such simulations do allow the exploration of the sensitivity of MRE to detect a change in mechanical properties with disease, to assess the linearity of MRE measures with respect to underlying properties and the potential influence of factors such as imaging resolution.

Recent research has reported the advantages of spin-echo echo-planar imaging (SE-EPI) MRE over gradient-echo based MRE methods for the liver, in particular for 3 Tesla (T) where magnetic field inhomogeneity effects are pronounced in patients with high liver iron load and thus short transverse relaxation time (T_2^*) (Cunha *et al* 2018). Therefore SE-EPI MRE was acquired and compared with the simulated MRE in the same individual whose data was simulated.

2. Materials and methods

2.1. MRI acquisitions

MRI data was collected on a 3-T Philips Ingenia scanner (Philips Medical Systems, Best, Netherlands), with MRE implemented using the Resoundant acoustic wave delivery system (Resoundant Inc., Rochester, MN) (Venkatesh *et al* 2013). Calculations and image processing were carried out in MATLAB (R2017b, MathWorks Inc., Natick, Massachusetts, USA).

One healthy male volunteer (age 26 years) was scanned with informed consent and in accordance with local research ethics guidance.

In MRE, multiple acquisitions capture the wave field at different snap-shots in time. These are combined via discrete Fourier transform (DFT) to obtain a harmonic steady-state complex displacement field, **u**

$$u(\mathbf{x},\ t) = u(\mathbf{x}) \exp(i\omega t), \tag{1}$$

where ω is the angular frequency of the vibration. Time-steps are collected by varying the phase offset (α) between the mechanical wave and the MEG. In this study the number of phase offsets (N_{PO}) was set to 8, i.e. 8 values of α between 0 and 2π.

Four SE-EPI MRE acquisitions were made with different isotropic spatial resolutions and driver frequencies using the scan parameters: (1) Voxel dimension = 4 × 4 × 4 mm^3, Frequency (freq) = 60 Hz, field of view (FOV) = 384 × 384 × 24 mm^3, matrix = 96 × 96 × 6, repetition time (TR) = 600 ms, echo time (TE) = 58 ms, EPI factor = 39; (2) Voxel dimension = 5 × 5 × 5 mm^3, freq = 60 Hz, FOV = 400 × 400 × 30 mm^3; matrix = 80 × 80 × 6, TR = 600 ms, TE = 58 ms, EPI factor = 33; (3) Voxel dimension = 6 × 6 × 6 mm^3, freq = 60 Hz, FOV = 384 × 384 × 36 mm^3; matrix = 64 × 64 × 6, TR = 600 ms, TE = 58 ms, EPI factor = 27; (4) Voxel dimension = 6 × 6 × 6 mm^3, freq = 50 Hz, FOV = 384 × 384 × 36 mm^3; matrix = 64 × 64 × 6, TR = 720 ms, TE = 70 ms, EPI factor = 27. One signal average was employed throughout. Each scan duration was 16 s, in which 8 phase offsets were collected during an end-expiration

breath-hold. In each acquisition six axial slices covering the central liver volume were collected. Voxel sizes were chosen based on the simulation results for healthy liver. The frequency was changed to explore variability in the degree of wave attenuation.

MRE acquisitions were repeated to collect each of the MEG directions (head-foot (H-F), anterior–posterior (A-P), right-left (R-L)), with the motion of the tissue in the direction of the applied MEG encoded as phase-shifts which are directly proportional to the displacements. Separate acquisitions confirmed the volunteer had T_2^*/T_2 values within a healthy liver range (Kritsaneepaiboon *et al* 2018).

For FEM preparation, a whole-body anatomical imaging was collected on the same subject using a multi-point gradient-echo based Dixon (mDixon) scan (Dixon 1984, Xiang 2006) using the scan parameters: FOV $= 448 \times 560 \times 300\,\text{mm}^3$, matrix $= 280 \times 280 \times 200$, voxel $= 1 \times 1 \times 1.5\,\text{mm}^3$; TR $= 3$ ms, TE $= 1.12$ and 1.99 ms, flip angle $= 10°$, signal averages $= 1$. The mDixon method was chosen as it provided a variety of contrasts to inform the data segmentation for the FEM: water-only, fat-only and in-phase and opposed-phase images.

2.2. Calculation of motion- and strain-based SNR to evaluate MRE accuracy

An aim of this study was to explore potential metrics for selection of higher-quality elastogram data, and both motion- and strain-based SNR were considered. Motion-based SNR is likely to be more informative than imaging-SNR; where the measured motion is proportional to the phase-shift accrued by the tissue moving in the MEG.

The DFT of measured displacements obtaining the harmonic steady-state can be described as fitting a sinusoid S to each voxel of the data (for each motion direction):

$$S = \text{Re}\{ue^{i\omega t}\}, \tag{2}$$

where u is the complex-valued amplitude for the voxel in a given direction. In McGarry *et al* (2011), the noise of the measured displacements N_{meas} was estimated as the standard deviation (SD) of differences between measured and fitted displacements:

$$N_{meas} = \sigma\{d_i - u\cos(\omega t_i)\}, \tag{3}$$

where σ indicates the SD over the phase offsets and d_i represents the measured displacements at the different phase offset time-steps t_i ($\omega t_i \equiv \alpha_i$). The noise of the fitted displacement amplitude N_{amp} was related to N_{meas} via the propagation of uncertainties through the DFT (McGarry *et al* 2011):

$$N_{amp} = \sqrt{\frac{2}{N_{PO}}}N_{meas}. \tag{4}$$

The SNR based on the measured displacements divided by N_{meas} is referred to as MM-SNR ('measured-motion' SNR), and that based on the real component of the steady-state amplitudes and N_{amp} is denoted MA-SNR ('motion-amplitude' SNR). Voxel-wise MA-SNR was calculated separately for the 3 motion directions and subsequently averaged over the directions.

As the focus here is to estimate shear elastic modulus, shear strain is likely to be a more pertinent quantity than tissue displacement, which may be dominated by bulk motion. Thus octahedral shear strain (OSS) was calculated (McGarry *et al* 2011). The deviatoric or shear strain component of the OSS is :

$$\epsilon_s = \frac{2}{3}\sqrt{(\epsilon_{xx}-\epsilon_{yy})^2 + (\epsilon_{xx}-\epsilon_{zz})^2 + (\epsilon_{yy}-\epsilon_{zz})^2 + 6(\epsilon_{xy}^2 + \epsilon_{xz}^2 + \epsilon_{yz}^2)}, \tag{5}$$

where ϵ_{xx} are unique components of strain in three directions (x, y and z).

Similar to McGarry *et al* (2011), the strain noise $\epsilon_s^{\text{noise}}$ was calculated by evaluating equation (5) with strain values calculated from N_{amp} for each direction x, y, z, and SNR based on the OSS:

$$\text{OSS-SNR} = \frac{\overline{\epsilon_s}}{\epsilon_s^{\text{noise}}}, \tag{6}$$

where $\overline{\epsilon_s}$ indicates time averaging over the phase offsets. As N_{amp} is positive, a random sign was assigned to the N_{amp} values to generate a realistic noise distribution prior to calculation of $\epsilon_s^{\text{noise}}$, as used in McGarry *et al* (2011). However, while in McGarry *et al* (2011) $\overline{\epsilon_s}$ was also averaged over a volume, in this work the OSS-SNR was calculated for individual voxels, thus allowing visualisation of the spatial distribution of the OSS-SNR.

2.3. Direct Inversion to calculate MRE elastograms

For a viscoelastic material with the assumption of isotropy and local homogeneity of the material properties, solving the Navier–Stokes equation for the propagation of an acoustic wave yields the viscoelastic moduli from the motion field (Sinkus *et al* 2005). Substituting the time harmonic curl of the motion field ($\mathbf{v} = \nabla \times \mathbf{u}$) into the viscoelastic wave equation gives the Helmholtz equation:

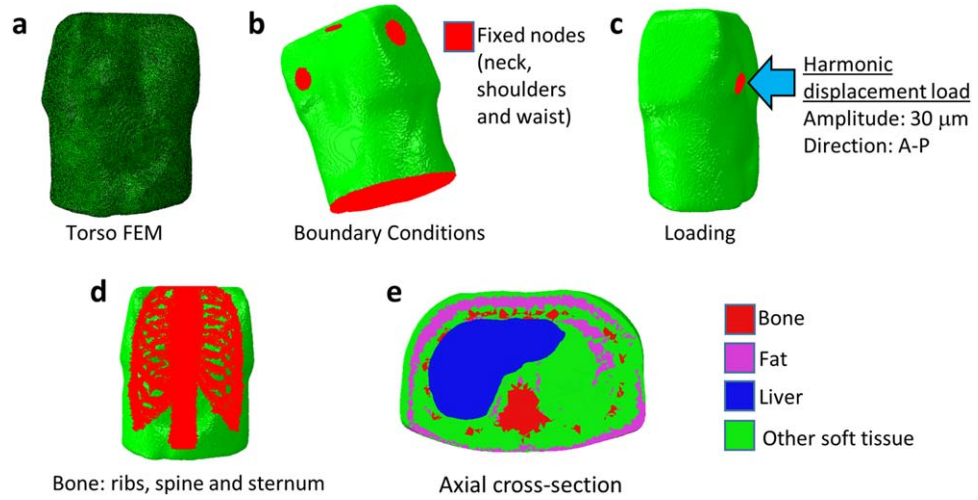

Figure 1. 3D FEM of human torso (a) torso FEM mesh; (b) boundary conditions of nodes with *x*-, *y*- and *z*-displacements fixed to zero at the positions of truncation at the neck, arms and waist (c) loading nodes position at the right of the sternal notch, and direction and amplitude of loading, i.e. anterior–posterior (A-P) and with real amplitude of 30 μm; (d) 3D view of elements assigned with the properties of bone, i.e. ribs, spine and sternum; (e) axial cross section of model with elements coloured according to the specified material models, i.e. liver, fat, bone, other soft tissue.

$$-\rho\omega^2\mathbf{v} = (G' + iG'')\,\nabla^2\mathbf{v}, \tag{7}$$

where ρ is the material density, $\nabla^2\mathbf{v}$ is the Laplacian of the curl (Sinkus *et al* 2005), and G' and G" are the storage and loss moduli describing the shear elasticity and viscosity respectively, which are the real and imaginary components of the complex shear modulus, G^*. In this study, the direct inversion approach of Sinkus *et al* 2005 is employed. The curl and Laplacian were calculated via finite differences, and G' and G" solved by 'direct inversion' of equation (7) via a least-squares calculation. In this study G' and G" were calculated for each voxel, from which $|G^*|$ was calculated, and the accuracy of $|G^*|$ compared with ground truth was reported.

In MRE, motion is encoded in the phase of the MR signal, which must be unwrapped and scaled by the appropriate motion-encoding scaling factor to obtain the underlying displacements (Muthupillai *et al* 1996). Alternatively, when direct inversion is employed it is not necessary to convert the phase-shifts into displacements, as the motion-encoding factor cancels out. For the acquired MRE data in this study, Laplacian phase unwrapping was employed (Dittmann *et al* 2016) prior to calculation of the steady-state harmonic phase values via DFT.

Previous MRE studies have reported that pre-filtering or smoothing of the data results in better visual appearance of the elastograms (Murphy *et al* 2013, Barnhill *et al* 2018). However, it is not clear what impact this has on accuracy. Spatial smoothing of the curl with a $3 \times 3 \times 3$ box filter was found to give optimum results in previous work (McGrath *et al* 2016) and hence this smoothing was explored for the simulated and acquired data.

Many other inversion methods have been developed for elasticity imaging (Doyley, 2012), including local frequency estimation (LFE) (Manduca *et al* 2001), iterative optimisation, such as the over-lapping subzone method (Van Houten *et al* 1999), and multi-frequency methods (Tzschätzsch *et al* 2016).

In order to provide a comparison with direct inversion, the LFE algorithm (MREWave, Mayo Clinic, www.mayo.edu/research/documents/mrewave) was also applied to the acquired MRE data and the simulated data with no added noise (see supplementary information). Three motion directions were incorporated and filtering was explored.

2.4. Simulation of liver MRE using an anthropomorphic phantom of the torso

Simulation of MRE was carried out using Abaqus 2017 (Dassault Systèmes Simulia Corp, Johnston, Rhode Island, USA), and used direct-solution steady-state dynamic analysis: a perturbation procedure for which the model response to an applied harmonic vibration is calculated about a base state, generating complex frequency-space steady-state nodal displacements **u** (equation (1)).

An anthropomorphic FEM of the torso was generated, consisting of sub-regions: liver, bone, fat and generalised soft tissue (figure 1). The bone region consisted of ribs, spine and sternum (figure 1(d)), and the fat included subcutaneous and visceral fat (figure 1(e)). The addition of bone and fat introduced material heterogeneity to enhance the realism of the model, and in particular the ribs and spine were added to simulate wave reflection and scattering effects. In MRE the compression wave delivered at the skin is partially mode-

Table 1. Modelled tissue material properties in torso FEM.

Tissue type	Frequency (Hz)	G′ (kPa)	G″(kPa)	$\lvert G^* \rvert$ (kPa)	Poisson's ratio	Density (kg m^{-3})	Shear wavelength (mm)
Liver - LM1	60	0.6	0.8	1.0	0.499	1000	13
Liver - LM2	60	1.833	0.8	2.0	0.499	1000	23
Liver - LM3	60	2.891	0.8	3.0	0.499	1000	28
Liver - LM4	60	3.919	0.8	4.0	0.499	1000	33
Liver - LM5	60	4.936	0.8	5.0	0.499	1000	37
Fat	60	0.95	0.32	1.0	0.499	1000	16
Soft tissue	60	4.5	2.2	5.0	0.499	1000	35
			Young's Modulus E (MPa)				
Bone	60	10			0.25	1830	779

converted to shear waves when passing through the ribs before reaching the liver, with some wave-energy also reflected off the spine into the liver.

The sub-regions were defined by a combination of manual and automated segmentation of the mDixon scan. The outer edges of the model were selected manually from the water-only images, and for computational efficiency the model excluded the arms and was truncated at the neck and waist. Liver and bone regions were manually segmented using the water-only images, while fat was segmented automatically using signal-thresholding on the fat-only images. Binary masks were generated for each sub-region. While the automated segmentation steps could be completed rapidly, the manual segmentation of the rib cage was the most costly in terms of time and took several hours to complete.

FE meshes were prepared using ISO2MESH software, an open-source mesh generation toolbox , that uses surface and volumetric meshing algorithms from the computational geometry algorithms library (CGAL, www.cgal.org) (Tran *et al* 2020) and Tetgen (wias-berlin.de/software/tetgen). A combined multi-label mask of the torso and liver was made and used to create a linear four-node tetrahedral element mesh using the 'vol2mesh' function of ISO2MESH, which meshes each labelled region as a distinct, closed surface, ensuring there are shared nodes at region interfaces. The total number of model elements was 5117 417, with 4501 646 in the liver sub-mesh. The maximum volume of the liver elements was set to 1 mm^3, the average element edge-length for the liver sub-mesh was 1.5 mm, and for the outer torso mesh 6.5 mm. A higher mesh density was prescribed for the liver, compared to outside the liver, to allow generation of simulated voxel sizes in the range of interest ($\geqslant$2 mm isotropic). The processing time for the torso FEM MRE simulation was ~7 h, with parallel use of 8 processors on a dual-quad core PC with 256 GB RAM. Separate testing of a smaller tissue model for which three FEMs were generated with 0.5, 1 and 2 mm^3 element volumes, demonstrated that the mean $\lvert G^* \rvert$ converged for all three element volumes at 2 mm simulated isotropic voxel resolution.

Fat was distributed across the torso volume, and therefore was not suitable for the creation of sub-meshes. The bone structure of the rib cage would have required very fine meshing for accurate representation, and this would have placed a high computational requirement on the parts of the FEM outside liver, when here the priority was for simulation accuracy inside the liver. Instead, the material properties for bone and fat were ascribed to individual elements of the torso model by identifying the elements whose centroids fell within the volume for each tissue type, as defined by the binary masks. Generalised soft tissue properties were assigned to the remaining elements of the torso. The material properties for all tissues are shown in table 1. Those assigned to the liver were varied between five sets of liver materials (LM1-LM5) which were estimated from MRE literature for healthy and diseased liver (Asbach *et al* 2008, Venkatesh *et al* 2013), and the other properties were ascribed based on literature values, e.g. for bone the cortical bone properties of the spine (Lee *et al* 2000). The liver properties could also have been estimated from *ex vivo* tissue measurements to provide an alternative and objective evaluation; however *ex vivo* measurements would not have allowed for the influence of blood pressure and the surrounding tissue matrix. All materials except bone were modelled as viscoelastic, while bone was modelled as linear elastic. Furthermore, all materials except bone were modelled as near-incompressible with hybrid elements (linear pressure) elements, in order to avoid volumetric locking by discretizing and solving for the pressure field independently of the displacements.

For the boundary conditions (BCs) (figure 1(b)) nodes were selected at the neck, shoulders and waist, and were fixed. These BCs achieved the dual purpose of tethering the model in space, and also had the benefit of reducing wave reflections from surfaces where the model was truncated, i.e. in reality waves would be free to pass through to the head, arms, abdomen and legs. Loading nodes (figure 1(c)) were selected on the model surface at a position corresponding to that used, and which is recommended, for liver MRE acquisitions, i.e. at the front of the body, over the lower ribs and to the right of the sternal notch (Quantitative Imaging Biomarkers

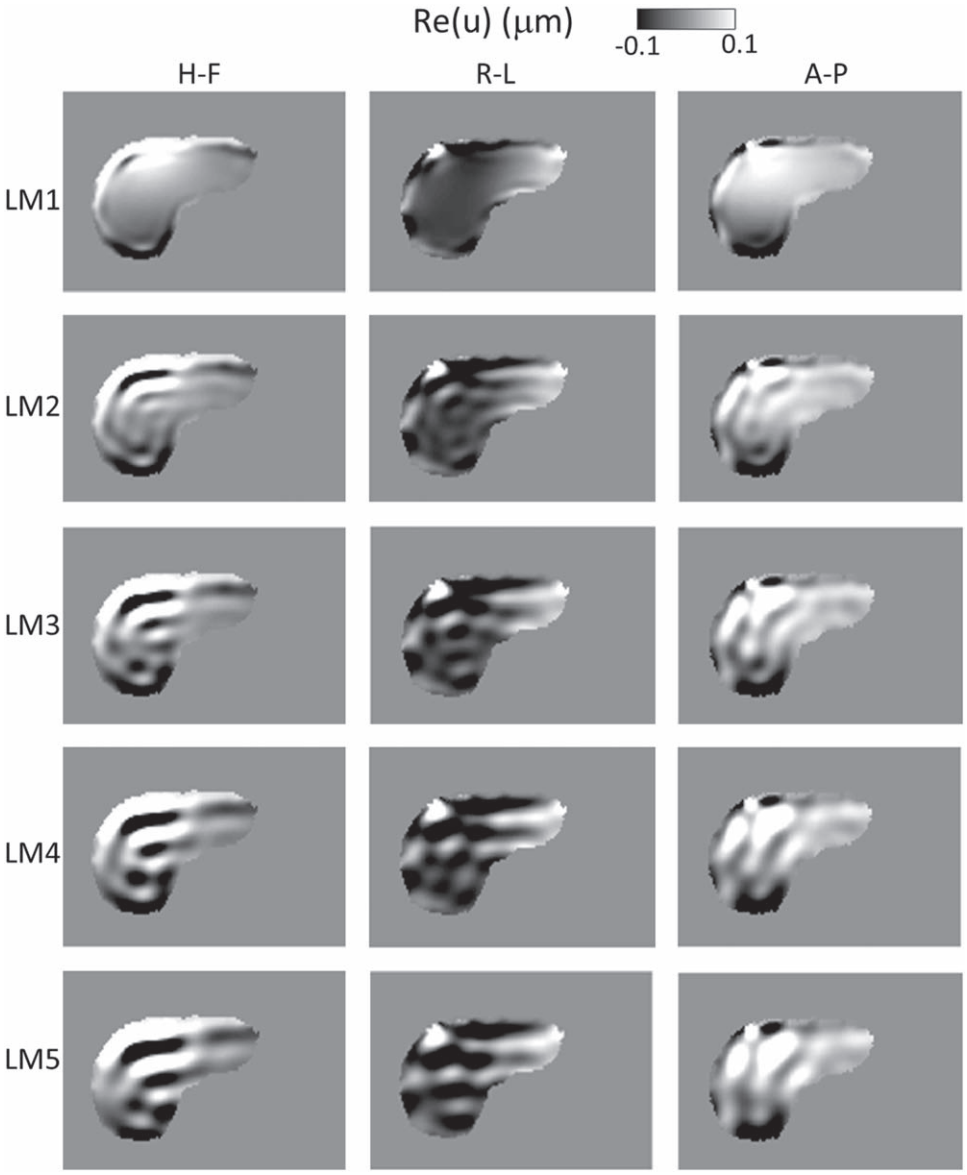

Figure 2. Maps of the real components of the simulated steady-state displacements in the head-foot (HF), right-left (RL) and anterior–posterior (AP) directions for liver models LM1-LM5 ($|G^*|_{GT} = 1, 2, 3, 4,$ and 5 kPa).

Alliance, 2018). MRE was simulated by delivering a harmonic displacement to the loading nodes at 30 μm amplitude and 60 Hz frequency in the anterior–posterior direction.

The nodal displacements were interpolated onto an isotropic 'virtual-voxel' grid with a step-size of 1 mm, using the MATLAB implementation of the 'Natural Neighbour' interpolation algorithm (Sibson 1981). The data was resampled to different isotropic resolutions by averaging the 1 mm data over varying cubic volumes to simulate the imaging partial-volume effect. Virtual phase-offset images ($N_{PO} = 8$) were calculated by multiplying the interpolated steady-state $\mathbf{u}(x)$ (equation (1)) by $\exp(i\alpha)$, and selecting the real component. Gaussian noise was added for the specified MM-SNR from the range 1–10 000, and the steady-state displacements recalculated by DFT.

3. Results

3.1. Simulated MRE motion data with no added noise

The real components of the simulated displacement fields in the H-F, R-L and A-P directions for LM1-LM5 are shown in figure 2. The wave patterns differ considerably with LM. For LM1 (ground truth $|G^*|_{GT} = 1$ kPa, i.e. healthy liver) the waves are attenuated before reaching the liver centre. At higher $|G^*|_{GT}$ (moving to LM5), the waves travel further into the liver, and are reflected from the far boundary, resulting in interference patterns. For

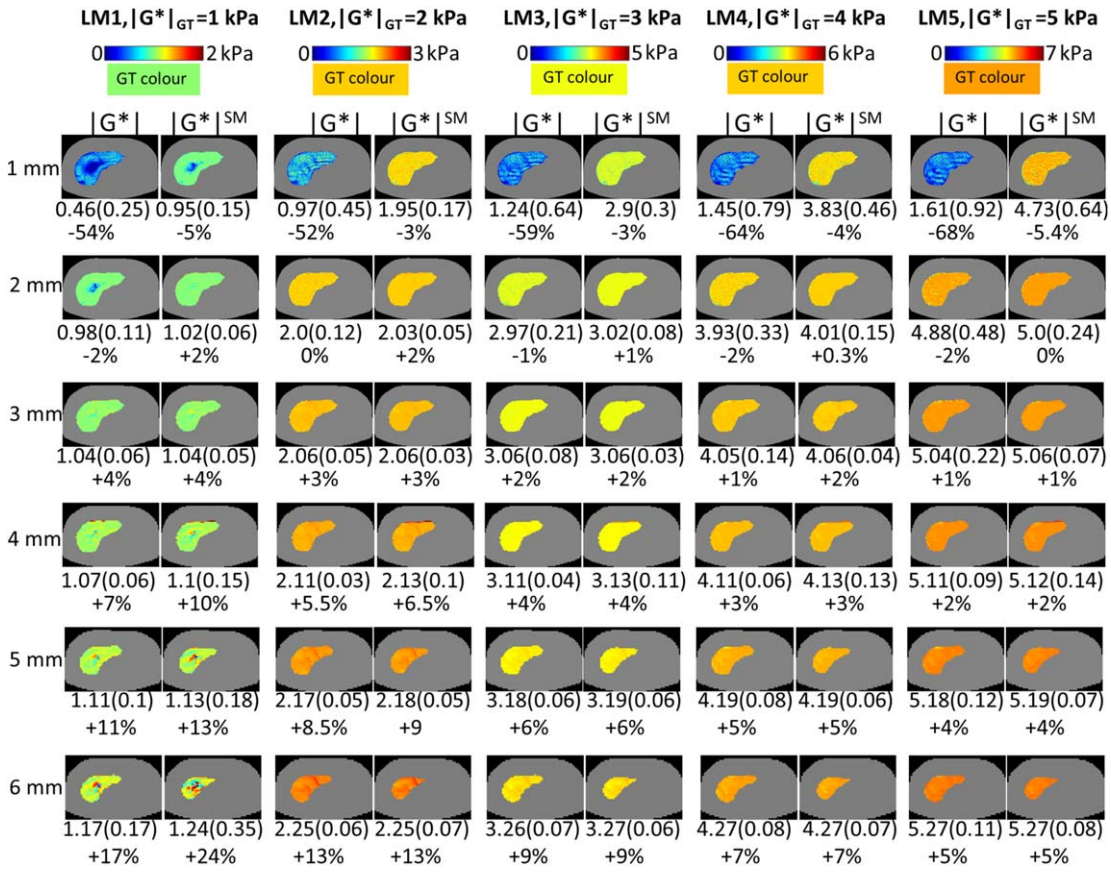

Figure 3. Results of MRE simulations in 3D liver models with homogeneous material properties according to models LM1-LM5 (ground truth $|G^*|_{GT} = 1$–5 kPa) and with no added noise. The $|G^*|$ maps without and with ($|G^*|^{SM}$) 3D box smoothing of the curl for central axial slices through the liver volume and for different isotropic simulated voxel sizes (1–6 mm). Eroded masks of the liver volume, excluding a margin of ~8 mm from the liver edges, is applied to the displayed images. The mean (standard deviation) are shown for $|G^*|$ and $|G^*|^{SM}$ for the eroded liver volumes. To provide a visual reference, for each LM, the colour of the ground truth $|G^*|$ is shown in a box under the colour bar.

a given LM, the displacements in the three directions are of comparable amplitudes, with unpredictable patterns, especially for the A-P and R-L directions. See supporting information videos S1-S9 for animations of the simulated motion for LM2.

3.2. Effect of imaging resolution on simulated MRE accuracy with no added noise

Figure 3 shows simulated elastograms with no added noise for LM1-LM5 and isotropic voxel dimensions 1–6 mm, with the mean and SD, and percentage error on the mean compared with ground truth. For display and subsequent analysis the 3D mask of the liver volume was eroded by a margin of ~8 mm to exclude edge values which result from errors in the direct inversion near the interface of the liver with surrounding tissue (i.e. due to the assumption of local homogeneity in direct inversion and the complexity of the wave field at the boundaries where transmitted, reflected, and refracted waves are combined). Elastograms are compared without smoothing ($|G^*|$) and with ($|G^*|^{SM}$) 3D box filter smoothing of the curl. The focus is on the smoothed results, as the errors from simulation (even without added noise) warrant smoothing. For all LM the mean $|G^*|^{SM}$ values closest to the ground truth are at 2 mm resolution, with errors on the mean as low as 0% for LM5. In theory the results at 1 mm resolution for the 3D liver should exceed the accuracy of 2 mm. However as the average element edge-length for the 3D liver mesh was 1.5 mm, there was insufficient nodal density in the mesh to provide optimum results at 1 mm voxel size.

In general the elastograms are smooth at higher spatial resolutions (e.g. 2 mm), while at coarser resolutions artefactual patterns appear due to under-sampling of the complicated wave fields, as seen in 2D brain tissue simulations in McGrath *et al* (2016). Also, similarly to the data in McGrath *et al* (2016), there is a directly proportional overestimate of mean $|G^*|$ as the voxel size increases. In figure 3, at 2 mm resolution, for higher ground truth $|G^*|$ (e.g. $|G^*|_{GT} = 5$ kPa) the error artefacts are less prevalent compared to lower $|G^*|_{GT}$ (i.e. 1 and 2 kPa), and as the voxel size increases the artefacts are more accentuated for the low $|G^*|_{GT}$ simulations. For LM1, $|G^*|$ is overestimated in the centre of the liver as the wave amplitude has been attenuated to near zero, and the apparently long wavelengths are reconstructed as stiffer material.

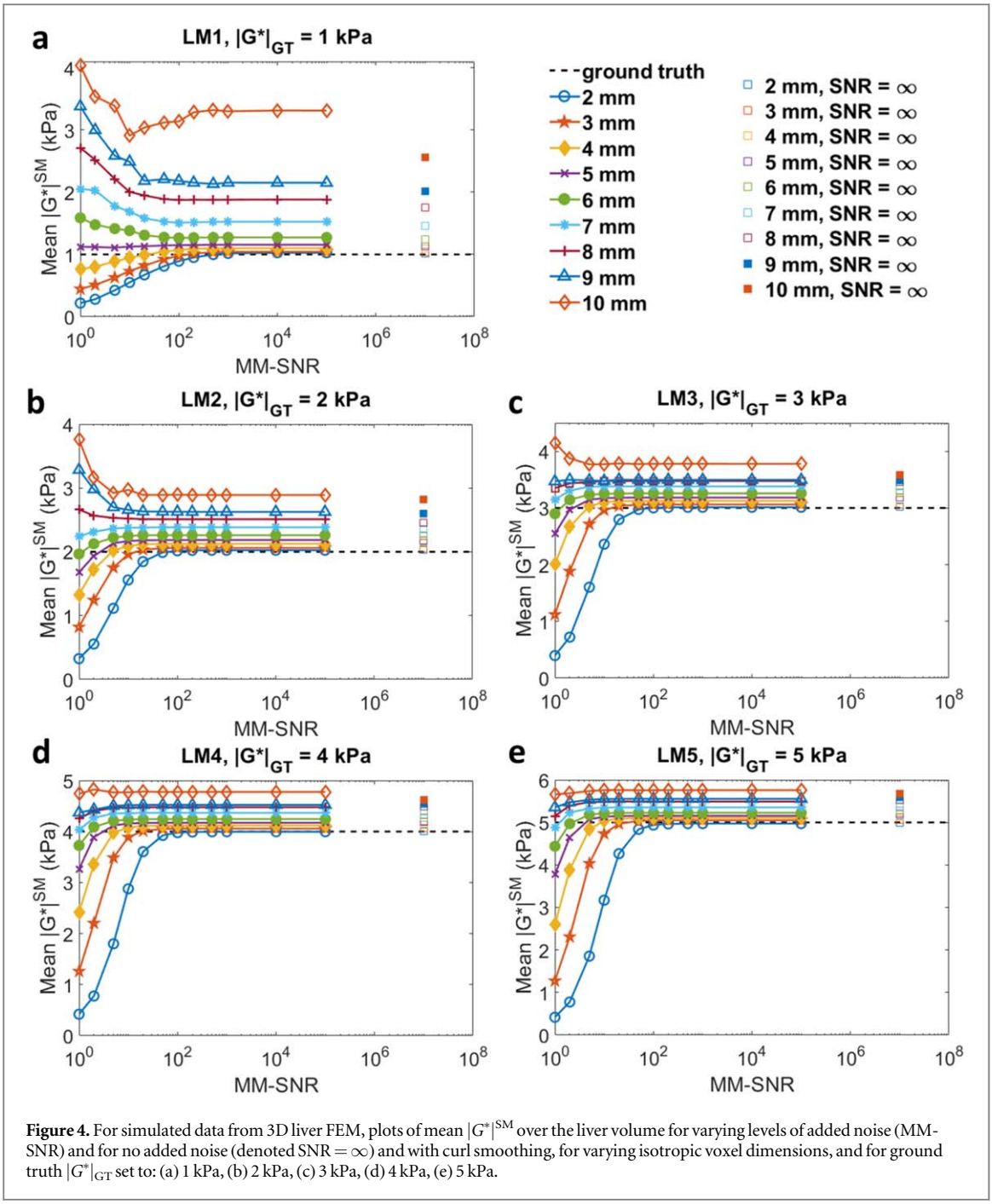

Figure 4. For simulated data from 3D liver FEM, plots of mean $|G^*|^{SM}$ over the liver volume for varying levels of added noise (MM-SNR) and for no added noise (denoted SNR $= \infty$) and with curl smoothing, for varying isotropic voxel dimensions, and for ground truth $|G^*|_{GT}$ set to: (a) 1 kPa, (b) 2 kPa, (c) 3 kPa, (d) 4 kPa, (e) 5 kPa.

3.3. Effect of added noise and imaging resolution on simulated MRE accuracy

Figure 4 plots the mean $|G^*|^{SM}$ for the eroded liver volumes versus levels of added noise (MM-SNR) for different resolutions and for LM1-LM5. The relationship between inversion accuracy, noise and resolution is complicated. In general, increased MM-SNR led to more accurate estimates of $|G^*|$. However, for larger voxel sizes $|G^*|$ was overestimated, as is the case for no added noise (figure 3). For lower MM-SNR, larger voxel sizes are needed to recover $|G^*|$, and the optimum voxel sizes increase with $|G^*|$.

Figure 5 plots the mean $|G^*|^{SM}$ over the (eroded) liver volume against the ground truth values for the different voxel sizes for the instance of no added noise and added noise with MM-SNR $= 1, 2, 5, 10$ and 20. Table 2 provides the optimum voxel size for each liver material LM1-LM5 and for all LMs combined for varying MM-SNR. As an example, if MM-SNR $\leqslant 5$ and one wants to focus on the distinguishing between liver tissue of 2 and 3 kPa (i.e. early-stage liver fibrosis) then the optimum isotropic voxel size would be 4–6 mm.

3.4. Comparison of simulated and acquired liver MRE at matched imaging resolutions and MA-SNR

Matching resolutions and motion-SNR levels were compared between acquisitions and simulations, allowing assessment of acquired-elastogram accuracy.

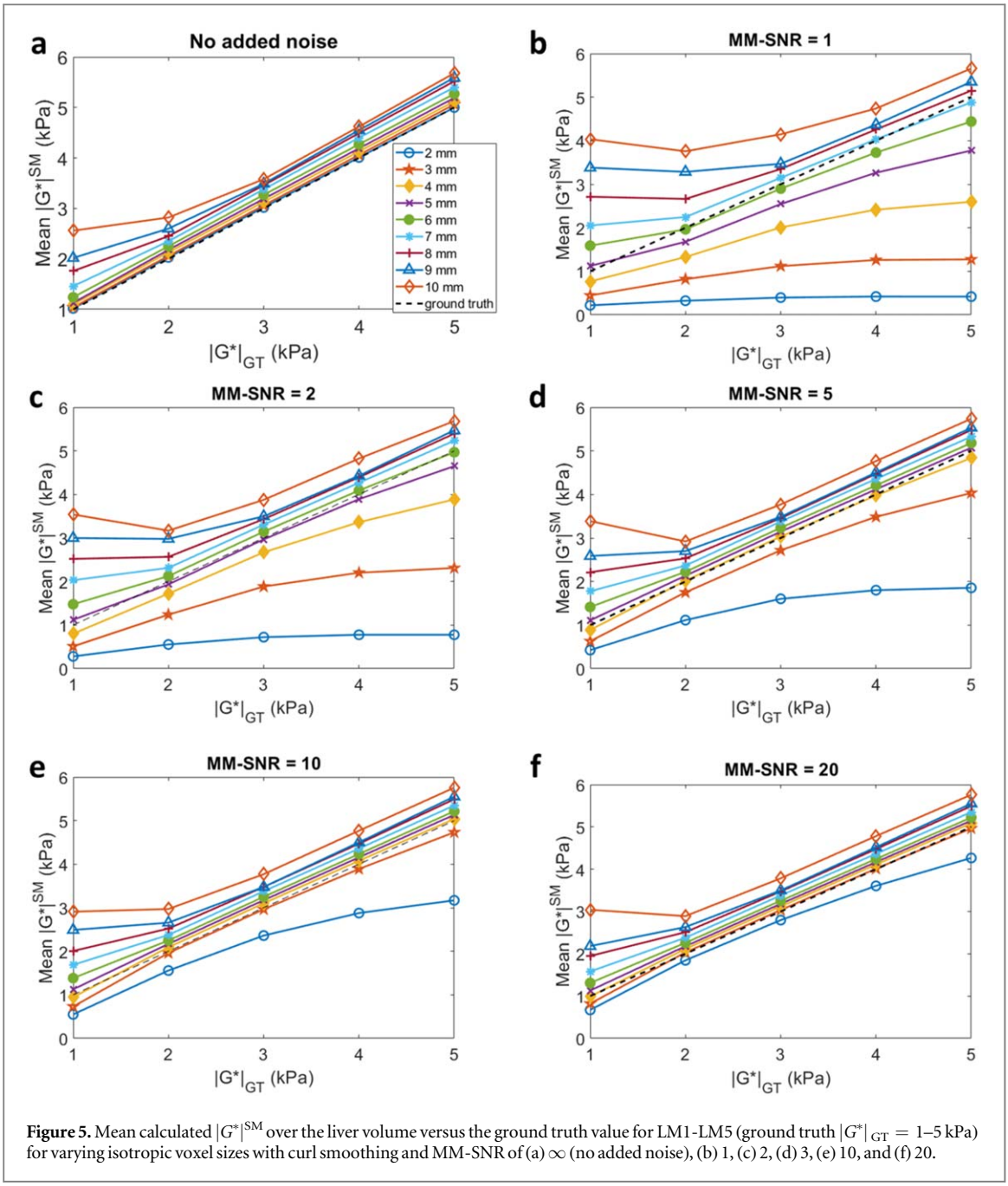

Figure 5. Mean calculated $|G^*|^{SM}$ over the liver volume versus the ground truth value for LM1-LM5 (ground truth $|G^*|_{GT}$ = 1–5 kPa) for varying isotropic voxel sizes with curl smoothing and MM-SNR of (a) ∞ (no added noise), (b) 1, (c) 2, (d) 3, (e) 10, and (f) 20.

Table 2. Isotropic voxel dimensions to minimise the error in mean $|G^*|^{SM}$ for liver MRE.

Isotropic voxel dimensions to minimise the error in mean $\|G^*\|^{SM}$ for liver MRE (mm)						
MM-SNR	1	2	5	10	20	∞ (No added noise)
$\|G^*\|_{GT}$ (kPa)						
1	5	5	5	4	4	2
2	6	5	4	3	3	2
3	6	5	4	3	3	2
4	7	6	4	4	3	2
5	7	6	5	4	3	2
Voxel dimension to minimise root mean square error for all $\|G^*\|_{GT}$	6	5	4	4	3	2

Figure 6 presents simulated results at 4, 5 and 6 mm resolution with MM-SNR of 1, 2, 5 and 10 for LM1, and figure 7 presents the equivalent for LM2. LM1 and LM2 were chosen as healthy liver is thought to have $|G^*|$ in the range of 1–2 kPa (Asbach *et al* 2008). The mean and SDs in $|G^*|$ are shown along with the percentage error of the mean compared with ground truth, and the errors vary greatly with MM-SNR and resolution, and between applying smoothing or not.

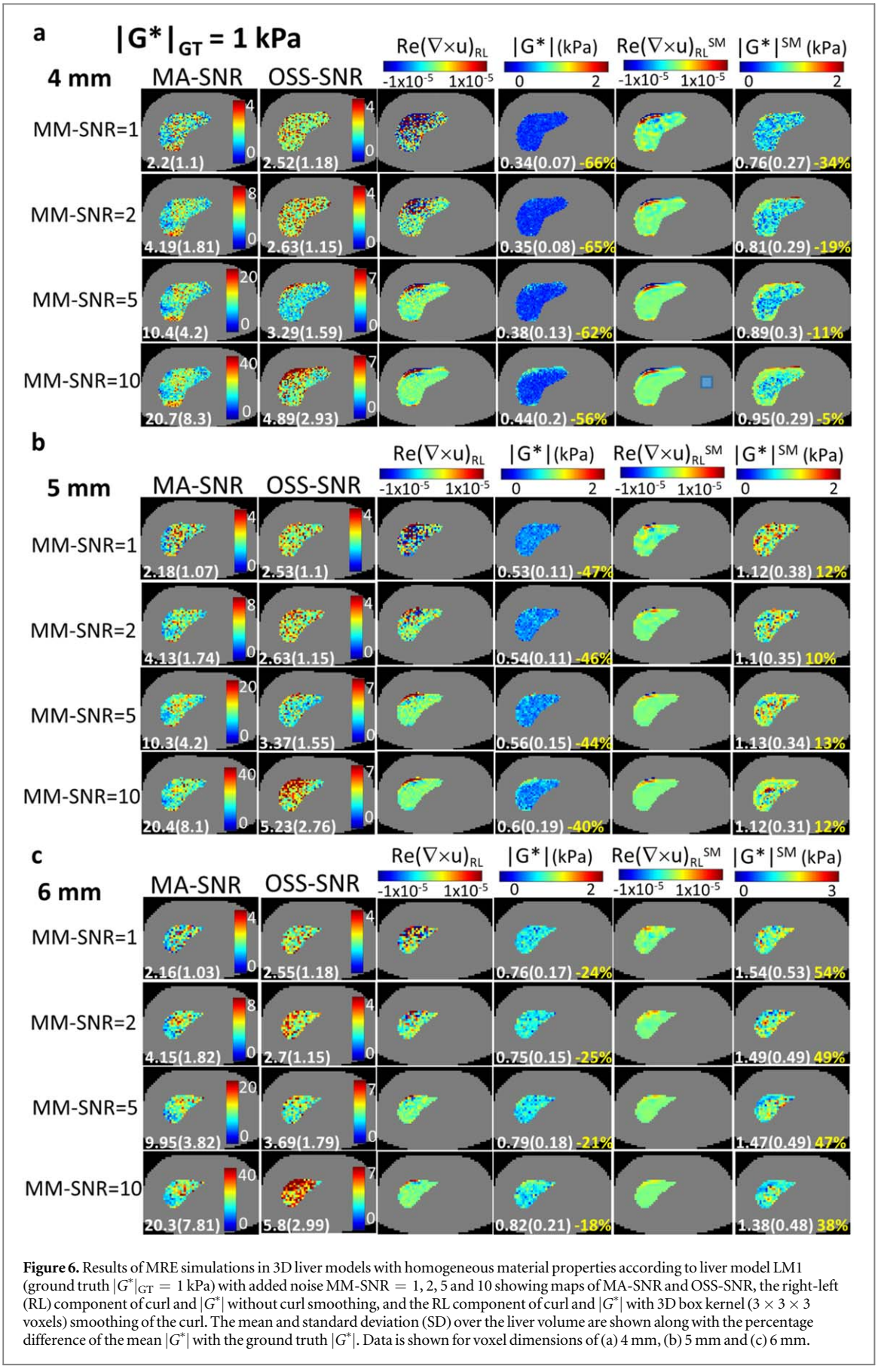

Figure 6. Results of MRE simulations in 3D liver models with homogeneous material properties according to liver model LM1 (ground truth $|G^*|_{GT} = 1$ kPa) with added noise MM-SNR $= 1, 2, 5$ and 10 showing maps of MA-SNR and OSS-SNR, the right-left (RL) component of curl and $|G^*|$ without curl smoothing, and the RL component of curl and $|G^*|$ with 3D box kernel ($3 \times 3 \times 3$ voxels) smoothing of the curl. The mean and standard deviation (SD) over the liver volume are shown along with the percentage difference of the mean $|G^*|$ with the ground truth $|G^*|$. Data is shown for voxel dimensions of (a) 4 mm, (b) 5 mm and (c) 6 mm.

In figures 8 and 9, for the central 2 slices of the acquired 6 slices, the unwrapped phase, MA-SNR and OSS-SNR maps, and the curl and $|G^*|$ maps are shown without and with smoothing respectively. Figure 8 shows data at 4 and 5 mm at 60 Hz frequency, and figure 9 shows data at 6 mm for 50 and 60 Hz frequency.

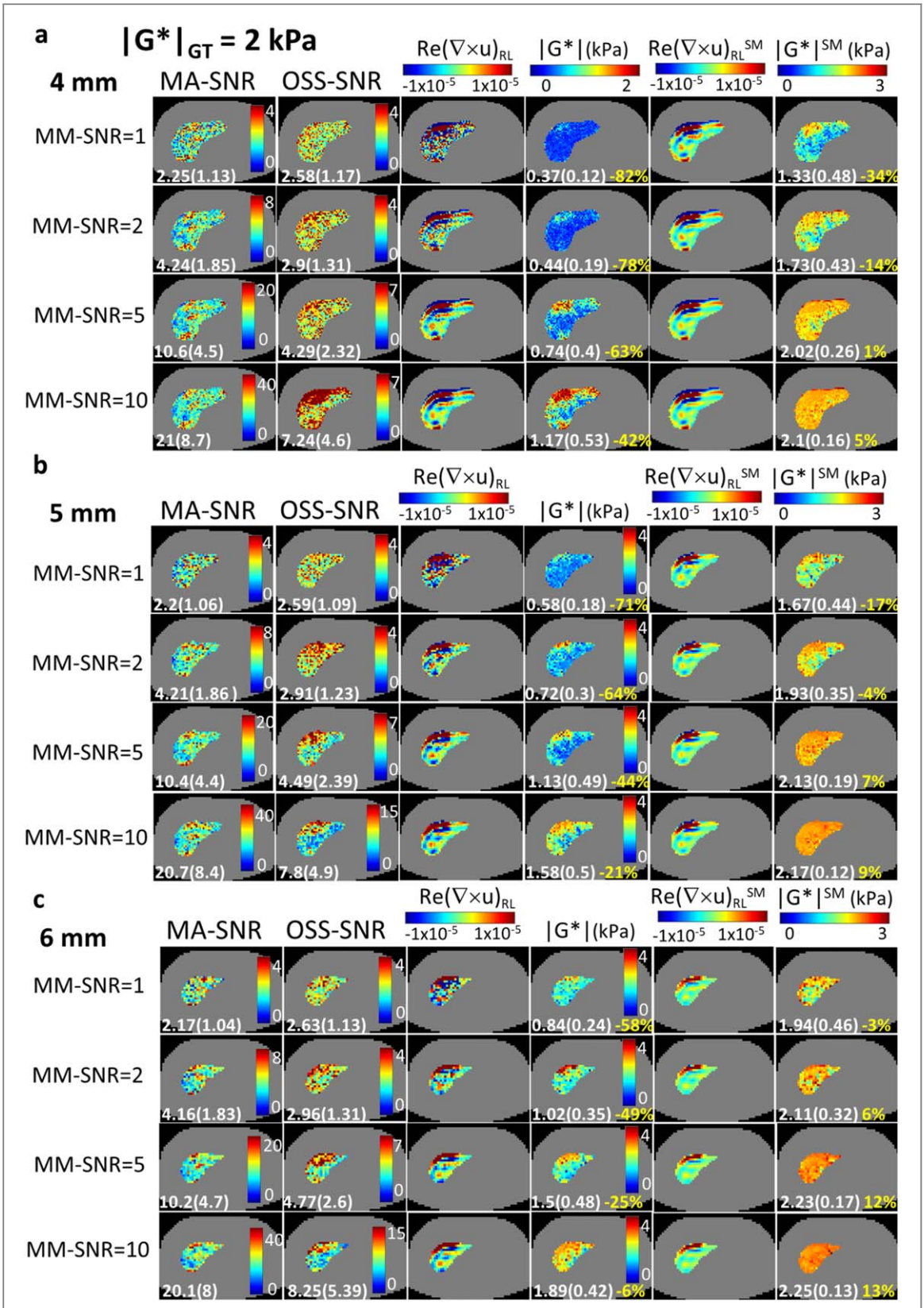

Figure 7. Results of MRE simulations in 3D liver models with homogeneous material properties according to liver model LM2 (ground truth $|G^*|_{GT} = 2$ kPa) with added noise MM-SNR $= 1, 2, 5$ and 10 showing maps of MA-SNR and OSS-SNR, the right-left (RL) component of curl and $|G^*|$ without curl smoothing, and the RL component of curl and $|G^*|$ with 3D box kernel ($3 \times 3 \times 3$ voxels) smoothing of the curl. The mean and standard deviation (SD) over the liver volume are shown along with the percentage difference of the mean $|G^*|$ with the ground truth $|G^*|$. Data is shown for voxel dimensions of (a) 4 mm, (b) 5 mm and (c) 6 mm.

The mean MA-SNR values of the acquired data are quite low and increase slightly with voxel size, i.e. at 60 Hz, MA-SNR increases from 1.49 to 1.59 and 1.73 from 4 to 5 and 6 mm respectively. This is mainly driven by an increase in imaging-SNR with larger voxel size, but it does not increase linearly with voxel volume as the

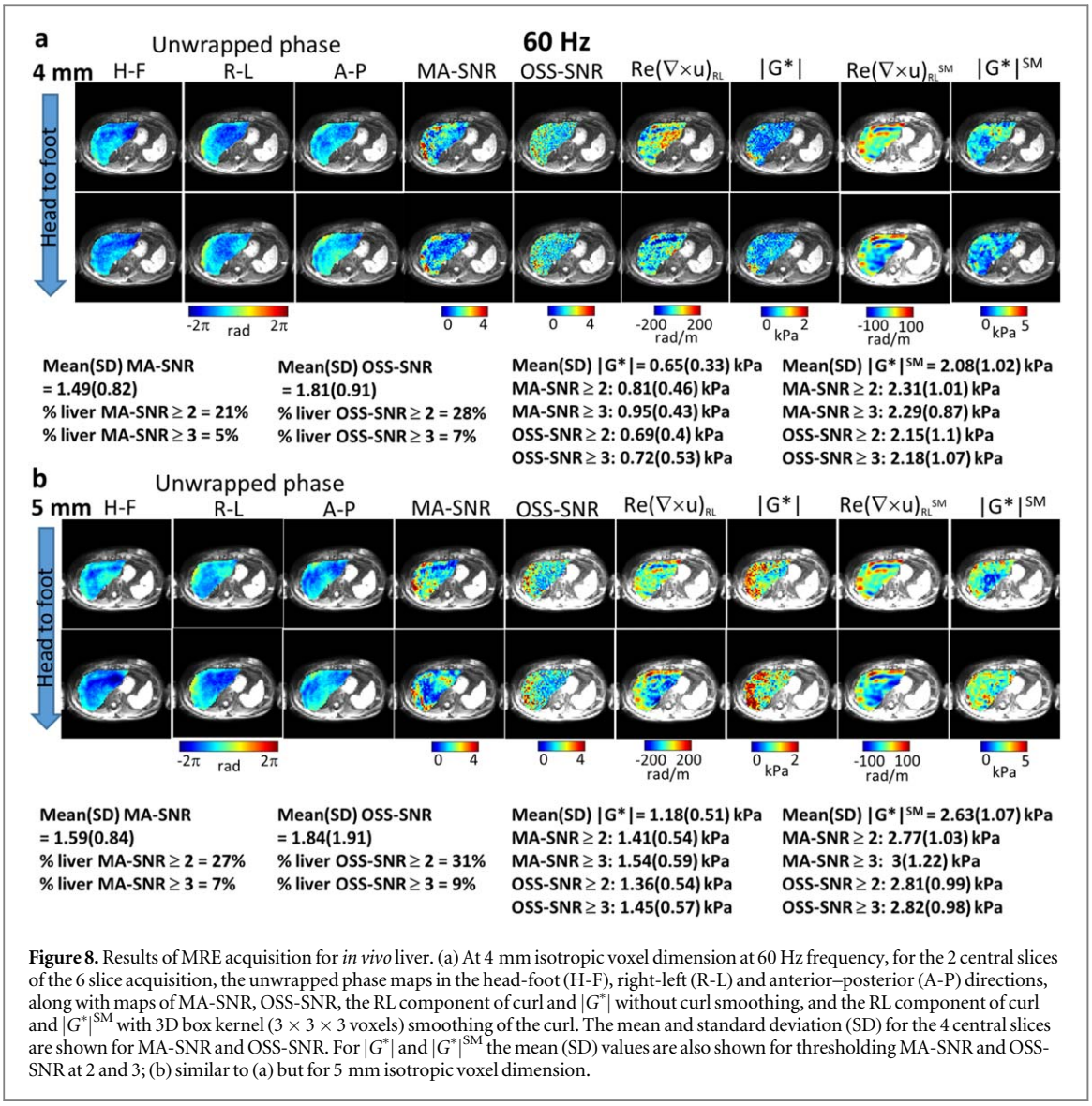

Figure 8. Results of MRE acquisition for *in vivo* liver. (a) At 4 mm isotropic voxel dimension at 60 Hz frequency, for the 2 central slices of the 6 slice acquisition, the unwrapped phase maps in the head-foot (H-F), right-left (R-L) and anterior–posterior (A-P) directions, along with maps of MA-SNR, OSS-SNR, the RL component of curl and $|G^*|$ without curl smoothing, and the RL component of curl and $|G^*|^{SM}$ with 3D box kernel ($3 \times 3 \times 3$ voxels) smoothing of the curl. The mean and standard deviation (SD) for the 4 central slices are shown for MA-SNR and OSS-SNR. For $|G^*|$ and $|G^*|^{SM}$ the mean (SD) values are also shown for thresholding MA-SNR and OSS-SNR at 2 and 3; (b) similar to (a) but for 5 mm isotropic voxel dimension.

harmonic motion estimates will be affected by loss of spatial resolution. Decreasing the frequency to 50 Hz resulted in no change in MA-SNR. In viscoelastic liver the motion field will vary with frequency, but also the imaging-SNR will change with altered acquisition parameters. Mean OSS-SNR also varies slightly: at 60 Hz OSS-SNR has a mean value of 1.81 at 4 mm and 1.84 at 5 mm, and at 6 mm this increases to 1.99, while at 50 Hz and 6 mm it decreases to 1.93. These changes are influenced by changing strain estimates over different imaging graphical prescriptions and frequency-dependent motion fields, in combination with varying noise contributions to the imaging signal.

For the acquired data, the mean $|G^*|$ at 60 Hz with no smoothing increases with voxel size from 0.65 to 1.18 and 1.77 kPa, and at 50 Hz it is reduced to 1.12 kPa. With smoothing the equivalent values are 2–3 times higher: 2.08, 2.63, 3.77 and 2.77 kPa. By creating masks based on thresholds of 2 and 3 in MA-SNR and OSS-SNR it was found that the mean $|G^*|$ tended to increase with the threshold.

Based on the MA-SNR values in the acquired data, it could be determined that the simulations with MM-SNR $=$ 1 and 2 were the nearest equivalent (i.e. with $N_{PO} = 8$ MA-SNR is approximately 2 and 4). For LM1 at MM-SNR $=$ 1 and 2, the most accurate mean $|G^*|$ values were at 5 mm with smoothing, i.e. 10% and 12% error (figure 6(b)). For LM2 at MM-SNR $=$ 1 the most accurate mean $|G^*|$ was at 6 mm with smoothing, i.e. -3% (figure 7(c)), and at MM-SNR $=$ 2 the best was at 5 mm with smoothing, i.e. -4% (figure 7(b)). As the $|G^*|$ values of the LM1 simulation are greatly biased by errors from the attenuated wave amplitude in the centre of the liver, and a similar degree of attenuation does not appear to occur in the acquisitions at 50 or 60 Hz, the LM2 simulation is seemingly a closer comparison to the acquired data. On that basis it could be deemed that for MM-SNR $=$ 1–2 (MA-SNR $=$ 2–4) the more reliable acquired elastograms are at 5 and 6 mm with smoothing, resulting in the mean $|G^*|$ for the acquired liver being estimated in the range of 2.63 and 3.77 kPa. However, also

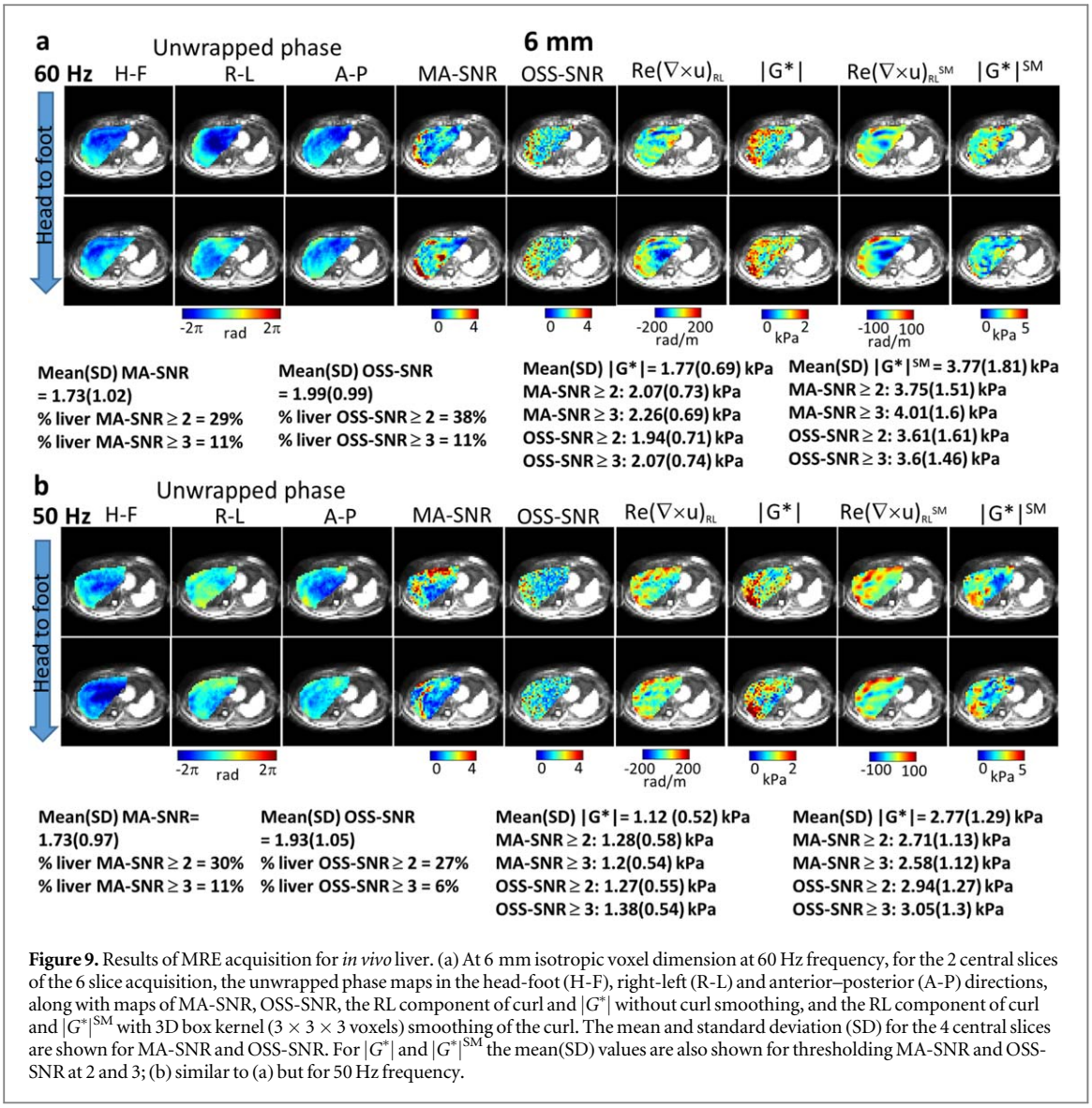

Figure 9. Results of MRE acquisition for *in vivo* liver. (a) At 6 mm isotropic voxel dimension at 60 Hz frequency, for the 2 central slices of the 6 slice acquisition, the unwrapped phase maps in the head-foot (H-F), right-left (R-L) and anterior–posterior (A-P) directions, along with maps of MA-SNR, OSS-SNR, the RL component of curl and $|G^*|$ without curl smoothing, and the RL component of curl and $|G^*|^{SM}$ with 3D box kernel ($3 \times 3 \times 3$ voxels) smoothing of the curl. The mean and standard deviation (SD) for the 4 central slices are shown for MA-SNR and OSS-SNR. For $|G^*|$ and $|G^*|^{SM}$ the mean(SD) values are also shown for thresholding MA-SNR and OSS-SNR at 2 and 3; (b) similar to (a) but for 50 Hz frequency.

of note is that at 5 and 6 mm (with smoothing) the errors for 1 kPa ground truth could be as high as 54% at 6 mm (figure 6(c)), and for a 2 kPa ground truth the absolute value of the error as high as 17% at 5 mm (figure 7(b)).

3.5. LFE inversion comparison

Supplementary figure S1 (available online at stacks.iop.org/PMB/66/225005/mmedia) shows the LFE elastograms with and without Gaussian band pass filtering for the acquired MRE data. Mean values over the slice with filtering are comparable with those for the direct inversion results with smoothing.

Supplementary figures S2 and S3 show results for the simulated data (with no added noise) without and with filtering respectively. It can be seen that only certain areas of the liver have values close to the ground truth (i.e. those areas closer to the point of wave delivery) and the results vary with liver tissue model (LM) and resolution. However, as this was an initial test with LFE, exploration of the optimisation of the algorithm with this simulated data was not carried out, and should be the subject of future investigations.

4. Discussion

4.1. The influence of imaging resolution on MRE accuracy

When no noise is added, one would expect flat simulated elastograms for uniform ground truth properties. However, simulated elastograms with no added noise had an artefact pattern, especially for LM1, where the displacement amplitudes were low at the liver centre, and smoothing accentuated this effect. These artefacts arise from a combination of error sources: (1) limited accuracy, which is a function of the FE mesh resolution and interpolation; (2) errors introduced to direct inversion when the voxel dimension is insufficiently small to

sample the wave field, particularly when the wavelength is short, or when the motion has a complicated pattern due to wave interference. In McGrath *et al* (2016) it was shown that with an appropriately small voxel size these errors can be reduced or eliminated. Indeed, in this study, for $|G^*|_{GT} \geqslant 2$ kPa at resolutions 2–4 mm the simulated liver elastograms were approximately uniform; while as the voxel size increased artefactual patterns emerged.

Other workers using 2D models and 3D geometric phantoms have made similar observations to this study with regard to optimum resolutions for given underlying properties and noise levels (Papazoglou *et al* 2008, Honarvar *et al* 2017, Yue *et al* 2017). The reason behind the dependence on imaging resolution is bound up with the finite difference calculation of the derivatives for the curl and Laplacian on a wave field. Aliasing of the waveforms occurs at insufficient sampling resolutions, and (when no noise is added) this results in over-estimates of $|G^*|$. At high resolutions (and no added noise) exact ground truth values can be recovered. When noise is added at high resolution this tends to cause underestimates of $|G^*|$, as the noise creates the impression of shorter wavelengths. Increasing the finite difference step-size can offset the influence of noise, as shown in Papazoglou *et al* (2008), Honarvar *et al* (2017), Yue *et al* (2017). At larger steps-size the gradient and therefore derivative values are greater, and hence the influence of noise becomes proportionately less.

The simulated motion fields indicate MRE waves travel into the liver from different directions, i.e. waves scattered from the ribs and reflected from the spine, and these may combine to form interference patterns in the liver centre. What was additionally identified in this study is these interference patterns can have effectively shorter wavelengths than the surrounding tissue, and hence the effect of under-sampling can be more pronounced in certain areas leading to an artefact pattern in the elastogram.

However, it is likely that wave attenuation and scattering in the real liver tissue would reduce the influence of reflected waves, and often pre-processing such as directional filtering is employed to reduce errors from reflections (Manduca *et al* 2003).

When noise was added to the simulated reflections of this study, different artefact patterns appeared in the elastograms, which were a combination of motion-noise and under-sampling of the wave field. In agreement with the findings of others (Papazoglou *et al* 2008, Honarvar *et al* 2017, Yue *et al* 2017), lower sampling resolutions could offset the influence of noise on the mean $|G^*|$, and for a given scenario of noise, underlying material properties, anatomy and wave delivery, a finite optimum imaging resolution could be identified. However, lower sampling resolutions can also increase the errors of direct inversion due to poorer estimates of the derivatives.

In Yue *et al* (2017) it was identified that for direct inversion with finite differences the number of voxels per shear wavelength should be $\geqslant$8.3. In Hu (2020) direct inversion was compared with LFE, and it was found that direct inversion required $\geqslant$10 voxels per wavelength, compared to a limit of 2 for LFE. The shear wavelengths for LM1-LM5 of this study are 13, 23, 28, 33 and 37 mm. Hence at 1 mm resolution the wavefields for all tissue models should be sufficiently resolved, provided that wave interference does not result in effectively shorter wavelengths in portions of the images. At 2 mm resolution the wavefields of LM2-LM5 should still be sufficiently resolved.

The findings of this study highlight how critical spatial resolution is to MRE accuracy. The choice of MRI voxel dimension is a trade-off between preserving spatial resolution or SNR. Liver MRE is often carried out using non-isotropic imaging resolutions, e.g. $4.7 \times 4.9 \times 10\ \text{mm}^3$ (Quantitative Imaging Biomarkers Alliance 2018), but more recent work has moved to isotropic graphical prescriptions which are suited to 3D inversion (Guo *et al* 2014, Sinkus *et al* 2018). For methods that measure one (through-plane) motion direction and solve for a 2D slice, such as the one-motion-direction implementation of Multi-model direct inversion (Yoshimitsu *et al* 2017), data is often acquired for larger voxels and reconstructed by the scanner to a higher resolution in-plane. Polynomial fits are used to estimate derivatives, and hence the noise and resolution issues identified here are obviated.

The acquisition voxel dimensions employed in this study (4, 5 and 6 mm) were chosen based on the simulation results for healthy liver (LM1-LM2) and low MA-SNR ($<$10). Although previous work has highlighted the relationship of accuracy to both resolution and noise in more simplistic geometries (Papazoglou *et al* 2008, Honarvar *et al* 2017, Yue *et al* 2017), unique in this work is that predictions have been made based on an anthropomorphic personalised liver model, which is matched to the MRE acquisition, allowing a fuller evaluation of liver MRE accuracy. Comparison of the MRE acquisition with simulations at matching resolutions and MA-SNR levels indicated which resolutions are likely to have yielded elastograms closest to the true underlying properties, and also what the magnitude of error might be in the acquired elastograms. Therefore this study indicates that MRE imaging resolution must be chosen carefully based on the expected range of $|G^*|$. However, even when an optimum resolution has been identified, possible errors on the order of 54% ($|G^*|_{GT} = 1$ kPa, 6 mm, with smoothing) exist. In liver disease, $|G^*|$ will increase with the progressive stages of fibrosis, but can vary by $<$1 kPa between stages (Venkatesh *et al* 2013). Errors of this magnitude could be critical in distinguishing healthy and diseased liver, and the fibrosis stages. However, it is likely that the error magnitudes

predicted by this study exceed those in practice, due to the simplicity of the simulation, pre-processing and direct inversion approach employed, which amplifies the influence of noise through derivative calculation.

The artefacts in the simulated elastograms have a structure which could be misinterpreted as true variations with disease or anatomy (i.e. the vascular tree). In the acquired MRE elastograms there is a structured variation in $|G^*|$, which may indeed be associated with liver anatomy, or might be influenced by under-sampling of the wave field.

Partial-volume errors occur at the liver boundaries for the simulated and acquired data. Additionally, more complicated motion fields will occur at the tissue interfaces, as waves are scattered and refracted due to acoustic impedance mismatch, which when under-sampled can cause elastogram errors (McGrath *et al* 2016). Coupled with this is the inherent assumption of local-homogeneity in direct inversion, which causes errors at the boundaries of tissues with different properties (McGrath *et al* 2016). The liver $|G^*|$ variations in the acquired elastograms might be artefacts resulting from the assumption of local homogeneity, or indeed the further assumption of isotropy. Recent work has developed algorithms avoiding these assumptions (Barnhill *et al* 2018, Fovargue *et al* 2018, Sinkus *et al* 2000). However, any inversion algorithm is likely to be hampered by insufficient spatial-sampling of the displacements. Hence, these observations indicate that methodological improvements should be pursued to increase resolution, e.g. by reducing echo time through use of higher harmonic frequency MEGs (Herzka *et al* 2009) and leveraging the increased SNR to obtain higher resolution data. Alternatively, imaging during free-breathing or applying retrospective gating (as opposed to imaging during breath-hold) would allow higher resolutions while preserving SNR (Tzschätzsch *et al* 2016), through collecting multiple signal averages or phase offsets. Another approach to offset the effect of undersampling is to use interpolation (Yue *et al* 2017), but this employs assumptions of the local homogeneity of the tissue biomechanics. Methods such as the multi-model direct inversion (Yoshimitsu *et al* 2017) employ polynomial fitting for derivative calculation, which can also offset problems with under sampling and noise.

Other studies on MRE validation have identified important factors which determine MRE accuracy. For example in Tweten *et al* (2017) it was found that with respect to identifying anisotropic material properties, multiple slow and fast shear waves with different propagation directions should be present, and directional filter inversion with LFE was compared with curl-based methods.

4.2. Motion-based and strain-based SNR for evaluation of MRE accuracy

By applying MA-SNR and OSS-SNR threshold-masks, different mean $|G^*|$ values were obtained, which tended to increase with threshold. This is a similar approach to methods such as multi-scale and multi-model direct inversion which incorporate cross-hatching on the elastograms representing 95% confidence thresholds on model fitting (Yoshimitsu *et al* 2017).

MRE-measured motion depends on the phase accrual of the tissue moving in the MEG, which can be improved by: (1) increasing MEG amplitude; (2) more efficient wave delivery; (3) frequency-optimisation to reduce wave attenuation in viscoelastic tissue. Higher MA-SNR could also be achieved by increasing imaging-SNR, increasing N_{PO} (e.g. by using free-breathing) or reducing TE (e.g. by using MEGs at higher harmonic frequencies).

Changing imaging resolution resulted in slight variations in MA-SNR and OSS-SNR, which were driven by a combination of factors. Although imaging-noise is reduced in larger voxels, the displacement and strain measures will also vary with resolution. These initial observations indicate that voxel-wise MA-SNR and OSS-SNR could be used to guide the choice of MRE acquisition parameters and as a metric for summary-statistic preparation.

4.3. Comparison with LFE

The initial evaluation of LFE demonstrated that similar results could be obtained for the acquired data when using LFE with filtering, compared with the direct inversion with smoothing. However for the simulated data only portions of the liver slice elastograms had values close to ground truth. In Hu (2020) LFE and direct inversion were shown to produce different results dependent on frequency and resolution. Future studies will carry out a fuller investigation and optimisation of LFE.

4.4. Study limitations

Limitations of this study are: (1) only one personalised FEM was generated; (2) homogeneous material properties were prescribed for the simulated liver; (3) Other anatomical aspects were not considered in the simulation, such as the organ capsule, pulsations from blood vessels, variations in fat and muscle or fluid (i.e. ascites), or aspects of liver disease such as atrophy; (4) the MRE driver position was not varied; (5) more advanced methods of noise reduction such as in Barnhill *et al* (2017) were not explored; (6) likewise methods of reducing the effects of reflection and interference were not applied such as in Manduca *et al* (2003). The direct

inversion method has assumptions of isotropy and local homogeneity, and involves calculation of third order derivatives, which amplifies imaging-noise. Future work will use this methodology to incorporate: (1) a range a FEM models generated from patients and volunteers; (2) variations in liver properties with anatomy and disease, heterogeneity and anisotropy; (3) comparison of repeat MRE acquisitions at different driver positions; (4) comparison with other inversion methods, which may be less sensitive to spatial resolution and noise, and pre-processing methods to reduce the influence of noise and reflections.

5. Conclusion

This simulation study has demonstrated important considerations for the optimisation of liver MRE. A range of factors were found to greatly impact MRE results: (1) imaging resolution; (2) data smoothing during inversion, (3) MA-SNR and OSS-SNR threshold. The simulated liver elastogram error was dependent on ground truth properties in combination with imaging resolution and motion-SNR, suggesting that liver MRE should be planned according to the expected liver $|G^*|$. For example, in healthy liver ($|G^*| = 2$ kPa) and an anticipated MA-SNR < 5, the optimum imaging resolution is predicted to be 5–6 mm. To obtain greater accuracy for diseased liver ($|G^*| \geqslant 3$ kPa), an increase in voxel size should be considered.

It was determined that at typical voxel sizes the error on the mean $|G^*|$ could be on the order of 54% for healthy liver ($|G^*| = 1$ kPa) at 60 Hz; an uncertainty of 0.54 kPa. As liver $|G^*|$ can vary between stages of fibrosis by <1 kPa, this consideration is vital in the development of liver MRE as a disease biomarker. However further work is required to fully explore and determine the limitations of these findings.

Acknowledgments

This work was supported by the Medical Research Council Grant [grant number MC_PC_16055]. Financial support was also received from the NIHR Biomedical Research Centre (NIHR BRC); Gastrointestinal and Liver Disorder theme, Nottingham University Hospitals NHS Trust and University of Nottingham. This article presents independent research funded and supported by the NIHR Nottingham Digestive Diseases Biomedical Research Unit, Nottingham University Hospitals NHS Trust and University of Nottingham. Views expressed are those of the authors and not necessarily those of the NHS, NIHR or Department of Health.

Ethical statement

The study was approved by the University of Nottingham Medical School Ethics Committee (Approval number: H1408201428). The scan on the one healthy subject was conducted in accordance with the principles embodied in the Declaration of Helsinki and in accordance with local statutory requirements.

CRediT author statement

Deirdre McGrath: Conceptualization, Methodology, Software, Formal analysis, Investigation, Writing-Original Draft and Revision, Visualization.

Christopher Bradley: Investigation, Writing-Review and Editing.

Susan Francis: Investigation, Writing-Review and Editing, Supervision, Project administration, Funding acquisition.

ORCID iDs

Deirdre M McGrath https://orcid.org/0000-0002-0823-8932
Christopher R Bradley https://orcid.org/0000-0002-2174-2279
Susan T Francis https://orcid.org/0000-0003-0903-7507

References

Asbach P, Klatt D, Hamhaber U, Braun J, Somasundaram R, Hamm B and Sack I 2008 Assessment of liver viscoelasticity using multifrequency MR elastography *Magn. Reson. Med.* **60** 373–9

Barnhill E, Davies P J, Ariyurek C, Fehlner A, Braun J and Sack I 2018 Heterogeneous multifrequency direct inversion (HMDI) for magnetic resonance elastography with application to a clinical brain exam *Med. Image Anal.* **46** 180–8

Barnhill E, Hollis L, Sack I, Braun J, Hoskins P R, Pankaj P, Brown C, van Beek E J R and Roberts N 2017 Nonlinear multiscale regularisation in MR elastography: towards fine feature mapping *Med. Image Anal.* **35** 133–45
Cunha G M, Glaser K J, Bergman A, Luz R P, de Figueiredo E H and Lobo Lopes F P P 2018 Feasibility and agreement of stiffness measurements using gradient-echo and spin-echo MR elastography sequences in unselected patients undergoing liver MRI *Br. J. Radiol.* **91** 1087
Dittmann F, Hirsch S, Tzschatzsch H, Guo J, Braun J and Sack I 2016 *In vivo* wideband multifrequency MR elastography of the human brain and liver *Magn. Reson. Med.* **76** 1116–26
Dixon W T 1984 Simple proton spectroscopic imaging *Radiology* **153** 189–94
Doyley M M 2012 Model-based elastography: a survey of approaches to the inverse elasticity problem *Phys. Med. Biol.* **57** R35–73
Fovargue D, Kozerke S, Sinkus R and Nordsletten D 2018 Robust MR elastography stiffness quantification using a localized divergence free finite element reconstruction *Med. Image Anal.* **44** 126–42
Guo J, Hirsch S, Streitberger K J, Kamphues C, Asbach P, Braun J and Sack I 2014 Patient-activated three-dimensional multifrequency magnetic resonance elastography for high-resolution mechanical imaging of the liver and spleen *RoFo : Fortschr. auf dem Geb. Rontgenstrahlen und der Nuklearmedizin* **186** 260–6
Herzka D A, Kotys M S, Sinkus R, Pettigrew R I and Gharib A M 2009 Magnetic resonance elastography in the liver at 3 Tesla using a second harmonic approach *Magn. Reson. Med.* **62** 284–91
Honarvar M, Sahebjavaher R S, Rohling R and Salcudean S E 2017 A comparison of finite element-based inversion algorithms, local frequency estimation, and direct inversion approach used in MRE *IEEE Trans. Med. Imaging* **36** 1686–98
Hu L 2020 Requirements for accurate estimation of shear modulus by magnetic resonance elastography: a computational comparative study *Comput. Methods Programs Biomed.* **192** 105437
Kritsaneepaiboon S, Ina N, Chotsampancharoen T, Roymanee S and Cheewatanakornkul S 2018 The relationship between myocardial and hepatic T_2 and T_2^* at 1.5T and 3T MRI in normal and iron-overloaded patients *Acta Radiol.* 59 (Stockholm, Sweden: Sage Publications) 355–62 (Stockholm, Sweden : 1987)
Lee C K, Kim Y E, Lee C S, Hong Y M, Jung J M and Goel V K 2000 Impact response of the intervertebral disc in a finite-element model *Spine* **25** 2431–9
Madsen E L, Hobson M A, Frank G R, Shi H, Jiang J, Hall T J, Varghese T, Doyley M M and Weaver J B 2006 Anthropomorphic breast phantoms for testing elastography systems *Ultrasound Med. Biol.* **32** 857–74
Madsen E L, Kelly-Fry E and Frank G R 1988 Anthropomorphic phantoms for assessing systems used in ultrasound imaging of the compressed breast *Ultrasound Med. Biol.* **14** 183–201
Manduca A, Lake D S, Kruse S A and Ehman R L 2003 Spatio-temporal directional filtering for improved inversion of MR elastography images *Med. Image Anal.* **7** 465–73
Manduca A, Oliphant T E, Dresner M A, Mahowald J L, Kruse S A, Amromin E, Felmlee J P, Greenleaf J F and Ehman R L 2001 Magnetic resonance elastography: non-invasive mapping of tissue elasticity *Med. Image Anal.* **5** 237–54
Mathew R P and Venkatesh S K 2018 Imaging of hepatic fibrosis *Curr. Gastroenterol. Rep.* **20** 45
McGarry M D, Van Houten E E, Perrinez P R, Pattison A J, Weaver J B and Paulsen K D 2011 An octahedral shear strain-based measure of SNR for 3D MR elastography *Phys. Med. Biol.* **56** N153–64
McGrath D M 2018 *Biomechanics of Soft Tissues: Principles and Applications* ed A Al Mayah (Boca Raton: CRC Press) pp 55–94
McGrath D M, Foltz W D, Al-Mayah A, Niu C J and Brock K K 2012 Quasi-static magnetic resonance elastography at 7 T to measure the effect of pathology before and after fixation on tissue biomechanical properties *Magn. Reson. Med.* **68** 152–65
McGrath D M, Ravikumar N, Beltrachini L, Wilkinson I D, Frangi A F and Taylor Z A 2017 Evaluation of wave delivery methodology for brain MRE: insights from computational simulations *Magn. Reson. Med.* **78** 341–56
McGrath D M, Ravikumar R, Wilkinson I D, Frangi A F and Taylor Z 2016 Magnetic resonance elastography of the brain: an *in silico* study to determine the influence of cranial anatomy *Magn. Reson. Med.* **76** 645–62
Morisaka H, Motosugi U, Ichikawa S, Nakazawa T, Kondo T, Funayama S, Matsuda M, Ichikawa T and Onishi H 2018 Magnetic resonance elastography is as accurate as liver biopsy for liver fibrosis staging *J. Magn. Reson. Imaging : JMRI* **47** 1268–75
Murphy M C, Huston J 3rd, Jack C R Jr, Glaser K J, Senjem M L, Chen J, Manduca A, Felmlee J P and Ehman R L 2013 Measuring the characteristic topography of brain stiffness with magnetic resonance elastography *PLoS One* **8** e81668
Muthupillai R, Lomas D J, Rossman P J, Greenleaf J F, Manduca A and Ehman R L 1995 Magnetic resonance elastography by direct visualization of propagating acoustic strain waves *Science* **269** 1854–7
Muthupillai R, Rossman P J, Lomas D J, Greenleaf J F, Riederer S J and Ehman R L 1996 Magnetic resonance imaging of transverse acoustic strain waves *Magn. Reson. Med.* **36** 266–74
Papazoglou S, Hamhaber U, Braun J and Sack I 2008 Algebraic helmholtz inversion in planar magnetic resonance elastography *Phys. Med. Biol.* **53** 3147–58
Quantitative Imaging Biomarkers Alliance (QIBA) 2018 QIBA Profile: Magnetic Resonance Elastography of the Liver; Stage 2: Consensus Profile- https://qibawiki.rsna.org/images/a/a5/MRE-QIBAProfile-2018-05-02-CONSENSUS.pdf
Sibson R 1981 *Interpreting Multivariate Data* ed B V Chichester (NJ, USA: John Wiley) pp 21–36978-0471280392
Singh S *et al* 2015 Diagnostic performance of magnetic resonance elastography in staging liver fibrosis: a systematic review and meta-analysis of individual participant data *Clin. Gastroenterol. Hepatol.* **13** 440–51.e6
Sinkus R, Lambert S, Abd-Elmoniem K Z, Morse C, Heller T, Guenthner C, Ghanem A M, Holm S and Gharib A M 2018 Rheological determinants for simultaneous staging of hepatic fibrosis and inflammation in patients with chronic liver disease *NMR Biomed.* **31** e3956
Sinkus R, Lorenzen J, Schrader D, Lorenzen M, Dargatz M and Holz D 2000 High-resolution tensor MR elastography for breast tumour detection *Phys. Med. Biol.* **45** 1649–64
Sinkus R, Tanter M, Xydeas T, Catheline S, Bercoff J and Fink M 2005 Viscoelastic shear properties of *in vivo* breast lesions measured by MR elastography *Magn. Reson. Imaging* **23** 159–65
Tran A P, Yan S and Fang Q 2020 Improving model-based functional near-infrared spectroscopy analysis using mesh-based anatomical and light-transport models *Neurophotonics* **7** 015008
Tweten D J, Okamoto R J and Bayly P V 2017 Requirements for accurate estimation of anisotropic material parameters by magnetic resonance elastography: a computational study *Magn. Reson. Med.* **78** 2360–72
Tzschätzsch H, Guo J, Dittmann F, Hirsch S, Barnhill E, Jöhrens K, Braun J and Sack I 2016 Tomoelastography by multifrequency wave number recovery from time-harmonic propagating shear waves *Med. Image Anal.* **30** 1–10
Van Houten E E, Paulsen K D, Miga M I, Kennedy F E and Weaver J B 1999 An overlapping subzone technique for MR-based elastic property reconstruction *Magn. Reson. Med.* **42** 779–86

Venkatesh S K, Yin M and Ehman R L 2013 Magnetic resonance elastography of liver: technique, analysis, and clinical applications *J. Magn. Reson. Imaging* **37** 544–55

Xiang Q S 2006 Two-point water-fat imaging with partially-opposed-phase (POP) acquisition: an asymmetric Dixon method *Magn. Reson. Med.* **56** 572–84

Yin M, Talwalkar J A, Glaser K J, Manduca A, Grimm R C, Rossman P J, Fidler J L and Ehman R L 2007 Assessment of hepatic fibrosis with magnetic resonance elastography *Clin. Gastroenterol. Hepatol.* **5** 1207–13

Yoshimitsu K, Shinagawa Y, Mitsufuji T, Mutoh E, Urakawa H, Sakamoto K, Fujimitsu R and Takano K 2017 Preliminary comparison of multi-scale and multi-model direct inversion algorithms for 3T MR elastography *Magn. Reson. Med. Sci.* **16** 73–7

Yue J L, Tardieu M, Julea F, Boucneau T, Sinkus R, Pellot-Barakat C and Maitre X 2017 Acquisition and reconstruction conditions *in silico* for accurate and precise magnetic resonance elastography *Phys. Med. Biol.* **62** 8655–70

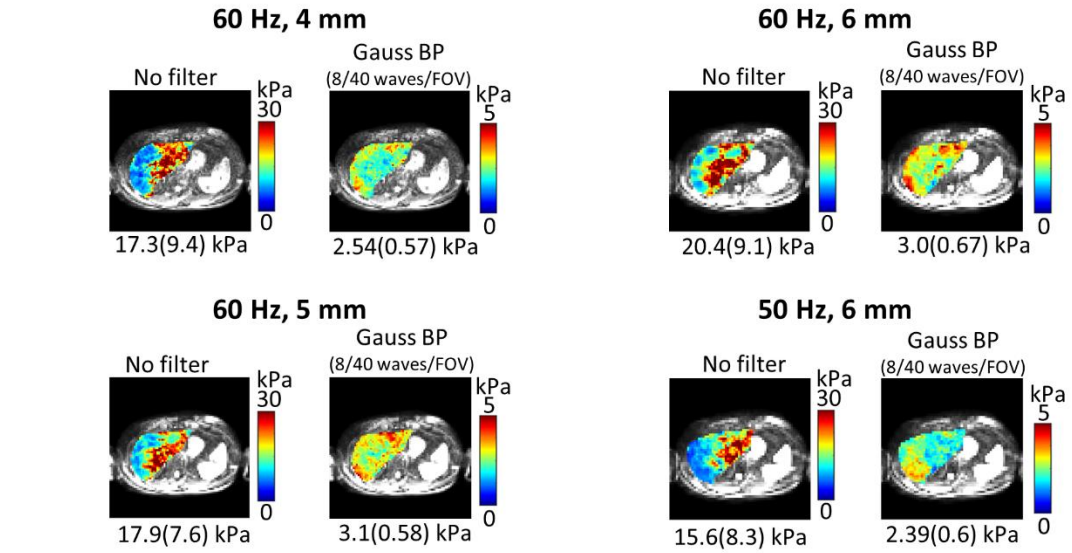

Supplementary Figure S1: Shear Modulus G^{LFE} reconstructed by Local Frequency Estimation with three motion directions for acquired MRE liver data for 60 Hz and voxel sizes 4, 5 and 6 mm, and for 50 Hz and 6 mm voxel size. Slice #3 in each case is shown (corresponding to the first row in Figures 8a-b, and 9a-b), without filtering (left) and with filtering (right) with a Gaussian Band Pass filter with 8/40 waves/FOV. These parameters where chosen heurestically based on what gave the visually most uniform result. The mean and standard deviation over the liver for the slice is given below each image. The mean values with filtering are comparable with mean values from direct inversion with smoothing (Figures 8a-b and 9a-b).

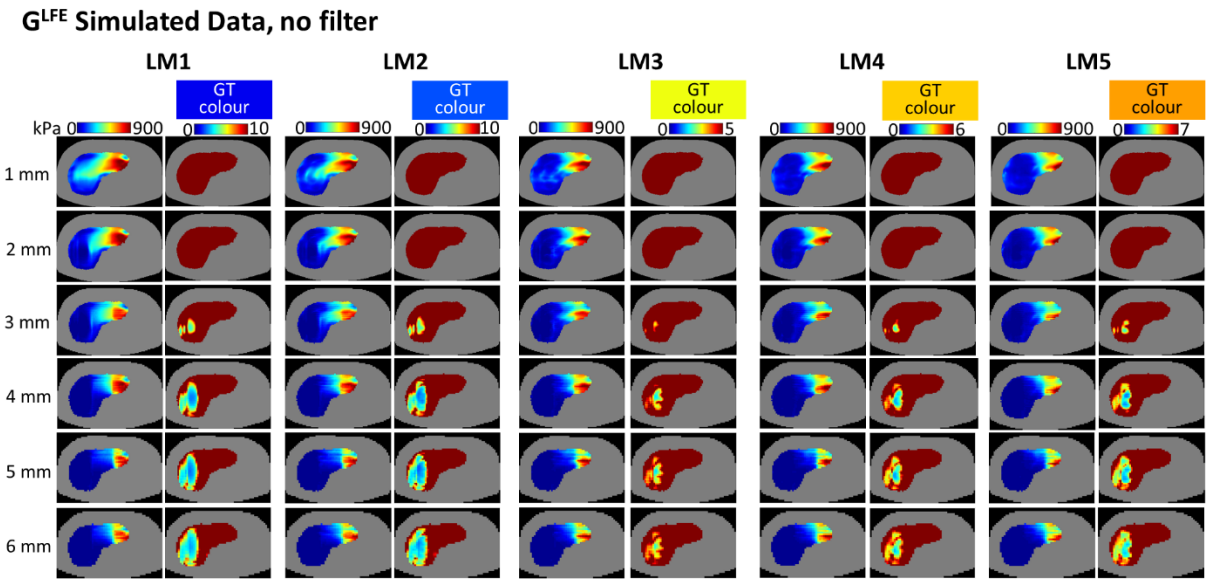

Supplementary Figure S2: Shear Modulus G^{LFE} reconstructed by Local Frequency Estimation with three motion directions for simulated MRE data with no added noise for LM1-LM5 and voxels sizes 1-6 mm. In this instance no filtering is applied. A central slice is displayed in each case and is shown twice with windowing at different colourbar limits to demonstrate the full dynamic range: the left image is windowed from 0 to 900 kPa, and the right image at a colour range closer to the ground truth. The ground truth colour (GT colour) is shown in the title colour as the reference.

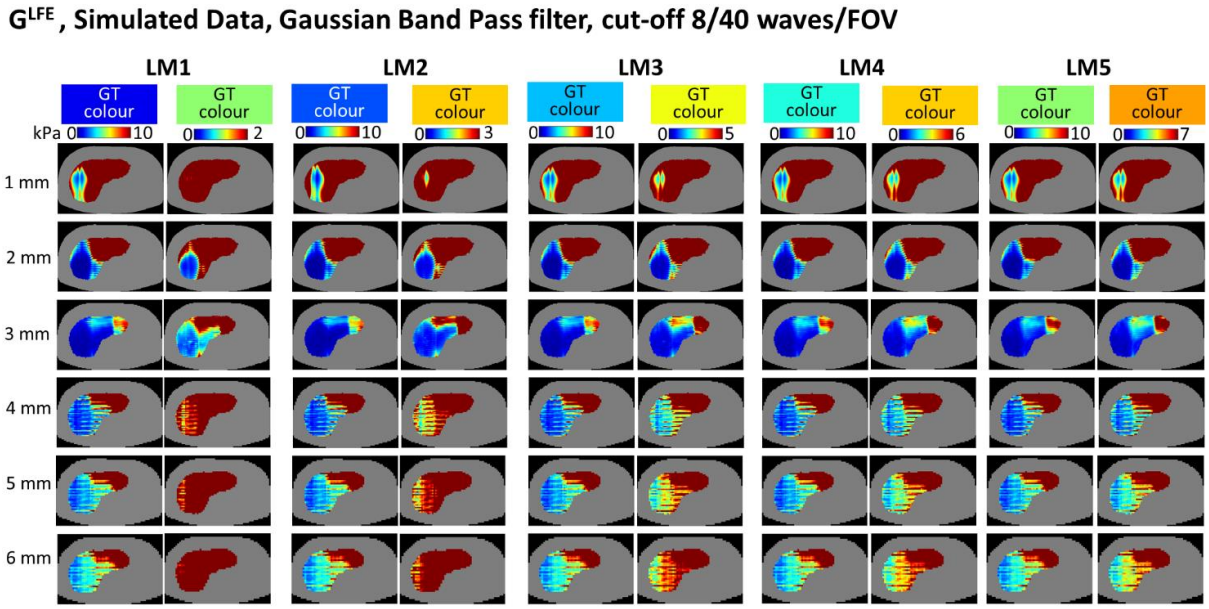

Supplementary Figure S3: Shear Modulus G^{LFE} reconstructed by Local Frequency Estimation with three motion directions for simulated MRE data with no added noise for LM1-LM5 and voxels sizes 1-6 mm. In this instance Gaussian Band Pass filtering with 8/40 waves/FOV applied, which are the same settings chosen for the acquired data. A central slice is displayed in each case and is shown twice with windowing at different colourbar limits to demonstrate the full dynamic range: the left image is windowed from 0 to 10 kPa, and the right image at a colour range closer to the ground truth. The ground truth colour (GT colour) is also shown as a reference.

VIDEO CAPTIONS

Supporting Information Video S1: Video of animation of simulated MRE displacements (real component) in the anterior-posterior direction in an axial cross-section of the torso FEM for homogeneous liver material properties and model LM2 at 60 Hz.

Supporting Information Video S2: Video of animation of simulated MRE displacements (real component) in the head-foot direction in an axial cross-section of the torso FEM for homogeneous liver material properties and model LM2 at 60 Hz.

Supporting Information Video S3: Video of animation of simulated MRE displacements (real component) in the right-left direction in an axial cross-section of the torso FEM for homogeneous liver material properties and model LM2 at 60 Hz.

Supporting Information Video S4: Video of animation of simulated MRE displacements (real component) in the anterior-posterior direction in a coronal cross-section at an anterior position of the torso FEM for homogeneous liver material properties and model LM2 at 60 Hz.

Supporting Information Video S5: Video of animation of simulated MRE displacements (real component) in the anterior-posterior direction in a coronal cross-section at an anterior position (more central than the position in video S4) of the torso FEM for homogeneous liver material properties and model LM2 at 60 Hz.

Supporting Information Video S6: Video of animation of simulated MRE displacements (real component) in the anterior-posterior direction in a coronal cross-section at central position (more posterior than the position in video S5) of the torso FEM for homogeneous liver material properties and model LM2 at 60 Hz.

Supporting Information Video S7: Video of animation of simulated MRE displacements (real component) in the anterior-posterior direction in a coronal cross-section at posterior position (more posterior than the position in video S6) of the torso FEM for homogeneous liver material properties and model LM2 at 60 Hz.

Supporting Information Video S8: Video of animation of simulated MRE displacements (real component) in the anterior-posterior direction in a coronal cross-section at posterior position (more posterior than the position in video S7) of the torso FEM for homogeneous liver material properties and model LM2 at 60 Hz.

Supporting Information Video S9: Video of animation of simulated MRE displacements (real component) in the anterior-posterior direction on the outer surface of the torso FEM for homogeneous liver material properties and model LM2 at 60 Hz.

9.8 Conference Proceedings A: Bradley CR, Buchanan C, Cox EF, Francis ST. Assessment of Optimal Technique for Measurement of Medullary Perfusion. InProc. Intl. Soc. Mag. Reson. Med 2018 (Vol. 26, p. 4600).

4600

Assessment of Optimal Technique for Measurement of Medullary Perfusion

Chris R Bradley[1,2], Charlotte E Buchanan[1], Eleanor F Cox[1,2], and Susan T Francis[1,2]

[1]Sir Peter Mansfield Imaging Centre, School of Physics and Astronomy, University of Nottingham, Nottingham, United Kingdom, [2]NIHR Nottingham Biomedical Research Centre, University of Nottingham, Nottingham, United Kingdom

Synopsis

The ability to assess medullary perfusion is important in kidney disease, for example in acute kidney injury (AKI) in which reduced medullary blood flow is implicated. In this study, we compare the use of a spin echo (SE) EPI and balanced FFE (bFFE) readout at multiple post label delay (PLD) times to determine the optimal readout scheme and to assess the number of ASL pairs required to compute medullary perfusion. Using a bFFE FAIR ASL scheme, it is possible to quantify tissue perfusion within the renal medulla.

Purpose

Arterial spin labelling (ASL) has been shown to provide a method to non-invasively assess renal cortex perfusion[1], typically using a flow-sensitive alternating inversion recovery (FAIR) labelling scheme. Here, we evaluate the viability of using a respiratory triggered FAIR-ASL scheme to assess renal medulla perfusion. We compare the use of a spin echo (SE) EPI and balanced FFE (bFFE) readout[2], collect data at multiple post label delay (PLD) times and assess the number of ASL pairs required to compute medullary perfusion. The assessment of medullary important is important in kidney disease, for example to study the pathophysiology in acute kidney injury (AKI) in which reduced medullary blood flow has been implicated[3].

Methods

MR Acquisition: 4 healthy volunteers (2 Male, average age 25 years) were scanned on a Philips 3T Ingenia scanner (Best, Netherlands) using dual-transmit and a 16 channel anterior and 16 channel posterior body coil. Localiser bFFE scans were collected in 3 orthogonal planes to aid ASL planning. Data was collected using a respiratory-triggered pulsed FAIR ASL scheme (in-plane pre-saturation, Non-Selective (NS) slab thickness 400 mm, Selective (S) slab thickness 45 mm)[1]. Coronal-oblique slices through the long axis of the kidney were acquired in descend (lateral-medial) order with the minimum temporal slice separation allowed by specific absorption rate (SAR) limits. Imaging parameters for the ASL data was 3x3x5 mm^3 voxels, in-plane FOV of 288x288 mm^2, SENSE factor 2, volume shimming. Data was collected using either a SE-EPI readout (TE= 27ms, temporal slice spacing 53 ms) or a bFFE readout (TE/TR = 1.73/3.5 ms, temporal slice spacing 250 ms). FAIR ASL data was collected at a range of post label delays (PLD): 500, 800, 1100, 1300 and 1500ms. 50 selective/non-selective pairs were acquired at each PLD. A base magnetisation M_0 image and an inversion recovery data set to compute a T_1 map were acquired for each readout scheme.

Data Analysis: Analysis was performed using in-house MATLAB scripts[1]. Each selective/non-selective pair within the PLD set were motion corrected to the first label image. Perfusion weighted (ΔM) maps were computed from (selective-non-selective) images and averaged. Regions of interest (ROI) were drawn in the medulla and cortex (ensuring no partial volume effects between tissue types) and in the background to assess noise (Figure 1). These ROIs were used to evaluate the signal-to-noise ratio (SNR) within the cortex and the medulla for each readout scheme. In addition, the number of averages needed to measure medullary perfusion was computed by varying number of averages (3,4,5,10,15,20,25,50 and 100).

Results

Figure 1 compares the FAIR-ASL perfusion weighted images for a SE-EPI readout and bFFE readout, significant improvement in detection of medulla signal is seen for the bFFE scheme. Figure 2 shows that the signal within the medulla tissue is a factor of 2.2 greater than the noise floor for the bFFE readout ($P<0.0001$), and has a contrast-to-noise ratio (CNR) between cortex and medulla of 23, whilst the SE-EPI is signal limited for medulla perfusion assessment. Figure 3 shows bFFE ΔM maps with varying number of averages. Figure 4 shows the perfusion weighted signal intensity compared to the noise floor, the medulla signal was significantly higher (>2.3) than the noise floor, even for a low (10) number of averages ($P=0.004$). Figure 5 shows the perfusion weighted signal change as a function of PLD time for the cortex, medulla and noise.

Discussion

Here we show that the bFFE readout is the optimal readout scheme of choice for the assessment of renal medulla perfusion. The bFFE scheme has a higher perfusion CNR than that of SE-EPI, due to in part to the short TE. The signal observed in the medulla is significantly higher than the noise floor in the perfusion weighted maps at all PLDs. We show that it is possible to estimate medulla perfusion with as few as 10 ASL pairs using a bFFE FAIR-ASL scheme.

Conclusion

Using a bFFE FAIR ASL scheme, it is possible to quantify tissue perfusion within the renal medulla. This scheme can be applied to assess medullary perfusion in renal disease, for example to study changes that occur in acute kidney injury, which has been suggested to arise from hypoxia of the medulla and altered medullary perfusion.

Acknowledgements

No acknowledgement found.

References

1.) Multiparametric Renal Magnetic Resonance Imaging: Validation, Interventions, and Alterations in Chronic Kidney Disease. Cox EF, Buchanan CE, Bradley CR, Prestwich B, Mahmoud H, Taal M, Selby NM, Francis ST. Front Physiol. 2017 Sep 14;8:696.

2.) Buchanan CE, Cox EF, Francis ST, editors. Evaluation of readout schemes for Arterial Spin Labelling in the Human Kidney. Int Soc Mag Reson Med; 2015.

3.) Hueper K, Gutberlet M, Rong S, et al. Acute Kidney Injury: Arterial Spin Labeling to Monitor Renal Perfusion Impairment in Mice—Comparison with Histopathologic Results and Renal Function. Radiology, 2013;270:117-124

Figures

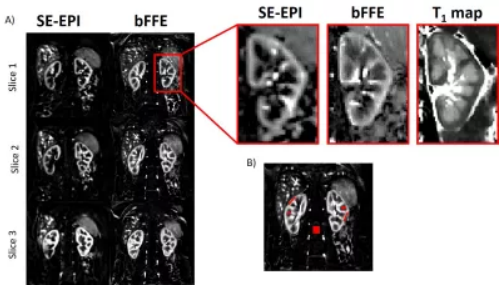

Figure 1. A) Spin-Echo and bFFE perfusion weighted (ΔM) maps collected at the nominal PLD of 1500ms (actual PLD for a given slice dependent on slice number and temporal slice spacing). Signal is clearly visible above the background noise in the bFFE. B) Example of ROIs placement in medulla, cortex and background to compute a noise level.

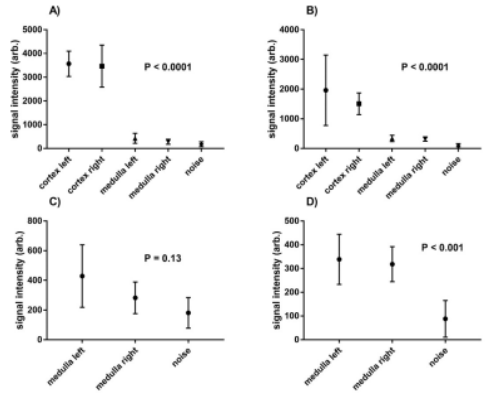

Figure 2.) A.) Signal intensities in cortex and medulla for the spin echo ΔM map. Cortex signal is much higher than the medulla and noise. B.) Signal intensities in cortex and medulla for the bFFE ΔM map. Note here the medulla signal is above the noise floor C.) Highlights that the medulla signal is not significantly higher than the noise in the spin echo ΔM maps (P=0.13). C.) Highlights that the medulla signal for the bFFE readout is significantly higher than that of the noise floor (P<0.001).

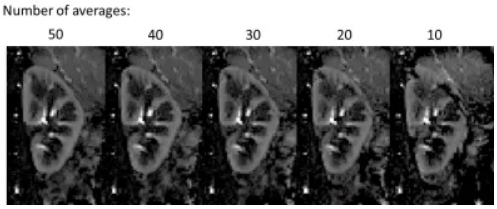

Figure 3.) Perfusion weighted (ΔM) images for the bFFE scheme with images shown for varying numbers of averages (50-10).

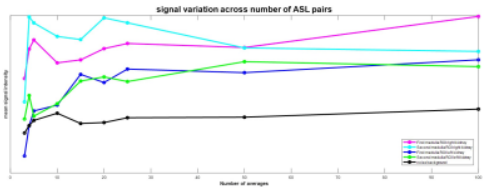

Figure 4.) Signal in four medulla ROIs (two in left kidney and two in the right kidney), the signal in all ROIs were significantly higher than that of the noise ROI (P=0.004).

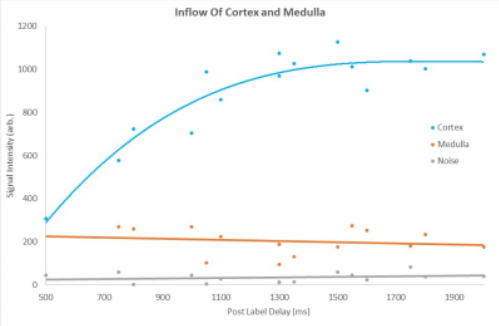

Figure 5.) Perfusion weighted signal in the renal cortex and medulla measured using a bFFE readout scheme.

Proc. Intl. Soc. Mag. Reson. Med. 26 (2018)
4600

9.9 Conference Proceedings B: Bradley CR, Scott R, Cox EF, Palaniyappan N, Guha IN, Aithal GP, Francis ST. Quantitative MRI to assess portal hypertension in cirrhosis patients at 3T. InProc. Intl. Soc. Mag. Reson. Med 2019 (Vol. 27, p. 1738).

1738

Quantitative MRI to assess portal hypertension in cirrhosis patients at 3T

Chris R Bradley[1,2], Rob E Scott[2], Eleanor F Cox[1,2], Naaventhan Palaniyappan[2], Indra Neil Guha[2], Guruprasad P Aithal[2], and Susan T Francis[1,2]

[1]Sir Peter Mansfield Imaging Centre, University of Nottingham, Nottingham, United Kingdom, [2]NIHR Nottingham Biomedical Research Centre, University of Nottingham, Nottingham, United Kingdom

Synopsis

We have previously validated MRI as a surrogate measure of Hepatic Venous Pressure Gradient (HVPG) at 1.5T using T_1 relaxation time and splanchnic haemodynamics. Here, we explore the use of quantitative 3T MRI to assess portal hypertension. A strong correlation between HVPG and fat suppressed IR SE-EPI T_1 ($p<0.0001$) and a correlation with superior mesenteric artery (SMA) velocity ($p=0.02$) was observed. MOLLI T_1 showed a weak correlation with HVPG ($p=0.11$) compared with SE-EPI ($p<0.001$) in a matched patient subset. A fat suppressed IR SE-EPI T_1 scheme and SMA velocity can be used as a surrogate for HVPG at 3T.

Purpose

The majority of complications in liver cirrhosis arise from portal hypertension. Hepatic Venous Pressure Gradient (HVPG) [1] is the gold standard method for the assessment of portal hypertension, but is highly invasive and performed only in a restricted number of centres. We have previously validated MRI as a surrogate measure of HVPG at 1.5T using T_1 relaxation time and haemodynamics [2]. Here, in a new cohort, we aim to assess quantitative MRI at 3T to assess portal hypertension.

Methods

43 patients were prospectively recruited (22 NAFLD/12 ALD/9 other. 59yrs (range 27-83). 27 male) after undergoing a HVPG measurement for clinical indications, MRI was performed within 12 days of a HVPG measurement on a 3T Philips Ingenia DDAS scanner.

MR Protocol:

Balanced Turbo Field Echo (bTFE) localisers were acquired in 3 orthogonal planes to quantify liver and spleen volume and identify vessels of interest. Longitudinal relaxation time (T_1) of the liver and spleen was measured using two methods (i) a respiratory triggered inversion recovery fat-suppressed spin-echo EPI scheme (9 axial slices, 10 inversion times (TI) 100 - 1500ms, 58ms temporal slice spacing, acquired in ascending/descending slice order to increase the TI dynamic range [2]) (ii) a 5-3-3 (Philips Cardiac Native) heart-rate triggered modified Look-Locker inversion recovery (MOLLI) scheme [3] (1 slice per breath hold for 4 slices), the acquisition time of each scheme was ~3 minutes. Transverse relaxation time (T_2*) of the liver was measured using a multishot-fast field echo (mFFE) sequence (12 echoes, TE1 2.5ms, ΔTE 2.5ms) to assess liver iron content. Liver and spleen fat fractions were measured using mDIXON QUANT (Philips Medical Systems). Phase-contrast (PC)-MRI was used to assess velocity, area and bulk flow in the splanchnic circulation (splenic artery [SPA] and superior mesenteric artery [SMA]) [2].

Data Analysis:

SE-EPI T_1 data at each inversion time was motion corrected using a non-rigid body model, and then fit on a voxel-by-voxel basis to generate M_0 and T_1 maps (MATLAB, Mathworks). MOLLI T_1 maps were produced online (Philips Medical Systems, Best NL). mFFE data were fit on a voxel-by-voxel basis to generate T_2* maps. Fat fraction maps were created using mDIXON QUANT software (Philips Medical systems, Best NL). Histogram analysis was performed to assess the distribution of T_1, T_2* and fat within the liver, with the mode of the distribution used to represent tissue T_1/T_2*/Fat % and FWHM to assess heterogeneity. Q-flow software (Philips Medical Systems) was used to analyse the PC-MRI data to compute mean vessel cross sectional area, velocity, and flux over the cardiac cycle.

Statistical Analysis:

All data was Shapiro-Wilk normality tested, a Pearson correlation test was used for normally distributed data and a Spearman correlation test used for non-parametric data. Coefficients of variance have been assessed previously [4, 5].

Results

The HVPG measures ranged from 2-23 mmHg, with a strong correlation between HVPG and SE-EPI T_1 ($p<0.0001$) and a correlation with SMA velocity ($p=0.02$), Figure 1. Figure 2 shows a subset of patients for whom both SE-EPI and MOLLI T_1 measurements were collected, MOLLI T_1 shows a weak correlation with HVPG ($p=0.11$) compared with SE-EPI ($p<0.001$). Further, the difference in measured T_1 between the two schemes was associated with fat fraction, a higher fat fraction leading to longer MOLLI T_1 (Fig.2C). Splenic T_1 as measured by both SE-EPI and MOLLI correlated equally well with HVPG up to a portal pressure of 10mmHg ($p=0.029$, $p=0.032$ respectively), >10mmHg no significance was observed (Figure 3). Figure 4 compares two patients with similar liver tissue T_1 measured by SE-EPI, but with differing levels of liver tissue fat, illustrating the differing measured MOLLI T_1 values.

Discussion

In agreement with our work at 1.5T, we have shown that 3T liver tissue T_1 as measured with SE-EPI and SMA mean velocity show a good correlation with degree of portal hypertension and so can be used as a surrogate measure to the HVPG test. We show that an IR fat suppressed SE-EPI sequence provides the optimal scheme for evaluating liver tissue T_1 when compared to MOLLI, as this method is independent of liver tissue fat (which has previously been shown to limit MOLLI T_1 values) [3]. The IR SE-EPI scheme is also free breathing and so is less demanding on the patient. Splenic Tissue T_1 has strong correlation for clinically insignificant HVPG measures but cannot be used to predict portal pressure above 10mmHg.

Conclusion

As shown at 1.5T, T_1 measured using a fat suppressed SE-EPI inversion recovery scheme and SMA mean velocity over the cardiac cycle can be used as a surrogate for the HVPG test at 3T.

Acknowledgements

Financial support from NIHR Nottingham Digestive Diseases Biomedical Research Centre, Nottingham University Hospitals NHS Trust and University of Nottingham.

References

1. Groszmann RJ, Wongcharatrawee S (2004) The hepatic venous pressure gradient: Anything worth doing should be done right. Hepatology 39:280–283 . doi: 10.1002/hep.20062
2. Palaniyappan N, Cox E, Bradley C, et al (2016) Non-invasive assessment of portal hypertension using quantitative magnetic resonance imaging. J Hepatol 65:1131–1139 . doi: 10.1016/j.jhep.2016.07.021
3. Mozes FE, Tunnicliffe EM, Pavlides M, Robson MD (2016) Influence of fat on liver T 1 measurements using modified Look-Locker inversion recovery (MOLLI) methods at 3T. J Magn Reson Imaging 44:105–111 . doi: 10.1002/jmri.25146
4. Cox EF, Palaniyappan N, Aithal GP, et al (2018) Using MRI to study the alterations in liver blood flow, perfusion, and oxygenation in response to physiological stress challenges: Meal, hyperoxia, and hypercapnia. J Magn Reson Imaging. doi: 10.1002/jmri.26341
5. Cox EF, Palaniyappan N, Aithal GP, et al (2018) MRI assessment of altered dynamic changes in liver haemodynamics following a meal challenge in compensated cirrhosis. Eur Radiol Exp 2:26 . doi: 10.1186/s41747-018-0056-3

Figures

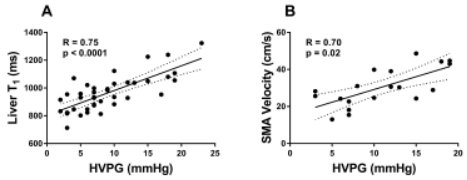

Fig 1. **A** Liver Tissue T_1 measured with a fat suppressed inversion recovery SE-EPI shows a strong correlation (R = 0.75, p < 0.0001) with HVPG, **B** SMA mean velocity also shows a significant correlation with HVPG (R = 0.70, p < 0.02).

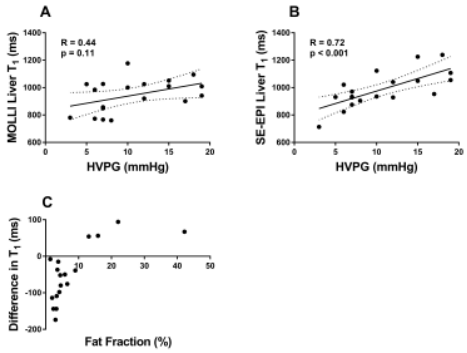

Fig 2. **A** subset of 18 of the 43 patients in the cohort had liver tissue T_1 measured using IR SE-EPI and MOLLI. A Liver Tissue T_1 measured with a MOLLI scheme shows a trend to correlate with HVPG (R = 44, p = 0.11) **B** IR fat-suppressed SE-EPI shows significant correlation (R = 0.72, p < 0.001) over the same subset of patients. **C** The difference in measured T_1 between IR SE-EPI and MOLLI showing the dependence of the MOLLI T_1 measure on liver tissue fat fraction.

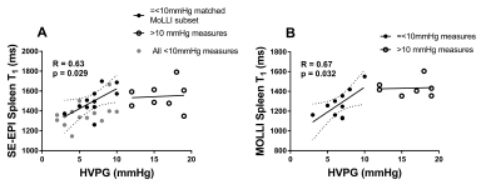

Fig 3. Spleen tissue T_1 correlates with HVPG for HVPG =< 10mmHg for both **A** IR fat-suppressed SE-EPI (R = 0.63, p = 0.029) and **B** MOLLI (R = 0.67, p = 0.032). For HVPG >10 mmHg there is no correlation between HVPG and spleen T_1.

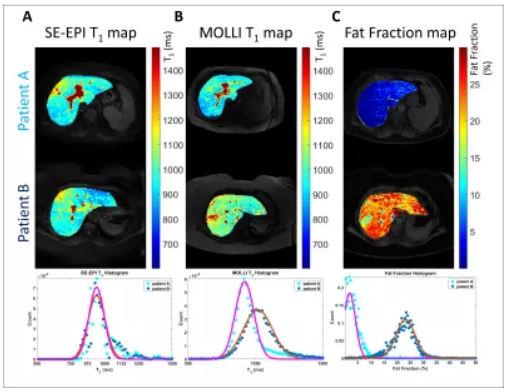

Fig 4. **A** T_1 maps and histograms of two patients with similar T_1 as measured by IR fat suppressed SE-EPI (Patient A: 942±56ms, Patient B: 942±63ms). **B** Geometrically matched MOLLI T_1 maps and histograms (Patient A: 920±68ms, Patient B: 1018±253ms). **C** Geometrically matched fat fraction maps and histograms (Patient A: 1.9±2%, Patient B: 23±4%). The resultant MOLLI T_1 map is dependent on the fat fraction within the liver.

Proc. Intl. Soc. Mag. Reson. Med. 27 (2019)
1738

9.10 Conference Proceedings C: Bradley CR, McGrath D, Cox EF, Francis ST. Effect of spatial resolution on Gradient Echo Magnetic Resonance Elastography at 3T. InProc. Intl. Soc. Mag. Reson. Med 2020 (Vol. 28, p. 2493).

2493

Effect of spatial resolution on Gradient Echo Magnetic Resonance Elastography at 3T

Chris R Bradley[1,2], Deirdre McGrath[1,2], Eleanor F Cox[1,2], and Susan T Francis[1,2]
[1]Sir Peter Mansfield Imaging Centre, University of Nottingham, Nottingham, United Kingdom, [2]NIHR Nottingham Biomedical Research Centre, Nottingham University Hospitals NHS Trust and University of Nottingham, Nottingham, United Kingdom

Synopsis

Iron-mediated T_2* effects are more prominent in MRE data acquired at 3T compared to 1.5 T, and have been suggested to lead to failure rates of up to 15% for MRE at 3T. MRE based liver stiffness was measured using the QIBA recommendation with a 2D gradient-recalled-echo MRE sequence using a 1.5x4.5x10 mm^3 acqusition. For comparison, MRE data was also collected at 4.5mm isotropic spatial resolution. A larger voxel volume in the MRE acquisition provided higher SNR which in turn resulted in a higher proportion of voxels being fit for stiffness with confidence >0.95.

Introduction

Magnetic Resonance Elastography (MRE) is becoming an accepted biomarker of liver injury and is being widely adopted for clinical trials using the Quantitative Imaging Biomarker Alliance (QIBA) recommendations. However, higher failure rates of the gradient-recalled-echo (GRE) MRE sequences are observed, particularly in patients with fatty liver disease and/or iron overload. The iron-mediated T_2* effects are more prominent at 3 T than 1.5 T, and have been suggested to lead to failure rates of up to 15 % for MRE at 3 T [1]. Here we assess the effect of liver T_2* and acquired spatial resolution on GRE MRE stiffness maps.

Methods

5 healthy volunteers (3M/2F, BMI 23.1 ± 1 kg/m^2, age range 24-27 years) and 2 patients with liver disease (both Non-Alcoholic SteatoHepatitis, NASH) (1M/1F, BMI 29.9 ± 4 kg/m^2, age range 31 - 51 years) were recruited. Participants attended an MRI scan after an overnight fast. Data was collected on a 3 T Philips Ingenia DDAS scanner (DS Anterior coil + posterior bed coil) to assess liver stiffness as assessed by MRE, liver tissue T_2*.

Data acquisition:

MRE based liver stiffness was measured using the QIBA recommendation with a 2D GRE MRE sequence (FOV 360x375 mm, voxel 1.5x4.5x10 mm^3, TE = 20 ms, TR = 50 ms, 4 axial slices through the liver, slice gap 1 mm, 1 slice acquired per 18 second breath hold) [2]. For comparison, data was also collected at 4.5 mm isotropic spatial resolution with matched FOV, TE/TR and slice positioning. For both acquisitions, the passive acoustic driver (Resoundant, Rochester, MN) was placed against the lower right chest at the level of the xiphoid in the midclavicular line, and continuous vibrations of 60 Hz were applied. Liver T_2* maps were collected using multi-echo fast-field echo (mFFE) data acquired at 12 echo times (TE1 = 2.5 ms, ΔTE = 2.5 ms, 9 axial slices, 3x3x8 mm^3 voxel).

Data Analysis:

T_2*: Manual ROIs were drawn on the scanner computed T_2* map images, avoiding large blood vessels, bile ducts, and edges of the liver parenchyma. Histogram analysis was then performed to assess the distribution of T_2* within the liver, the mode of the distribution was used to represent tissue T_2* and FWHM to assess heterogeneity.

MRE: From the acquired magnitude and phase images, the scanner computed elastograms depicting the spatial distribution of the shear stiffness (ie, magnitude of the complex modulus, |G*|) in kPa, and confidence masks computed from voxels with confidence values >0.95. Data were then reshaped to match the resolution of the T_2* maps. Liver stiffness measurements were calculated based on mode values from the elastograms within the intersection of manually drawn ROIs and confidence masks. The percentage of the liver in which a confidence mask was formed was computed. In addition liver stiffness values were computed within each confidence mask for each spatial resolution of MRE data.

Results

Figure 1 shows example liver stiffness maps computed for the non-isotropic and isotropic resolutions in two participants, one participant with a short T_2* (12 ms mode) and one with a longer T_2* (22 ms mode). For shorter liver T_2* values, the percentage of the liver fit as defined by the confidence map is reduced when using the non-isotropic GRE-MRE protocol compared with the isotropic protocol, Fig. 2. Mean liver stiffness for the non-isotropic GRE-MRE protocol was 2.4 ± 2 kPa and 1.9 ± 1.4 kPa for the isotropic protocol.

Discussion

Participants who have shorter liver T_2* associated with higher iron content within the liver tissue, have a smaller percentage of the liver which fits with confidence (confidence >0.95), Fig. 2. The GRE acquisition is limited to a TE of 20 ms as the MRE motion encoding gradient frequency is set to match the mechanical driving frequency of 60 Hz. As a result, signal-to-noise ratio is limited in participants with a shorter liver T_2* as rapid dephasing of the signal occurs during the echo time. We show that by choosing an isotropic resolution with larger voxel volume (91.1 ml isotropic compared to 67.5 ml for the non-isotropic QIBA recommendation), the goodness of fit in the stiffness maps is improved, and not dependent on the T_2* of the liver, allowing successful spatial mapping of stiffness over a larger area of the liver (Fig. 2).

Conclusion

Using a isotropic voxel size with larger volume as compared to the QIBA recommendation for the GRE MRE acquisition provides a higher SNR which in turn results in a higher proportion of voxels being fit for stiffness with confidence >0.95 within the liver tissue.

Acknowledgements

We would like to thank the NIHR Nottingham BRC research nurses who conducted patient enrolment

References

1. Dong Wook Kim, So Yeon Kim, Hee Mang Yoon, Kyung Won Kim and Jae Ho Byun. Comparison of technical failure of MR elastography for measuring liver stiffness between gradient-recalled echo and spin-echo echo-planar imaging: A systematic review and meta-analysis. J Magn Reson Imaging. 2019 Aug 27.

2. QIBA MR Elastography of the Liver Biomarker Committee. Magnetic Resonance Elastography of the Liver. Profile Stage: Consensus. QIBA, May 2, 2018. Available from: http://qibawiki.rsna.org/index.php/Profiles

Figures

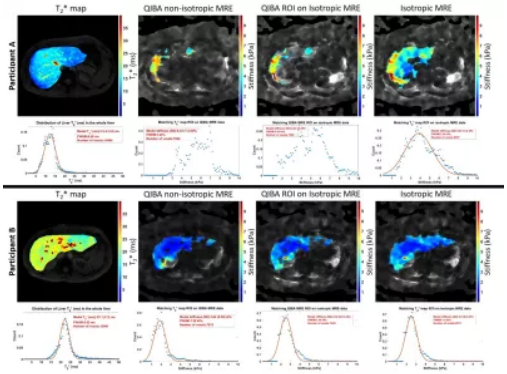

Figure 1: T_2* and MRE derived liver stiffness maps shown for the non-isotropic and isotropic MRE protocols for subjects with short (**A**) and long (**B**) liver T_2*. For MRE, the intersection of ROI and confidence masks are shown, in addition the ROI from the confidence mask of the non-isotropic map is applied to the isotropic map. Participant **A**, low T_2*, has a lower area of confidence for the non-isotropic MRE. In contrast, a larger area of fit confidence was found for isotropic MRE. Participant **B** with a longer T_2* has a similar fit in stiffness values between resolutions.

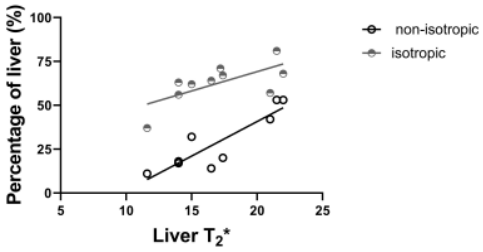

Figure 2: The percentage of the liver fit with confidence using the non-isotropic and isotropic GRE-MRE protocols versus liver T_2*. Shorter T_2* values reduce the percentage of liver fit for the non-isotropic protocol as compared to the isotropic protocol.

9.11 Conference Proceedings D: Bradley CR, Scott R, Cox EF, Palaniyappan N, Guha IN, Aithal GP, Francis ST. Quantitative MRI to assess portal hypertension in cirrhosis patients. InProc. Intl. Soc. Mag. Reson. Med 2020 (Vol. 28, p. 0323).

0323

Quantitative MRI to assess portal hypertension in cirrhosis patients

Chris R Bradley[1,2], Rob A Scott[2], Eleanor F Cox[1,2], Naaventhan Palaniyappan[2], I Neil Guha[2], Guruprasad P Aithal[2], and Susan T Francis[1,2]
[1]Sir Peter Mansfield Imaging Centre, University of Nottingham, Nottingham, United Kingdom, [2]NIHR Nottingham Biomedical Research Centre, Nottingham University Hospitals NHS Trust and University of Nottingham, Nottingham, United Kingdom

Synopsis

Hepatic venous pressure gradient (HVPG) is the gold standard method for the assessment of portal pressure, but highly invasive. We scanned patients with portal hypertension at both 1.5T and 3T to assess MRI parameters related to portal pressure as defined by HVPG. Iron-corrected liver T_1 highly correlated over the full range of HVPG (3T p<0.0002, 1.5T p<0.0001), spleen T_1 and superior mesenteric artery velocity correlated up to HVPG of 15 mmHg (spleen T_1: 3T p<0.0003, 1.5T p<0.0006; SMA velocity: p<<0.00001), after which at HVPG >15 mmHg no correlation was observed.

Introduction

The majority of complications in liver cirrhosis arise from portal hypertension. Hepatic Venous Pressure Gradient (HVPG) [1] is the gold standard method for assessment of portal hypertension, but is highly invasive and performed in only a limited number of centres. We previously validated MRI as a surrogate measure of HVPG at 1.5T using liver T_1 and splanchnic haemodynamics [2]. Here, we combine a new cohort of patients scanned at 3T MRI with those at 1.5T [2] to examine the relation of MRI measures with HVPG for individual patient care.

Methods

Participants underwent HVPG measurement for clinical indications and MRI was performed within 6 weeks in a fasted state. 43 patients (22 Non-alcoholic fatty liver disease (NAFLD)/11 Alcohol-related liver disease (ArLD)/10 other, 60±11 years) were scanned on a 3T Philips Ingenia scanner and collated with a previous cohort of 30 patients (11 NAFLD/9 ArLD/5 autoimmune hepatitis/5 other, 55±13 years) scanned on a 1.5T Philips Achieva scanner [2]. Liver stiffness was measured using transient elastography (Fibroscan®).

MR Protocol:

T_1 longitudinal relaxation time of the liver and spleen was measured using a respiratory triggered inversion recovery fat-suppressed spin-echo EPI scheme (3T: 9 axial slices, 10 inversion times (TI) 100-1500ms, 58ms temporal slice spacing, ascending/descending slice order; 1.5T: 9 axial slices, 13 inversion times 100-1200ms in 100ms steps and 1500ms). Liver and spleen transverse relaxation time (T_2*) was measured using a multishot-fast field echo (mFFE) sequence (3T: 12 echoes, TE1 2.5ms, ΔTE 2.5ms) to assess liver iron content. Phase-contrast (PC)-MRI was used to assess flow in the superior mesenteric artery (SMA), splenic artery (SPA) and ascending aorta. Liver and spleen fat fraction and volume were measured using mDIXON QUANT (Philips Medical Systems).

Data Analysis:

SE-EPI T_1 data was motion corrected and fit to generate a T_1 map (MATLAB), T_1 maps were corrected for iron content using the mFFE-computed T_2* maps [3]. Histogram analysis was performed to compute the mode of T_1, T_2* within the liver. Q-flow software (Philips Medical Systems) was used to analyse the PC-MRI data to compute mean vessel cross-sectional area, velocity, and flux over the cardiac cycle. Cardiac index was computed by correcting the ascending aorta flux for body surface area. Liver and spleen volume were estimated using Analyze9.

Statistical Analysis:

Data was Shapiro-Wilk normality tested, and correlations assessed with the full range of HVPG, HVPG up to 15 and >15mmHg (an independent risk factor for adverse liver related outcomes [4,5]) using a Pearson or Spearman test. Coefficients of variation have been assessed previously [6].

Results

HVPG ranged from 1-23mmHg, with a strong linear correlation between HVPG and iron corrected liver T_1 (p<0.0002, Fig. 1A), liver volume showed no change (Fig. 1B). Spleen T_1 (Fig. 2A) correlated with HVPG up to a portal pressure of 15mmHg (spleen T_1: p<0.0003 at 3T, p<0.0006 at 1.5T), after which (>15mmHg) no significance was observed, spleen volume showed a similar pattern (Fig. 2B). SMA velocity also showed a significant increase up to 15mmHg (p<<0.00001, Fig. 2C), after which it declined. SPA velocity correlated with HVPG (p<0.0004, Fig. 2D). SMA velocity and spleen T_1 correlated at 3T (p<0.002, Fig. 2E). No correlation was seen between cardiac index and HVPG (Fig. 3). Liver stiffness measured from Fibroscan® weakly correlated with HVPG in the 3T cohort (R=0.29, P=0.10), reaching significance for the combined cohort (R=0.44, P<0.001), Fig. 4.

Discussion

Liver T_1 at 3T highly correlated across the full range of HVPG (Fig. 1), as previously shown at 1.5T [2]. Importantly, we show across both 1.5 and 3 T that spleen T_1 increases with increased HVPG only up to 15mmHg (Fig. 2), after which a reduction in spleen T_1 is seen. This pattern is also reflected in spleen volume and SMA velocity, with a significant correlation between spleen T_1 and SMA velocity. This suggests that as sphanchnic flow increases and splenic venous flow into the portal vein is impeded by elevated portal pressure, congestion of intrasplenic blood and spleen enlargement occurs, with the spleen T_1 plateauing at blood T for each field strength (~1800ms at 3T, 1300ms at 1.5T [7]). The drop in splanchnic MRI measures at HVPG >15mmHg is likely due to an increase in collaterals [8]. The finding of a threshold HVPG of 15mmHg is in line with a lack of correlation at high HVPG between HVPG and splenic stiffness from Fibroscan® [9]. The assessment of multi-organ measures in this study suggests MRI provides a way to identify the potential therapeutic window in portal hypertension [8]. The 1.5T cohort had a strong correlation between liver stiffness from Fibroscan® and HVPG which was not seen in the 3T cohort, likely due to the higher prevalence of varices or higher BMI (BMI >30 in 59% participants at 3T and 41% at 1.5T) in the 3T cohort.

Conclusion

Liver T_1 is a good surrogate measure for the prediction of portal pressure. Spleen T_1, spleen volume and SMA flow correlate up to a HVPG of 15 mmHg, after which a reduction is observed, which together could predict when the window of therapeutic opportunity begins to close, and when beta blocker therapy may become less effective or have adverse effects.

Acknowledgements

Financial support from NIHR Nottingham Digestive Diseases Biomedical Research Centre, Nottingham University Hospitals NHS Trust and University of Nottingham.

References

1. Groszmann RJ, Wongcharatrawee S (2004) The hepatic venous pressure gradient: Anything worth doing should be done right. Hepatology 39:280–283 . doi: 10.1002/hep.20062

2. Palaniyappan N, Cox E, Bradley C, et al (2016) Non-invasive assessment of portal hypertension using quantitative magnetic resonance imaging. J Hepatol 65:1131–1139 . doi: 10.1016/j.jhep.2016.07.021

3. Wood JC, Enriquez C, Ghugre N, et al (2005) MRI R2 and R2* mapping accurately estimates hepatic iron concentration in transfusion-dependent thalassemia and sickle cell disease patients. Blood 106:1460–1465 . doi: 10.1182/blood-2004-10-3982

4. Merkel, C., et al., The hemodynamic response to medical treatment of portal hypertension as a predictor of clinical effectiveness in the primary prophylaxis of variceal bleeding in cirrhosis. Hepatology, 2000. Nov;32(5):930-4 doi: 10.1053/jhep.2000.19322

5. Silva-Junior, G., et al., The prognostic value of hepatic venous pressure gradient in patients with cirrhosis is highly dependent on the accuracy of the technique. Hepatology, 2015. 62(5): p. 1584-92. doi: 10.1002/hep.28031.

6. Bradley CR, Cox EF, Scott RA, et al (2018) Multi-organ assessment of compensated cirrhosis patients using quantitative magnetic resonance imaging. J Hepatol 69:1015–1024 . doi: 10.1016/j.jhep.2018.05.037

7. Zhang X, Petersen ET, Ghariq E, et al (2013) In vivo blood T(1) measurements at 1.5 T, 3 T, and 7 T. Magn Reson Med 70:1082–6 . doi: 10.1002/mrm.24550

8. Krag A, Wiest R, Albillos A, Lotte Gluud L The window hypothesis: haemodynamic and non-haemodynamic effects of b-blockers improve survival of patients with cirrhosis during a window in the disease. doi: 10.1136/gutjnl-2011-301348

9. Tseng Y, Li F, Wang J, et al (2018) Spleen and liver stiffness for noninvasive assessment of portal hypertension in cirrhotic patients with large esophageal varices. J Clin Ultrasound 46(7):442–449. doi: 10.1002/jcu.22635.

Figures

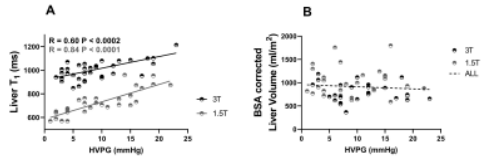

Figure 1: **A** Iron-corrected liver tissue T_1 shows a significant correlation with hepatic venous pressure gradient (HVPG) at both 3T (R=0.60 P<0.0002) and 1.5T (R=0.84 P<0.0001). **B** No correlation of body surface area (BSA) corrected liver volume with HVPG.

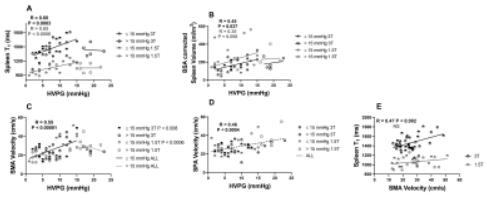

Figure 2: **A** Spleen T_1 correlated with hepatic venous pressure gradient (HVPG) up to 15 mmHg at 1.5T (R=0.65, P<0.0006) and 3T (R=0.60, P<0.0003); **B** Body surface area (BSA) corrected spleen volume correlates with HVPG up to 15 mmHg for 3T (R=0.45 P=0.037) and 1.5T (R=0.38, P<0.066) **C** Superior mesenteric artery (SMA) velocity correlates with HVPG up to 15 mmHg for 1.5T and 3T data combined (R=0.55, P<0.00001), after which SMA velocity reduces; **D** Splenic artery (SPA) velocity correlated with HVPG (R=0.47, P<0.002); **E** Correlation of spleen T_1 with SMA velocity at 3T (R=0.47, P<0.002).

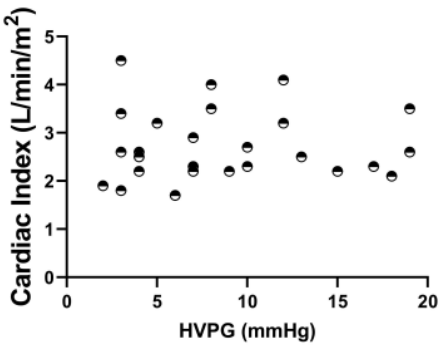

Figure 3: Cardiac Index at 3T shows no correlation with hepatic venous pressure gradient (HVPG).

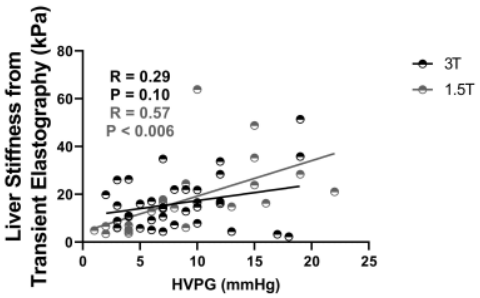

Figure 4: Liver stiffness measured using transient elastography (TE) from Fibroscan® correlates with HVPG at 1.5T (R=0.57, P<0.006), and shows a trend at 3T (R=0.29, P=0.10), with a combined cohort correlation of R=0.44 and P<0.001.

Proc. Intl. Soc. Mag. Reson. Med. 28 (2020)
0323

9.12 Conference Proceedings E: Bradley CR, Mcgrath D, Cox EF, Palaniyappan N, Scott R, Guha IN, Aithal GP, Francis ST. The association of Liver Stiffness with Liver tissue T1 and Superior Mesenteric Artery blood flow across disease severity. InProc. Intl. Soc. Mag. Reson. Med 2022 (Vol. 30, p. 0604).

0604

The association of Liver Stiffness with Liver tissue T_1 and Superior Mesenteric Artery blood flow across disease severity.

Christopher R Bradley[1,2], Deirdre Mcgrath[1,2], Eleanor F Cox[1,2], Naaventhan Palaniyappan[2], Robert Scott[2], Indra N Guha[2], Guruprasad P Aithal[2], and Susan T Francis[1,2]
[1]Sir Peter Mansfield Imaging Centre, University of Nottingham, Nottingham, United Kingdom, [2]NIHR Biomedical Research Centre, Nottingham University Hospitals NHS Trust, Nottingham, United Kingdom

Synopsis

We assess liver stiffness measured using magnetic resonance elastography (MRE) and longitudinal relaxation time T_1 in three groups: healthy volunteers, non-alcoholic fatty liver disease patients and compensated cirrhosis patients. MRE liver stiffness was measured using the Quantitative Imaging Biomarker Alliance (QIBA) recommendation. T_1 longitudinal relaxation time of the liver was measured using a respiratory triggered inversion recovery fat-suppressed spin-echo echo planar imaging scheme. A positive correlation between Liver tissue T_1 and Liver stiffness (R=0.70, p<0.0001) across the 3 groups was observed. Superior mesenteric artery flow also correlates with liver stiffness (R=0.62, p<0.002) suggesting worsening hyperdynamic circulation with progressive fibrosis.

Introduction

Magnetic resonance elastography (MRE) liver stiffness and liver longitudinal Relaxation time (T_1) using a modified look-locker inversion recovery scheme (MOLLI) are becoming accepted biomarkers in clinical studies of liver disease[1,2]. Together liver tissue T_1 measured with spin-echo echo planar imaging (SE-EPI) (microstructure) and superior mesenteric artery (SMA) flow (haemodynamics) have been shown to provide surrogate measures of portal pressure as measured by hepatic venous pressure gradient (HVPG)[3]. Here we assess the relationship between liver stiffness measured using 2D-GRE MRE, with measures of liver tissue T_1 (comparing both SE-EPI and MOLLI T_1 mapping methods) and SMA blood flow, and their link to liver disease severity.

Methods

7 healthy volunteers (HV) (5M/2F, BMI 23.1±1 kg/m^2, 24-27 years), 12 biopsy confirmed non-alcoholic Fatty Liver Disease (NAFLD) patients (5M/7F, BMI 34.1±5.6 kg/m^2, 20-75years) and 7 biopsy confirmed compensated cirrhosis (CC) patients (aetiology: 3 NAFLD/2 ALD/2 HBV, BMI 31.3±4 kg/m^2, 45-85 years) were recruited. Participants attended an MRI scan after an overnight fast.
Data was collected on a 3T Philips Ingenia scanner. This included a 2D-GRE MRE measure using the Quantitative Imaging Biomarker Alliance (QIBA) recommendation (FOV 360x375mm^2, voxel 1.5x4.5x10mm^3, TE/TR=20/50ms, 4 axial slices, slice gap 1mm, 1 slice per 18s breath hold, 4 slices acquired) with vibrations applied at 60Hz[4]. Liver T_1 was measured using a respiratory-triggered inversion recovery fat-suppressed SE-EPI scheme (9 axial slices, 3x3x8mm^3 voxel, 10 inversion times between 100-1500ms, 58ms temporal slice spacing, ascending/descending slice order acquired in ~ 3 minutes)[3] and a 5(3)3 native MOLLI T_1 scheme[5]. Liver T_2* maps were collected using a multi-echo fast-field echo (m-FFE) data acquired at 12 echo times (TE1=2.5ms, ΔTE=2.5ms, 9 axial slices, 3x3x8mm^3 voxel). Fat fraction maps were acquired using the mDIXON Quant scheme. SMA flow was assessed using phase contrast MRI with V_{ENC} = 140cm/s[6].

Data Analysis

Scanner computed elastograms provided maps of the spatial distribution of the shear stiffness in kPa, with confidence masks computed from voxels with confidence values >0.95. Manually drawn ROIs were created in accordance with the QIBA recommendations (within ~1 cm of liver boundary, including at least 500 voxels)[4]. Histogram analysis was then performed to assess the modal stiffness.
SE-EPI liver T_1 data was motion corrected and fit to generate a T_1 map (MATLAB). MOLLI liver T_1 maps, liver Tissue T_2* maps and fat fraction maps were scanner computed. Manual ROIs were drawn on map images, avoiding large blood vessels, bile ducts, and edges of the liver parenchyma. Histogram analysis was performed and the mode of the distribution used to represent liver tissue T_1, T_2* and fat fraction. Q-flow software (Philips) provided an estimate of SMA velocity, flux, and cross-sectional area.

Statistical Analysis

Data was Shapiro-Wilk normality tested, correlations were assessed using a Pearson test. Multiple regression analysis was performed in 20 patients to assess the relationship between MRE with T_1, fat fraction and T_2*.

Results

Figure 1 shows there was a highly significant positive correlation of SE-EPI liver T_1 (R=0.70, p<0.0001) and mean SMA velocity (R=0.62, p<0.002) with liver MRE stiffness. Figure 2 provides example stiffness and SE-EPI T_1 maps with disease severity. Figure 3 compares those subjects who had both SE-EPI and MOLLI Liver T_1 measures vs MRE; SE-EPI T_1 correlates with liver stiffness (R=0.84, p<0.0001), no significant correlation was observed for MOLLI T_1. Liver stiffness was not correlated with either fat fraction or liver tissue T_2* (Fig. 4A). A negative correlation was observed between SE-EPI liver tissue T_1 and fat fraction (R=0.56, p=0.016), whereas no correlation is observed between MOLLI tissue T_1 and fat fraction (Fig. 4B). Fat fraction correlated with the difference between the two measures of Liver T_1 (MOLLI T_1– SE-EPI T_1) (Fig. 4C). Table 1 shows multiple regression analysis of independent variables: liver tissue T_1, fat fraction and liver tissue T_2* to predict liver stiffness. The analysis shows that SE-EPI liver T_1 is sufficient to predict liver stiffness (R=0.98), whereas MOLLI liver T_1 requires inclusion of liver fat fraction (R=0.97). Liver T_2* does not contribute to either prediction model.

Discussion

The strong correlation observed between liver stiffness and both SE-EPI liver Tissue T_1 and SMA velocity suggest liver stiffness is a good additional measure to compliment these measures of liver disease severity, and suggests that liver stiffness could also provide a good predicter of HVPG[3,7]. MOLLI liver T_1 has previously been shown to correlate with liver stiffness in a much larger cohort (n=155, R=0.49, p<0.001)[2]. However, we did not observe a significant correlation between MOLLI liver T_1 and liver stiffness in our smaller cohort. This is likely due to MOLLI T_1 being dependent on many factors, such as the degree of fat in the liver tissue[8,9]. In this cohort, SE-EPI T_1 negatively correlates with fat fraction as the CC cohort has lower fat fraction but more severe liver disease when compared with the NAFLD group. We propose that SE-EPI T_1 is the more sensitive T_1 measure to be used in conjunction with MRE and SMA velocity to provide a powerful tool for assessment of liver disease and portal pressure.

Acknowledgements

This work was funded by NIHR Biomedical Research Centre, Nottingham University Hospitals NHS Trust.

References

1. Erden A, Öz DK, Peker E, et al (2021) MRI quantification techniques in fatty liver: the diagnostic performance of hepatic T1, T2, and stiffness measurements in relation to the proton density fat fraction. Diagnostic Interv Radiol 27:7. https://doi.org/10.5152/DIR.2020.19654

2. Obmann VC, Mertineit N, Marx C, et al (2019) Liver MR relaxometry at 3T – segmental normal T1 and T2* values in patients without focal or diffuse liver disease and in patients with increased liver fat and elevated liver stiffness. Sci Reports 2019 91 9:1–11. https://doi.org/10.1038/s41598-019-44377-y

3. Palaniyappan N, Cox E, Bradley C, et al (2016) Non-invasive assessment of portal hypertension using quantitative magnetic resonance imaging. J Hepatol 65:1131–1139. https://doi.org/10.1016/j.jhep.2016.07.021

4. Quantitative Imaging Biomarkers Alliance (2017) QIBA Profile : Magnetic Resonance Elastography of the Liver. 1–65

5. Banerjee R, Pavlides M, Tunnicliffe EM, et al (2014) Multiparametric magnetic resonance for the non-invasive diagnosis of liver disease. J Hepatol 60:69–77. https://doi.org/10.1016/j.jhep.2013.09.002

6. Bradley CR, Cox EF, Scott RA, et al (2018) Multi-organ assessment of compensated cirrhosis patients using quantitative magnetic resonance imaging. J Hepatol 69:1015–1024. https://doi.org/10.1016/j.jhep.2018.05.037

7. Danielsen KV, Hove JD, Nabilou P, et al (2021) Using MR elastography to assess portal hypertension and response to beta-blockers in patients with cirrhosis. Liver Int 41:2149–2158. https://doi.org/10.1111/liv.14981

8. Mozes FE, Tunnicliffe EM, Pavlides M, Robson MD (2016) Influence of fat on liver *T* $_1$ measurements using modified Look-Locker inversion recovery (MOLLI) methods at 3T. J Magn Reson Imaging 44:105–111. https://doi.org/10.1002/jmri.25146

9. Mozes FE, Tunnicliffe EM, Moolla A, et al (2019) Mapping tissue water T1 in the liver using the MOLLI T1 method in the presence of fat, iron and B0 inhomogeneity. NMR Biomed 32:e4030. https://doi.org/10.1002/NBM.4030

Figures

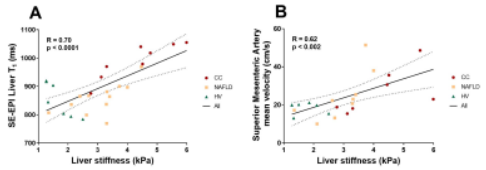

A A significant positive correlation between SE-EPI Liver T_1 and Liver stiffness as measured using 2D GRE-MRE (R=0.70, p <00001). **B** A significant positive correlation between Superior Mesenteric Artery mean velocity and 2D-GRE MRE liver stiffness (R=0.62, p<0.002).

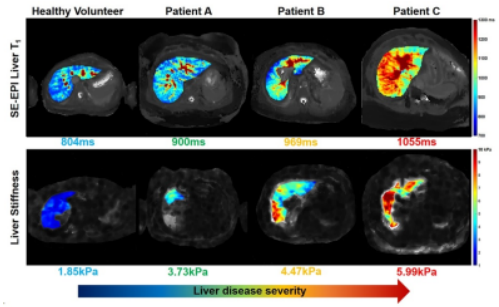

Four example participants with increasing liver disease severity. Maps are shown for increasing liver stiffness (2D GRE-MRE) and liver tissue T_1 (SE-EPI). Modal liver stiffness and T_1 values are provided for each participant.

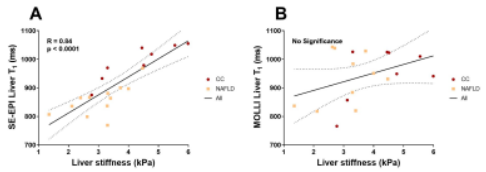

Those participants who had both SE-EPI Liver T_1 and MOLLI Liver T_1 measurements plot against MRE liver stiffness measurement. A strong correlation is seen between SE-EPI T_1 and MRE stiffness (R=0.84, p<0.0001) (**A**), no correlation was observed between MOLLI T_1 and MRE stiffness (**B**).

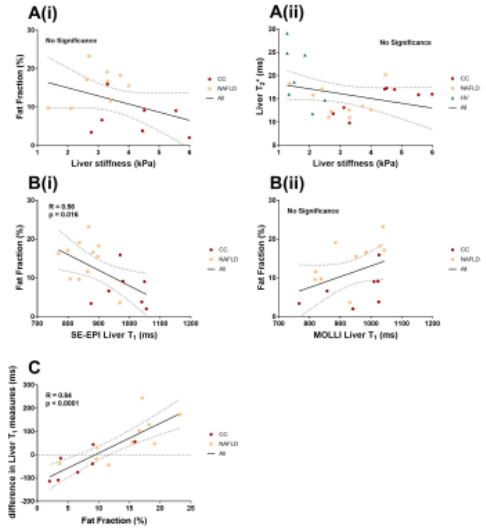

A No correlation between liver stiffness and (i) fat fraction and (ii) liver tissue T_2*. **B** (i) A negative correlation between fat fraction and SE-EPI Liver T_1 (R=0.56, p=0.016). (ii) No correlation between fat fraction and MOLLI Liver T_1. **C** A significant correlation between the difference in liver T_1 between MOLLI and SE-EPI (MOLLI minus SE-EPI) and fat fraction (R=0.84, p<0.0001).

Multiple Regression analysis for MRE including SE-EPI Liver T_1 (R = 0.98)				
Parameter estimates	Variable	β_x Estimate	p value	p value summary
β_1	SE-EPI liver T_1	0.006197	0.0021	**
β_2	Liver Fat fraction	-0.05830	0.1100	ns
β_3	Liver T_2*	-0.09607	0.3071	ns
Multiple Regression analysis for MRE including MOLLI Liver T_1 (R = 0.97)				
Parameter estimates	Variable	β_x Estimate	p value	p value summary
β_1	MOLLI T_1	0.006759	0.0048	**
β_2	Liver Fat fraction	-0.1394	0.0224	*
β_3	Liver T_2*	-0.08456	0.4024	ns

Table 1: Multiple regression analysis for liver stiffness *liver stiffness = (β_1 * liver tissue T_1) + (β_2 * liver fat fraction) + (β_3 * liver tissue T_2*)* including each liver tissue T_1 method (SE-EPI and MOLLI).

Proc. Intl. Soc. Mag. Reson. Med. 30 (2022)
0604

9.13 Conference Proceedings F: Bradley CR, Cox EF, Francis ST. Translation of a non-contrast quantitative MRI protocol for portal pressure prediction InProc. Intl. Soc. Mag. Reson. Med 2023 (Vol. 31, p. *To Be Confirmed*).

Translation of a non-contrast quantitative MRI protocol for portal pressure prediction

Chris R Bradley[1,2], Eleanor F Cox[1,2], and Susan T Francis[1,2]
[1]University of Nottingham, Nottingham, United Kingdom, [2]NIHR Biomedical Research Centre, Nottingham, United Kingdom

Synopsis

Most complications in liver cirrhosis arise from portal hypertension. Using a vendor-specific fat suppressed spin-echo echo planar imaging T_1 mapping method along with measures of flow within the superior mesenteric artery, we previously validated MRI as a surrogate measure of portal pressure at 1.5 and 3T. Here we translate this work to three MR vendors (GE, Philips and Siemens) using commercially available sequences allowing multi-site studies of assessment of portal pressure. Importantly, this could provide a non-invasive measure of portal pressure for clinical use to replace current invasive gold standard measures.

Introduction

Most complications in liver cirrhosis arise from portal hypertension. The current gold standard method to measure portal pressure is the Hepatic Venous Pressure Gradient (HVPG)[1]. However, HVPG is highly invasive and can only be prescribed at specialist hepatology centres. MRI surrogates of portal pressure are now being explored using non-contrast methods of T_1 mapping combined with haemodynamic measures[2], or methods using more specialised imaging techniques such as 4DFlow[3], or hardware for MR elastrography (MRE)[4].

We previously validated MRI as a surrogate measure of HVPG at 1.5T[2] and 3T[5] on Philips scanners using fat suppressed spin-echo echo planar imaging (SE-EPI) liver T_1 and splanchnic haemodynamics through phase contrast (PC)-MRI of the superior mesenteric artery (SMA) (Figure 1A). Our prior work used a vendor-specific bespoke-coded T_1 mapping scheme to collect a multi-slice respiratory triggered fat suppressed SE-EPI sequence with whole liver coverage in ~3 minutes. We showed this fat suppressed SE-EPI acquisition was superior to MOLLI for measuring liver T_1, since fat significantly influences the MOLLI T_1 measurement[5,6] (Figure 1B). PC-MRI for assessment of SMA haemodynamics is routinely available on all clinical MRI scanners.

Here, we translate our MRI measure of portal pressure for use across vendors by using a commercially available vendor-provided SE-EPI T_1 mapping sequence in a short clinically feasible time without the need for specialised hardware or sequences. To address this, we first show that a single slice SE-EPI T_1 mapping measure is representative of the whole liver in portal hypertension, since when using vendor-provided sequences only single slice measures can be acquired within an acceptable time. We then build an MRI protocol using vendor-product single slice fat suppressed SE-EPI T_1 mapping sequences and PC-MRI measures of SMA velocity for each of the three major MR vendors (GE, Philips, Siemens). The T_1 accuracy of each vendor-product single slice SE-EPI fat-suppressed T_1 mapping sequence is assessed with a phantom and in healthy volunteers.

Methods

Multi-slice T_1 maps collected in our prior 3T study[5] of portal hypertension were reanalyzed. The mode of the liver T_1 value across all slices was compared to the mode of liver T_1 from the central slice only to provide confirmation that a single slice T_1 map is representative of the whole liver in patients with portal hypertension.
Parameters for vendor-product sequences allowing free-breathing fat suppressed SE-EPI T_1 mapping to be collected are given in Table 1. For each vendor-product T_1 mapping sequence, a NIST System phantom (CalibreMRI™, CO, USA) was scanned and T_1 values across the reference balls compared with their reference NIST T_1 values. In addition, two healthy male volunteers were each scanned with vendor-product sequences on a 1.5T Siemens Sola, a 3T Philips Ingenia and a 3T GE Premier scanner. Our vendor-specific bespoke-coded T_1 mapping scheme of a respiratory triggered inversion recovery fat-suppressed spin-echo EPI scheme was also acquired on the 3T Philips Ingenia (9 axial slices, 15 inversion times 100 – 1500 ms in 100 ms steps, 58 ms temporal slice spacing, acquired in ascending/descending slice order to increase the dynamic range of inversion times)[4,5]. Data were fit voxel-wise using a 3-parameter model across inversion times to compute T_1 maps on the NIST phantom spheres and in vivo.

Results

Figure 2 correlates the mode of single slice liver T_1 measures with the mode of the whole liver measures in patients with portal hypertension and shows a highly significant correlation ($R = 0.99$, $p < 0.0001$). Figure 3 shows the accuracy of vendor-product sequence SE-EPI T_1 mapping measures against NIST phantom reference T_1 values (Siemens: $R=0.99$, $p<0.0001$. Philips: $R=0.99$, $p<0.0001$. GE: $R=0.99$, $p<0.0001$). Figure 4 shows T_1 maps for an example healthy subject across vendors, and the modal fits on the distribution of T_1 values within an ROI within liver tissue (Siemens 1.5T: 590±34ms; GE 3T: 777±68ms; Philips 3T: 770±46ms, multislice: 783±76ms).

Discussion

Here we show that, in portal hypertension patients, a single slice of the liver is representative of the whole liver, and so can be used in MRI surrogate measures of HVPG. We set-up single slice vendor-provided fat suppressed SE-EPI liver T_1 schemes on each of the three major vendors - GE, Philips, and Siemens. The fat suppressed SE-EPI scheme is chosen over a MOLLI T_1 mapping scheme due to the significant influence of fat on MOLLI liver T_1 [6]. Cross-vendor SE-EPI T_1 measures are validated on a NIST phantom. In healthy subjects, liver T_1 values are shown to match literature T_1 values of healthy liver tissue T_1 at 1.5T: 586±39ms[7] and 3T: 809±71ms[8], with a ratio of 1:1.38 as predicted between 1.5:3T[8]. In future work we will expand this model validation across each vendor at each field strength to generate comparator studies in healthy subjects and patients with liver disease.

Conclusion

We have demonstrated that a fat suppressed SE-EPI T_1 protocol for evaluation of liver tissue T_1 can be acquired on any major vendor at 1.5 or 3T. This work shows promise for widespread translation of prior vendor-specific SE-EPI T_1 based-methods that can, together with haemodynamic information, provide a surrogate of portal pressure.

Acknowledgements

This work was funded by the Nottingham NIHR Biomedical Research Centre.

References

1. Groszmann RJ, Wongcharatrawee S (2004) The hepatic venous pressure gradient: Anything worth doing should be done right. Hepatology 39:280–283 . doi: 10.1002/hep.20062

2. Palaniyappan N, Cox EF, Bradley CR, et al (2016) Non-invasive assessment of portal hypertension using quantitative magnetic resonance imaging. J Hepatol 65:1131–1139. doi: 10.1016/j.jhep.2016.07.021

3. Roldan-Alzate A, Frydrychowicz A, Niespodzany E et al (2013) In Vivo Validation of 4D Flow MRI for Assessing theHemodynamics of Portal Hypertension. J Magn Reson Imaging 37:1100-1108

4. Shi Y, Qi Y, Lan, G et al (2021) Three-dimensional MR Elastography Depicts Liver Inflammation, Fibrosis, and Portal Hypertension in Chronic Hepatitis B or C. Radiol 301:154–162

5. Bradley CR, Scott RA, Cox EF, et al (2020) Quantitaive MRI to assess portal hypertension in cirrhosis patients. Proc Intl Soc Mag Reson Med 28:0323.

6. Mozes F, Tunnicliffe E, Pavlides M et al (2016) Influence of fat on liver T_1 measurements using modified Look-Locker inversion recovery (MOLLI) methods at 3T. J Magn Reson Imaging 44(1):105-111.

7. Bradley CR, Cox EF, Scott RA et al (2018) Multi-organ assessment of compensated cirrhosis patients using quantitative magnetic resonance imaging. J hepatol 69(5):1015-1024. doi: 10.1016/j.jhep.2018.05.037

8. de Bazelaire, C. M. J., Duhamel, G. D., Rofsky et al (2004). MR Imaging Relaxation Times of Abdominal and Pelvic Tissues Measured in Vivo at 3.0 T: Preliminary Results1. Radiol 230(3):652–659. https://doi.org/10.1148/RADIOL.2303021331

Figures

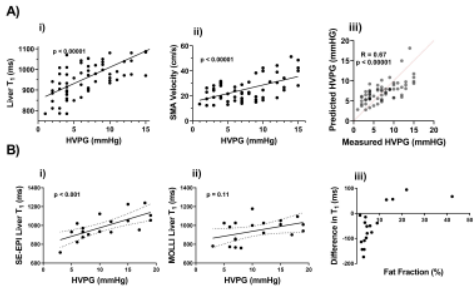

Figure 1. A The strong correlation between **i**) fat suppressed Spin Echo Echo Planar Imaging (SE-EPI) Liver T_1, **ii**) superior mesenteric artery (SMA) velocity and measured HVPG; **iii**) the combined multiple linear regression predictive model using Liver T_1 and SMA velocity to predict Hepatic Venous Pressure Gradient (HVPG).

B In a subset of patients, the comparison of **i**) SE-EPI T_1 and **ii**) MOLLI T_1 as a predictor of HVPG, and **iii**) the influence of fat on the measured MOLLI T_1 value.

Parameter	GE	Philips	Siemens
Sequence	2D Spin Echo EPI	SE-EPI	2d epi
Field of View (mm^2)	384 x 384	384 x 384	384 x 384
TE (ms)	28	28	25
TR (s)	10	10	10
Inversion Times (ms)	100, 200, 300, 400, 500, 600, 700, 800, 900, 1100, 1300, 1500	100, 200, 300, 400, 500, 600, 700, 800, 900, 1100, 1300, 1500	100, 200, 300, 400, 500, 600, 700, 800, 900, 1100, 1300, 1500
Breathing method	Trained breathing	Respiratory-triggered	Navigated
Fat Suppression	Chem sat: ASPIR	Fat suppression: SPIR	Fat suppression: SPIR
Acceleration	ASSET 2	SENSE 2	GRAPPA 2

Table 1. Image acquisition parameters for vendor-product single-slice fat suppressed

Spin Echo Echo Planar Imaging (SE-EPI) T_1 mapping sequences available on the GE, Philips and Siemens scanners.

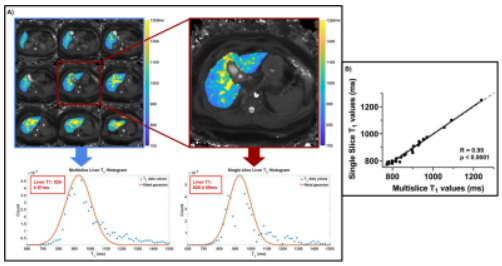

Figure 2. A) Example multi-slice liver T_1 map from a patient with portal hypertension showing the distribution of T_1 values from voxels within the liver, from which the mode of the histogram is computed for the prediction of hepatic venous pressure gradient. **B**) A strong correlation between the mode of the histogram computed from single slice and multislice T_1 maps ($R = 0.99$, $p < 0.0001$).

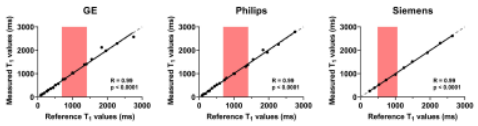

Figure 3. Comparison of NIST System phantom T_1 reference values and T_1 values measured using fat suppressed spin-echo echo planar imaging acquisition method. Grey dashed line represents the line of identity and the pink region covers the range of T_1 values expected in liver tissue across healthy subject and liver disease states.

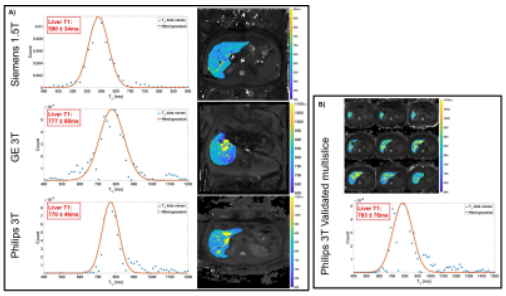

Figure 4. A Example T_1 maps created from T_1 data acquired using the vendor-product single slice fat suppressed spin-echo echo planar imaging(SE-EPI) commercially available sequences compared to the already Philips multi-slice fat suppressed SE-EPI T_1 mapping method which has previously been validated against HVPG (**B**).

10. Appendices

10.1 Appendix A: SPRINGER NATURE LICENSE: 5556390231892

SPRINGER NATURE LICENSE
TERMS AND CONDITIONS

May 26, 2023

This Agreement between Mr. Christopher Bradley ("You") and Springer Nature ("Springer Nature") consists of your license details and the terms and conditions provided by Springer Nature and Copyright Clearance Center.

License Number	5556390231892
License date	May 26, 2023
Licensed Content Publisher	Springer Nature
Licensed Content Publication	Digestive Diseases and Sciences
Licensed Content Title	Cirrhotic Multiorgan Syndrome
Licensed Content Author	Søren Møller et al
Licensed Content Date	Jun 26, 2015
Type of Use	Thesis/Dissertation
Requestor type	academic/university or research institute
Format	electronic
Portion	figures/tables/illustrations
Number of figures/tables/illustrations	1
Will you be translating?	no
Circulation/distribution	1 - 29

Author of this Springer Nature content	no
Title	Probing organ structure, function and physiology using Quantitative Magnetic Resonance Imaging techniques
Institution name	University of Nottingham
Expected presentation date	May 2023
Order reference number	1
Portions	Figure 4.
Requestor Location	Mr. Christopher Bradley 33 Mayfield Road Chaddesden Derby, DE21 6FX United Kingdom Attn: University of Nottingham
Total	0.00 GBP

Terms and Conditions

Springer Nature Customer Service Centre GmbH Terms and Conditions

The following terms and conditions ("Terms and Conditions") together with the terms specified in your [RightsLink] constitute the License ("License") between you as Licensee and Springer Nature Customer Service Centre GmbH as Licensor. By clicking 'accept' and completing the transaction for your use of the material ("Licensed Material"), you confirm your acceptance of and obligation to be bound by these Terms and Conditions.

1. Grant and Scope of License

1. 1. The Licensor grants you a personal, non-exclusive, non-transferable, non-sublicensable, revocable, world-wide License to reproduce, distribute, communicate to the public, make available, broadcast, electronically transmit or create derivative works using the Licensed Material for the purpose(s) specified in your RightsLink Licence Details only. Licenses are granted for the specific use requested in the order and for no other use, subject to these Terms and Conditions. You acknowledge and agree that the rights granted to you under this License do not include the right to modify, edit, translate, include in collective works, or create derivative works of the Licensed Material in whole or in part unless expressly stated in your RightsLink Licence Details. You may use the Licensed Material only as permitted under this Agreement and will not reproduce, distribute, display, perform, or otherwise use or

exploit any Licensed Material in any way, in whole or in part, except as expressly permitted by this License.

1. 2. You may only use the Licensed Content in the manner and to the extent permitted by these Terms and Conditions, by your RightsLink Licence Details and by any applicable laws.

1. 3. A separate license may be required for any additional use of the Licensed Material, e.g. where a license has been purchased for print use only, separate permission must be obtained for electronic re-use. Similarly, a License is only valid in the language selected and does not apply for editions in other languages unless additional translation rights have been granted separately in the License.

1. 4. Any content within the Licensed Material that is owned by third parties is expressly excluded from the License.

1. 5. Rights for additional reuses such as custom editions, computer/mobile applications, film or TV reuses and/or any other derivative rights requests require additional permission and may be subject to an additional fee. Please apply to journalpermissions@springernature.com or bookpermissions@springernature.com for these rights.

2. Reservation of Rights

Licensor reserves all rights not expressly granted to you under this License. You acknowledge and agree that nothing in this License limits or restricts Licensor's rights in or use of the Licensed Material in any way. Neither this License, nor any act, omission, or statement by Licensor or you, conveys any ownership right to you in any Licensed Material, or to any element or portion thereof. As between Licensor and you, Licensor owns and retains all right, title, and interest in and to the Licensed Material subject to the license granted in Section 1.1. Your permission to use the Licensed Material is expressly conditioned on you not impairing Licensor's or the applicable copyright owner's rights in the Licensed Material in any way.

3. Restrictions on use

3. 1. Minor editing privileges are allowed for adaptations for stylistic purposes or formatting purposes provided such alterations do not alter the original meaning or intention of the Licensed Material and the new figure(s) are still accurate and representative of the Licensed Material. Any other changes including but not limited to, cropping, adapting, and/or omitting material that affect the meaning, intention or moral rights of the author(s) are strictly prohibited.

3. 2. You must not use any Licensed Material as part of any design or trademark.

3. 3. Licensed Material may be used in Open Access Publications (OAP), but any such reuse must include a clear acknowledgment of this permission visible at the same time as the figures/tables/illustration or abstract and which must indicate that the Licensed Material is not part of the governing OA license but has been reproduced with permission. This may be indicated according to any standard referencing system but must include at a minimum 'Book/Journal title, Author, Journal Name (if applicable), Volume (if applicable), Publisher, Year, reproduced with permission from SNCSC'.

4. STM Permission Guidelines

4. 1. An alternative scope of license may apply to signatories of the STM Permissions Guidelines ("STM PG") as amended from time to time and made available at

https://www.stm-assoc.org/intellectual-property/permissions/permissions-guidelines/.

4. 2. For content reuse requests that qualify for permission under the STM PG, and which may be updated from time to time, the STM PG supersede the terms and conditions contained in this License.

4. 3. If a License has been granted under the STM PG, but the STM PG no longer apply at the time of publication, further permission must be sought from the Rightsholder. Contact journalpermissions@springernature.com or bookpermissions@springernature.com for these rights.

5. Duration of License

5. 1. Unless otherwise indicated on your License, a License is valid from the date of purchase ("License Date") until the end of the relevant period in the below table:

Reuse in a medical communications project	Reuse up to distribution or time period indicated in License
Reuse in a dissertation/thesis	Lifetime of thesis
Reuse in a journal/magazine	Lifetime of journal/magazine
Reuse in a book/textbook	Lifetime of edition
Reuse on a website	1 year unless otherwise specified in the License
Reuse in a presentation/slide kit/poster	Lifetime of presentation/slide kit/poster. Note: publication whether electronic or in print of presentation/slide kit/poster may require further permission.
Reuse in conference proceedings	Lifetime of conference proceedings
Reuse in an annual report	Lifetime of annual report
Reuse in training/CME materials	Reuse up to distribution or time period indicated in License
Reuse in newsmedia	Lifetime of newsmedia
Reuse in coursepack/classroom materials	Reuse up to distribution and/or time period indicated in license

6. Acknowledgement

6. 1. The Licensor's permission must be acknowledged next to the Licensed Material in print. In electronic form, this acknowledgement must be visible at the same time as the figures/tables/illustrations or abstract and must be hyperlinked to the journal/book's homepage.

6. 2. Acknowledgement may be provided according to any standard referencing system and at a minimum should include "Author, Article/Book Title, Journal name/Book imprint, volume, page number, year, Springer Nature".

7. Reuse in a dissertation or thesis

7. 1. Where 'reuse in a dissertation/thesis' has been selected, the following terms apply: Print rights of the Version of Record are provided for; electronic rights for use only on institutional repository as defined by the Sherpa guideline (www.sherpa.ac.uk/romeo/) and only up to what is required by the awarding institution.

7. 2. For theses published under an ISBN or ISSN, separate permission is required. Please contact journalpermissions@springernature.com or bookpermissions@springernature.com for these rights.

7. 3. Authors must properly cite the published manuscript in their thesis according to current citation standards and include the following acknowledgement: '*Reproduced with permission from Springer Nature*'.

8. License Fee

You must pay the fee set forth in the License Agreement (the "License Fees"). All amounts payable by you under this License are exclusive of any sales, use, withholding, value added or similar taxes, government fees or levies or other assessments. Collection and/or remittance of such taxes to the relevant tax authority shall be the responsibility of the party who has the legal obligation to do so.

9. Warranty

9. 1. The Licensor warrants that it has, to the best of its knowledge, the rights to license reuse of the Licensed Material. **You are solely responsible for ensuring that the material you wish to license is original to the Licensor and does not carry the copyright of another entity or third party (as credited in the published version).** If the credit line on any part of the Licensed Material indicates that it was reprinted or adapted with permission from another source, then you should seek additional permission from that source to reuse the material.

9. 2. EXCEPT FOR THE EXPRESS WARRANTY STATED HEREIN AND TO THE EXTENT PERMITTED BY APPLICABLE LAW, LICENSOR PROVIDES THE LICENSED MATERIAL "AS IS" AND MAKES NO OTHER REPRESENTATION OR WARRANTY. LICENSOR EXPRESSLY DISCLAIMS ANY LIABILITY FOR ANY CLAIM ARISING FROM OR OUT OF THE CONTENT, INCLUDING BUT NOT LIMITED TO ANY ERRORS, INACCURACIES, OMISSIONS, OR DEFECTS CONTAINED THEREIN, AND ANY IMPLIED OR EXPRESS WARRANTY AS TO MERCHANTABILITY OR FITNESS FOR A PARTICULAR PURPOSE. IN NO EVENT SHALL LICENSOR BE LIABLE TO YOU OR ANY OTHER PARTY OR ANY OTHER PERSON OR FOR ANY SPECIAL, CONSEQUENTIAL, INCIDENTAL, INDIRECT, PUNITIVE, OR EXEMPLARY DAMAGES, HOWEVER CAUSED, ARISING OUT OF OR IN CONNECTION WITH THE DOWNLOADING, VIEWING OR USE OF THE LICENSED MATERIAL REGARDLESS OF THE FORM OF ACTION, WHETHER FOR BREACH OF CONTRACT, BREACH OF WARRANTY, TORT, NEGLIGENCE, INFRINGEMENT OR OTHERWISE (INCLUDING, WITHOUT LIMITATION, DAMAGES BASED ON LOSS OF PROFITS, DATA, FILES, USE, BUSINESS OPPORTUNITY OR CLAIMS OF THIRD PARTIES), AND WHETHER OR NOT THE PARTY HAS BEEN ADVISED OF THE POSSIBILITY OF SUCH DAMAGES. THIS LIMITATION APPLIES NOTWITHSTANDING ANY FAILURE OF ESSENTIAL PURPOSE OF ANY LIMITED REMEDY PROVIDED HEREIN.

10. Termination and Cancellation

10. 1. The License and all rights granted hereunder will continue until the end of the applicable period shown in Clause 5.1 above. Thereafter, this license will be terminated and all rights granted hereunder will cease.

10. 2. Licensor reserves the right to terminate the License in the event that payment is not received in full or if you breach the terms of this License.

11. General

11. 1. The License and the rights and obligations of the parties hereto shall be construed, interpreted and determined in accordance with the laws of the Federal Republic of Germany without reference to the stipulations of the CISG (United Nations Convention on Contracts for the International Sale of Goods) or to Germany´s choice-of-law principle.

11. 2. The parties acknowledge and agree that any controversies and disputes arising out of this License shall be decided exclusively by the courts of or having jurisdiction for Heidelberg, Germany, as far as legally permissible.

11. 3. This License is solely for Licensor's and Licensee's benefit. It is not for the benefit of any other person or entity.

Questions? For questions on Copyright Clearance Center accounts or website issues please contact springernaturesupport@copyright.com or +1-855-239-3415 (toll free in the US) or +1-978-646-2777. For questions on Springer Nature licensing please visit https://www.springernature.com/gp/partners/rights-permissions-third-party-distribution

Other Conditions:

Version 1.4 - Dec 2022

Questions? customercare@copyright.com.

10.2 Appendix B: BMJ PUBLISHING GROUP LTD. LICENSE: 5556390707034

BMJ PUBLISHING GROUP LTD. LICENSE
TERMS AND CONDITIONS

May 26, 2023

This Agreement between Mr. Christopher Bradley ("You") and BMJ Publishing Group Ltd. ("BMJ Publishing Group Ltd.") consists of your license details and the terms and conditions provided by BMJ Publishing Group Ltd. and Copyright Clearance Center.

License Number	5556390707034
License date	May 26, 2023
Licensed Content Publisher	BMJ Publishing Group Ltd.
Licensed Content Publication	Gut
Licensed Content Title	The window hypothesis: haemodynamic and non-haemodynamic effects of β-blockers improve survival of patients with cirrhosis during a window in the disease
Licensed Content Author	Aleksander Krag,Reiner Wiest,Agustín Albillos,Lise Lotte Gluud
Licensed Content Date	Jul 1, 2012
Licensed Content Volume	61
Licensed Content Issue	7
Type of Use	Dissertation/Thesis
Requestor type	Individual
Format	Electronic

Portion	Figure/table/extract
Number of figure/table/extracts	1
Descriptionof figure/table/extracts	Figure 1
Will you be translating?	No
Circulation/distribution	10
Order reference number	2
Title	Probing organ structure, function and physiology using Quantitative Magnetic Resonance Imaging techniques
Institution name	University of Nottingham
Expected presentation date	May 2023
Order reference number	2
Portions	Figure 1
Requestor Location	Mr. Christopher Bradley 33 Mayfield Road Chaddesden Derby, DE21 6FX United Kingdom Attn: University of Nottingham
Publisher Tax ID	GB674738491
Total	0.00 GBP

Terms and Conditions

BMJ Terms and Conditions for Permissions

When you submit your order you are subject to the terms and conditions set out below. You will also have agreed to the Copyright Clearance Center's ("CCC") terms and conditions regarding billing and payment https://s100.copyright.com/App/PaymentTermsAndConditions.jsp. CCC are acting as BMJ Publishing Group Limited's ("BMJs") agent.

Subject to the terms set out herein, BMJ hereby grants to you (the Licensee) a non-exclusive, non-transferable licence to re-use material as detailed in your request for this/those purpose(s) only and in accordance with the following conditions:

1) **Scope of Licence:** Use of the Licensed Material(s) is restricted to the ways specified by you during the order process and any additional use(s) outside of those specified in that request, require a further grant of permission.

2) **Acknowledgement:** In all cases, due acknowledgement to the original publication with permission from BMJ should be stated adjacent to the reproduced Licensed Material. The format of such acknowledgement should read as follows:
"Reproduced from [publication title, author(s), volume number, page numbers, copyright notice year] with permission from BMJ Publishing Group Ltd."

3) **Third Party Material**: BMJ acknowledges to the best of its knowledge, it has the rights to licence your reuse of the Licensed Material, subject always to the caveat that images/diagrams, tables and other illustrative material included within, which have a separate copyright notice, are presumed as excluded from the licence. Therefore, you should ensure that the Licensed Material you are requesting is original to BMJ and does not carry the copyright of another entity (as credited in the published version). If the credit line on any part of the material you have requested in any way indicates that it was reprinted or adapted by BMJ with permission from another source, then you should seek permission from that source directly to re-use the Licensed Material, as this is outside of the licence granted herein.

4) **Altering/Modifying Material:** The text of any material for which a licence is granted may not be altered in any way without the prior express permission of BMJ. If adaptation of the material has been approved via bmj.permissions@bmj.com you must include the disclaimer: "Adapted by permission from BMJ Publishing Group Limited. [publication title, author, volume number, page numbers, copyright notice year]

5) **Reservation of Rights:** BMJ reserves all rights not specifically granted in the combination of (i) the licence details provided by you and accepted in the course of this licensing transaction, (ii) these terms and conditions and (iii) CCC's Billing and Payment Terms and Conditions.

6) **Timing of Use:** First use of the Licensed Material must take place within 12 months of the grant of permission.

7) **Creation of Contract and Termination:** Once you have submitted an order via RightsLink and this is received by CCC, and subject to you completing accurate details of your proposed use, this is when a binding contract is in effect and our acceptance occurs. As you are ordering rights from a periodical, to the fullest extent permitted by law, you will have no right to cancel the contract from this point other than for BMJ's material breach or fraudulent misrepresentation or as otherwise permitted under a statutory right. Payment must be made in accordance with CCC's Billing and Payment Terms and conditions. In the event that you breach any material condition of these terms and condition or any of CCC's Billing and Payment Terms and Conditions, the license is automatically terminated upon written notice from BMJ or CCC or as otherwise provided for in CCC's Billing and Payment Terms and Conditions, where these apply. Continued use of materials where a licence has been terminated, as well as any use of the Licensed Materials beyond the scope of an unrevoked

licence, may constitute intellectual property rights infringement and BMJ reserves the right to take any and all action to protect its intellectual property rights in the Licensed Materials.

8) **Warranties:** BMJ makes no express or implied representations or warranties with respect to the Licensed Material and to the fullest extent permitted by law this is provided on an "as is" basis. For the avoidance of doubt BMJ does not warrant that the Licensed Material is accurate or fit for any particular purpose.

9) **Limitation of Liability:** To the fullest extent permitted by law, BMJ disclaims all liability for any indirect, consequential or incidental damages (including without limitation, damages for loss of profits, information or interruption) arising out of the use or inability to use the Licensed Material or the inability to obtain additional rights to use the Licensed Material. To the fullest extent permitted by law, the maximum aggregate liability of BMJ for any claims, costs, proceedings and demands for direct losses caused by BMJ's breaches of its obligations herein shall be limited to twice the amount paid by you to CCC for the licence granted herein.

10) **Indemnity:** You hereby indemnify and hold harmless BMJ and their respective officers, directors, employees and agents, from and against any and all claims, costs, proceeding or demands arising out of your unauthorised use of the Licensed Material.

11) **No Transfer of License:** This licence is personal to you, and may not be assigned or transferred by you without prior written consent from BMJ or its authorised agent(s). BMJ may assign or transfer any of its rights and obligations under this Agreement, upon written notice to you.

12) **No Amendment Except in Writing:** This licence may not be amended except in a writing signed by both parties (or, in the case of BMJ, by CCC on BMJ's behalf).

13) **Objection to Contrary terms:** BMJ hereby objects to any terms contained in any purchase order, acknowledgment, check endorsement or other writing prepared by you, which terms are inconsistent with these terms and conditions or CCC's Billing and Payment Terms and Conditions. These terms and conditions, together with CCC's Billing and Payment Terms and Conditions (which to the extent they are consistent are incorporated herein), comprise the entire agreement between you and BMJ (and CCC) and the Licensee concerning this licensing transaction. In the event of any conflict between your obligations established by these terms and conditions and those established by CCC's Billing and Payment Terms and Conditions, these terms and conditions shall control.

14) **Revocation:** BMJ or CCC may, within 30 days of issuance of this licence, deny the permissions described in this licence at their sole discretion, for any reason or no reason, with a full refund payable to you should you have not been able to exercise your rights in full. Notice of such denial will be made using the contact information provided by you. Failure to receive such notice from BMJ or CCC will not, to the fullest extent permitted by law alter or invalidate the denial. For the fullest extent permitted by law in no event will BMJ or CCC be responsible or liable for any costs, expenses or damage incurred by you as a result of a denial of your permission request, other than a refund of the amount(s) paid by you to BMJ and/or CCC for denied permissions.

15) **Restrictions to the license**:

15.1) **Promotion:** BMJ will not give permission to reproduce in full or in part any Licensed Material for use in the promotion of the following:

a) non-medical products that are harmful or potentially harmful to health

b) medical products that do not have a product license granted by the Medicines and Healthcare products Regulatory Agency (MHRA) or its international equivalents. Marketing of the product may start only after data sheets have been released to members of the medical profession and must conform to the marketing authorization contained in the product license.

16) **Translation**: This permission is granted for non-exclusive world English language rights only unless explicitly stated in your licence. If translation rights are granted, a professional translator should be employed and it must be a true reproduction, accurately conveying the original meaning and of the same quality.

17) **STM Permissions Guidelines**: For content reuse in journals that qualify for permission under the STM Permissions Guidelines (which may be updated from time to time) the terms and conditions of the Guidelines supersede those in this licence. https://www.stm-assoc.org/intellectual-property/permissions/permissions-guidelines/

18) **General:** Neither party shall be liable for failure, default or delay in performing its obligations under this Licence, caused by a Force Majeure event which shall include any act of God, war, or threatened war, act or threatened act of terrorism, riot, strike, lockout, individual action, fire, flood, drought, tempest or other event beyond the reasonable control of either party.

18.1) In the event that any provision of this Agreement is held to be invalid, the remainder of the provisions shall continue in full force and effect.

18.2) There shall be no right whatsoever for any third party to enforce the terms and conditions of this Agreement. The Parties hereby expressly wish to exclude the operation of the Contracts (Rights of Third Parties) Act 1999 and any other legislation which has this effect and is binding on this agreement.

18.3) To the fullest extent permitted by law, this Licence will be governed by the laws of England and shall be governed and construed in accordance with the laws of England. Any action arising out of or relating to this agreement shall be brought in courts situated in England save where it is necessary for BMJ for enforcement to bring proceedings to bring an action in an alternative jurisdiction.

V1.1

Questions? customercare@copyright.com.

10.3 Appendix C: Adobe Stock Additional Terms and License Agreement

Adobe Stock Additional Terms

Last updated December 5, 2022. Replaces all prior versions.

These Additional Terms govern your use of the Adobe Stock Services and the Stock Assets (as defined below) and are incorporated into the Adobe General Terms of Use (**"General Terms"**) located at www.adobe.com/go/terms (these Additional Terms and the General Terms are collectively referred to as **"Terms"**). All rights and licenses granted to you under these Adobe Stock Additional Terms are subject to your compliance with the Terms. Capitalized terms not defined here have the same meaning as defined in the General Terms.

1. **Definitions**

1.1. "**Audio Work(s)**" means the audio tracks (including all sound recordings, musical compositions, and any other recordings containing sounds or a series of sounds, embodied therein) that are designated as Adobe Stock assets on any Websites, except that "Audio Work" does not include any audio that may be in a Work.

1.2. "**Editorial Work(s)"** means any Stock Assets designed as "editorial use only" on the Website(s).

1.3. "**Audio Project**" means a specific project created by you that combines an Audio Work with images, video, narration, or other materials as permitted in the Terms.

1.4. "**Stock Asset(s)**" means one or both of Audio Work(s) and Work(s).

1.5. "**Website(s)**" means Adobe Stock Services available at www.stock.adobe.com (or successor URL), or other Adobe websites or applications that make available Stock Assets for license.

1.6. **"Work(s)"** means the Pro Images (as defined below) as well as the photographs, illustrations, images, vectors, videos, 3D assets, template assets, and other pictorial or graphic works designated as Adobe Stock assets on any Websites, and for clarity, does not mean any Audio Work(s).

2. **Ownership.** Except as expressly granted in the Terms, we and our licensors retain all rights, title, and interest in and to the Stock Assets. No title or ownership interest in or to the Stock Assets is transferred to you by virtue of the Terms.

3. **License Terms and Specific Restrictions Applicable to Works**

3.1. **Standard License and Specific Restrictions for Works.** The license described in this section 3.1 is referred to as a "**Standard License**".

(A) **Standard License for Works.** Under a Standard License, we grant you a non-exclusive, perpetual, worldwide, non-transferable and non-sublicensable (except pursuant to section 6 (Additional Rights)) license to use, reproduce, archive, modify, and display the Work, in all media, for (1) advertising, marketing, promotional and decoration purposes; and (2) personal and non-commercial uses, up to 500,000 times as further described in section 3.1(B) (**"Standard License Specific Restrictions"**).

(B) **Standard License Specific Restrictions for Works.** In addition to the restrictions in section 7 (Restrictions), the following restrictions apply to any Work under a Standard License:

(1) you may not, in the aggregate, (a) cause or allow a Work to appear on more than 500,000 printed materials (including copies of such materials); or (b) incorporate a Work into a live, recorded, or digital production if the audience is expected to exceed 500,000 viewers, except the restriction on audience size does not apply to Works displayed only on websites, social media sites, or mobile applications;

(2) you may not incorporate a Work into merchandise intended for sale or distribution, including on-demand products, unless (a) the Work has been modified to the extent that the new work, as incorporated into such merchandise, is not substantially similar to the Work and can qualify as an original work of authorship; or (b) the primary value of such merchandise does not lie with the Work itself;

(3) you may not use, include, or incorporate the Work in any electronic template or design template application (e.g., a web design or presentation template, or templates for electronic greeting cards or business cards); and

(4) you may not use, reproduce, distribute, or display the Work with a press release that includes the distribution of the stand-alone image file.

3.2. **Enhanced License and Specific Restrictions for Works.** The license described in this section 3.2 is referred to as an "**Enhanced License**".

(A) **Enhanced License for Works.** Under an Enhanced License, we grant you the same rights as under a Standard License, except without the limitation on the number of reproductions or viewers set forth in section (1) of 3.1(B) (Standard License Specific Restrictions for Works).

(B) **Enhanced License Specific Restrictions for Works.** The restrictions in sections 3.1(B)(2) through 3.1(B)(4) (Standard License Specific Restrictions for Works), and in section 7 (Restrictions) apply to any Work under an Enhanced License.

3.3. **Extended License and Specific Restrictions for Works.** The license described in this section 3.3 is referred to as an "**Extended License**".

(A) **Extended License for Works.** Under an Extended License, we grant you the same rights as under an Enhanced License, in addition to the right to use, reproduce, distribute, and display the Work:

(1) for incorporation into merchandise and template files intended for sale or distribution, without limitation on the number of reproductions or viewers, provided the recipient is only permitted to use or access the Work as incorporated into the merchandise or template; and

(2) in a press release that includes distribution of the stand-alone image file to the media, provided the Work is only published in connection with the press release, and not used or disseminated in any other manner.

For clarity, and without limitation, you may use the Work in connection with (a) electronic templates and design template applications; (b) merchandise such as mugs, t-shirts, posters, and greeting cards; and (c) "print on demand" services.

(B) **Extended License Restrictions for Works.** The restrictions in section 7 (Restrictions) apply to any Work under an Extended License.

4. **License Terms and Specific Restrictions Applicable to Audio Works.** If there is a conflict between this section 4 and any other section of the Terms, this section 4 controls with respect to Audio Works only.

4.1. **Audio Standard License and Specific Restrictions**. The license described in this section 4.1 is referred to as an "**Audio Standard License**".

(A) **Audio Standard License**. Under an Audio Standard License, we grant you a non-exclusive, perpetual, worldwide, non-transferable (except pursuant to section 6 (Additional Rights)), non-sublicensable (except as to 4.1(A)(3) below) license to:

(1) synchronize and otherwise combine the Audio Work with video, audio, and other materials, to create an unlimited number of Audio Projects;

(2) adapt, edit, and modify the Audio Work in Audio Projects (including converting the file format, pitch-shifting, time compression, cutting, and trimming);

(3) reproduce, copy, transmit, broadcast, display, publicly perform, and otherwise distribute the Audio Work as incorporated into an Audio Project (except as specified in 4.2(A) (Audio Extended License)); and

(4) subject to any and all applicable restrictions, use Audio Projects for any purpose, including advertising, marketing, promotional, and commercial.

(B) **Audio Standard License Specific Restrictions**. In addition to the restrictions in section 4.3 (Audio Work Restrictions) and section 7.1 (General Restrictions), you may not use an Audio Work in any Audio Project as specified in sections 4.2(A)(1)-(7) (Audio Extended License) without first obtaining an Audio Extended License.

4.2. **Audio Extended License and Restrictions**. The license described in this section 4.2 is referred to as an "**Audio Extended License**".

(A) **Audio Extended License**. Under an Audio Extended License, we grant you the same rights as under an **Audio** Standard License, in addition to the right to reproduce, copy, transmit, broadcast, display, publicly perform, or otherwise distribute Audio Projects in:

(1) radio;

(2) television;

(3) paid-access streaming video services;

(4) paid-access on-demand video services;

(5) theatrical releases;

(6) computer software applications (including mobile applications and video games); and

(7) physical point of sale locations (such as shopping malls, point of sale systems, in-store displays, and showroom videos).

(B) **Audio Extended License Restrictions.** The restrictions in section 4.3 (Audio Works Restrictions) and section 7.1 (General Restrictions) apply to any Audio Work under an Audio Extended License.

4.3. **Audio Work Restrictions.** In addition to the restrictions in section 7.1 (General Restrictions) and any restrictions specific to a license type, you must not:

(A) use any Audio Work in a way that alters its fundamental character, such as to create remixes or mashups; make any other alterations for the purpose of creating new music; or otherwise alter the Audio Work except as expressly provided in section (1) of 4.1(A) (Audio Standard License);

(B) use any Audio Work as a theme song in an Audio Project specified in sections 4.2(A)(1)-(7) (Audio Extended License);
(C) incorporate any Audio Work into any electronic template or design template application (e.g., a web design or presentation template, or templates for electronic greeting cards or business cards);

(D) offer any Audio Work on a stand-alone basis or as a listening-only experience, such as a track on an album; or

(E) upload or make available any Audio Work as combined solely with a still image or simple one-shot video on a streaming platform (e.g. creating a playlist by using an Audio Work in combination with a visual element, where the visual element adds little to no value).

5. **Comp License for Stock Assets.** The license described in this section 5 is referred to as a "**Comp License**".
5.1. A Comp License version of a Stock Asset is downloaded as either a watermarked Work or an Audio Work that is a compressed AAC file with a .m4a file extension, unless otherwise indicated on the Website.

5.2. For up to 90 days from the date of download of a Stock Asset, you may use, reproduce, modify, adapt or display "comp" (i.e. composite, or preview) versions of that Stock Asset solely for previewing how the Stock Asset may look or sound in production or an Audio Project. For clarity, under a Comp License, you are not permitted to use a Stock Asset in a final production or Audio Project, or to make a Stock Asset publicly available in any manner.

5.3. There is no guarantee that any Stock Asset you download under a Comp License will be available for license thereafter. Any use of a Stock Asset under a Comp License is on an "AS IS" basis with no representation, warranties, or indemnities of any kind.

6. **Additional Rights.** Subject to the Terms and any applicable restrictions, you may have the following additional rights:

(A) **Employer Use.** You may license a Stock Asset for the benefit of your employer ("**Employer Assets**"), in which case you:

(1) represent and warrant that you have full legal authority to bind your employer to these Terms;

(2) are solely responsible and liable for use of the Employer Assets; and

(3) must obtain additional licenses for any Employer Asset(s) you intend to use for yourself.

(B) **Client Use**. You may license and use a Stock Asset in combination with other content or materials as part of a project for the benefit of a client ("**Client Project**"), provided that you purchase new licenses for any additional use of that Stock Asset by you on your own behalf or for the benefit of any other client. In connection with a Client Project, you may permit your client to use the Stock Asset under enforceable written terms no less restrictive than this Agreement. Notwithstanding the foregoing, you must not (A) resell licenses to Stock Assets or (B) use a Pro Image in a Client Project.

(C) **Employee and Contractor Use**. You may share Stock Assets with employees or subcontractors, provided that:

(1) such employees and subcontractors agree in an enforceable written agreement to abide by the restrictions in the Terms;

(2) such employees and subcontractors only use the Stock Asset on your behalf; and

(3) you are solely responsible and liable for use of the Stock Asset by your employee or contractor.

(D) **Social Media Use**. You may use a Stock Asset on ~~a~~ third-party social media platforms or websites in accordance with the applicable third-party user agreement, provided that doing so does not exceed the scope of the license granted to you hereunder.

7. **Restrictions.**

7.1. **General Restrictions.** You must not:

(A) use the Stock Assets in any way that allows a third party to use, download, extract or access the Stock Assets (1) as a stand-alone file; or (2) in a way that exceeds the scope of the license to the Stock Assets;

(B) use the Stock Assets with material that violates any third-party rights, or otherwise take any action in connection with the Stock Assets that infringes the intellectual property or other rights of any person or entity,

such as the moral rights of the creator of the Stock Assets or the rights of any person who, or any person whose property, appears in or is associated with the Stock Assets;

(C) register, or apply to register, a trademark, design mark, service mark, sound mark, or tradename, that uses any Stock Asset (in whole or in part); or claim ownership rights in an attempt to prevent any third party from using a Stock Asset;

(D) use the Stock Assets in a manner that is pornographic or defamatory, or that violates any applicable laws, rules, or regulations;

(E) use the Stock Assets in a manner, or in connection with a subject, that a reasonable person could consider unflattering, immoral, offensive, obscene, or controversial, taking into account the nature of the Stock Assets, examples of which could include ads for tobacco; adult entertainment clubs or similar venues or services; implied or stated endorsements of political parties or other opinion-based movements; or implying mental or physical impairment;

(F) use the Stock Assets contrary to any additional restrictions displayed on the Website in the details panel of such Stock Assets;

(G) remove, obscure or alter any proprietary notices associated with the Stock Assets, or give any express or implied misrepresentation that you or another third party are the creator or holder of Intellectual Property Rights in any Stock Assets;

(H) use (or allow third parties to use) the Adobe Stock Services (or any content, data, output, or other information received or derived from the Adobe Stock Services, such as Stock Assets): (1) to directly or indirectly create, train, test, or otherwise improve any machine learning algorithms or artificial intelligence systems, including any architectures, models, or weights; or (2) with technologies designed or intended for the identification of natural persons;

(I) access Stock Assets filtered out by safe search unless you are over 18 and live in a country where adult content is legal; or

(J) use or exploit the Stock Assets in any manner other than as expressly provided in these Terms.

7.2. **Editorial Works Restrictions.** For Editorial Work(s):

(A) you may only use these Editorial Works (1) in a manner that maintains the editorial context and meaning of the Editorial Works; (2) in relation to events or topics that are newsworthy or of general interest to the public; and (3) in compliance with any additional third-party licensor restrictions displayed on the Website in the details panel of such Editorial Works;

(B) you must not (1) use these Editorial Works for any commercial (e.g., promotional, endorsement, advertorial or merchandising) purpose including use in connection with any non-fungible tokens (NFTs) or similar technology for the sale of digital assets; or (2) modify these Editorial Works, except for minor adjustments for technical quality or slight cropping or resizing; and

(C) to use editorial Editorial Works for a commercial purpose, you must first (1) obtain a license directly from the copyright owner of the Editorial Works; and (2) secure additional permissions as necessary.

8. **Attribution**

8.1. for Editorial Works or if a Stock Asset is used in an editorial manner, then a credit line must be placed in a way that is reasonable to the applicable use, in this format: “[Contributor Name]/stock.adobe.com” or as designated on the Website;

8.2. if the Stock Asset is used in an audiovisual production, you must use commercially reasonable efforts to include attribution for Adobe Stock in accordance with industry standards, and where possible in the following format: (1) For Works: [Contributor Name]/stock.adobe.com; and (2) For Audio Works: "["Song Title”] performed by [Artist's Name]/stock,adobe.com"; and

8.3. if attribution is not already provided and a Stock Asset is used in a context where any other stock content provider receives attribution, you also must include substantially similar attribution for Adobe Stock.

9. **Special Terms for Subscription Users, Business Users, VIP, and Teams**

9.1. **Subscription User Account**. You may not transfer your subscription or allow others to use your subscription, even if they are your affiliates, colleagues, contractors, or employees. However, you may license Stock Assets multiple times through the subscription.

9.2. **Business Users.** If a Business User obtains a license to any Stock Asset, such license is granted to the Business, whether such license was obtained before or after the date the Terms were last updated. The Business User’s use of any Stock Assets is governed by the Business’s agreement with us. A Stock Asset licensed by a Business may be used only by Business Users from a single legal entity and may not be used by affiliates. For clarity, the foregoing restriction applies to Stock Assets licensed pursuant to Pro Edition Plans (as defined below) and Adobe Stock credits purchased via Adobe’s VIP program.

9.3. **Adobe Stock Credits in VIP.** If you purchase Adobe Stock credits via Adobe’s VIP program, then (A) credit purchases are not refundable; and (B) unused credits automatically expire 12 months from the date of purchase.

9.4. **Special Terms for Pro Edition Plans**. The terms of this section 9.4 apply only to Pro Images that are licensed as part of a Pro Edition Plan by a Teams Customer or an Enterprise VIP Customer. If there is a conflict between this section 9.4 and any other section of the Terms, this section 9.4 controls with respect to Pro Images only.

(A) **Definitions.**

(1) “**Pro Edition Plan**” means any Creative Cloud plan that: (a) includes “Pro Edition” in the name; (b) is available to Teams Customers and Enterprise VIP Customers; and (c) includes the right to download and license an unlimited number of Pro Images.

(2) “**Grace Period**” means the 30 days immediately following the termination or expiration of your Pro Edition Plan.

(3) “**Pro Image(s)**” means, as part of a Pro Edition Plan, (A) only those photographs, illustrations, and vectors designated by Adobe as “standard” Works that Customer may license as part of a Pro Edition Plan; and (B) any other asset types listed in the Stock Product Description (available at https://helpx.adobe.com/legal/product-descriptions/stock.html or successor URL) as being available to you for license as part of a Pro Edition Plan. For clarity, an asset type is not a “Pro Image” unless expressly listed in this definition.

(4) “**Teams Customer(s)**” means Creative Cloud for teams customers that have purchased a Pro Edition Plan for teams, including via VIP.

(5) “**Enterprise VIP Customer(s)**” means Creative Cloud for enterprise customers that have purchased a Pro Edition Plan for enterprise via VIP.

(B) **License for Pro Images.** Pro Images are licensed to (1) Teams Customers under an Enhanced License; and (2) Enterprise VIP Customers under an Extended License.

(C) **Limitations on License for Pro Images.**

(1) The license to Pro Images set forth in this section 9.4 is perpetual for those specific uses of the Pro Images you have used during the term of your Pro Edition Plan, including any extensions or renewals, as well as the Grace Period.

(2) Only users licensed for a Pro Edition Plan may use the Adobe Stock APIs (as defined in the Adobe Developer Additional Terms) to access Pro Images.

(3) You agree not to stockpile Pro Images or otherwise abuse access to Pro Edition Plan.

(D) **Effect of Termination or Expiration of Pro Edition Plan.** You will have a Grace Period to make use of any Pro Images downloaded and paid for prior to the termination or expiration of your Pro Edition Plan, and any such Pro Images used in a project or other end use prior to the end of the Grace Period remain subject to the Terms. Any Pro Images downloaded and paid for, but not so used before the end of the Grace Period, are not considered licensed. For clarity, you may not download Pro Images during the Grace Period. Other than during the Grace Period, you may not use a Pro Image for the first time, or in a new context (such as on new or different merchandise), after the termination or expiration of your Pro Edition Plan. By way of example, if, prior to such termination or expiration, you printed a promotional brochure with a Pro Image on it, you may continue to produce that brochure in perpetuity, but after the end of the Grace Period, you may not use that same Pro Image in a different brochure, project or other end use.

10. **Our Indemnification Obligations.**

10.1. **Our Duty to Indemnify.** Provided that an Indemnified Stock Asset is used in accordance with the Terms, and subject to section 10.2 (Conditions to Indemnification), we will defend any third-party claim, action, or legal proceeding made against a person or entity during the term of the Terms that alleges that your use of the Indemnified Stock Asset directly infringes the third party's copyright, trademark, publicity rights, or privacy rights ("**Infringement Claim**"). We will pay you the damages, losses, costs, expenses, or liabilities directly attributable to an Infringement Claim and which are either finally awarded by a court of competent jurisdiction against you or agreed to in a written settlement agreement signed by us. "**Indemnified Stock Asset**" means a Stock Asset (excluding Editorial Works) that you have downloaded and paid for.

10.2. **Conditions to Indemnification.** We will have no liability for any Infringement Claim:

(A) that arises from: (1) any modification of a Stock Asset; (2) any combination of a Stock Asset with any other materials or information; (3) any use of a Stock Asset after we have instructed you to stop using the Stock Asset; (4) any use under a Comp License; or (5) the context in which the Stock Asset is used; or

(B) if you fail to: (1) notify us in writing of the Infringement Claim promptly upon the earlier of learning or receiving notice of it, to the extent we are prejudiced by this failure; (2) provide us with reasonable assistance as requested for the defense or settlement of the Infringement Claim; (3) provide us with the exclusive right to control, and the authority to settle, the Infringement Claim; or (4) refrain from making admissions about the Infringement Claim without our prior written consent.

10.3. **Limitation of Liability. Notwithstanding anything to the contrary contained in the Terms or in any other agreement between you and us, irrespective of the number of times the Stock Asset is downloaded or licensed, our total maximum aggregate liability with respect to any Stock Asset will in no event exceed US$10,000 per Stock Asset. Notwithstanding any otherwise applicable statute(s) of limitation, any action or dispute resolution**

proceeding must be commenced within two years of the act, event, or occurrence giving rise to the claim.

10.4. **Sole and Exclusive Remedy**. The foregoing states our entire liability and obligation, and your sole and exclusive remedy, with respect to any Stock Asset or Infringement Claim.

11. **Your Indemnification Obligations**. Without limiting the obligations in the General Terms, you will indemnify us and our subsidiaries, affiliates, officers, agents, employees, partners, and licensors from any claim, demand, loss, or damages, including reasonable attorneys' fees, arising out of or related to your use of the Stock Assets (except as indemnified under section 10 (Our Indemnification Obligations)) or your violation of the Terms.

12. **Disclaimers**. We are not responsible, and expressly disclaim any liability, for:

(A) any use of Comp Licenses;

(B) the accuracy of any Stock Asset, including any related descriptions, categories, captions, titles, metadata, or keywords included with any Stock Asset; and

(C) feedback, materials, or answers to questions provided to you by us or our representatives, whether about these Terms, your use or proposed use of a Stock Asset, or otherwise, all of which are provided as a courtesy only and do not constitute legal advice.

13. **Reservation.**

13.1. If you have actual knowledge, or if you reasonably believe, that a Stock Asset may be subject to a third-party claim, then you must promptly notify Adobe in writing. If Adobe reasonably believes that a Stock Asset may be subject to a third-party claim, then Adobe may instruct you to cease all use, reproduction, modification, display, performance, distribution, and possession of such Stock Asset, in which case you must (1) promptly comply with such instructions; and (2) ensure your clients, distributors, employees, and employers, as applicable, also stop using the Stock Asset.

13.2. We may, at any time (1) discontinue the licensing of any Stock Asset; and (2) deny the downloading of any Stock Asset.

14. **Effect of Termination.**

14.1. If your subscription ends, or upon termination of these Additional Terms, then:

(A) you will forfeit all rights, title and interest in and to any and all unused credits or unused standard assets from a subscription plan, as applicable;

(B) except as set forth in section 9.4(D) (Effect of Termination of Pro Edition Plan), any perpetual licenses granted as to Stock Assets will survive and you may continue to use those licensed Stock Assets;

(C) you should download any Stock Assets that you have licensed, as such licensed Stock Assets may not be available after termination or expiration; and

(D) you should make note of any license validation codes issued upon license of an Audio Work, as such license validation codes may not be available after termination or expiration.

14.2. If we terminate your right to use any Stock Asset(s) due to your breach of the Terms, you must cease all use, reproduction, modification, display, performance, distribution, and possession of any such Stock Asset(s).

15. **Injunctive Relief.** In the event of your or others' unauthorized access to, or use of, the Stock Assets in violation of these Terms, you agree that we are entitled to apply for injunctive remedies (or an equivalent type of urgent legal relief) in any jurisdiction, without providing notice or opportunity to cure.

Adobe_Stock_Terms-en_US-20221205

10.4 Appendix D: British Journal of Radiology License: 1358961-1

Marketplace

Order Date	26-May-2023	Type of Use	Republish in a thesis/dissertation
Order License ID	1358961-1		
ISSN	0007-1285	Publisher	BRITISH INSTITUTE OF RADIOLOGY,
		Portion	Image/photo/illustration

LICENSED CONTENT

Publication Title	The British journal of radiology	Rightsholder	British Institute of Radiology
Article Title	Human whole body line-scan imaging by NMR.	Publication Type	Journal
Author/Editor	British Institute of Radiology.	Start Page	921
		End Page	922
Date	01/01/1896	Issue	611
Language	English	Volume	51
Country	United Kingdom of Great Britain and Northern Ireland		

REQUEST DETAILS

Portion Type	Image/photo/illustration	Distribution	Worldwide
Number of Images / Photos / Illustrations	1	Translation	Original language of publication
Format (select all that apply)	Electronic	Copies for the Disabled?	No
		Minor Editing Privileges?	No
Who Will Republish the Content?	Academic institution	Incidental Promotional Use?	No
Duration of Use	Life of current edition	Currency	GBP
Lifetime Unit Quantity	Up to 499		
Rights Requested	Main product		

NEW WORK DETAILS

Title	Probing organ structure, function and physiology using Quantitative Magnetic Resonance Imaging techniques	Institution Name	University of Nottingham
		Expected Presentation Date	2023-06-15
Instructor Name	Christopher Bradley		

ADDITIONAL DETAILS

Order Reference Number	3

The Requesting Person/Organization to Appear on the License	Christopher Bradley

REQUESTED CONTENT DETAILS

Title, Description or Numeric Reference of the Portion(s)	Figure 1	**Title of the Article/Chapter the Portion Is From**	Human whole body line-scan imaging by NMR.
Editor of Portion(s)	Mansfield, P; Pykett, I L; Morris, P G	**Author of Portion(s)**	Mansfield, P; Pykett, I L; Morris, P G
Volume / Edition	51	**Issue, if Republishing an Article From a Serial**	611
Page or Page Range of Portion	921-922	**Publication Date of Portion**	1978-11-01

RIGHTSHOLDER TERMS AND CONDITIONS

BJR and DMFR are hybrid open access titles. Please check the original article for open access status, as these require different permissions

Marketplace Permissions General Terms and Conditions

The following terms and conditions ("General Terms"), together with any applicable Publisher Terms and Conditions, govern User's use of Works pursuant to the Licenses granted by Copyright Clearance Center, Inc. ("CCC") on behalf of the applicable Rightsholders of such Works through CCC's applicable Marketplace transactional licensing services (each, a "Service").

1) **Definitions.** For purposes of these General Terms, the following definitions apply:

"License" is the licensed use the User obtains via the Marketplace platform in a particular licensing transaction, as set forth in the Order Confirmation.

"Order Confirmation" is the confirmation CCC provides to the User at the conclusion of each Marketplace transaction. "Order Confirmation Terms" are additional terms set forth on specific Order Confirmations not set forth in the General Terms that can include terms applicable to a particular CCC transactional licensing service and/or any Rightsholder-specific terms.

"Rightsholder(s)" are the holders of copyright rights in the Works for which a User obtains licenses via the Marketplace platform, which are displayed on specific Order Confirmations.

"Terms" means the terms and conditions set forth in these General Terms and any additional Order Confirmation Terms collectively.

"User" or "you" is the person or entity making the use granted under the relevant License. Where the person accepting the Terms on behalf of a User is a freelancer or other third party who the User authorized to accept the General Terms on the User's behalf, such person shall be deemed jointly a User for purposes of such Terms.

"Work(s)" are the copyright protected works described in relevant Order Confirmations.

2) **Description of Service.** CCC's Marketplace enables Users to obtain Licenses to use one or more Works in accordance with all relevant Terms. CCC grants Licenses as an agent on behalf of the copyright rightsholder identified in the relevant Order Confirmation.

3) **Applicability of Terms.** The Terms govern User's use of Works in connection with the relevant License. In the event of any conflict between General Terms and Order Confirmation Terms, the latter shall govern. User acknowledges that Rightsholders have complete discretion whether to grant any permission, and whether to place any limitations on any grant, and that CCC has no right to supersede or to modify any such discretionary act by a Rightsholder.

4) **Representations; Acceptance.** By using the Service, User represents and warrants that User has been duly authorized by the User to accept, and hereby does accept, all Terms.

5) **Scope of License; Limitations and Obligations.** All Works and all rights therein, including copyright rights, remain the sole and exclusive property of the Rightsholder. The License provides only those rights expressly set forth in the terms and conveys no other rights in any Works

6) **General Payment Terms.** User may pay at time of checkout by credit card or choose to be invoiced. If the User chooses to be invoiced, the User shall: (i) remit payments in the manner identified on specific invoices, (ii) unless otherwise specifically stated in an Order Confirmation or separate written agreement, Users shall remit payments upon receipt of the relevant invoice from CCC, either by delivery or notification of availability of the invoice via the Marketplace platform, and (iii) if the User does not pay the invoice within 30 days of receipt, the User may incur a service charge of 1.5% per month or the maximum rate allowed by applicable law, whichever is less. While User may exercise the rights in the License immediately upon receiving the Order Confirmation, the License is automatically revoked and is null and void, as if it had never been issued, if CCC does not receive complete payment on a timely basis.

7) **General Limits on Use.** Unless otherwise provided in the Order Confirmation, any grant of rights to User (i) involves only the rights set forth in the Terms and does not include subsequent or additional uses, (ii) is non-exclusive and non-transferable, and (iii) is subject to any and all limitations and restrictions (such as, but not limited to, limitations on duration of use or circulation) included in the Terms. Upon completion of the licensed use as set forth in the Order Confirmation, User shall either secure a new permission for further use of the Work(s) or immediately cease any new use of the Work(s) and shall render inaccessible (such as by deleting or by removing or severing links or other locators) any further copies of the Work. User may only make alterations to the Work if and as expressly set forth in the Order Confirmation. No Work may be used in any way that is unlawful, including without limitation if such use would violate applicable sanctions laws or regulations, would be defamatory, violate the rights of third parties (including such third parties' rights of copyright, privacy, publicity, or other tangible or intangible property), or is otherwise illegal, sexually explicit, or obscene. In addition, User may not conjoin a Work with any other material that may result in damage to the reputation of the Rightsholder. Any unlawful use will render any licenses hereunder null and void. User agrees to inform CCC if it becomes aware of any infringement of any rights in a Work and to cooperate with any reasonable request of CCC or the Rightsholder in connection therewith.

8) **Third Party Materials.** In the event that the material for which a License is sought includes third party materials (such as photographs, illustrations, graphs, inserts and similar materials) that are identified in such material as having been used by permission (or a similar indicator), User is responsible for identifying, and seeking separate licenses (under this Service, if available, or otherwise) for any of such third party materials; without a separate license, User may not use such third party materials via the License.

9) **Copyright Notice.** Use of proper copyright notice for a Work is required as a condition of any License granted under the Service. Unless otherwise provided in the Order Confirmation, a proper copyright notice will read substantially as follows: "Used with permission of [Rightsholder's name], from [Work's title, author, volume, edition number and year of copyright]; permission conveyed through Copyright Clearance Center, Inc." Such notice must be provided in a reasonably legible font size and must be placed either on a cover page or in another location that any person, upon gaining access to the material which is the subject of a permission, shall see, or in the case of republication Licenses, immediately adjacent to the Work as used (for example, as part of a by-line or footnote) or in the place where substantially all other credits or notices for the new work containing the republished Work are located. Failure to include the required notice results in loss to the Rightsholder and CCC, and the User shall be liable to pay liquidated damages for each such failure equal to twice the use fee specified in the Order Confirmation, in addition to the use fee itself and any other fees and charges specified.

10) **Indemnity.** User hereby indemnifies and agrees to defend the Rightsholder and CCC, and their respective employees and directors, against all claims, liability, damages, costs, and expenses, including legal fees and expenses, arising out of any use of a Work beyond the scope of the rights granted herein and in the Order Confirmation, or any use of a Work which has been altered in any unauthorized way by User, including claims of defamation or infringement of rights of copyright, publicity, privacy, or other tangible or intangible property.

11) **Limitation of Liability.** UNDER NO CIRCUMSTANCES WILL CCC OR THE RIGHTSHOLDER BE LIABLE FOR ANY DIRECT, INDIRECT, CONSEQUENTIAL, OR INCIDENTAL DAMAGES (INCLUDING WITHOUT LIMITATION DAMAGES FOR LOSS OF BUSINESS PROFITS OR INFORMATION, OR FOR BUSINESS INTERRUPTION) ARISING OUT OF THE USE OR INABILITY TO USE A WORK, EVEN IF ONE OR BOTH OF THEM HAS BEEN ADVISED OF THE POSSIBILITY OF SUCH DAMAGES. In any event, the total liability of the Rightsholder and CCC (including their respective employees and directors) shall not exceed the total amount actually paid by User for the relevant License. User assumes full liability for the actions and omissions of its principals, employees, agents, affiliates, successors, and assigns.

12) **Limited Warranties.** THE WORK(S) AND RIGHT(S) ARE PROVIDED "AS IS." CCC HAS THE RIGHT TO GRANT TO USER THE RIGHTS GRANTED IN THE ORDER CONFIRMATION DOCUMENT. CCC AND THE RIGHTSHOLDER DISCLAIM ALL OTHER WARRANTIES RELATING TO THE WORK(S) AND RIGHT(S), EITHER EXPRESS OR IMPLIED, INCLUDING WITHOUT LIMITATION IMPLIED WARRANTIES OF MERCHANTABILITY OR FITNESS FOR A PARTICULAR PURPOSE. ADDITIONAL RIGHTS MAY BE REQUIRED TO USE ILLUSTRATIONS, GRAPHS, PHOTOGRAPHS, ABSTRACTS, INSERTS, OR OTHER PORTIONS OF THE WORK (AS OPPOSED TO THE ENTIRE WORK) IN A MANNER CONTEMPLATED BY USER; USER UNDERSTANDS AND AGREES THAT NEITHER CCC NOR THE RIGHTSHOLDER MAY HAVE SUCH ADDITIONAL RIGHTS TO GRANT.

13) **Effect of Breach.** Any failure by User to pay any amount when due, or any use by User of a Work beyond the scope of the License set forth in the Order Confirmation and/or the Terms, shall be a material breach of such License. Any breach

not cured within 10 days of written notice thereof shall result in immediate termination of such License without further notice. Any unauthorized (but licensable) use of a Work that is terminated immediately upon notice thereof may be liquidated by payment of the Rightsholder's ordinary license price therefor; any unauthorized (and unlicensable) use that is not terminated immediately for any reason (including, for example, because materials containing the Work cannot reasonably be recalled) will be subject to all remedies available at law or in equity, but in no event to a payment of less than three times the Rightsholder's ordinary license price for the most closely analogous licensable use plus Rightsholder's and/or CCC's costs and expenses incurred in collecting such payment.

14) **Additional Terms for Specific Products and Services.** If a User is making one of the uses described in this Section 14, the additional terms and conditions apply:

a) ***Print Uses of Academic Course Content and Materials (photocopies for academic coursepacks or classroom handouts).*** For photocopies for academic coursepacks or classroom handouts the following additional terms apply:

i) The copies and anthologies created under this License may be made and assembled by faculty members individually or at their request by on-campus bookstores or copy centers, or by off-campus copy shops and other similar entities.

ii) No License granted shall in any way: (i) include any right by User to create a substantively non-identical copy of the Work or to edit or in any other way modify the Work (except by means of deleting material immediately preceding or following the entire portion of the Work copied) (ii) permit "publishing ventures" where any particular anthology would be systematically marketed at multiple institutions.

iii) Subject to any Publisher Terms (and notwithstanding any apparent contradiction in the Order Confirmation arising from data provided by User), any use authorized under the academic pay-per-use service is limited as follows:

A) any License granted shall apply to only one class (bearing a unique identifier as assigned by the institution, and thereby including all sections or other subparts of the class) at one institution;

B) use is limited to not more than 25% of the text of a book or of the items in a published collection of essays, poems or articles;

C) use is limited to no more than the greater of (a) 25% of the text of an issue of a journal or other periodical or (b) two articles from such an issue;

D) no User may sell or distribute any particular anthology, whether photocopied or electronic, at more than one institution of learning;

E) in the case of a photocopy permission, no materials may be entered into electronic memory by User except in order to produce an identical copy of a Work before or during the academic term (or analogous period) as to which any particular permission is granted. In the event that User shall choose to retain materials that are the subject of a photocopy permission in electronic memory for purposes of producing identical copies more than one day after such retention (but still within the scope of any permission granted), User must notify CCC of such fact in the applicable permission request and such retention shall constitute one copy actually sold for purposes of calculating permission fees due; and

F) any permission granted shall expire at the end of the class. No permission granted shall in any way include any right by User to create a substantively non-identical copy of the Work or to edit or in any other way modify the Work (except by means of deleting material immediately preceding or following the entire portion of the Work copied).

iv) Books and Records; Right to Audit. As to each permission granted under the academic pay-per-use Service, User shall maintain for at least four full calendar years books and records sufficient for CCC to determine the numbers of copies made by User under such permission. CCC and any representatives it may designate shall have the right to audit such books and records at any time during User's ordinary business hours, upon two days' prior notice. If any such audit shall determine that User shall have underpaid for, or underreported, any photocopies sold or by three percent (3%) or more, then User shall bear all the costs of any such audit; otherwise, CCC shall bear the costs of any such audit. Any amount determined by such audit to have been underpaid by User shall immediately be paid to CCC by User, together with interest thereon at the rate of 10% per annum from the date such amount was originally due. The provisions of this paragraph shall survive the termination of this License for any reason.

b) ***Digital Pay-Per-Uses of Academic Course Content and Materials (e-coursepacks, electronic reserves, learning management systems, academic institution intranets).*** For uses in e-coursepacks, posts in electronic reserves, posts in learning management systems, or posts on academic institution intranets, the following additional terms apply:

i) The pay-per-uses subject to this Section 14(b) include:

A) **Posting e-reserves, course management systems, e-coursepacks for text-based content,** which grants authorizations to import requested material in electronic format, and allows electronic access to this material to members of a designated college or university class, under the direction of an instructor designated by the college or university, accessible only under appropriate electronic controls (e.g., password);

B) **Posting e-reserves, course management systems, e-coursepacks for material consisting of photographs or other still images not embedded in text,** which grants not only the authorizations described in Section 14(b)(i)(A) above, but also the following authorization: to include the requested material in course materials for use consistent with Section 14(b)(i)(A) above, including any necessary resizing, reformatting or modification of the resolution of such requested material (provided that such modification does not alter the underlying editorial content or meaning of the requested material, and provided that the resulting modified content is used solely within the scope of, and in a manner consistent with, the particular authorization described in the Order Confirmation and the Terms), but not including any other form of manipulation, alteration or editing of the requested material;

C) **Posting e-reserves, course management systems, e-coursepacks or other academic distribution for audiovisual content,** which grants not only the authorizations described in Section 14(b)(i)(A) above, but also the following authorizations: (i) to include the requested material in course materials for use consistent with Section 14(b)(i)(A) above; (ii) to display and perform the requested material to such members of such class in the physical classroom or remotely by means of streaming media or other video formats; and (iii) to "clip" or reformat the requested material for purposes of time or content management or ease of delivery, provided that such “clipping” or reformatting does not alter the underlying editorial content or meaning of the requested material and that the resulting material is used solely within the scope of, and in a manner consistent with, the particular authorization described in the Order Confirmation and the Terms. Unless expressly set forth in the relevant Order Conformation, the License does not authorize any other form of manipulation, alteration or editing of the requested material.

ii) Unless expressly set forth in the relevant Order Confirmation, no License granted shall in any way: (i) include any right by User to create a substantively non-identical copy of the Work or to edit or in any other way modify the Work (except by means of deleting material immediately preceding or following the entire portion of the Work copied or, in the case of Works subject to Sections 14(b)(1)(B) or (C) above, as described in such Sections) (ii) permit "publishing ventures" where any particular course materials would be systematically marketed at multiple institutions.

iii) Subject to any further limitations determined in the Rightsholder Terms (and notwithstanding any apparent contradiction in the Order Confirmation arising from data provided by User), any use authorized under the electronic course content pay-per-use service is limited as follows:

A) any License granted shall apply to only one class (bearing a unique identifier as assigned by the institution, and thereby including all sections or other subparts of the class) at one institution;

B) use is limited to not more than 25% of the text of a book or of the items in a published collection of essays, poems or articles;

C) use is limited to not more than the greater of (a) 25% of the text of an issue of a journal or other periodical or (b) two articles from such an issue;

D) no User may sell or distribute any particular materials, whether photocopied or electronic, at more than one institution of learning;

E) electronic access to material which is the subject of an electronic-use permission must be limited by means of electronic password, student identification or other control permitting access solely to students and instructors in the class;

F) User must ensure (through use of an electronic cover page or other appropriate means) that any person, upon gaining electronic access to the material, which is the subject of a permission, shall see:

- a proper copyright notice, identifying the Rightsholder in whose name CCC has granted permission,
- a statement to the effect that such copy was made pursuant to permission,
- a statement identifying the class to which the material applies and notifying the reader that the material has been made available electronically solely for use in the class, and
- a statement to the effect that the material may not be further distributed to any person outside the class, whether by copying or by transmission and whether electronically or in paper form, and User must also

ensure that such cover page or other means will print out in the event that the person accessing the material chooses to print out the material or any part thereof.

G) any permission granted shall expire at the end of the class and, absent some other form of authorization, User is thereupon required to delete the applicable material from any electronic storage or to block electronic access to the applicable material.

iv) Uses of separate portions of a Work, even if they are to be included in the same course material or the same university or college class, require separate permissions under the electronic course content pay-per-use Service. Unless otherwise provided in the Order Confirmation, any grant of rights to User is limited to use completed no later than the end of the academic term (or analogous period) as to which any particular permission is granted.

v) Books and Records; Right to Audit. As to each permission granted under the electronic course content Service, User shall maintain for at least four full calendar years books and records sufficient for CCC to determine the numbers of copies made by User under such permission. CCC and any representatives it may designate shall have the right to audit such books and records at any time during User's ordinary business hours, upon two days' prior notice. If any such audit shall determine that User shall have underpaid for, or underreported, any electronic copies used by three percent (3%) or more, then User shall bear all the costs of any such audit; otherwise, CCC shall bear the costs of any such audit. Any amount determined by such audit to have been underpaid by User shall immediately be paid to CCC by User, together with interest thereon at the rate of 10% per annum from the date such amount was originally due. The provisions of this paragraph shall survive the termination of this license for any reason.

c) ***Pay-Per-Use Permissions for Certain Reproductions (Academic photocopies for library reserves and interlibrary loan reporting) (Non-academic internal/external business uses and commercial document delivery).*** The License expressly excludes the uses listed in Section (c)(i)-(v) below (which must be subject to separate license from the applicable Rightsholder) for: academic photocopies for library reserves and interlibrary loan reporting; and non-academic internal/external business uses and commercial document delivery.

i) electronic storage of any reproduction (whether in plain-text, PDF, or any other format) other than on a transitory basis;

ii) the input of Works or reproductions thereof into any computerized database;

iii) reproduction of an entire Work (cover-to-cover copying) except where the Work is a single article;

iv) reproduction for resale to anyone other than a specific customer of User;

v) republication in any different form. Please obtain authorizations for these uses through other CCC services or directly from the rightsholder.

Any license granted is further limited as set forth in any restrictions included in the Order Confirmation and/or in these Terms.

d) ***Electronic Reproductions in Online Environments (Non-Academic-email, intranet, internet and extranet).*** For "electronic reproductions", which generally includes e-mail use (including instant messaging or other electronic transmission to a defined group of recipients) or posting on an intranet, extranet or Intranet site (including any display or performance incidental thereto), the following additional terms apply:

i) Unless otherwise set forth in the Order Confirmation, the License is limited to use completed within 30 days for any use on the Internet, 60 days for any use on an intranet or extranet and one year for any other use, all as measured from the "republication date" as identified in the Order Confirmation, if any, and otherwise from the date of the Order Confirmation.

ii) User may not make or permit any alterations to the Work, unless expressly set forth in the Order Confirmation (after request by User and approval by Rightsholder); provided, however, that a Work consisting of photographs or other still images not embedded in text may, if necessary, be resized, reformatted or have its resolution modified without additional express permission, and a Work consisting of audiovisual content may, if necessary, be "clipped" or reformatted for purposes of time or content management or ease of delivery (provided that any such resizing, reformatting, resolution modification or “clipping” does not alter the underlying editorial content or meaning of the Work used, and that the resulting material is used solely within the scope of, and in a manner consistent with, the particular License described in the Order Confirmation and the Terms.

15) **Miscellaneous.**

a) User acknowledges that CCC may, from time to time, make changes or additions to the Service or to the Terms, and that Rightsholder may make changes or additions to the Rightsholder Terms. Such updated Terms will replace the

prior terms and conditions in the order workflow and shall be effective as to any subsequent Licenses but shall not apply to Licenses already granted and paid for under a prior set of terms.

b) Use of User-related information collected through the Service is governed by CCC's privacy policy, available online at www.copyright.com/about/privacy-policy/.

c) The License is personal to User. Therefore, User may not assign or transfer to any other person (whether a natural person or an organization of any kind) the License or any rights granted thereunder; provided, however, that, where applicable, User may assign such License in its entirety on written notice to CCC in the event of a transfer of all or substantially all of User's rights in any new material which includes the Work(s) licensed under this Service.

d) No amendment or waiver of any Terms is binding unless set forth in writing and signed by the appropriate parties, including, where applicable, the Rightsholder. The Rightsholder and CCC hereby object to any terms contained in any writing prepared by or on behalf of the User or its principals, employees, agents or affiliates and purporting to govern or otherwise relate to the License described in the Order Confirmation, which terms are in any way inconsistent with any Terms set forth in the Order Confirmation, and/or in CCC's standard operating procedures, whether such writing is prepared prior to, simultaneously with or subsequent to the Order Confirmation, and whether such writing appears on a copy of the Order Confirmation or in a separate instrument.

e) The License described in the Order Confirmation shall be governed by and construed under the law of the State of New York, USA, without regard to the principles thereof of conflicts of law. Any case, controversy, suit, action, or proceeding arising out of, in connection with, or related to such License shall be brought, at CCC's sole discretion, in any federal or state court located in the County of New York, State of New York, USA, or in any federal or state court whose geographical jurisdiction covers the location of the Rightsholder set forth in the Order Confirmation. The parties expressly submit to the personal jurisdiction and venue of each such federal or state court.

Last updated October 2022

10.5 Appendix E: Creative Commons: Attribution-NoDerivatives 4.0 International

Creative Commons Legal Code

Attribution-NoDerivatives 4.0 International

Official translations of this license are available in other languages.

Creative Commons Corporation (“Creative Commons”) is not a law firm and does not provide legal services or legal advice. Distribution of Creative Commons public licenses does not create a lawyer-client or other relationship. Creative Commons makes its licenses and related information available on an “as-is” basis. Creative Commons gives no warranties regarding its licenses, any material licensed under their terms and conditions, or any related information. Creative Commons disclaims all liability for damages resulting from their use to the fullest extent possible.

Using Creative Commons Public Licenses

Creative Commons public licenses provide a standard set of terms and conditions that creators and other rights holders may use to share original works of authorship and other material subject to copyright and certain other rights specified in the public license below. The following considerations are for informational purposes only, are not exhaustive, and do not form part of our licenses.

Considerations for licensors: Our public licenses are intended for use by those authorized to give the public permission to use material in ways otherwise restricted by copyright and certain other rights. Our licenses are irrevocable. Licensors should read and understand the terms and conditions of the license they choose before applying it. Licensors should also secure all rights necessary before applying our licenses so that the public can reuse the material as expected. Licensors should clearly mark any material not subject to the license. This includes other CC-licensed material, or material used under an exception or limitation to copyright.

Considerations for the public: By using one of our public licenses, a licensor grants the public permission to use the licensed material under specified terms and conditions. If the licensor’s permission is not necessary for any reason–for example, because of any applicable exception or limitation to copyright–then that use is not regulated by the license. Our licenses grant only permissions under copyright and certain other rights that a licensor has authority to grant. Use of the licensed material may still be restricted for other reasons, including because others have copyright or other rights in the material. A licensor may make special requests, such as asking that all changes be marked or described. Although not required by our licenses, you are encouraged to respect those requests where reasonable.

Creative Commons Attribution-NoDerivatives 4.0 International Public License

By exercising the Licensed Rights (defined below), You accept and agree to be bound by the terms and conditions of this Creative Commons Attribution-NoDerivatives 4.0 International Public License ("Public License"). To the extent this Public License may be interpreted as a contract, You are granted the Licensed Rights in consideration of Your acceptance of these terms and conditions, and the Licensor grants You such rights in consideration of benefits the Licensor receives from making the Licensed Material available under these terms and conditions.

Section 1 – Definitions.

a. **Adapted Material** means material subject to Copyright and Similar Rights that is derived from or based upon the Licensed Material and in which the Licensed Material is translated, altered, arranged, transformed, or otherwise modified in a manner requiring permission under the Copyright and Similar Rights held by the Licensor. For purposes of this Public License, where the Licensed Material is a musical work, performance, or sound recording, Adapted Material is always produced where the Licensed Material is synched in timed relation with a moving image.
b. **Copyright and Similar Rights** means copyright and/or similar rights closely related to copyright including, without limitation, performance, broadcast, sound recording, and Sui Generis Database Rights, without regard to how the rights are labeled or categorized. For purposes of this Public License, the rights specified in Section 2(b)(1)-(2) are not Copyright and Similar Rights.
c. **Effective Technological Measures** means those measures that, in the absence of proper authority, may not be circumvented under laws fulfilling obligations under Article 11 of the WIPO Copyright Treaty adopted on December 20, 1996, and/or similar international agreements.
d. **Exceptions and Limitations** means fair use, fair dealing, and/or any other exception or limitation to Copyright and Similar Rights that applies to Your use of the Licensed Material.
e. **Licensed Material** means the artistic or literary work, database, or other material to which the Licensor applied this Public License.
f. **Licensed Rights** means the rights granted to You subject to the terms and conditions of this Public License, which are limited to all Copyright and Similar Rights that apply to Your use of the Licensed Material and that the Licensor has authority to license.
g. **Licensor** means the individual(s) or entity(ies) granting rights under this Public License.
h. **Share** means to provide material to the public by any means or process that requires permission under the Licensed Rights, such as reproduction, public display, public performance, distribution, dissemination, communication, or importation, and to make material available to the public including in ways that members of the public may access the material from a place and at a time individually chosen by them.
i. **Sui Generis Database Rights** means rights other than copyright resulting from Directive 96/9/EC of the European Parliament and of the Council of 11 March 1996 on the legal protection of databases, as amended and/or succeeded, as well as other essentially equivalent rights anywhere in the world.
j. **You** means the individual or entity exercising the Licensed Rights under this Public License. **Your** has a corresponding meaning.

Section 2 – Scope.

a. **License grant**.

1. Subject to the terms and conditions of this Public License, the Licensor hereby grants You a worldwide, royalty-free, non-sublicensable, non-exclusive, irrevocable license to exercise the Licensed Rights in the Licensed Material to:
   A. reproduce and Share the Licensed Material, in whole or in part; and
   B. produce and reproduce, but not Share, Adapted Material.
2. Exceptions and Limitations. For the avoidance of doubt, where Exceptions and Limitations apply to Your use, this Public License does not apply, and You do not need to comply with its terms and conditions.
3. Term. The term of this Public License is specified in Section 6(a).
4. Media and formats; technical modifications allowed. The Licensor authorizes You to exercise the Licensed Rights in all media and formats whether now known or hereafter created, and to make technical modifications necessary to do so. The Licensor waives and/or agrees not to assert any right or authority to forbid You from making technical modifications necessary to exercise the Licensed Rights, including technical modifications necessary to circumvent Effective Technological Measures. For purposes of this Public License, simply making modifications authorized by this Section 2(a)(4) never produces Adapted Material.
5. Downstream recipients.
   A. Offer from the Licensor – Licensed Material. Every recipient of the Licensed Material automatically receives an offer from the Licensor to exercise the Licensed Rights under the terms and conditions of this Public License.
   B. No downstream restrictions. You may not offer or impose any additional or different terms or conditions on, or apply any Effective Technological Measures to, the Licensed Material if doing so restricts exercise of the Licensed Rights by any recipient of the Licensed Material.
6. No endorsement. Nothing in this Public License constitutes or may be construed as permission to assert or imply that You are, or that Your use of the Licensed Material is, connected with, or sponsored, endorsed, or granted official status by, the Licensor or others designated to receive attribution as provided in Section 3(a)(1)(A)(i).

b. **Other rights**.

1. Moral rights, such as the right of integrity, are not licensed under this Public License, nor are publicity, privacy, and/or other similar personality rights; however, to the extent possible, the Licensor waives and/or agrees not to assert any such rights held by the Licensor to the limited extent necessary to allow You to exercise the Licensed Rights, but not otherwise.
2. Patent and trademark rights are not licensed under this Public License.
3. To the extent possible, the Licensor waives any right to collect royalties from You for the exercise of the Licensed Rights, whether directly or through a collecting society under any voluntary or waivable statutory or compulsory licensing scheme. In all other cases the Licensor expressly reserves any right to collect such royalties.

Section 3 – License Conditions.

Your exercise of the Licensed Rights is expressly made subject to the following conditions.

a. **Attribution**.

1. If You Share the Licensed Material, You must:

   A. retain the following if it is supplied by the Licensor with the Licensed Material:
      i. identification of the creator(s) of the Licensed Material and any others designated to receive attribution, in any reasonable manner requested by the Licensor (including by pseudonym if designated);
      ii. a copyright notice;
      iii. a notice that refers to this Public License;
      iv. a notice that refers to the disclaimer of warranties;
      v. a URI or hyperlink to the Licensed Material to the extent reasonably practicable;
   B. indicate if You modified the Licensed Material and retain an indication of any previous modifications; and
   C. indicate the Licensed Material is licensed under this Public License, and include the text of, or the URI or hyperlink to, this Public License.

   For the avoidance of doubt, You do not have permission under this Public License to Share Adapted Material.
2. You may satisfy the conditions in Section 3(a)(1) in any reasonable manner based on the medium, means, and context in which You Share the Licensed Material. For example, it may be reasonable to satisfy the conditions by providing a URI or hyperlink to a resource that includes the required information.
3. If requested by the Licensor, You must remove any of the information required by Section 3(a)(1)(A) to the extent reasonably practicable.

Section 4 – Sui Generis Database Rights.

Where the Licensed Rights include Sui Generis Database Rights that apply to Your use of the Licensed Material:

a. for the avoidance of doubt, Section 2(a)(1) grants You the right to extract, reuse, reproduce, and Share all or a substantial portion of the contents of the database, provided You do not Share Adapted Material;
b. if You include all or a substantial portion of the database contents in a database in which You have Sui Generis Database Rights, then the database in which You have Sui Generis Database Rights (but not its individual contents) is Adapted Material; and
c. You must comply with the conditions in Section 3(a) if You Share all or a substantial portion of the contents of the database.

For the avoidance of doubt, this Section 4 supplements and does not replace Your obligations under this Public License where the Licensed Rights include other Copyright and Similar Rights.

Section 5 – Disclaimer of Warranties and Limitation of Liability.

a. **Unless otherwise separately undertaken by the Licensor, to the extent possible, the Licensor offers the Licensed Material as-is and as-available, and makes no representations or warranties of any kind concerning the Licensed Material, whether express, implied, statutory, or other. This includes, without limitation, warranties of title, merchantability, fitness for a particular purpose, non-infringement, absence of latent or other defects, accuracy, or the presence or absence of errors, whether or not known or discoverable. Where disclaimers of warranties are not allowed in full or in part, this disclaimer may not apply to You.**
b. **To the extent possible, in no event will the Licensor be liable to You on any legal theory (including, without limitation, negligence) or otherwise for any direct, special, indirect, incidental, consequential, punitive, exemplary, or other losses, costs, expenses, or damages arising out of this Public License or use of the Licensed Material, even if the Licensor has been advised of the possibility of such losses, costs, expenses, or damages. Where a limitation of liability is not allowed in full or in part, this limitation may not apply to You.**

c. The disclaimer of warranties and limitation of liability provided above shall be interpreted in a manner that, to the extent possible, most closely approximates an absolute disclaimer and waiver of all liability.

Section 6 – Term and Termination.

a. This Public License applies for the term of the Copyright and Similar Rights licensed here. However, if You fail to comply with this Public License, then Your rights under this Public License terminate automatically.
b. Where Your right to use the Licensed Material has terminated under Section 6(a), it reinstates:

    1. automatically as of the date the violation is cured, provided it is cured within 30 days of Your discovery of the violation; or
    2. upon express reinstatement by the Licensor.

    For the avoidance of doubt, this Section 6(b) does not affect any right the Licensor may have to seek remedies for Your violations of this Public License.
c. For the avoidance of doubt, the Licensor may also offer the Licensed Material under separate terms or conditions or stop distributing the Licensed Material at any time; however, doing so will not terminate this Public License.
d. Sections 1, 5, 6, 7, and 8 survive termination of this Public License.

Section 7 – Other Terms and Conditions.

a. The Licensor shall not be bound by any additional or different terms or conditions communicated by You unless expressly agreed.
b. Any arrangements, understandings, or agreements regarding the Licensed Material not stated herein are separate from and independent of the terms and conditions of this Public License.

Section 8 – Interpretation.

a. For the avoidance of doubt, this Public License does not, and shall not be interpreted to, reduce, limit, restrict, or impose conditions on any use of the Licensed Material that could lawfully be made without permission under this Public License.
b. To the extent possible, if any provision of this Public License is deemed unenforceable, it shall be automatically reformed to the minimum extent necessary to make it enforceable. If the provision cannot be reformed, it shall be severed from this Public License without affecting the enforceability of the remaining terms and conditions.
c. No term or condition of this Public License will be waived and no failure to comply consented to unless expressly agreed to by the Licensor.
d. Nothing in this Public License constitutes or may be interpreted as a limitation upon, or waiver of, any privileges and immunities that apply to the Licensor or You, including from the legal processes of any jurisdiction or authority.

Creative Commons is not a party to its public licenses. Notwithstanding, Creative Commons may elect to apply one of its public licenses to material it publishes and in those instances will be considered the “Licensor.” The text of the Creative Commons public licenses is dedicated to the public domain under the CC0 Public Domain Dedication. Except for the limited purpose of indicating that material is shared under a Creative Commons public license or as otherwise permitted by the Creative Commons policies published at creativecommons.org/policies, Creative Commons does not authorize the use of the trademark “Creative Commons” or any other trademark or logo of Creative Commons without its prior written consent including, without limitation, in connection with any unauthorized modifications to any of its public licenses or any other arrangements, understandings, or agreements concerning use of licensed material. For the avoidance of doubt, this paragraph does not form part of the public licenses.

Creative Commons may be contacted at creativecommons.org.

Additional languages available: العربية, čeština, Dansk, Deutsch, Ελληνικά, Español, euskara, suomeksi, français, Frysk, hrvatski, Bahasa Indonesia, italiano, 日本語, 한국어, Lietuvių, latviski, te reo Māori, Nederlands, norsk, polski, português, română, русский, Slovenščina, svenska, Türkçe, українська, 中文, 華語. Please read the FAQ for more information about official translations.